

Fabien Renault

A Lagrangian slug capturing scheme for gas-liquid flows in pipes

Thesis for the degree of philosophiae doctor

Trondheim, June 2007

Norwegian University of
Science and Technology
Faculty of Engineering Science and Technology
Department of Energy and Process Engineering

NTNU
Norwegian University of Science and Technology

Thesis for the degree of philosophiae doctor

Faculty of Engineering Science and Technology
Department of Energy and Process Engineering

©Fabien Renault

ISBN 978-82-471-3179-4 (printed ver.)
ISBN 978-82-471-3182-4 (electronic ver.)
ISSN 1503-8181

Theses at NTNU, 2007:145

Printed by Tapir Uttrykk

NORGES TEKNISKE OG
NATURVITENSKAPELIGE UNIVERSITETET

*A Lagrangian slug
capturing scheme for
gas-liquid flows in
pipes*

Fabien RENAULT

Doctoral thesis submitted for the degree of doctor philosophiae

May 2007

Supervisor: Prof. Ole Jørgen Nydal

Abstract

In this thesis a new Lagrangian numerical scheme for the simulation of gas-liquid flows in pipelines is presented. Based on an approximate two-fluid model, this new scheme, called LASSI (Lagrangian Approximate Scheme for Slug Initiation) is dedicated to the modelling of the transition between stratified and slug flow. It is able to capture directly the slug initiation process and to track the motion of every single slug in the pipe without numerical diffusion. It can thus be qualified as a slug capturing and slug tracking scheme.

The scheme is based on the decoupling between the fast pressure dynamics governing the motion of the slugs and the much slower liquid transport in the bubbles. The liquid motion in the bubbles is then approximately modelled by a modified version of the shallow water equations, in which the influence of the Bernoulli suction force is subtracted from the traditional hydrodynamical term. The fully Lagrangian structure of the scheme makes it possible to accurately capture the transport of the fast interfacial waves whose growth can eventually result in a slug initiation.

The model predictions are compared with some experimental results obtained in the NTNU multiphase flow laboratory or taken from the literature. Several flow conditions are considered, in particular the case of hydrodynamic slugging in near-horizontal flows, slugging in an upwards pipe, severe slugging, and slugging triggered by fast transients. Numerical predictions are also compared with theoretical considerations regarding the stability of stratified flow.

Contents

Slug capturing	viii
Acknowledgements	x
Summary	xii
1 Introduction	1
1.1 Gas-liquid flow in pipelines	1
1.2 The transition between stratified and slug flow	2
1.3 The modelling of slug flow with gas-liquid flow schemes	5
1.4 Modelling the slug initiation with a transient scheme for gas-liquid flow	7
1.5 Objective and scope of this thesis	9
1.6 Applications	10
1.7 Presentation of the papers	10
1.8 Structure of the introductory part	12
2 Closure laws	15
2.1 Friction factors	15
2.1.1 A short review	15
2.1.2 Importance of the interfacial friction factor on the transition from stratified to slug flow	17
2.1.3 Implementation in LASSI	19
2.2 Slug border closures	19
2.2.1 Slug front	19
2.2.2 Bubble nose	20
2.2.3 Nature of the slug-bubble and bubble-slug borders	21
2.3 Wake effect	23
2.4 Gas law	24
3 Details of the LASSI scheme	27
3.1 Introduction	27
3.2 The model	28
3.2.1 The general two-fluid model	28
3.2.2 Simplifying the two-fluid model	28
3.2.3 The LASSI model	31
3.3 Grid	31

3.4	Solution procedure	32
3.5	Pressure momentum step	34
3.5.1	Discretization of the equations	34
3.5.2	Solving procedure	36
3.6	Void wave	38
3.6.1	The shallow water equations	38
3.6.2	Solving the Riemann problem	39
3.6.3	Calculating the fluxes	41
3.6.4	Front tracking	42
3.6.5	Updating holdup and velocities	44
3.6.6	Slug fronts	44
3.7	List management	45
3.7.1	Implementation	45
3.7.2	Splitting	46
3.7.3	Merging	46
3.7.4	Slug initiation	48
3.8	Boundary treatment	48
3.8.1	Inlet	48
3.8.2	Outlet	50
4	Influence of the integration parameters on the predictions	55
4.1	Influence of the section size on the slug length	55
4.2	Influence of the section length and of the time step on the transition point from stratified to slug flow	57
5	References	61
6	Nomenclature	66
A	Void wave step: the different cases	69
A.1	Void wave variables	69
A.2	Case of β_M greater than one	70
A.3	Average holdup within a rarefaction wave	71
A.4	Tables	72
B	Stability analysis of an upwind-differentiated two-fluid model	85
B.1	The two-fluid model	86
B.2	An Eulerian scheme based on the two-fluid model	86
B.2.1	Grid	86
B.2.2	Notations	87
B.2.3	Discretized equations	87
B.3	Stability analysis of an upwind Eulerian two-fluid model scheme	89
B.3.1	Combined Momentum Equation	89
B.3.2	The system of equations	90
B.3.3	Stability analysis of the system	91

B.3.4	Dispersion Equation	95
B.3.5	Stability criterion	97
B.3.6	Importance of the numerical surface tension	100
B.3.7	Importance of the numerical extra-stabilizing term	100
C	Influence of high order terms on the initiation process	105
C.1	Principle	105
C.2	The dynamic pressure terms	106
C.3	Effect of the derived high order terms on slug initiation: a numerical experimentation	107
C.3.1	Scheme used	107
C.3.2	Well-posed case (case 1)	107
C.3.3	Ill-posed case (case 2)	108
C.4	Conclusions	109
D	Geometrical relations within the pipe	117
D.1	The geometrical variables of two-phase flow in a circular pipe	117
D.2	Resolution of a pipe	117

List of Figures

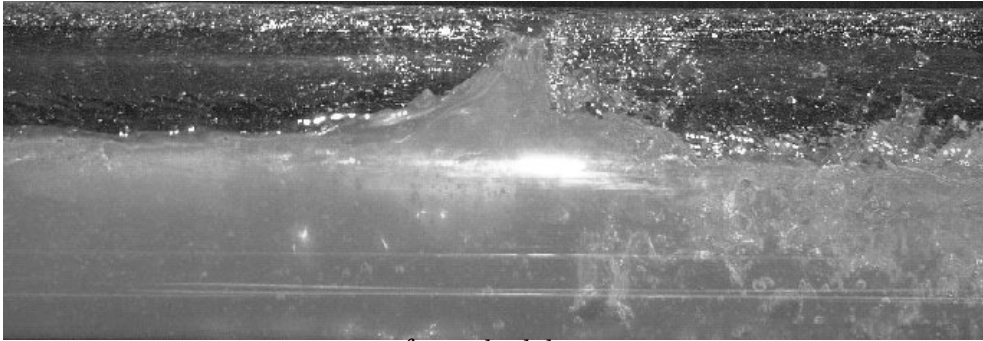
1.1	Flow patterns in horizontal gas-liquid flows (Taitel, 2000)	2
1.2	Simplified flowmap (Kristiansen, 2004)	3
1.3	A severe slugging cycle as simulated by the LASSI scheme	4
1.4	Pictures of a slug initiation. Taken from Woods, Hulburt, Hanratty (2000).	4
1.5	The unit cell model. Based on Bendiksen et al. (1996)	6
1.6	Grid used in the slug tracking scheme SLUGGIT	7
2.1	Influence of the interfacial friction ratio on the stability of stratified flow on a $(U_l^S - U_g^S)$ flowmap	18
2.2	Influence of the interfacial friction ratio on the stability of stratified flow on a $(\frac{h_l}{D} - U_g^S)$ flowmap	18
2.3	Sketch of a slug propagating in an upwards pipe	20
2.4	Nature of the slug-bubble and bubble-slug borders	22
3.1	The grid used in the Lassi scheme	32
3.2	The LASSI solution procedure	33
3.3	The LASSI Pressure Momentum step	37
3.4	Determination of the intermediate state (β_M, U_M) in the Riemann Problem	41
3.5	Calculating the characteristics of a section-section border	42
3.6	Interface tracking in the LASSI scheme	43
3.7	Void wave calculation in LASSI	45
3.8	Slug front update procedure	46
3.9	The LASSI void wave solving procedure	47
3.10	Object-Oriented implementation of the LASSI scheme	48
3.11	Splitting of the long sections in LASSI	49
3.12	Merging of the short sections in LASSI	50
3.13	Slug initiation in LASSI	51
3.14	Void wave step in the inlet	51
3.15	Section splitting at the inlet	52
3.16	Outlet treatment in the LASSI scheme	53
4.1	Sketch of the pipe geometry	56
4.2	Computed slug length distribution at various locations using 2 cm long sections and a 2 ms time step	58

4.3	Computed slug length distribution at various locations using 1 cm long sections and a 1 ms time step	59
A.1	Void wave calculation in LASSI	70
A.2	Rarefaction wave between the left and intermediate state	73
B.1	Staggered grid for an upstream-differentiated two-fluid scheme	87
B.2	Numerical flowmaps for water and air	102
C.1	Stratified-slug transition for an air-water flow in a one inch pipe	110
C.2	Holdup profiles computed in the well-posed case, without the derived high order terms (Case 1A)	111
C.3	Holdup profiles computed in the well-posed case, with the derived high order terms (Case 1B)	112
C.4	Fourier analysis of the holdup profiles obtained in the well-posed case with (case 1B, shown as squares) and without (case 1A, shown as a solid line) the derived high-order differential terms	113
C.5	Holdup profiles computed in the ill-posed case, without the derived high order terms (Case 2A)	114
C.6	Holdup profiles computed in the ill-posed case, with the derived high order terms (Case 2B)	115
C.7	Fourier analysis of the holdup profiles obtained in the ill-posed case with (case 2B, shown as squares) and without (case 2A, shown as a solid line) the derived high-order differential terms	116
D.1	Circular pipe geometry	118

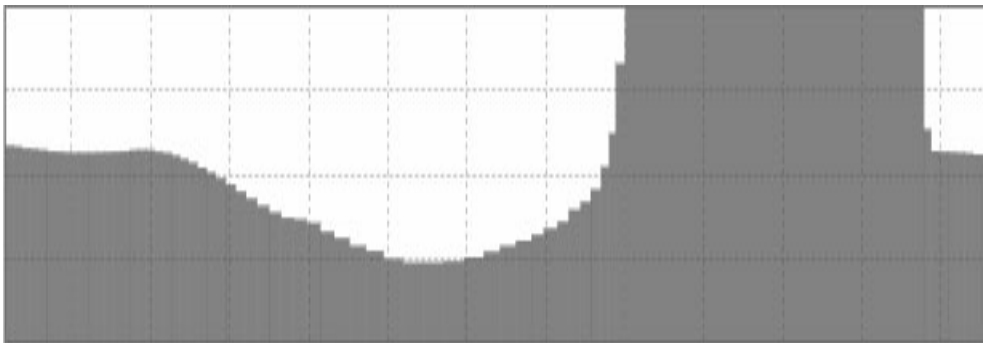
List of Tables

2.1	Bubble turning point criteria in LASSI	23
4.1	Influence of the time step and the section length on the critical liquid superficial velocity	60
A.1	Details of the void wave step in the Rarefaction-Rarefaction case . . .	74
A.2	Details of the void wave step in the Rarefaction-Shock case	75
A.3	Details of the void wave step in the Shock-Rarefaction case	76
A.4	Details of the void wave step in the Shock-Shock case	77
A.5	Details of the void wave step in the Saturated Shock-Shock case	78
A.6	Details of the void wave step in the Rarefaction-Rarefaction case . . .	79
A.7	Details of the void wave step in the Rarefaction-Rarefaction case . . .	80
A.8	Details of the void wave step in the Rarefaction-Rarefaction case . . .	81
A.9	Details of the void wave step in the Section-Slug case	82
A.10	Details of the void wave step in the Slug-Section case	83
B.1	Relative importance of the numerical and physical surface tension in various conditions	100
B.2	Numerical flowmaps for ExxsolD80 and air	103
D.1	Relations of interest in a circular pipe	118

Slug capturing



from the lab...



...to the computer

Acknowledgements

I would like to thank my supervisor, professor Ole Jørgen Nydal, for inviting me to work as a PhD student at the department of Energy and Process Engineering in the Norwegian University of Science and Technology in the city of Trondheim and for his constant encouragement and guidance.

The work presented in this thesis was undertaken as a part of the PhD programme "Multiphase Transport". I am personally very grateful to Total Norge (and especially to Alan Burns, Oddgeir Johansen, Emile Leporcher and Wilfried Vandersippe) whose financial support allowed me to join the programme in 2002. Besides Total Norge, the programme as a whole was also supported by Chevron, ENI, IFE, Norsk Hydro, the Norwegian Research Council, Scandpower SPT, Shell, SINTEF and Statoil. Meetings were organised every six months with representatives of the sponsors, and always resulted in pertinent comments and useful suggestions.

I am grateful to Vincent GRUEZ and Pierre LUQUET, two of "my" interns who conducted experiments on a small-scale loop together with me in Trondheim as their final MSc project, providing me with the empirical data I needed to write the second paper of this thesis. I also wish to thank particularly Monika Johansen, my fellow PhD student and co-author of the third paper of this thesis, who enthusiastically accepted my cooperation proposal and performed the experiments presented in the third paper.

My fellow PhD students Gaël Chupin, Tore Flåtten, George Johson, Jørn Kjølaas, Olav Kristiansen and Trygve Wangensteen as well as post-doc Pascal Klebert all offered me their support through these years and provided me with advice and constructive criticisms. The JAVA interface initially developed by Mathieu Rossier for the SLUGGIT code proved extremely useful to me.

Finally, I can not conclude without expressing my gratitude to my wife Zhenyi and my family for their patience and support.

⁰On the previous page, the picture showing a liquid slug right after its initiation was taken in the NTNU multiphase flow labs by Gaël Chupin, PhD. The picture of the computed slug is a snapshot of a LASSI computation.

Summary

This thesis consists of an introductory part and four papers.

The introductory part mainly describes the details of the implementation of the presented scheme. In addition, more general issues regarding slug capturing with two-fluid models are dealt with in appendix B and C where are respectively investigated the consequences of upstream differentiation on the area of stability of the two-fluid model schemes and the influence of the inclusion of the high order differential terms derived in the fourth paper of this thesis on the slug capturing abilities of an Eulerian two-fluid model scheme.

The main part of the thesis consists of the following papers:

- *A simple slug capturing and slug tracking scheme for gas-liquid pipe flow. Paper 1: Presentation of the scheme.* Fabien Renault and Ole Jørgen Nydal. *Preprint.*
- *A simple slug capturing and slug tracking scheme for gas-liquid pipe flow. Paper 2: Application to slug length determination in a small scale flow loop.* Fabien Renault, Ole Jørgen Nydal, Vincent Gruez and Pierre Luquet. *Preprint.*
- *An experimental and numerical study of flow regime transitions associated with fast flow rate changes in gas-liquid pipe flow.* Fabien Renault, Monika Johansen and Ole Jørgen Nydal. *Preprint.*
- *Influence of dynamic pressure terms on stratified two-phase flow stability.* Fabien Renault and Ole Jørgen Nydal. Presented at the 5th International Conference on Multiphase Flow, ICMF'04, Yokohama, Japan, May 30-June 4, 2004.

The three first papers are aimed at validating the presented scheme for various flow conditions. The first paper demonstrates the ability of the LASSI scheme to correctly predict the experimentally observed transition between stratified and hydrodynamic slug flow in near-horizontal pipes, as well as its fast-front tracking abilities. In the second paper, some experiments performed on a V-shaped small-scale air-water loop at the NTNU flow lab are used to validate the ability of the scheme to satisfactorily reproduce the obtained slug length distributions in normal bend slugging and severe slugging. In the third paper, the LASSI scheme is used to investigate the transitions between slug and stratified flow triggered by fast variations in the inlet flow rates. The predictions are then compared with the experiments conducted at the NTNU lab in a 6 cm diameter pipe.

Chapter 1

Introduction

1.1 Gas-liquid flow in pipelines

Gas-liquid flow refers to the simultaneous transport of a gas phase and a liquid phase in a single pipeline. Oil and natural gas in pipelines and water and vapour mixtures in power plants are good examples of industrial gas-liquid flows. Compared to single (gas or liquid) phase flow, the most outstanding characteristic of gas-liquid flow lies in the great variety of *flow regimes* that can occur.

In a horizontal pipe at atmospheric pressure, at low flow rates, the gas phase naturally flows on top of the liquid layer. This flow regime is called stratified flow. As the liquid flow rate increases, the interface between the gas and the liquid phase becomes unstable, waves appear and grow until a wave crest finally bridges the pipe, forming a liquid pocket occupying all the pipe section and called a slug. In the slug flow regime, gas bubbles and liquid slugs, which can contain small gas bubbles, alternately surge along the pipe.

In the slug flow region, if we increase the liquid flow rate while maintaining the gas flow rate constant, the share of the pipe volume occupied by the gas phase within the pipe, or *void fraction* will progressively decrease until the different slugs finally merge and occupy all the pipe. We then encounter the dispersed bubble regime characterized by small gas bubbles flowing within the liquid phase.

Starting back from slug flow, if we decide to increase the gas flow rate while maintaining the liquid flow rate constant this time, the liquid velocity and the void fraction will increase. The slugs eventually vanish, and we then reach annular flow in which the lighter phase flows in the center of the pipe while the heavier phase is contained as a thin moving film on the pipe wall.

Figure 1.1 taken from Taitel (2000) represents the different flow regimes that can be

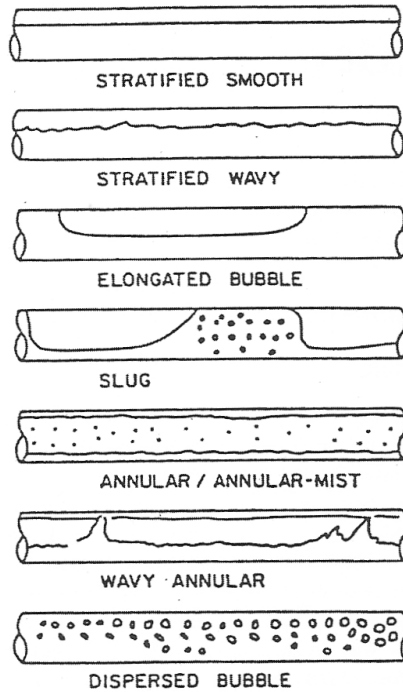


Figure 1.1: Flow patterns in horizontal gas-liquid flows (Taitel, 2000)

encountered in gas-liquid pipe flow. Figure 1.2, a schematic flowmap taken from Kristiansen (2004) indicates the prevailing flow regime for a given gas superficial velocity U_g^S (defined as the ratio between the gas volume flow rate and the pipe cross-sectional area) and liquid superficial velocity U_l^S . The influence of the pipe inclination (β is the angle between the pipe and the horizontal, a negative value indicating a downward inclination) and of the pressure on the transition between stratified and slug flow is also shown.

1.2 The transition between stratified and slug flow

One of the greatest challenges of two-phase flow computations lies in the modelling of flow regime transitions, because a flow regime transition can both be difficult to predict and have a tremendous impact on the characteristics of the flow. At comparable flow rates, different flow regimes can be characterized by a quite different holdup, pressure drop, gas-liquid friction or sound velocity. For low gas densities for example, the transition from stratified to slug flow can result in a discontinuity in the liquid holdup.

The modelling of the transition between stratified and slug flow represents indeed a certain challenge, because of its chaotic nature, and because of the great variety of

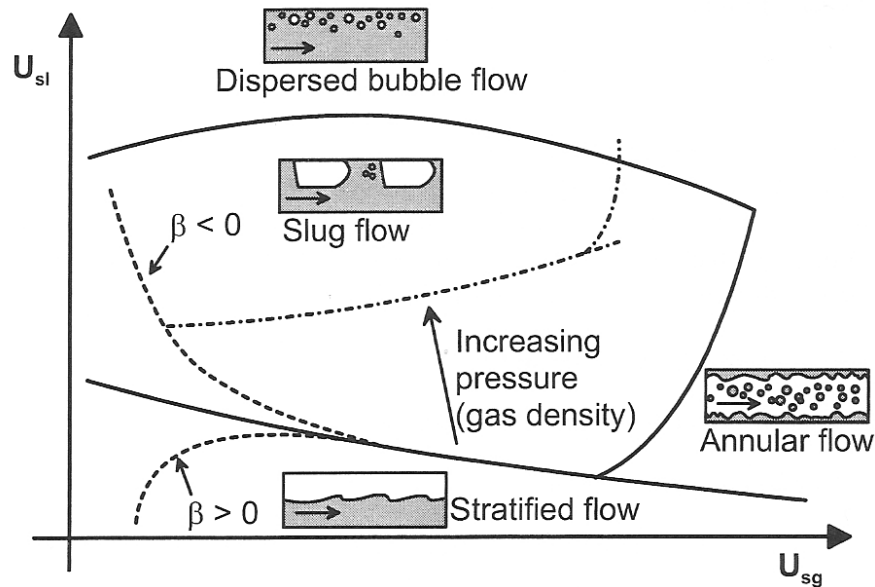


Figure 1.2: Simplified flowmap (Kristiansen, 2004)

slug initiation mechanisms. Slugs can be initiated due to liquid accumulation at the low points of the pipe until the liquid forms a blockade which will travel down the pipe as a slug. If the upstream gas compressibility is high enough however, the slug formed at a low point of the pipe will not be expelled directly and the inlet pressure will increase as the gas accumulates upstream of the slug. When the upstream pressure is high enough to remove the slug, all the accumulated liquid and gas finally exits the pipe in a blow-out phase characterized by very high velocities. Then the liquid starts to accumulate again at the low point and a new cycle is started. Such phenomenon is called severe slugging and can be seen as the most extreme expression of slug flow. An example of a severe slugging cycle taken from the third article of this thesis is shown in figure 1.3.

Another mechanism for the transition from stratified to slug flow is the sometimes quite slow growth of small perturbations at the gas-liquid interface due to the hydrodynamic instability of stratified flow at those conditions. The combined destabilizing effect of the friction forces and of the Bernoulli suction force will indeed lead to the formation and growth of interfacial waves until a slug is initiated. This mechanism is well-shown on the pictures presented in figure 1.4 which was taken from Woods et al. (2000).

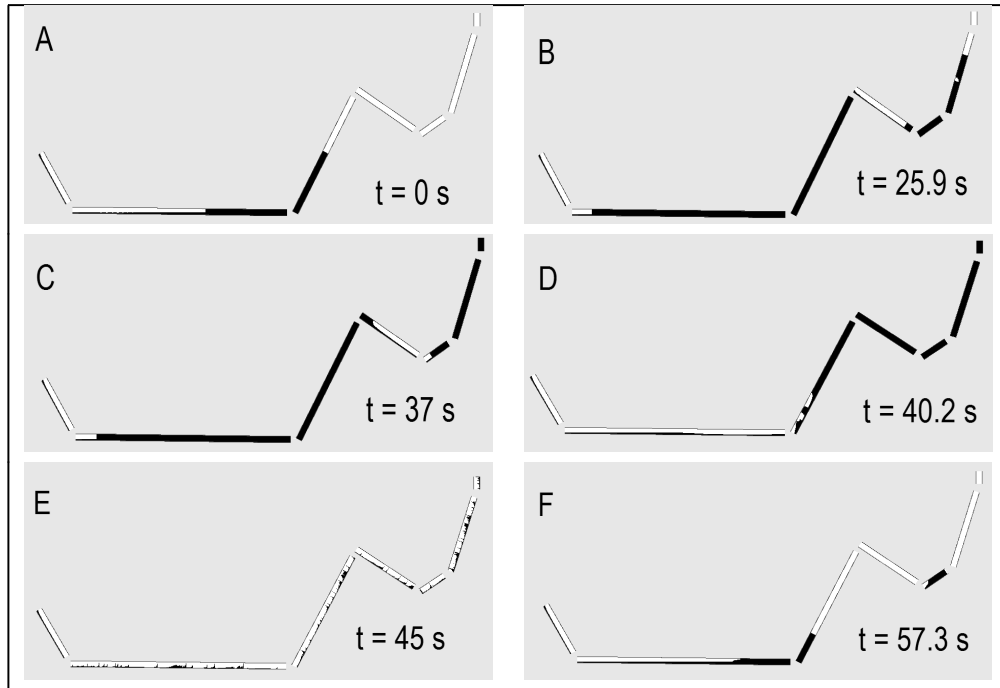


Figure 1.3: A severe slugging cycle as simulated by the LASSI scheme

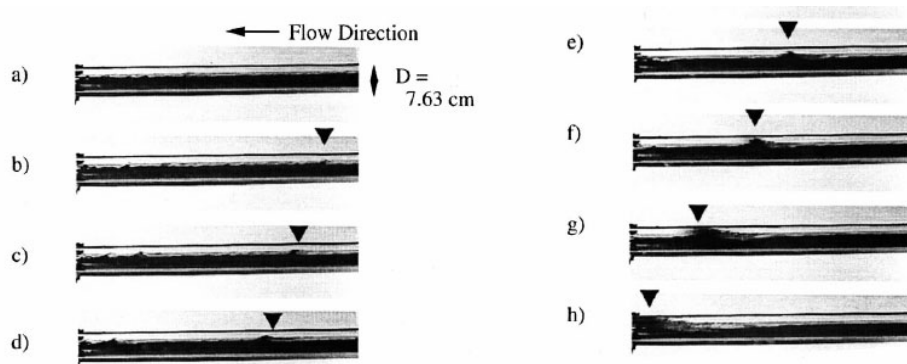


Figure 1.4: Pictures of a slug initiation. Taken from Woods, Hulburt, Hanratty (2000).

Slugs can also be initiated due to some operational transients, for example when the inlet gas flow rate is quickly increased. Those phenomena are investigated in the third paper of this thesis. System-dependent effects can also play an important role: when a previously initiated slug leaves the pipe, the pressure within the pipe decreases and the gas in excess is evacuated. As a consequence, the gas velocity within the pipe increases, which can under certain circumstances, trigger a slug initiation. This phenomenon was observed in particular in Kristiansen (2004, p239) who noticed in some cases a good correlation between the departure of a slug and the initiation of a new slug.

1.3 The modelling of slug flow with gas-liquid flow schemes

Slug flow is of special interest because of its inherent unsteady nature, and the potential adverse effects it can have in terms of production stability or pipe fatigue. However, its intrinsically transient nature makes it harder to simulate with standard transport schemes.

Computer codes designed to model transient two-phase flows such as RELAP (Ransom et al., 1982) and CATHARE (Barre et al., 1990) were first developed in the early 1980s in order to suit the needs of the nuclear industry. They were quickly followed by codes aimed at the oil industry as OLGA (Bendiksen et al., 1991), or TACITE (Pauchon et al., 1993).

As most of the general purpose transient multiphase codes use an Eulerian formulation based on a fixed grid, the special case of slug flow raised some special issues. Indeed, hydrodynamic slugs can be rather small, typically in the order of ten diameters long only and stationary grids have a strong tendency to diffuse the slug fronts. Extremely refined grids are thus needed if slugs are to be tracked individually in an Eulerian formulation without any special process.

To overcome this problem, two different approaches have arisen: the "unit cell" approach and the "slug tracking" approach. In the "unit cell" approach, the ambition to follow each individual slug in the pipe is given up and slug flow is rather treated in a statistical manner. The pipe flow is then considered to be a succession of identical "unit cells", composed of a slug and a gas bubble, as shown in figure 1.5. This method (Bendiksen et al., 1996), was used for example in OLGA or TACITE and is adequate for averaged liquid holdup and pressure drop prediction in pipelines. However, this method has its shortcomings, for example for the modelling of large slugs travelling long distances as these are prone to numerical diffusion. In addition, the use of a unit

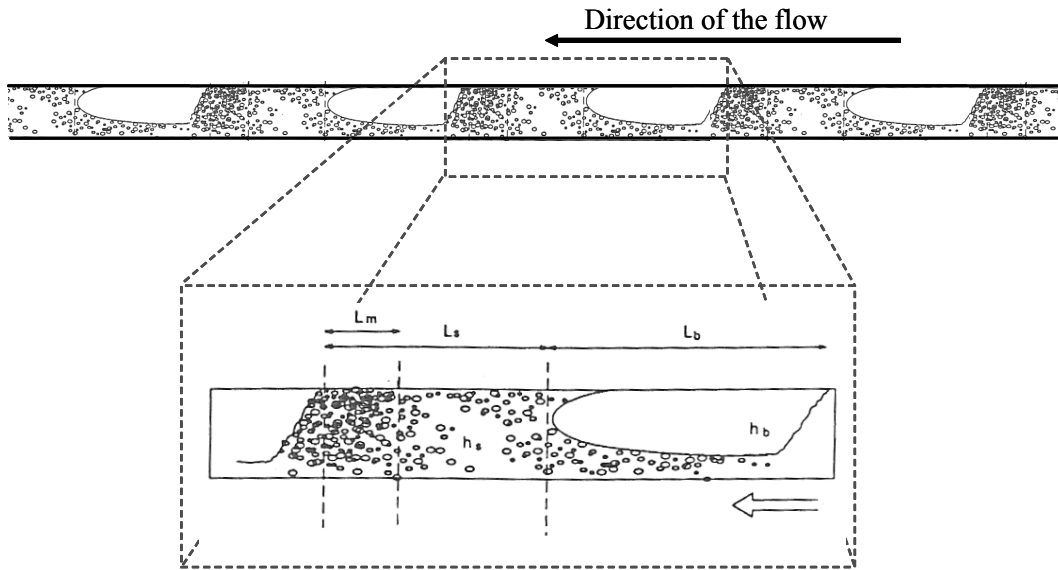


Figure 1.5: The unit cell model. Based on Bendiksen et al. (1996)

cell model makes sometimes difficult the implementation of physical closures for the bubble nose velocity or the gas entrainment within the slugs.

As a consequence, "slug tracking" schemes were developed, in which each individual slug is tracked as it propagates along the pipe. The position of each slug front and bubble nose is calculated from conservation laws or experimental closures. Examples of such slug tracking schemes include Nydal and Banerjee (1996) and Zheng et al. (1994). Those schemes proved able to capture a lot of the physics involved in slug propagation, but suffer however from limitations regarding the modelling of the bubbles. Figure 1.6 represents a sketch of the grid used in the SLUGGIT scheme presented in Nydal and Banerjee (1996).

The Eulerian OLGA code was incorporated a slug tracking option that superimposes a Lagrangian front tracking model on the Eulerian grid. This improves the prediction of terrain slugging and gives information about slug lengths and frequencies. The model has given results that compare well with both experimental data and some field data, although a weakness of the slug tracking module of OLGA is the fixed user specified grid that may lead to grid dependent solutions (Larsen et al., 1997).

The new scheme PETRA (Larsen et al., 1997) includes an adaptive and moving grid together with a fully integrated slug tracking model.

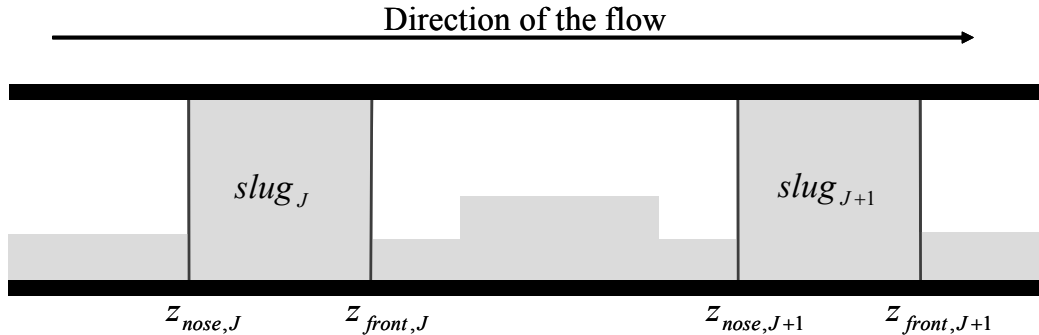


Figure 1.6: Grid used in the slug tracking scheme SLUGGIT

1.4 Modelling the slug initiation with a transient scheme for gas-liquid flow

The previous section showed how two-phase flow schemes, either by using a unit cell model or by relying on a slug tracking mechanism, could model the transport of slugs along the pipe. One of the biggest remaining issues lies however in the slug initiation mechanism itself. Where, when, how often and how big are the slugs initiated are questions that need to be answered for a slug tracking scheme to yield realistic results.

Multiphase codes such as RELAP, OLGA or PETRA make use of the so-called two-fluid model which consists of a set of four differential equations representing mass and momentum conservation for each of the phases. As the use of the two-fluid model spread in industrial codes some concerns appeared regarding the well-posedness area of the model. Indeed, it was early shown (Ramshaw and Trapp, 1978) that the two-fluid model becomes ill-posed as a hyperbolic problem when the Bernoulli suction force exceeds the hydrostatic force. As the Bernoulli suction typically overcomes the hydrostatic force in the last final stages of slug initiation, this problem was both considered a threat to the stability the two-fluid model and a strong indication that slug capturing, i.e. the direct computation of the slug initiation process, would be impossible with the two-fluid model. Physically, one can explain the ill-posedness of the two-fluid model in certain conditions by the fact that some physical aspects, such as surface tension or more complex viscous effects, are not included in the two-fluid model.

An example of an ill-posed problem would be the time-reversed heat equation. If we open a door between two rooms of equal sizes, one at 20 degrees and one at 10 degrees, it is relatively easy to calculate how heat will be transferred from the warm room to the cold room, leading eventually to a stable situation where both rooms have

reached their final equilibrium temperature of 15 degrees. On the other hand, if we simply know that the final temperature of the two rooms is 15 degrees, it is impossible to calculate what were the initial temperatures of the two rooms. Some information has been lost in the diffusion process and it is therefore impossible to go back in time by solving the time-reversed heat equation.

As the two-fluid model was thought to be unable to capture the initiation of slugs, the slug tracking schemes relied on some semi-empirical criteria such as the Taitel and Dukler (1976) criterion or the Minimum Holdup criterion. However, one can doubt that a criterion-based approach could be able to cope with the most complicated pipe geometries or gas transient effects. More practically, the implementation of those criteria into standard transport models like the two-fluid model is tedious and subject to some numerical difficulties. Moreover, this approach requires further closures in addition to the transition criterion itself, like the initiation position and the initial slug length. No matter how difficult, this criterion-based approach was necessary as long as no direct slug initiation was thought possible with the two-fluid model.

A first hint that slug capturing (i.e. the automatic initiation of slugs from a stratified flow) was possible with the two-fluid model was provided by Lin and Hanratty (1986) and Barnea and Taitel (1993) who showed that the linear stability analysis of the two-fluid model yielded a criterion, denoted as Viscous Kelvin Helmholtz or VKH that successfully predicted the transition from stable stratified flow to non-stratified flow (which can be roll waves regime or slug flow according to the conditions). Hence, we could infer that a faithful implementation of the two-fluid model (numerically stable whenever the two-fluid model is stable, and numerically unstable whenever the two-fluid model is unstable) should be expected to predict accurately this transition. This hypothesis was confirmed numerically by Issa and Kempf (2003) who first demonstrated the ability of the two-fluid model to automatically capture the initiation of slugs and follow their development as they travel along the pipe. Slugs are not tracked by a special moving grid like in slug tracking schemes, but simply transported over a regular still grid. However, the TRIOMPH code presented by ISSA and Kempf requires the iterative solving of the transport equations on a very fine grid and is therefore computationally demanding, which might make any field-scale application difficult.

1.5 Objective and scope of this thesis

The objective of this thesis was to provide original solutions regarding the question of slug initiation in slug tracking schemes such as SLUGGIT (Banerjee and Nydal, 1996). This was done by relying on the slug capturing ability of the two-fluid model, as shown by Issa and Kempf (2003). The proposed scheme, called LASSI (Lagrangian Approximate Scheme for Slug Initiation) can be seen as an intermediary between a full two-fluid model such as TRIOMPH (Issa and Kempf) and a very simplified scheme such as SLUGGIT.

The LASSI scheme is both slug capturing (the slugs appear automatically without the use of any criterion), and slug tracking (each slug is followed individually as it propagates along the pipe). Some approximations were made regarding the dynamics in order to increase considerably the computational speed, as compared to an iterative scheme such as TRIOMPH.

Given the great variety of two-phase pipe flow, the scope of this thesis has been limited to stratified and slug flow, and especially the transition between those two flow regimes. Roll waves and wavy flow regimes have also been investigated because the transition between stratified and slug flow sometimes happens in a way that involves waves and roll waves. The other flow regimes such as annular flow are out of the scope of this thesis. No effort was dedicated to improve on the modelling of steady-state flows either, as considerable theoretical and experimental efforts have already been dedicated to this goal.

As explained in this short introduction, the transition from stratified to slug flow can occur in many ways. At low pressure and low velocities, transition occurs from a slowly growing wave that eventually bridges the pipe and forms a slug. At higher velocities and pressures, the transition can occur when roll waves overtake each other. Slug initiation also occurs in bends, and the pipe geometry plays a tremendous role for gravity dominated flows. When the flow rates are low enough, severe slugging is the most dramatic and spectacular form of slugging. Another very important way of slug formation is due to transient effects, such as a sharp variation in the inlet flow rates, or more subtle effects such as a slug exiting a pipe. All those effects lead to slug formation and a good slug capturing code should be able to make consistent predictions in all those cases. The three first papers of this thesis are thus dedicated to the validation of the ability of the LASSI code to respectively initiate adequately hydrodynamic slugs in near-horizontal pipes, capture the characteristics of slug flow in an upwards pipe after a bend and initiate slugs triggered by rapid variations of the inlet flow rates. The case of severe slugging is treated both in the second and third

papers of this thesis.

1.6 Applications

The work conducted for this thesis has two possible applications. First, the proposed scheme and code can be used as a tool to reproduce experimental work conducted at moderate pressures and flow rates. Compared with the industry codes, the LASSI scheme is very well suited to simulate typical lab cases, i.e. relatively short pipes with complex geometries that require a fine discretization. The scheme could in particular be of assistance to any experimentator and researcher wishing to investigate cases involving slug initiation or study the influence on the transition between stratified and slug flow of various parameters such as the friction factors, wake effect, pipe geometry, transient effects...

The other possible application of the work done is of course industrial two-phase codes which need models and numerical recipes to be able to model efficiently the transition from stratified to slug flow. Those industrial two-phase codes are of great importance for the development of increasingly long transportation pipes in the oil industry.

1.7 Presentation of the papers

A simple slug capturing and slug tracking scheme for gas-liquid pipe flow.

Part 1: Presentation of the scheme. Fabien Renault, Ole-Jørgen Nydal.

This paper presents an original slug capturing and slug tracking scheme, named LASSI (Lagrangian Approximate Scheme for Slug Initiation) for transient simulations of gas-liquid flow in pipes. The scheme is based on the two criteria that govern the transition from stratified to slug flow: the stratified stability criterion or Viscous Kelvin Helmholtz and the slug stability criterion or Minimum Holdup. The presented scheme is able to generate slugs automatically without the use of any initiation models, and to track them along the pipe, as they propagate according to a bubble nose velocity relation. The details of the scheme are presented and the scheme is successfully validated against experiments in its ability to predict the correct flowmap. In addition, a new derivation of the VKH criterion is presented, and some concerns regarding the modelling of the Bernoulli suction force with an upwind-differentiated two-fluid model are raised.

A simple slug capturing and slug tracking scheme for gas-liquid pipe flow. Part 2: Application to slug length determination in a small scale loop. Fabien Renault, Ole-Jørgen Nydal.

The hydrodynamical characteristics of slug flow in a small scale loop were investigated experimentally and numerically. Using optical sensors, the length, front velocity and tail velocity of every individual slug were measured at various locations along the pipe. The experiments clearly show that for the shorter slugs the slug tail velocity exceeds the slug front velocity hence leading to the disappearing of small slugs and to an increase of the average slug length. The influence of the upstream flow regime (stratified or slug flow) is also investigated and shown to be negligible at sufficient distance. In addition, the transition between normal slug flow and severe slugging is studied by gradually increasing the upstream gas volume. The experimental observations were compared to the predictions of the Lagrangian slug capturing code LASSI and there is on the whole a fair agreement between the numerical predictions and the experimental results.

An experimental and numerical study of flow regime transitions associated with fast flow rate changes in gas-liquid pipe flow. Fabien Renault, Monika Johansen, Ole-Jørgen Nydal.

Flow regime transitions associated with fast changes in the inlet gas flow rate were investigated both experimentally in a 6 cm air-water pipe, and numerically with a Lagrangian slug capturing and slug tracking scheme. As liquid transport occurs at a much slower speed than the fast pressure wave associated with a change in the inlet gas velocity, a fast increase or decrease in the inlet gas flow rate creates an intermediate state characterized by the liquid holdup of the previous equilibrium state and the new gas flow rate. Experimentally, while a steady stratified flow regime was established in the pipe, a sudden increase in the inlet gas flow rate resulted in a short period of slug flow. Similarly, when the gas flow rate at the inlet was suddenly decreased, a short period of stratified flow was observed between two periods of established slug flow. Numerical predictions from the LASSI code were shown to be in good agreement with the experimental observations. The LASSI code was also used to reproduce the severe slugging regime observed experimentally in a S-shaped riser.

Influence of dynamic pressure terms on two-phase flow stability. Fabien Renault, Ole Jørgen Nydal.

This paper presents a modified version of the "Viscous Kelvin Helmholtz" criterion (based on the linear stability analysis of the two-fluid model) predicting transition between stratified and slug flow. In previous works a hydrostatic approximation was used to close the two-fluid model. Here an approach with a transverse momentum

balance to evaluate pressure terms is investigated. The obtained model is compared with the established criteria (Viscous Kelvin Helmholtz, Inviscous Kelvin Helmholtz, Milne-Thompson) and with experimental results. The proposed model compares better to experiments and is able to predict the wavelength of the perturbation responsible for the transition. This analysis might also provide numerical benefits for transient two-phase simulations.

1.8 Structure of the introductory part

Chapter 2 recalls all the closure laws (friction, bubble nose velocity, bubble turning point, wake effect, gas law...) used in the LASSI code. Their importance regarding slug initiation is briefly discussed.

The details of the LASSI scheme and of its implementation are described in **chapter 3** which goes deeper in the description than the overview provided in the beginning of the first paper. **Annex A** gives the exact description of the border velocities and fluxes used for the liquid transport.

In **chapter 4** is discussed the influence of the integration parameters (the time step and the section length) on the slug capturing abilities of the LASSI scheme. In particular, the influence of the section length on the computed slug length distribution in an upward pipe downstream of a bend is investigated. The impact of the section length and of the time step on the predicted transition point between stratified and slug flow is also studied.

A lot of attention has been given in the literature (and in this thesis) to the question of the stability area of the two-fluid model. The criterion produced by this stability analysis can be used in certain conditions to predict the transition between stratified and slug flow and the validity of this approach is the cornerstone to the whole ambition of building a slug capturing model based on the two-fluid model set of equations. However it is well-known that the discretisation process can have some consequences on the domain of stability of a system and there is no a priori reason for the discretized set of equations to have exactly the same area of stability than the original continuous two fluid model set of differential equations. This issue is investigated in **annex B** by analytically deriving the area of stability of an upwind Eulerian two-fluid model and comparing it with the usual Viscous Kelvin Helmholtz criterion.

In the fourth paper of this thesis, some high order differential terms accounting for the influence of transverse dynamic effects were derived for inclusion in the two-fluid model set of equations. Theoretically, one of the predicted effects of these high order terms was to modify the wavelength of the perturbation responsible for slug initiation, shifting it from infinity (as predicted by the VKH theory), towards the order of a few diameters, as reported by some experimentators for some flow conditions. The practical effect of the derived terms on the slug initiation process in an Eulerian slug capturing two-fluid model was investigated in **annex C** by comparing the results obtained with the original Eulerian scheme and the results obtained when the derived high order differential terms are added.

Chapter 2

Closure laws

2.1 Friction factors

2.1.1 A short review

Conservation of momentum for the liquid and gas phase in steady state can be expressed as (Taitel and Dukler, 1976):

$$A_l \frac{\partial}{\partial x} p = -\tau_l S_l + \tau_i S_i - \rho_l g A_l \sin \phi \quad (2.1)$$

$$A_g \frac{\partial}{\partial x} p = -\tau_g S_g - \tau_i S_i - \rho_g g A_g \sin \phi \quad (2.2)$$

The three shear stresses τ_l (liquid-wall friction), τ_g (gas-wall friction) and τ_i (gas-liquid friction) account for the effect of 3D friction forces in the 1D two-fluid model. Annex D provides more details on how the geometrical parameters S_l (liquid-wetted perimeter), S_g (gas-wetted perimeter) and S_i (interfacial width) are calculated.

The two-phase flows shear stresses are simply derived from their single-phase expressions:

$$\begin{aligned} \tau_l &= \frac{1}{8} \lambda_l \rho_l U_l |U_l| \\ \tau_g &= \frac{1}{8} \lambda_g \rho_g U_g |U_g| \\ \tau_i &= \frac{1}{8} \lambda_i \rho_g (U_g - U_l) |U_g - U_l| \end{aligned}$$

where λ_l , λ_g and λ_i are respectively the liquid-wall, gas-wall and interfacial friction factors.

The gas-wall and liquid-wall friction factors are calculated using single-phase relations, with Reynolds numbers Re_l and Re_g based on the following expressions for the hydraulic diameters D_{hl} and D_{hg} :

$$Re_l = \frac{U_l \rho_l D_{hl}}{\mu_l} \quad \text{and} \quad Re_g = \frac{U_g \rho_g D_{hg}}{\mu_g}$$

where $D_{hl} = 4 \frac{A_l}{S_l}$ and $D_{hg} = 4 \frac{A_g}{S_g + S_i}$

For laminar flow, the exact single-phase expressions are:

$$\lambda_{l,laminar} = \frac{64}{Re_l} \quad \lambda_{g,laminar} = \frac{64}{Re_g} \quad (2.3)$$

For turbulent flows, most friction factors used are semi-empirical models based on the single-phase turbulent boundary layer theory. Prandtl and Von Karman initially presented friction factors respectively for smooth and rough pipes. Nikuradse (1932) fitted the coefficients proposed by those two authors in order to match his experimental observations. It appeared that for low Reynolds numbers, the friction factor was a function of the Reynolds number only, while for very large Reynolds numbers, the friction factor depended only on the pipe wall roughness. Colebrook (1933) first proposed a correlation valid for all the range of pipe roughness ϵ :

$$\frac{1}{\sqrt{\lambda_{l,turbulent}}} = -2 \log \left(\frac{2.51}{Re_l \sqrt{\lambda_{l,turbulent}}} + \frac{\epsilon}{3.7 D_{hl}} \right) \quad (2.4)$$

The main drawback of this correlation lies in its implicit nature. The Colebrook equation has to be solved iteratively, and as friction factors need to be computed a huge number of times per simulation, this can prove computationally expensive. For this reason, the Håland (1983) correlation that provides an explicit value for λ_l is commonly used:

$$\frac{1}{\sqrt{\lambda_{l,turbulent}}} = -1.8 \log \left(\frac{6.9}{Re_l} + \left(\frac{\epsilon}{3.7 D_{hl}} \right)^{1.11} \right) \quad (2.5)$$

The same single-phase correlation is used in order to evaluate the gas-wall friction factor:

$$\frac{1}{\sqrt{\lambda_{g,turbulent}}} = -1.8 \log \left(\frac{6.9}{Re_g} + \left(\frac{\epsilon}{3.7 D_{hg}} \right)^{1.11} \right) \quad (2.6)$$

Some other authors use Blasius friction factors for smooth pipes. They have:

$$\frac{\lambda_{l,turbulent}}{4} = 0.0791 (Re_l)^{-0.25} \quad \frac{\lambda_{g,turbulent}}{4} = 0.0791 (Re_g)^{-0.25} \quad (2.7)$$

Those expressions are easier to handle manually for calculations and stability analysis (see for example Hurlburt and Hanratty, 2002). On the other hand they are only valid for hydraulic smooth pipes.

There is still a high uncertainty regarding the value of the friction relations and in particular the interfacial friction factor. The ratio $\frac{\lambda_i}{\lambda_g}$ is often simply given a value ranging between 1 (the liquid-gas interface is very smooth thus the liquid phase can be considered as a pipe wall for the gas phase) and 10 or more (the interface is very wavy therefore leading to a much greater exchange of momentum at the interface).

2.1.2 Importance of the interfacial friction factor on the transition from stratified to slug flow

The value of the interfacial friction factor plays an important role in the transition from stratified to slug flow, especially in horizontal or near-horizontal flows where the influence of the gravity is null or low. For given inlet flow rates U_l^S and U_g^S , an increase in the interfacial friction ratio $\frac{\lambda_i}{\lambda_g}$ will result in a decreased equilibrium holdup, as the liquid is provided more momentum by the gas. As a consequence, an increase in the interfacial friction ratio $\frac{\lambda_i}{\lambda_g}$ will lead to a larger stratified flow area on a $(U_l^S - U_g^S)$ flow map at the expense of the slug flow region since the transition from smooth stratified flow to slug flow essentially occurs at a given holdup. On the other hand, on a $(\frac{h_l}{D} - U_g^S)$ flowmap an increase in the interfacial friction ratio $\frac{\lambda_i}{\lambda_g}$ will on the contrary cause a reduction in the size of the stratified flow region. The reason is that for a given holdup and a given gas flow rate U_g^S , the action of the interfacial friction is destabilizing since it feeds energy to the small interfacial perturbations that get bigger and eventually bridge the pipe to form a slug.

This effect is shown on figure 2.1 and figure 2.2 which respectively show the neutral stability line between stratified and slug flow (according to the Viscous Kelvin Helmholtz analysis) on a $(U_l^S - U_g^S)$ flowmap and on a $(\frac{h_l}{D} - U_g^S)$ flowmap. Those graphs were computed for an air-water flow in a horizontal 1 inch diameter pipe at atmospheric pressure.

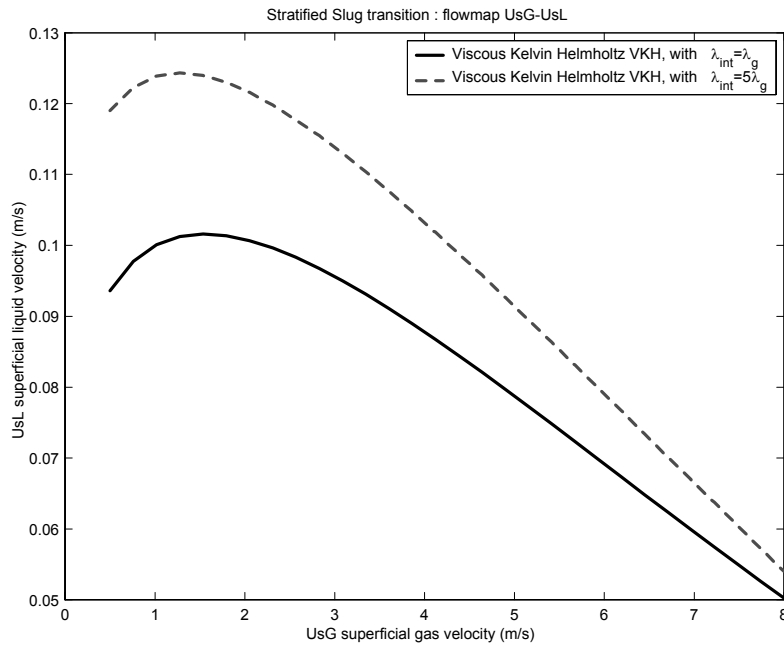


Figure 2.1: Influence of the interfacial friction ratio on the stability of stratified flow on a $(U_l^S - U_g^S)$ flowmap

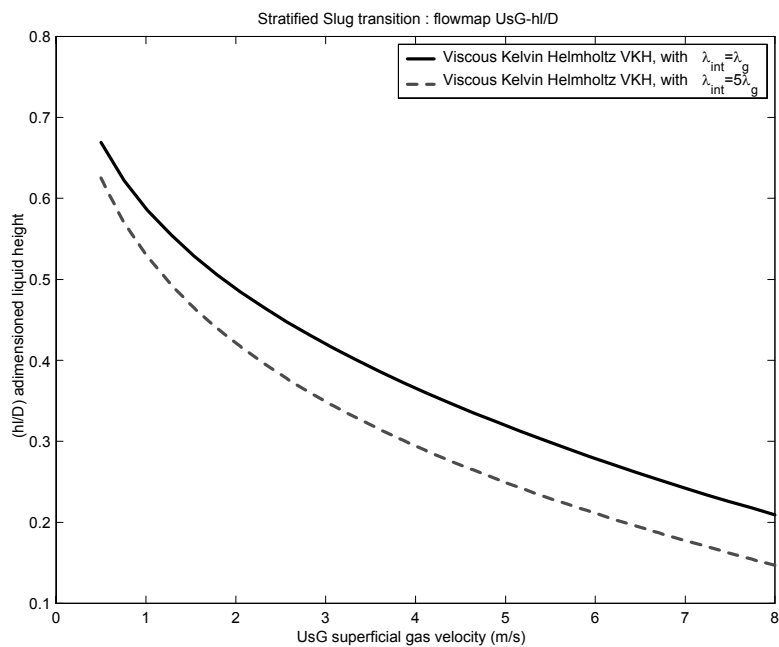


Figure 2.2: Influence of the interfacial friction ratio on the stability of stratified flow on a $(\frac{h_l}{D} - U_g^S)$ flowmap

2.1.3 Implementation in LASSI

In order to ensure a continuous transition of the friction factors across the transition to turbulent flow, the bigger friction factor of the two flow regimes was used:

$$\lambda_{l,LASSI} = \max(\lambda_{l,laminar}, \lambda_{l,turbulent}) \quad (2.8)$$

$$\lambda_{g,LASSI} = \max(\lambda_{g,laminar}, \lambda_{g,turbulent}) \quad (2.9)$$

For turbulent flows, the Håland correlation for friction factors were mostly used in the simulations presented in this thesis. A smooth pipe ($\epsilon = 0$) was used for all "theoretical" simulations, while a small value of $50 \mu m$ was used to simulate the "real-life" loops such as the S-riser loop (see paper III of this thesis) or the small scale loop (see paper II of this thesis). The Blasius friction factors were also used for some "theoretical" simulations, mainly to be able to more easily compare the obtained predictions with the results published by other researchers.

Regarding the ratio $\frac{\lambda_i}{\lambda_g}$, a value of 1 was used on a standard basis, though when this choice resulted in a predicted holdup too high compared to the experiments, a higher value (typically 2 or 5) was then used.

2.2 Slug border closures

In LASSI, the pipe is represented as a doubly-linked list of *objects* which can be either *slugs* (characterized by a holdup equal to one) or *sections* (see 3.7.1 for further details). In LASSI, a *section-slug* or a *slug-section* border can be either a bubble nose or a slug front. There is no intermediate position and those two "extreme" cases are dealt with by using the appropriate closures. For bubble noses, Bendiksen's closure is used while the "steep-front" (hydraulic shock) approximation is made for the slug fronts.

2.2.1 Slug front

In the LASSI scheme, the slug front is considered infinitely steep. This approximation is very strong as in reality the slug front is often several diameters long. However, the "steep-front" approximation allows the transportation of the front without any numerical dissipation and thus greatly facilitates the modelling. Due to the turning point criterion implemented in the code, the liquid velocity inside the *slug* is always greater

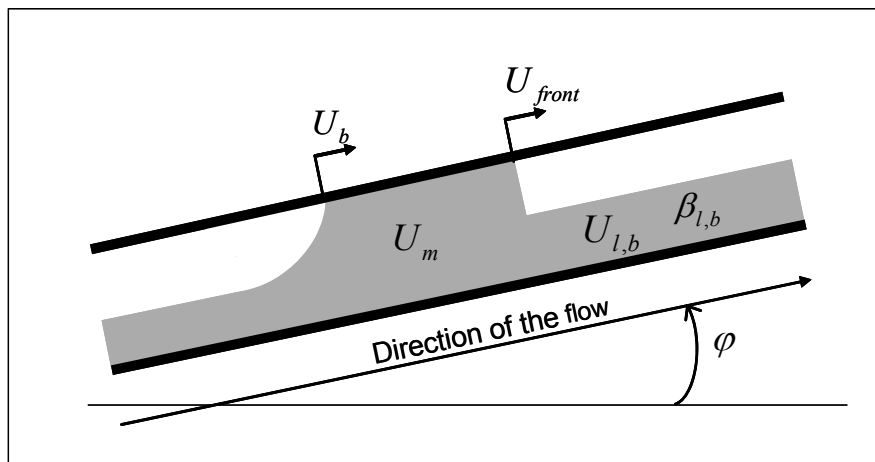


Figure 2.3: Sketch of a slug propagating in an upwards pipe

than the velocity of the liquid film ahead of the liquid front. As a consequence, the slug front velocity can be simply calculated in order to ensure liquid mass-conservation.

In the LASSI scheme, the CFL criterion is checked within each *section* for each time step. However, in the case of a slug front, an iteration process is implemented so that the *slug* is able to propagate across several *sections* in a single time step. By neglecting the influence of the slug on the bubble film ahead of it, the steep-front approximation indeed makes this treatment possible. This has a great impact on the minimal time step since the slug front velocity is much higher than the velocity of the liquid film.

Should the mixture velocity within the *slug* exceed the critical "turning point" velocity, then the *slug-bubble* border will be considered as a perfectly steep front, whose velocity can be determined by simple liquid conservation $U_{front} = \frac{U_{ls} - \beta_b U_{lb}}{1 - \beta_b}$ in the "no void in slug" case. U_{ls} is the liquid velocity within the *slug* and β_b and U_{lb} are respectively the liquid holdup and the liquid velocity within the liquid layer in front of the slug. Figure 2.3 shows the case of a slug in an upwards pipe.

2.2.2 Bubble nose

A lot of experimental and theoretical work has been done to propose models yielding the propagation velocity of Taylor bubbles in pipelines. Davies and Taylor (1949) studied experimentally and theoretically the rise of bubbles in stagnant liquid in vertical pipes and showed that in those conditions ν_0 , the bubble drift velocity in a stagnant liquid was given by $0.35\sqrt{gD}$. Nicklin et al. (1962) then first presented the relation

$U_{nose} = C_0 U_m + \nu_0$ for vertical pipes, using Davies and Taylor's expression of ν_0 and a coefficient C_0 ranging between 1.2 for fully developed turbulent flow to 2.0 for laminar flows. Zukoski (1966) measured the velocity of large bubbles in horizontal pipes of stagnant liquid and found a value of $0.54\sqrt{gD}$ for ν_0 .

In the LASSI scheme, the bubble noses are considered to propagate according to Bendiksen's law (Bendiksen et al., 1984). For low Froude numbers ($Fr = \frac{U_m}{\sqrt{gD}} < 3.5$), the bubble nose is located close to the top of the tube where the local liquid velocity is moderate, while for higher Froude numbers, the tip of the bubble moves down towards the centre of the pipe, where the liquid velocity is highest. The bubble nose velocity U_b is then given by $U_b = C_0 U_m + \nu_0$ where C_0 and ν_0 are calculated as:

$$\begin{aligned} C_{01} &= 1.05 + 0.15 \sin^2 \varphi & \nu_{01} &= (0.35 \sin \varphi + 0.54 \cos \varphi) \sqrt{gD} & \text{for } Fr < 3.5 \\ C_{02} &= 1.2 + 0.15 \sin^2 \varphi & \nu_{02} &= 0.35 \sin \varphi \sqrt{gD} & \text{for } Fr > 3.5 \end{aligned} \quad (2.10)$$

In practice C_0 and ν_0 are chosen in order to maximize U_b rather than using the Froude number, to ensure a continuous transition of the bubble nose velocity when the Froude number increases.

$$U_b = \max(C_{01} U_m + \nu_{01}, C_{02} U_m + \nu_{02}) \quad (2.11)$$

By implementing those experimental-based correlations directly into the code, the scheme is able to adequately reproduce the slug propagation velocity, which is arguably one of the most important parameter in gas-liquid slug flow. It is important to note that this key element is only a closure law for the LASSI scheme. Compared to the somehow purer full two-fluid model approach consisting in not using any ad-hoc correlation for the bubble nose velocity (see Issa and Kempf, 2003), the user has in the tracking scheme a freedom to change the bubble nose velocity correlation according to the desired field conditions. In a full two-fluid model approach, fitting the desired bubble propagation speed will require cautious and tedious tuning of the friction factors.

2.2.3 Nature of the slug-bubble and bubble-slug borders

Slug turning point

A criterion is needed to determine which of the two pure correlations, the steep front model and Taylor's bubble model is to be used at the given flow conditions. In other words, when is a *slug-bubble* border a front or a bubble nose? In the literature (see for example Nydal, 98) the critical velocity U_{crit} for the turning of the bubble is often

taken as the velocity that balances friction and gravity forces within the slug:

$$\frac{1}{2}\lambda_l\rho_l U_{crit}^2 S = \rho_l g \sin \varphi A \quad (2.12)$$

In downwards pipes the critical velocity U_{crit} is positive. A *bubble-slug* border is a nose if the mixture velocity within the *slug* is higher than U_{crit} , else it is a front. Conversely a *slug-bubble* border is a front if the mixture velocity within the *slug* exceeds U_{crit} and a nose otherwise. Figure 2.4 presents how the nature of the borders is determined.

For upwards inclined pipes, gravity and the friction forces both work towards the same direction in normal flow. As a consequence, the critical velocity U_{crit} is negative, meaning that a *slug-bubble* border will only be a nose if the *slug* is propagating fast enough towards the inlet of the pipe. This phenomenon seldom happens, but can occur for example at the end of the blow-out phase of a severe slugging event.

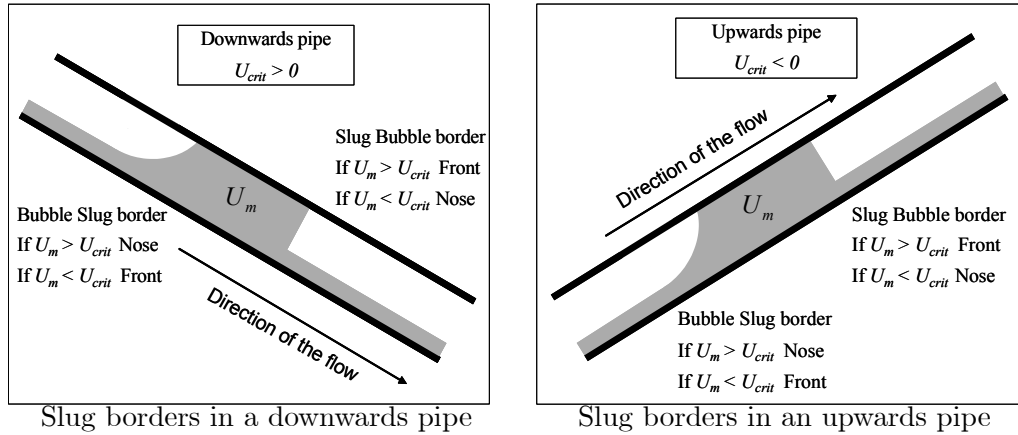


Figure 2.4: Nature of the slug-bubble and bubble-slug borders

In the SLUGGIT code (Nydal and Banerjee, 1996, Nydal, Audibert and Johansen, 2001), the nature of the slug borders is determined according to the turning point criterion for downwards pipe while *slug-bubble* borders are always considered as fronts in upwards pipe (similarly *bubble-slug* borders are always taken as nose in upwards pipe).

Implementation in LASSI

In LASSI as well as in all other slug-tracking codes, the slug front is modelled by using the steep-front approximation. The front velocity is calculated by considering liquid

mass conservation across the front ($U_{front} = \frac{U_{ls} - \beta_b U_{lb}}{1 - \beta_b}$ if there is no void in slug). In order for this approximation to be physically realistic, the inequality $U_{ls} > U_{lb}$ has to be fulfilled, otherwise the shock would be entropy violating. As a consequence, in LASSI, the nature of the border depends not only on the respective value of U_{ls} and U_{crit} but also on the value of U_{lb} . Table 2.1 sums-up the criteria actually implemented within the LASSI code.

slug-bubble border			bubble-slug border		
nature	$U_{ls} > U_{lb}$	$U_{ls} < U_{lb}$	nature	$U_{ls} > U_{lb}$	$U_{ls} < U_{lb}$
$U_{ls} > U_{crit}$	front	nose	$U_{ls} > U_{crit}$	nose	nose
$U_{ls} < U_{crit}$	nose	nose	$U_{ls} < U_{crit}$	nose	front

Table 2.1: Bubble turning point criteria in LASSI

Apart from some extreme transients that occur in severe slugging blow-outs for example, the additional test between U_{ls} and U_{lb} does not have any influence on the prediction of the border nature as the liquid velocity within the slugs tend to be much higher than the velocity of the liquid within the film. Moreover, in the case of downward pipes the critical velocity U_{crit} is usually greater than the equilibrium film velocity, making the additional test unnecessary.

2.3 Wake effect

The bubble nose propagation correlations available in the literature, including Bendiksen's are actually mostly relevant for very long slugs. In very long slugs, the liquid velocity distribution at the slug tail has had enough time and distance to reach an equilibrium. On the other hand, for very short slugs, the disturbances induced at the slug front are still present at the level of the slug tail. Those disturbances tend to modify the liquid velocity profile at the tail in a way that increases the bubble nose velocity. As a result, the slug tail velocity will be higher for shorter slugs. This phenomenon has strong consequences on the evolution of the slug length distribution along the pipe. Whether they appear at a bend or are created from the growth of a hydrodynamic disturbance, the slugs tend to be created relatively small and grow as they travel down the pipe. This "wake effect" has a tendency to "kill" the smaller slugs, as their tail velocity is higher than the one of longer slugs. In order to capture

the evolution of the slug length distribution along the pipe, it is crucial to model correctly the wake effect, i.e. the increase in the bubble nose velocity for the small slugs. We then express the bubble nose velocity as:

$$U_{nose} = W_{eff} \cdot U_{bendiksen} \quad (2.13)$$

where $U_{bendiksen} = C_0 U_m + \nu_0$ is the expression of the bubble nose velocity for an infinitely long slug, and W_{eff} is a parameter greater than one introduced to represent the contribution of the wake effect to the actual bubble nose velocity. For long slugs W_{eff} is close to one, while for shorter slugs it can reach more than twice this value (see for example Van Hout, Shemer and Barnea, 2003).

Several authors have investigated the phenomenon since Moissis and Griffith (1962) and proposed several correlations. The original Moissis and Griffith correlation was used, as in Nydal and Banerjee (1996). The expression used for W_{eff} was then, for a slug of length L_S :

$$W_{eff} = 1 + 8e^{-1.06 \frac{L_S}{D}} \quad (2.14)$$

More advanced models were proposed in Van Hout et al. (2003, 2001). The original Moissis and Griffith (1962) model is used in LASSI most of the time, though a maximum value of 2.0 is often used for W_{eff} . The wake effect and its influence on the evolution of the slug length distribution along the pipe is discussed further in the second paper of this thesis. It is important to note that the slug-tracking nature of LASSI makes it possible to implement any correlation or experimental closure to account for the wake effect. In this respect, the slug-tracking approach followed in LASSI is much more flexible than the pure resolution of the two-fluid model set of differential equations, as any desirable closure can be implemented easily. Furthermore, the wake effect being intrinsically a 3D effect, it is not expected to be captured by a general 2 fluid model using steady state closure laws.

2.4 Gas law

In paragraph 3.5 introducing the pressure-momentum step of the LASSI scheme, the discretized gas mass conservation equations are presented in the case where the gas compressibility $\frac{\partial \rho_g}{\partial p}$ is not a constant. The scheme should then be able to deal with any reasonable gas law provided the function $\frac{\partial \rho_g}{\partial p}(p)$ is given (the term reasonable designating here a gas law yielding a slowly varying $\frac{\partial \rho_g}{\partial p}(p)$ function).

In practice the gas law (the relation providing the gas density ρ_g as a function of the absolute pressure p) actually implemented in LASSI is of the form:

$$\rho_g(p) = \rho_{g,out} + \frac{\partial \rho_g}{\partial p} (p - p_{out}) \quad (2.15)$$

where the gas density at the outlet $\rho_{g,out}$, the absolute pressure at the outlet p_{out} and the gas compressibility $\frac{\partial \rho_g}{\partial p}$ are three constant parameters provided by the user before the simulation.

For a perfect gas, we have the relation $p = \rho \frac{R}{M} T$ where R is the perfect gas constant, M the molar mass of the gas, and T the absolute temperature. The gas compressibility of a perfect gas can then be instantly expressed as: $\frac{\partial \rho_g}{\partial p} = \frac{M}{RT}$. For air at room temperature, we then find $\frac{\partial \rho_g}{\partial p} = 1.1 \cdot 10^{-5} \text{ kg.m}^{-3}.\text{Pa}^{-1}$. While relatively neutral in the case of hydrodynamic slug flow, the gas compressibility has of course a tremendous importance in the case of severe slugging.

Chapter 3

Details of the LASSI scheme

3.1 Introduction

This chapter presents the details of the LASSI (Lagrangian Approximate Scheme for Slug Initiation) scheme. The scheme is based on the three following main principles.

- The fast pressure dynamics governing the motion of the liquid slugs, the gas velocity and the pressure profile along the pipe are decoupled from the much slower dynamics of liquid transport in the stratified flow regions.
- Stratified flow is modelled using a Lagrangian implementation of a simplified two-fluid model in which the liquid dynamics have been uncoupled from the pressure and the gas dynamics. The liquid motion in the bubbles is then approximately modelled by a modified version of the shallow water equations in which the influence of the Bernoulli suction force is subtracted from the traditional hydrodynamical term.
- Border velocities are chosen in order to best represent the structure of the flow. In particular the slugs are treated as distinct objects whose position is tracked as they move along the pipe. Similarly, the borders between the different sections move in order to follow as much as possible the ripples as they progressively grow into slugs.

This chapter is organised as follows. The derivation of the model and its underlying assumptions are first presented, using the two-fluid model as a starting point. Then the implementation of the model in a Lagrangian framework is described.

3.2 The model

3.2.1 The general two-fluid model

The two-fluid model is composed of the four following partial differential equations. Those equations express mass and momentum conservation independently for each phase.

$$\frac{\partial}{\partial t} (\rho_l \beta) + \frac{\partial}{\partial x} (\rho_l \beta U_l) = 0 \quad (3.1)$$

$$\frac{\partial}{\partial t} (\rho_g \alpha) + \frac{\partial}{\partial x} (\rho_g \alpha U_g) = 0 \quad (3.2)$$

$$\frac{\partial}{\partial t} (\rho_l \beta U_l) + \frac{\partial}{\partial x} (\rho_l \beta U_l^2) = -\frac{\tau_l S_l}{A} + \frac{\tau_i S_i}{A} - \rho_l g \beta \sin \phi - \beta \frac{\partial}{\partial x} p - \rho_l g \beta \cos \phi \frac{\partial}{\partial x} h_l \quad (3.3)$$

$$\frac{\partial}{\partial t} (\rho_g \alpha U_g) + \frac{\partial}{\partial x} (\rho_g \alpha U_g^2) = -\frac{\tau_g S_g}{A} - \frac{\tau_i S_i}{A} - \rho_g g \alpha \sin \phi - \alpha \frac{\partial}{\partial x} p - \rho_g g \alpha \cos \phi \frac{\partial}{\partial x} h_l \quad (3.4)$$

The subscript l and g refer respectively to the liquid and gas phase. ρ and U are respectively the density and velocity of the considered phase. τ_l is the liquid-wall friction, τ_g the gas-wall friction and τ_i the gas-liquid friction. S_l and S_g are the liquid-wetted and gas-wetted perimeter and S_i is the interfacial width. p is the pressure, h_l the liquid height and ϕ the angle between the pipe and the horizontal. Finally α is the void fraction (i.e. the ratio between the gas-occupied area and the total pipe area) and β is the holdup (i.e. the ratio between the liquid-occupied area and the total pipe area).

3.2.2 Simplifying the two-fluid model

Condition 1 *The liquid phase is incompressible*

The liquid density ρ_l can then be extracted from the partial derivatives in the liquid mass and momentum conservation equations.

$$\frac{\partial}{\partial t} (\beta) + \frac{\partial}{\partial x} (\beta U_l) = 0$$

$$\begin{aligned}
\frac{\partial}{\partial t} (\rho_g \alpha) + \frac{\partial}{\partial x} (\rho_g \alpha U_g) &= 0 \\
\frac{\partial}{\partial t} (\beta U_l) + \frac{\partial}{\partial x} (\beta U_l^2) &= -\frac{\tau_l S_l}{A \rho_l} + \frac{\tau_i S_i}{A \rho_l} - g \beta \sin \phi - \frac{\beta}{\rho_l} \frac{\partial}{\partial x} p - g \beta \cos \phi \frac{\partial}{\partial x} h_l \\
\frac{\partial}{\partial t} (\rho_g \alpha U_g) + \frac{\partial}{\partial x} (\rho_g \alpha U_g^2) &= -\frac{\tau_g S_g}{A} - \frac{\tau_i S_i}{A} - \rho_g g \alpha \sin \phi - \alpha \frac{\partial}{\partial x} p - \rho_g g \alpha \cos \phi \frac{\partial}{\partial x} h_l
\end{aligned}$$

Using the gas momentum conservation equation, the pressure drop can be expressed as:

$$\frac{\partial}{\partial x} p = -\frac{1}{\alpha} \frac{\partial}{\partial t} (\rho_g \alpha U_g) - \frac{1}{\alpha} \frac{\partial}{\partial x} (\rho_g \alpha U_g^2) - \rho_g g \cos \phi \frac{\partial}{\partial x} h_l - \rho_g g \sin \phi - \frac{\tau_g S_g}{A \alpha} - \frac{\tau_i S_i}{A \alpha}$$

Replacing this expression in the liquid momentum conservation equation gives:

$$\frac{1}{\beta} \left[\frac{\partial}{\partial t} (\beta U_l) + \frac{\partial}{\partial x} (\beta U_l^2) \right] = \left(\begin{array}{c} \frac{1}{\alpha \rho_l} \left(\frac{\partial}{\partial t} (\alpha \rho_g U_g) + \frac{\partial}{\partial x} (\alpha \rho_g U_g^2) \right) \\ + \frac{1}{\rho_l} F - \frac{\rho_l - \rho_g}{\rho_l} g \cos \phi \frac{\partial}{\partial x} h_l \end{array} \right) \quad (3.5)$$

where $F = -\frac{\tau_l S_l}{A_l} + \frac{\tau_g S_g}{A_g} + \tau_i S_i \left(\frac{1}{A_l} + \frac{1}{A_g} \right) - (\rho_l - \rho_g) g \sin \phi$ is the resulting volumic force acting on the liquid phase (using the same notations as in Barnea and Taitel, 1995).

The system to be solved is then:

$$\begin{aligned}
\frac{\partial}{\partial t} (\beta) + \frac{\partial}{\partial x} (\beta U_l) &= 0 \\
\frac{\partial}{\partial t} (\rho_g \alpha) + \frac{\partial}{\partial x} (\rho_g \alpha U_g) &= 0 \\
\frac{1}{\beta} \left[\frac{\partial}{\partial t} (\beta U_l) + \frac{\partial}{\partial x} (\beta U_l^2) \right] &= \frac{1}{\alpha \rho_l} \left(\frac{\partial}{\partial t} (\alpha \rho_g U_g) + \frac{\partial}{\partial x} (\alpha \rho_g U_g^2) \right) + \frac{1}{\rho_l} F - \frac{\rho_l - \rho_g}{\rho_l} g \cos \phi \frac{\partial}{\partial x} h_l \\
\frac{\partial}{\partial t} (\rho_g \alpha U_g) + \frac{\partial}{\partial x} (\rho_g \alpha U_g^2) &= -\frac{\tau_g S_g}{A} - \frac{\tau_i S_i}{A} - \rho_g g \alpha \sin \phi - \alpha \frac{\partial}{\partial x} p - \rho_g g \alpha \cos \phi \frac{\partial}{\partial x} h_l
\end{aligned}$$

Condition 2 *As regards local liquid dynamics, the gas phase can be considered as incompressible.*

A quick justification for this very strong assumption would be to note that for perfect gases, the density is proportional to the pressure, i.e. $\frac{1}{\rho_g} \frac{\partial}{\partial t} (\rho_g) = \frac{1}{p} \frac{\partial}{\partial t} (p)$. The pressure variations in space and in time are usually very small compared to the outlet pressure. On the other hand the gas volumic flow rate can be varying significantly in wavy flows.

We can then simplify the expression of the contribution of the gas dynamics in the liquid momentum conservation equation:

$$\frac{1}{\alpha\rho_l} \left(\frac{\partial}{\partial t} (\alpha\rho_g U_g) + \frac{\partial}{\partial x} (\alpha\rho_g U_g^2) \right) \approx \frac{1}{\alpha} \frac{\rho_g}{\rho_l} \left[\frac{\partial}{\partial t} (U_g^S) + \frac{\partial}{\partial x} \left(\frac{1}{\alpha} (U_g^S)^2 \right) \right] \quad (3.6)$$

Condition 3 *The derivatives of the mixture velocity can be neglected in the liquid dynamics.*

If we neglect the term in $\frac{\partial}{\partial t} (U_m)$ and use the liquid mass conservation equation $\frac{\partial}{\partial t} \beta + \frac{\partial}{\partial x} (\beta U_l) = 0$, developing $\frac{\partial}{\partial t} (U_g^S)$ gives:

$$\frac{\partial}{\partial t} (U_g^S) \approx -\frac{\partial}{\partial t} (\beta U_l) \approx -\beta \frac{\partial}{\partial t} U_l + U_l \frac{\partial}{\partial x} (\beta U_l)$$

Neglecting the term in $2U_g \frac{\partial}{\partial x} (U_m)$ we obtain:

$$\frac{\partial}{\partial x} \left(\frac{1}{\alpha} (U_g^S)^2 \right) \approx (U_g)^2 \frac{\partial}{\partial x} (\beta) - 2U_g \frac{\partial}{\partial x} (\beta U_l)$$

Then replacing the expression for:

$$\left[\frac{\partial}{\partial t} (U_g^S) + \frac{\partial}{\partial x} \left(\frac{1}{\alpha} (U_g^S)^2 \right) \right] \approx (U_g - U_l)^2 \frac{\partial}{\partial x} (\beta) - \beta \frac{\partial}{\partial t} U_l + \beta (U_l - 2U_g) \frac{\partial}{\partial x} (U_l)$$

into the combined gas and liquid momentum equation provides the relation:

$$\frac{\partial}{\partial t} (\beta U_l) + \frac{\partial}{\partial x} (\beta U_l^2) = \left[\frac{\beta \rho_g}{\alpha \rho_l} (U_g - U_l)^2 - \frac{\rho_l - \rho_g}{\rho_l} g \cos \phi \frac{A_l}{dh_l} \right] \frac{\partial}{\partial x} (\beta) + \frac{\beta}{\rho_l} F \quad (3.7)$$

$$+ \frac{\beta \rho_g}{\alpha \rho_l} [-\beta \frac{\partial}{\partial t} U_l + \beta (U_l - 2U_g) \frac{\partial}{\partial x} (U_l)]$$

Condition 4 *The gas momentum is negligible compared to the liquid momentum (i.e. $\rho_l U_l \gg \rho_g U_g$)*

The terms in $\frac{\partial}{\partial t} U_l$ and $\frac{\partial}{\partial x} (U_l)$ in the right-hand side can then be neglected compared to the left hand-side, hence yielding:

$$\frac{\partial}{\partial t} (\beta U_l) + \frac{\partial}{\partial x} (\beta U_l^2) \approx -\kappa \beta \frac{\partial}{\partial x} (\beta) + \frac{\beta}{\rho_l} F \quad (3.8)$$

with

$$\kappa = \frac{\rho_l - \rho_g}{\rho_l} g \cos \phi \frac{A}{dh_l} - \frac{1}{\alpha} \frac{\rho_g}{\rho_l} (U_g - U_l)^2 \quad (3.9)$$

3.2.3 The LASSI model

The LASSI model is therefore composed of the four following partial differential equations:

$$\begin{aligned} \frac{\partial}{\partial t} (\beta) + \frac{\partial}{\partial x} (\beta U_l) &= 0 \\ \frac{\partial}{\partial t} (\rho_g \alpha) + \frac{\partial}{\partial x} (\rho_g \alpha U_g) &= 0 \\ \frac{\partial}{\partial t} (\beta U_l) + \frac{\partial}{\partial x} (\beta U_l^2 + \frac{1}{2} \kappa \beta^2) &= \frac{\beta}{\rho_l} F(U_l, \beta, U_g^S) \\ \frac{\partial}{\partial t} (\rho_g \alpha U_g) + \frac{\partial}{\partial x} (\rho_g \alpha U_g^2) &= -\frac{\tau_g S_g}{A} - \frac{\tau_i S_i}{A} - \rho_g g \alpha \sin \phi - \alpha \frac{\partial}{\partial x} p - \rho_g g \alpha \cos \phi \frac{\partial}{\partial x} h_l \end{aligned}$$

Thanks to several reasonable approximations, and under the condition that $\rho_l U_l \gg \rho_g U_g$, which holds at low pressures, the liquid momentum equation can be uncoupled from the gas momentum equation to yield a modified shallow-water equation in which a Bernoulli suction term $\frac{1}{\alpha} \frac{\rho_g}{\rho_l} (U_g - U_l)^2$ is subtracted from the traditional hydrostatic term $\frac{\rho_l - \rho_g}{\rho_l} g \cos \phi \frac{A}{dh_l}$. It is important to note that the simplified system:

$$\frac{\partial}{\partial t} (\beta) + \frac{\partial}{\partial x} (\beta U_l) = 0 \quad (3.10)$$

$$\frac{\partial}{\partial t} (\beta U_l) + \frac{\partial}{\partial x} \left(\beta U_l^2 + \frac{1}{2} \kappa \beta^2 \right) = \frac{\beta}{\rho_l} F(U_l, \beta, U_g^S) \quad (3.11)$$

has the same area of well-posedness as the full two-fluid model and becomes ill-posed when and only when the coefficient κ becomes negative. The well-posedness condition yields the well-known Inviscid Kelvin-Helmholtz (IKH) criterion which can be written in its traditional form:

$$\text{well-posed} \Leftrightarrow \kappa > 0 \Leftrightarrow (U_g - U_l)^2 < \frac{\rho_l - \rho_g}{\rho_g} g \cos \phi \frac{A_g}{dh_l} \quad (3.12)$$

3.3 Grid

The grid used is shown in figure 3.1. LASSI is a slug tracking code, therefore the slugs are treated differently than regular grid cells. Besides the slugs, the general idea is to as much as possible track the perturbations and waves in order to follow their possible development into slugs. The pipe is divided in grid cells, which are called either *sections* or *slugs* according to whether or not the liquid bridges the pipe within them. In figure 3.1, the cell J+2 is a *slug*, all the other cells are *sections*. The grid is completely adaptive, the cell borders are moving at independent speeds and the cell lengths are variable. The border velocities (*section-section* border, *section-slug* border or *slug-section* border) are chosen in order to best reproduce the physics of the system.

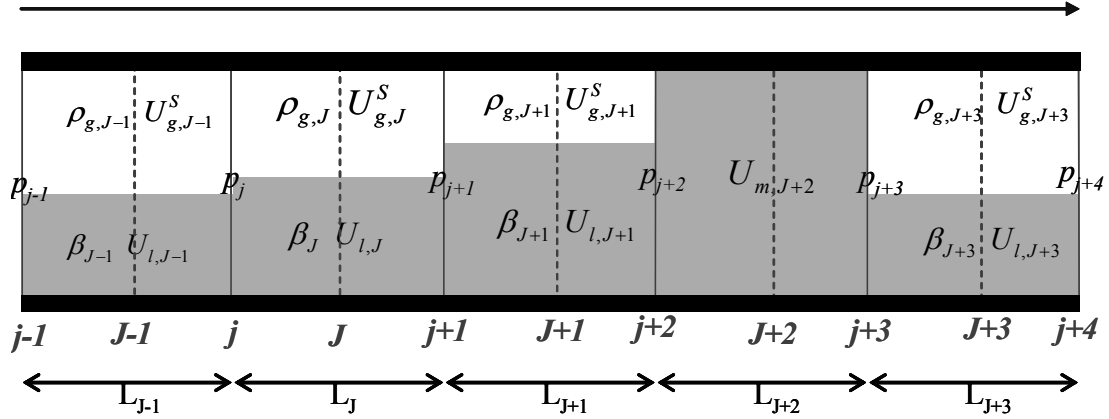


Figure 3.1: The grid used in the LASSI scheme

Although the void in slug case could be implemented without special difficulties, for the sake of simplicity, only the unaerated slug case is presented here. The *slugs* are then only characterized by their mixture velocity U_m (equal to the liquid velocity inside the slug U_{ls}).

The *sections* are characterized by their holdup β , their liquid velocity U_l , their gas mass flow rate $\rho_g U_g^S$, and their right pressure p . The pressure grid is staggered and centred on the cell borders. This original disposition allows to solve the void wave propagation on a non-staggered grid while the pressure-momentum equations are solved on a staggered grid. In addition the slug momentum equation is solved more accurately when the pressure values are stored on the borders.

3.4 Solution procedure

Sketch 3.2 introduces the LASSI solution procedure.

The first step is the Pressure-Momentum implicit computation where the pressure p and the gas fluxes $\rho_g U_g^S$ within the *sections* and the mixture velocity U_m within the *slugs* are calculated implicitly, using a simple and fast tridiagonal algorithm detailed later. Using the bubble turning criterion detailed in the closure law chapter, the nature of each of the *section-slug* and *slug-section* borders is set to either Front or Nose (refer to section 2.2 for a description of the closure used). Finally the liquid velocity is updated to take into account the work of the friction forces and gravity, yielding the intermediate liquid velocities $U_l^{n+1/2}$.

In the void wave step, liquid mass and momentum fluxes are evaluated using a La-

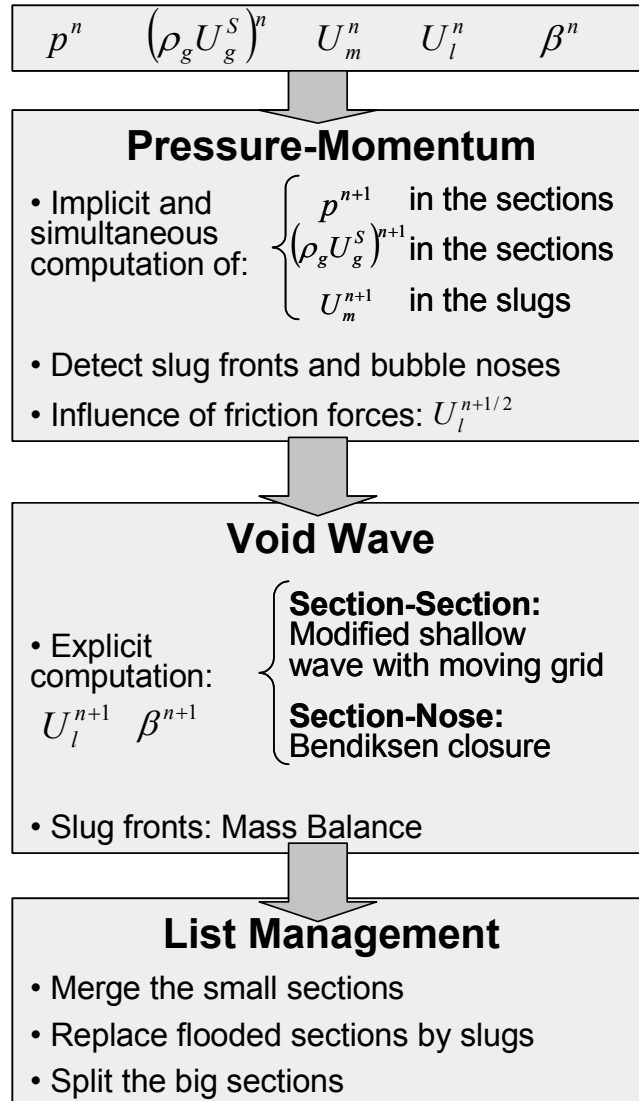


Figure 3.2: The LASSI solution procedure

grangian modified shallow water scheme, hence for each *section* J , the holdup β_J^{n+1} , the liquid velocity $U_{l,J}^{n+1}$ as well as the *section-section* border velocities are calculated from $(\beta_J^n, U_{l,J}^{n+1/2})$, $(\beta_{J-1}^n, U_{l,J-1}^{n+1/2})$ and $(\beta_{J+1}^n, U_{l,J+1}^{n+1/2})$. For *section-slug* and *slug-section* borders, Bendiksen's correlation is used when the border has been detected a bubble nose, while an iterative steep front model (which allows the slug to "eat" completely several *sections* in a single time-step, while ensuring liquid mass conservation) is used if a front has been detected.

Since the length of the *sections* is varying, some list management is needed, in order to prevent the appearance of very large or very short *sections*. List management is invoked a first time in the void wave step when the CFL criterion is checked: if the fast wave from the left border of a *section* is able to take over the slow wave from the right border of this *section* in a time inferior to the chosen time step, than this *section* is merged with one of its neighbours. If this happens, the border velocities and liquid fluxes are recalculated between the newly merged *section* and its neighbours. Finally, list management also occurs when a *section* that has exceeded a critical length, has to be split in two.

3.5 Pressure momentum step

This paragraph presents the details of the pressure-momentum step used in LASSI.

3.5.1 Discretization of the equations

Gas Mass conservation

As explained previously, a staggered grid is used to store the pressure values. Considering gas mass conservation within the pressure control volume j provides the relation:

$$V_{g,j} \frac{d\rho_{g,j}}{dt} = \frac{dm_{g,j}}{dt} - \rho_{g,j} \frac{dV_{g,j}}{dt} \quad (3.13)$$

where $V_{g,j}$ and $m_{g,j}$ are respectively the gas volume and the gas mass within the control volume j , and $\rho_{g,j}$ is the gas density at this control volume.

We then have : $\frac{dm_{g,j}}{dt} = (\rho_g U_g^S)_{J-1} - (\rho_g U_g^S)_J - \alpha_{J-1} \rho_{g,J-1} U_{b,J-1} + \alpha_J \rho_{g,J} U_{b,J}$ and $\frac{dV_{g,j}}{dt} = \alpha_J U_{b,J} - \alpha_{J-1} U_{b,J-1} + \beta_J U_{l,J} - \beta_{J-1} U_{l,J-1}$ where $U_{b,J}$ is the velocity of the J border. We can then write, with $V_{g,j}^n = \frac{1}{2} (\alpha_{J-1} L_{J-1} + \alpha_J L_J)$:

$$p_j^{n+1} = \varkappa_j^n \left[(\rho_g U_g^S)_{J-1}^{n+1} - (\rho_g U_g^S)_J^{n+1} \right] + \varrho_j^n \quad (3.14)$$

introducing:

$$\varkappa_j^n = \frac{\delta t}{V_{g,j}^n \left[\frac{\partial \rho_g}{\partial p} \right]_j^n}$$

$$\varrho_j^n = p_j^n + \frac{\delta t}{V_{g,j}^n \left[\frac{\partial \rho_g}{\partial p} \right]_j^n} \left(\begin{array}{l} \rho_{g,j}^n [(\beta U_l)_{J-1}^n - (\beta U_l)_J^n] \\ \alpha_{J-1}^n U_{b,J-1}^n \left(\rho_{g,j}^n - \rho_{g,J-1}^n \right) \\ + \alpha_J^n U_{b,J}^n \left(\rho_{g,J}^n - \rho_{g,j}^n \right) \end{array} \right)$$

The *section-slug* pressure control volume $j + 2$ is discretized as:

$$p_{j+2}^{n+1} = \varkappa_{j+2}^n \left[(\rho_g U_g^S)_{J+1}^{n+1} - \rho_{g,j+2}^n U_{m,J+2}^{n+1} \right] + \varrho_{j+2}^n \quad (3.15)$$

with:

$$\varkappa_{j+2}^n = \frac{\delta t}{V_{g,j+2}^n \left[\frac{\partial \rho_g}{\partial p} \right]_{j+2}^n}$$

$$\varrho_{j+2}^n = p_{j+2}^n + \frac{\delta t}{V_{g,j+2}^n \left[\frac{\partial \rho_g}{\partial p} \right]_{j+2}^n} \left(\begin{array}{l} \rho_{g,j+2}^n (\beta U_l)_{J+1}^n \\ \alpha_{J+1}^n U_{b,J+1}^n \left(\rho_{g,j+2}^n - \rho_{g,J+1}^n \right) \end{array} \right)$$

Gas momentum conservation

The gas momentum conservation equation:

$$\frac{\partial}{\partial t} (\rho_g U_g^S) + \frac{\partial}{\partial x} (\rho_g U_g^S U_g) + \alpha \frac{\partial}{\partial x} p = -\frac{\tau_g S_g}{A} - \frac{\tau_i S_i}{A} - \rho_g g \alpha \sin \phi \quad (3.16)$$

discretized around the J control volume gives, after replacing p_{j+1}^{n+1} and p_j^{n+1} in the pressure gradient term $\frac{\alpha_J^n}{L_J^n} (p_{j+1}^{n+1} - p_j^{n+1})$ by their expression above:

$$a_J^n (\rho_g U_g^S)_J^{n+1} = b_J^n (\rho_g U_g^S)_{J+1}^{n+1} + c_J^n (\rho_g U_g^S)_{J-1}^{n+1} + d_J^n \quad (3.17)$$

where:

- $a_J^n = \frac{1}{\delta t} + b_J^n + c_J^n + \frac{1}{8} \left(\frac{S_g}{A_g} \lambda_g |U_g| \right)_J^n + \frac{1}{8} \left(\frac{S_i}{A_i} \lambda_i |U_g - U_l| \right)_J^n$
- $b_J^n = -\frac{1}{L_J^n} \min(U_{g,j+1}^n - U_{b,j+1}^n, 0) + \frac{\alpha_J^n}{L_J^n} \varkappa_{j+1}^n$
- $c_J^n = \frac{1}{L_J^n} \max(U_{g,j}^n - U_{b,j}^n, 0) + \frac{\alpha_J^n}{L_J^n} \varkappa_j^n$

- $d_J^n = \frac{1}{\delta t} (\rho_g U_g^S)^n + \frac{\alpha_J^n}{L_J^n} (\varrho_J^n - \varrho_{J+1}^n) + \frac{1}{8} \left(\frac{S_i}{A} \lambda_i \rho_g U_l |U_g - U_l| \right)_J^n - \rho_{g,J}^n g \alpha_J^n \sin \phi$

Slug momentum conservation

The $J + 2$ slug, considered incompressible, is subject to the pressure difference across it, the gravity and the friction at the wall. It also loses some momentum by picking up low velocity liquid at its front and shedding high velocity liquid at its tail. The equation is here discretized for a slug with a front on its right and a bubble nose on its left, as an example:

$$\rho_l \frac{L_{J+2}^{n+1} U_{m,J+2}^{n+1} - L_{J+2}^n U_{m,J+2}^n}{\delta t} = \left[\begin{array}{l} -p_{j+3}^{n+1} + p_{j+2}^{n+1} - g \rho_l (h_R^n - h_L^n) - \frac{\lambda \rho_l}{2D} L_s^n U_{m,J+2}^{n+1} \left| U_{m,J+2}^n \right| \\ + \rho_l (U_f^n - U_{m,J+2}^n) U_{l,J+3}^n - \rho_l (U_b^n - U_{m,J+2}^n) U_{m,J+2}^{n+1} \end{array} \right]$$

where h_R^n and h_L^n are the liquid heights respectively at the right and at the left of the slug, U_f^n is the front velocity at the right and U_b^n is the bubble nose velocity at the left. This equation can be re-written as:

$$a_{J+2}^n U_{m,J+2}^{n+1} = b_{J+2}^n (\rho_g U_g^S)_{J+3}^{n+1} + c_{J+2}^n (\rho_g U_g^S)_{J+1}^{n+1} + d_{J+2}^n \quad (3.18)$$

with:

- $a_{J+2}^n = \frac{\rho_l L_{J+2}^n}{\delta t} + \rho_l \frac{\beta_{J+3}^n}{1 - \beta_{J+3}^n} (U_{m,J+2}^n - U_{l,J+3}^n) + \frac{\lambda \rho_l}{2D} L_{J+2}^n \left| U_{m,J+2}^n \right| + \rho_{g,j+3}^n \varkappa_{j+3}^n + \rho_{g,j+2}^n \varkappa_{j+2}^n$
- $b_{J+2}^n = \varkappa_{j+3}^n$
- $c_{J+2}^n = \varkappa_{j+2}^n$
- $d_{J+2}^n = \varrho_{j+2}^n - \varrho_{j+3}^n - g \rho_l (h_R - h_L) + \frac{\rho_l L_{J+2}^n}{\delta t} U_{m,J+2}^n + \rho_l \frac{\beta_{J+3}^n}{1 - \beta_{J+3}^n} (U_{m,J+2}^n - U_{l,J+3}^n) U_{l,J+3}^n$

3.5.2 Solving procedure

Sketch 3.3 introduces the solving procedure of the pressure momentum step in the LASSI scheme.

Gas mass correction

In order to ensure full gas mass conservation, a correction is needed. It is done at the unit level (a unit consists of all the *sections* between two *slugs*), since the exact gas mass within one unit can be tracked easily. The error between the tracked gas mass present in the bubble unit at the beginning of the time step $M_{g,unit}^n$ and the "observed

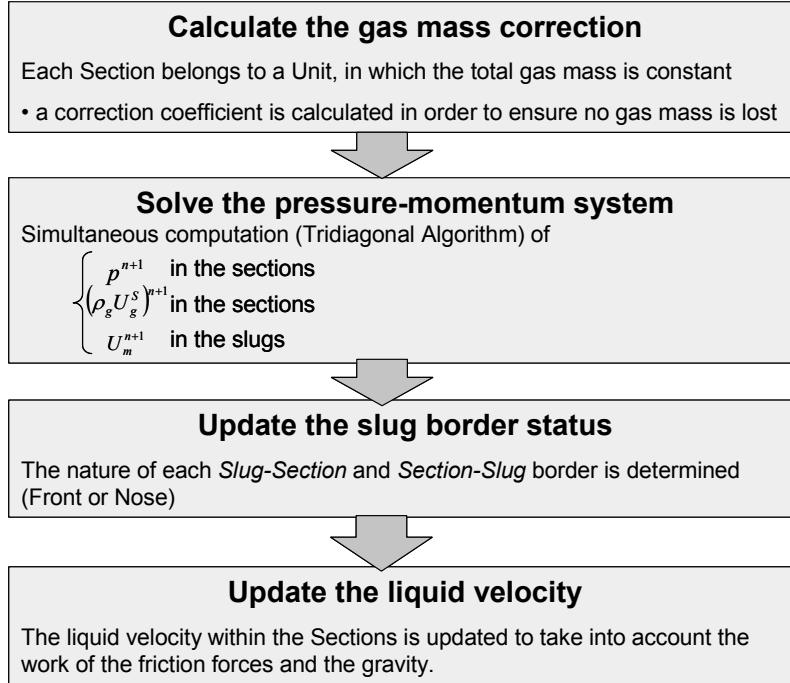


Figure 3.3: The LASSI Pressure Momentum step

gas mass" $M_{g,unit}^n$ resulting from the calculated pressure field is added as a correction coefficient to the ϱ_j^n coefficient in the equation $p_j^{n+1} = \alpha_j^n \left[(\rho_g U_g^S)_{J-1}^{n+1} - (\rho_g U_g^S)_J^{n+1} \right] + \varrho_j^n$.

$$correction = \frac{M_{g,unit}^n - M_{g,unit}^n}{V_{g,unit}^n} \frac{1}{\left[\frac{\partial \rho_g}{\partial p} \right]} \quad (3.19)$$

This method lacks precision because the correction is spread out evenly on every *section* of the unit instead of being tailored to each *section*. However, it provides a great stability to the pressure momentum equation and the amount of correction needed being extremely small, the error spreading is not believed to be overly prejudicial to the scheme accuracy.

Pressure-Momentum system

There is therefore only a tridiagonal system $a_j^n X_j^{n+1} = b_j^n X_j^{n+1} + c_j^n X_j^{n+1} + d_j^n$ to solve using the Thomas algorithm in order to evaluate the mixture velocity within the slugs, the pressure along the pipe, and the gas mass flow rate. The resolution is therefore extremely fast.

Slug border status update

Once the pressure-momentum system is solved, the mixture velocity within the slugs is known. By applying the bubble turning criterion exposed in section 2.2.3, it is then possible to determine the nature (Nose or Front) of each *slug-section* and *section-slug* border.

Liquid velocity update

Using the newly determined local mixture velocity, the liquid velocity within the *sections* is updated from the effect of the friction forces and the gravity:

$$U_{l,J}^{n+1/2} = \frac{1}{1 - \frac{\delta t}{\rho_l} \frac{\partial F}{\partial U_l}(\beta_J^n, U_{l,J}^n, U_{m,J}^{n+1})} \begin{bmatrix} U_{l,J}^n \\ + \frac{\delta t}{\rho_l} F(\beta_J^n, U_{l,J}^n, U_{m,J}^{n+1}) \\ - U_{l,J}^n \frac{\delta t}{\rho_l} \frac{\partial F}{\partial U_l}(\beta_J^n, U_{l,J}^n, U_{m,J}^{n+1}) \end{bmatrix} \quad (3.20)$$

The resulting volume force F is indeed a function of 3 variables (which can be either β, U_l and U_g or β, U_l^S and U_g^S or as here β, U_l and U_m). Introducing the partial derivative of F relative to U_l has a stabilizing effect on the scheme.

When the liquid holdup is extremely low ($\beta < 0.001$), this approach leads to a certain instability due to the great sensitivity of F in this area. As a consequence, when $\beta < 0.001$ the liquid velocity is simply set to its equilibrium value, i.e to U_l^* ensuring $F(\beta_J^n, U_l^*, U_{m,J}^{n+1}) = 0$. Finally, for practical reasons, U_l is simply set to zero when the holdup is differential ($\beta < 10^{-6}$).

3.6 Void wave

3.6.1 The shallow water equations

Thanks to the simplifications presented in 3.2.2, the gas and the liquid dynamics have been uncoupled. The void wave step thus simply aims at resolving the following modified shallow water system:

$$\frac{\partial}{\partial t} (\beta) + \frac{\partial}{\partial x} (\beta U_l) = 0 \quad (3.21)$$

$$\frac{\partial}{\partial t} (\beta U_l) + \frac{\partial}{\partial x} \left(\beta U_l^2 + \frac{1}{2} \kappa \beta^2 \right) = 0 \quad (3.22)$$

Compared to the shallow water equations, the only difference is that the Bernoulli effect term is subtracted from the hydrostatic term. The resolution is independent of the gas dynamics and takes place on a non-staggered grid. The grid used is completely flexible as the *section* border velocities are calculated as to as best as possible follow the characteristics of the flow. Given a left *section* characterized by a holdup β_L and a liquid velocity U_L and a right *section* characterized by a holdup β_R and a liquid velocity U_R , the objective is to calculate the *section-section* border velocity U_b as well as the mass and momentum fluxes between the two *sections*.

3.6.2 Solving the Riemann problem

The shallow water equations presented in section 3.6.1 are well-known and the Riemann problem between the left state (U_L, β_L) and the right state (U_R, β_R) can be solved numerically in an exact manner. Indeed, the solution consists in one intermediate state (U_M, β_M) which is connected to both the left state (U_L, β_L) and the right state (U_R, β_R) by either a shock or a rarefaction wave (Holden et al., 2002), depending on the conditions.

Shocks

A shock is characterized by the Rankine-Hugoniot condition which gives mass and momentum conservation across a front travelling at a constant velocity s . For a shock between (U_L, β_L) and (U_M, β_M) (slow shock), this condition can be written as the system:

$$\begin{aligned} s(\beta_M - \beta_L) &= \beta_M U_M - \beta_L U_L \\ s(\beta_M U_M - \beta_L U_L) &= (\beta_M U_M^2 + \frac{1}{2}\kappa\beta_M^2) - (\beta_L U_L^2 + \frac{1}{2}\kappa\beta_L^2) \end{aligned}$$

This system has only one entropy-conserving solution which consists of:

$$\beta_M > \beta_L \text{ and } U_M = U_L - \frac{1}{\sqrt{2}}\sqrt{\kappa}(\beta_M - \beta_L)\sqrt{\frac{1}{\beta_M} + \frac{1}{\beta_L}} \text{ (Left Shock: LS)} \quad (3.23)$$

For a shock between (U_M, β_M) and (U_R, β_R) (fast shock) the entropy-conserving solution will be:

$$\beta_M > \beta_R \text{ and } U_M = U_R + \frac{1}{\sqrt{2}}\sqrt{\kappa}(\beta_M - \beta_R) \sqrt{\frac{1}{\beta_M} + \frac{1}{\beta_R}} \text{ (Right Shock: RS)} \quad (3.24)$$

Rarefaction waves

Rarefaction waves are structures travelling with the system's characteristic speed $U - \sqrt{\kappa\beta}$ (slow wave) and $U + \sqrt{\kappa\beta}$ (fast wave) within which the flow variables β and U vary smoothly from one state to another. It can be shown (Holden et al., 2002) that within a rarefaction wave, the Riemann invariant ($U + 2\sqrt{\kappa\beta}$ for a slow wave and $U - 2\sqrt{\kappa\beta}$ for a fast wave) is a constant of the flow. It follows that the (U_L, β_L) state can be connected to the (U_M, β_M) state by a slow wave only provided that:

$$\beta_M < \beta_L \text{ and } U_M = U_L - 2\sqrt{\kappa} \left(\sqrt{\beta_M} - \sqrt{\beta_L} \right) \text{ (Left Wave: LW)} \quad (3.25)$$

Similarly one can connect the intermediate state (U_M, β_M) to the right state (U_R, β_R) by a fast wave provided that:

$$\beta_M < \beta_R \text{ and } U_M = U_R + 2\sqrt{\kappa} \left(\sqrt{\beta_M} - \sqrt{\beta_R} \right) \text{ (Right Wave: RW)} \quad (3.26)$$

Finding the intermediate state

The two states (U_L, β_L) and (U_R, β_R) being known, the intermediate state (U_M, β_M) can be determined as the intersection of the four curves (Left Shock LS, Left Wave LW, Right Shock RS, Right Wave RW) $U_M = f(\beta_M)$ detailed above. Due to the monotonous nature of those four functions, only a few iterations are needed to calculate U_M and β_M with great accuracy. The graph presented in figure 3.4 shows the four curves and the calculated intermediate state in the so-called "moving dam case" ($\beta_L = 0.5$, $\beta_R = 0.25$, $U_L = U_R = 10 \text{ m.s}^{-1}$).

The so-called left and right dry-bed cases (respectively β_L and β_R equals zero) and the appearing dry-bed case ($\beta_M = 0$, occurring when $U_L + 2\sqrt{\kappa\beta_L} < U_R - 2\sqrt{\kappa\beta_R}$) are special cases that do not present any particular difficulties to implement and are detailed further in Annex A. Another case of interest presented in Annex A is the

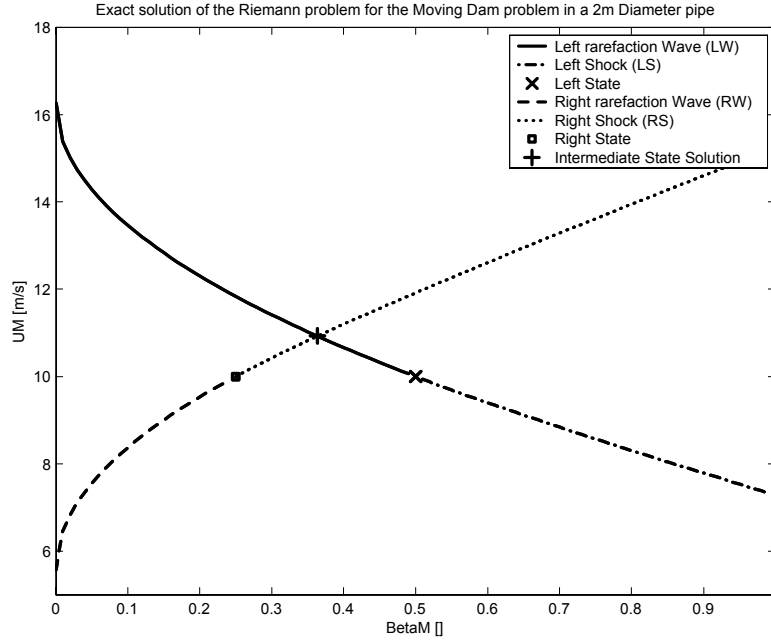


Figure 3.4: Determination of the intermediate state (β_M, U_M) in the Riemann Problem

Saturated Shock Shock case which occurs when the resolution of the shallow-water Riemann problem gives a predicted intermediate holdup β_M higher than one. This can clearly not occur in a pipe and this case is dealt with by setting β_M to one and calculating U_M in order to ensure momentum conservation.

3.6.3 Calculating the fluxes

Once the Riemann problem is solved and the intermediate state is found, the characteristics of the *section-section* border have to be determined in order to evaluate the holdup and momentum fluxes between the two *sections*. Sketch 3.5 presents the most general case that can arise between two states (U_L, β_L) and (U_R, β_R) . The resolution of the Riemann problem provides the value of the intermediate state (U_M, β_M) as well as the nature (rarefaction wave or front) of the transition between the intermediate state and the left and right states. This information allows us to calculate the left-intermediate border velocity U_{LL} as well as the intermediate-right border velocity U_{RR} . In addition to fluxes calculation, those velocities are of interest because they can be used to check if the CFL criterion is fulfilled (the fast wave associated with a border should not be able to catch up with the slow wave associated with the next border in a time shorter than the time step in use).

The question is now to decide how to choose the border velocity U_b between the left and the right *section*. As the grid is completely flexible, we have a great liberty in the choice of U_b . In order to limit the numerical diffusion it makes sense to choose a value comprised between U_{LL} and U_{RR} . If U_b is taken exactly equal to U_{LL} (respectively U_{RR}), the whole intermediate state is attributed to the right *section* (respectively the left *section*) and the scheme follows the left-intermediate (respectively the intermediate-right) border.

There is only one intermediate state (U_M, β_M) solution to the Riemann problem. However in the case of a rarefaction wave between the left state and the intermediate state for example, the holdup and velocity will change slowly and progressively between the two states. The average holdup in the rarefaction wave region will therefore be neither equal to β_L nor to β_M but rather in between. As a consequence in the most general case as presented in sketch 3.5, it makes sense to consider that $U_{LL} \leq U_b \leq U_{RR}$, $\beta_{ML} \neq \beta_{MR}$ and $U_{ML} \neq U_{MR}$.

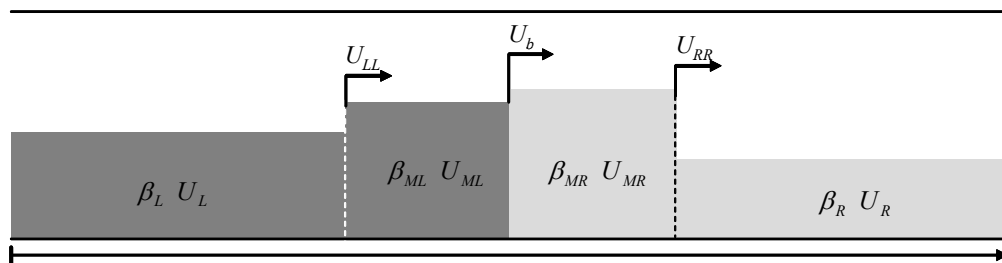


Figure 3.5: Calculating the characteristics of a section-section border

3.6.4 Front tracking

Regarding the choice of U_b , it is natural to take profit of the power of the Lagrangian approach to make the most of the information provided by the exact solution of the Riemann problem. It was decided to focus on the propagation of the fast fronts, as they are of special interest when it comes to modelling the transition. Modelling correctly the fast fronts allows also to follow ripples and roll-waves with limited diffusion. As a consequence, the border velocities and liquid fluxes are evaluated in the LASSI scheme as presented in figure 3.6. If a fast front is detected (case Rarefaction-Shock and Shock-Shock), the border velocity will be set to the fast front velocity in order to follow it. If no fast front is present (case Rarefaction-Rarefaction and Shock-Rarefaction), the border velocity will be set to follow the middle of the intermediate state. Liquid mass and liquid momentum fluxes follow automatically from conservation laws, once the

border velocity has been chosen. The reason for this dissymmetric treatment lies on the ambition to model as correctly as possible a wave composed by a smooth tail and a sharp fast front.

Annex A provides the details of the calculations performed to compute the different variables (U_{LL} , U_b , U_{RR} , β_{ML} , β_{MR} , U_{ML} and U_{MR}) in each of the different cases:

- Rarefaction-Rarefaction
- Rarefaction-Shock
- Shock-Rarefaction
- Shock-Shock
- Saturated Shock-Shock
- Rarefaction-Rarefaction with Appearing Dry Bed
- Rarefaction-Void
- Void-Rarefaction
- *section-slug* Nose
- *slug-section* Nose

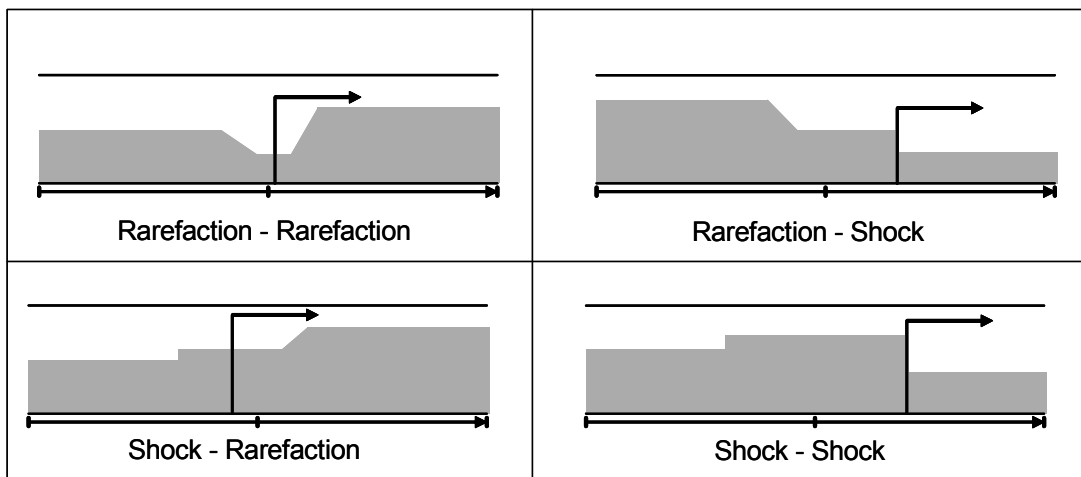


Figure 3.6: Interface tracking in the LASSI scheme

3.6.5 Updating holdup and velocities

Once the characteristics of each border have been calculated, the border positions as well as the holdup and liquid velocity within the *sections* are updated. The following relations are used:

$$\begin{aligned} z_{RR,j}^{n+1} &= z_j^n + U_{RR,j} \delta t & z_j^{n+1} &= z_j^n + U_{b,j} \delta t \\ z_{LL,j+1}^{n+1} &= z_{j+1}^n + U_{LL,j} \delta t & z_{j+1}^{n+1} &= z_{j+1}^n + U_{b,j+1} \delta t \end{aligned} \quad (3.27)$$

$$\beta_J^{n+1} = \frac{\beta_J^n (z_{LL,j+1}^{n+1} - z_{RR,j}^{n+1}) + \beta_{ML,j+1}^n (z_{j+1}^{n+1} - z_{LL,j+1}^{n+1}) + \beta_{MR,j}^n (z_{RR,j}^{n+1} - z_j^{n+1})}{z_{j+1}^{n+1} - z_j^{n+1}} \quad (3.28)$$

$$U_J^{n+1} = \frac{\beta_J^n U_J^n (z_{LL,j+1}^{n+1} - z_{RR,j}^{n+1}) + \beta_{ML,j+1}^n U_{ML,j+1}^n (z_{j+1}^{n+1} - z_{LL,j+1}^{n+1}) + \beta_{MR,j}^n U_{MR,j}^n (z_{RR,j}^{n+1} - z_j^{n+1})}{(z_{j+1}^{n+1} - z_j^{n+1}) \beta_J^{n+1}} \quad (3.29)$$

Figure 3.7 gives a clearer picture of the variables to compute and of the updating procedure.

3.6.6 Slug fronts

As explained in the closure laws chapter, the *slug* fronts are considered steep. The *slug* front positions are updated last, at the end of the void wave step, once the *sections* holdup and borders positions have already been updated. The top sketch of figure 3.8 shows a *slug* front at the beginning of the update *slug* front procedure. The *sections* at the right of the *slug* have already been updated, so there is a (purely virtual) "empty gap" between the *slug* front and the first *section* on the right.

At the beginning of the update front procedure (top sketch), the *slug* has to move towards the right and fill a volume equal to $U_{l,slug} \delta t$ (no void in slug case). Due to the fact that the slug turning point criterion implemented (see section 2.2.3) ensures us that $U_{l,slug} > U_{l,J}$, the *slug* will at least bridge the gap to the first *section* on the right (the opposite would have been clearly unphysical). The middle sketch of figure 3.8 shows the situation after the slug has filled the virtual void ahead of it. A loop implemented ensures that the slug moves forward until the total volume of $U_{l,slug} \delta t$ of void has been filled. An unlimited number of *sections* can therefore be eaten by the *slug* on a single time step, thanks to the steep front approach (in the bottom sketch of figure 3.8, the slug has "eaten" the whole J *section* and part of the $J + 1$ *section*).

Finally, sketch 3.9 shows the solving procedure of the void wave step.

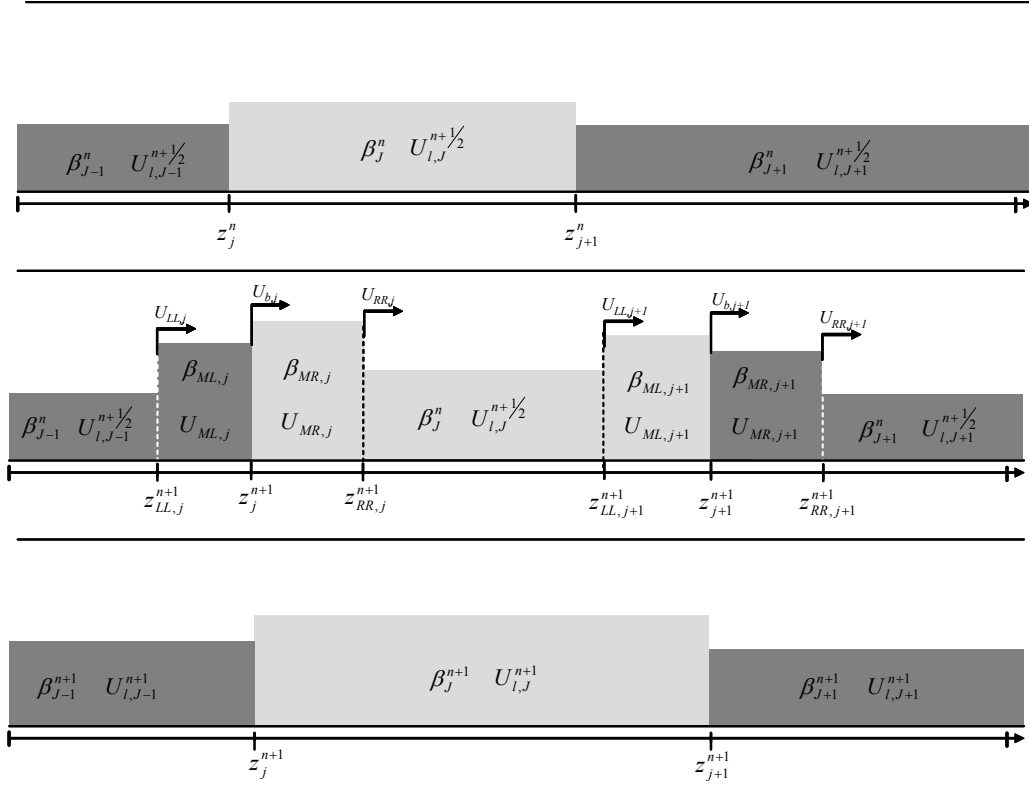


Figure 3.7: Void wave calculation in LASSI

3.7 List management

3.7.1 Implementation

The great power given by the adaptive grid comes with some implementation challenges: some grid cells become too small and the CFL criterion is no longer verified within them at the chosen time step (the fast wave from their left border takes over the slow wave from their right border). Some other grid cells become too large and have to be split in order to maintain the wanted spatial accuracy. Those difficulties are met by the use of an object oriented programming method in C++. The pipe is represented as a doubly-linked list of objects which can be either slugs or bubbles. Those objects can be taken away and deleted (if a slug dies for example, or if a *section* becomes too short), and new objects can be inserted (if the holdup in a bubble reaches one, than a slug is inserted). Figure 3.10 represents the different classes used in LASSI.

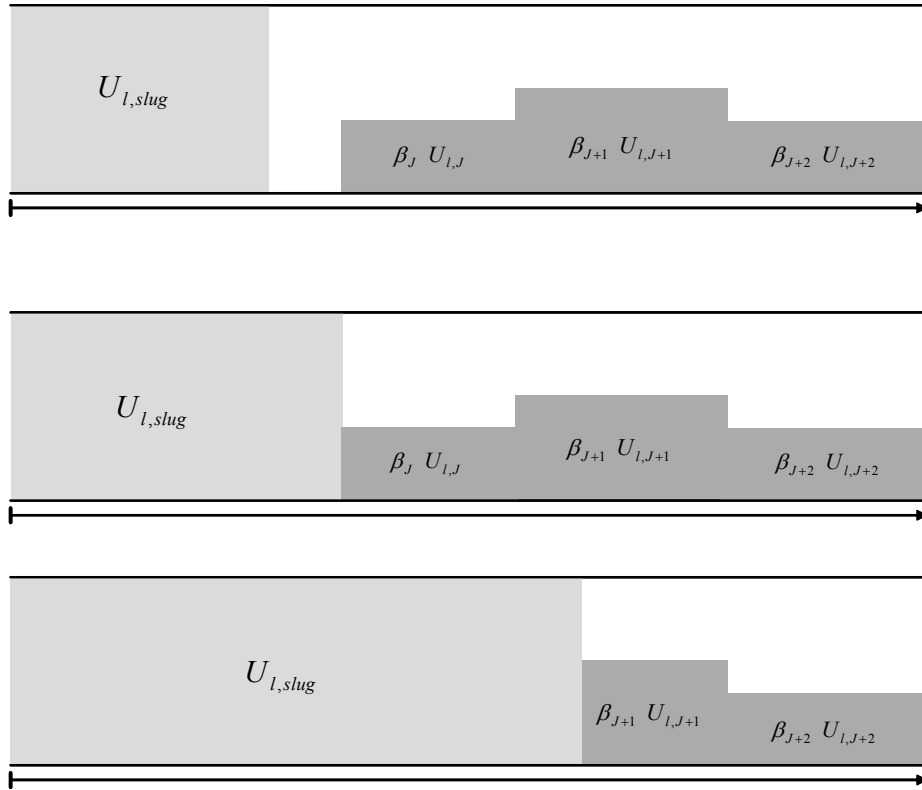


Figure 3.8: Slug front update procedure

3.7.2 Splitting

In LASSI the grid is completely adjustable and the *section* length evolves freely according to the border velocities calculated when solving the Riemann problem. In order to preserve the spatial accuracy of the scheme it is therefore necessary to split the *sections* which have become excessively long. This is done last in the List Management step of the scheme (3.2). Any *section* whose length is exceeding twice the `TargetLength` parameter is split in two *sections* of equal length and characteristics (such as holdup and liquid velocity). Figure 3.11 presents the splitting process in the LASSI scheme.

3.7.3 Merging

Sketch 3.9 presents the solving procedure of the void wave step. For each *section-section* border j , the three border velocities $U_{LL,j}$ (velocity of the border between the left state and the left intermediate state), $U_{b,j}$ (velocity of the border between the left intermediate state and the right intermediate state, which is used as the *section-section* border velocity) and $U_{RR,j}$ (velocity of the border between the right intermediate state

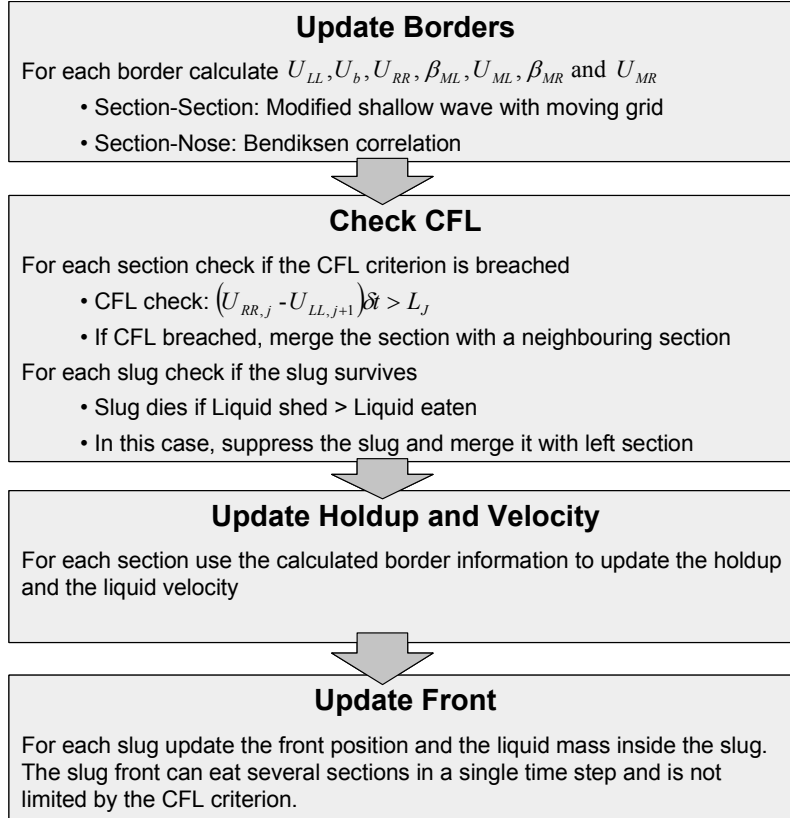


Figure 3.9: The LASSI void wave solving procedure

and the right state) are calculated as shown in figure 3.7. Clearly we need to ensure each timestep that the CFL criterion is ensured within each *section* J , that is to say that the inequality $(U_{RR,j} - U_{LL,j+1})\delta t < L_J$ is verified, where L_J is the length of *section* J .

As shown in the void wave solving procedure (figure 3.9), the Riemann problem is first solved for all borders of the pipe. After this, the CFL-inequality is checked for each *section*, and should the CFL criterion be breached in a *section*, the CFL-breaching *section* is merged with either its left or its right neighbour. A *section* can only be merged with another *section*, not with a *slug*. If both of the neighbouring *objects* are *sections*, the CFL-breaching *section* is merged with the *section* whose holdup is closest to the holdup of the CFL-breaching *section*. Figure 3.12 shows how the process takes place in the LASSI scheme.

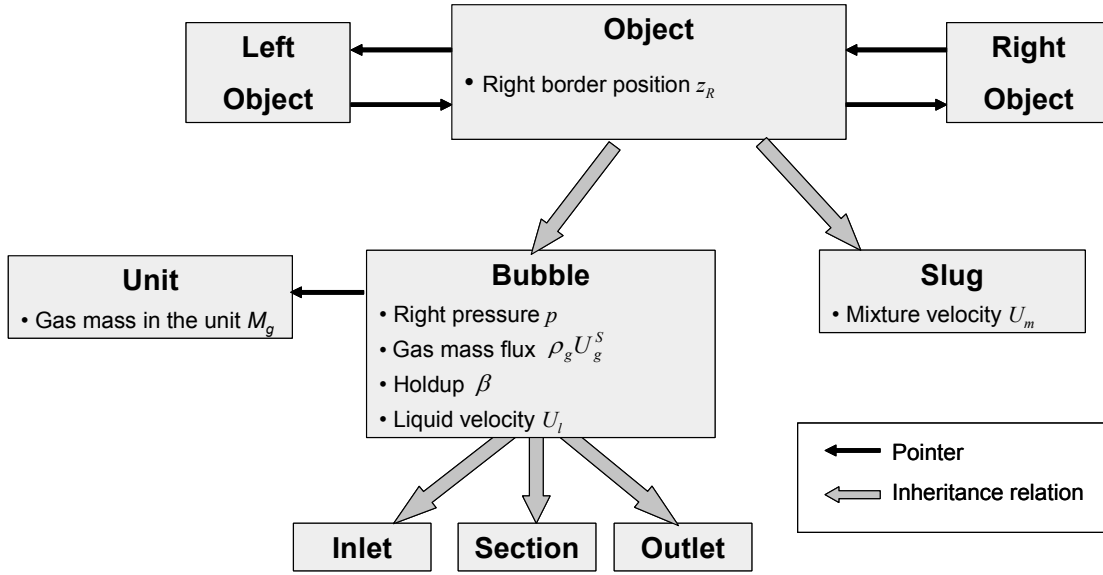


Figure 3.10: Object-Oriented implementation of the LASSI scheme

3.7.4 Slug initiation

Whenever the holdup within a given *section* exceeds a critical value β_{init} the *section* is removed and replaced with a *slug*. Typically a value of 0.98 is used for β_{init} . If a *slug* is present, either on the right or on the left of the section whose holdup is exceeding β_{init} , the flooded section is merged with the slug. The liquid mass corresponding to the difference between the holdup in the *slug* (1) and the holdup within the flooded *section* (anything between 0.98 and 1) is taken from the neighbouring sections, in order to ensure liquid mass conservation.

Figure 3.13 shows what happens when the two neighbouring objects of the flooded *section* are *sections*. Regarding the holdups of the neighbouring sections, the superscript * refers to the fact that the holdups have been decreased to ensure liquid mass conservation.

3.8 Boundary treatment

3.8.1 Inlet

The fully Lagrangian nature of the scheme requires that special concern is given to the inlet boundary treatment. *Sections* need to be created at the inlet, transported along the pipe, merged or split in the pipe according to the structure of the flow, and finally discarded when they exit the pipe at the outlet.

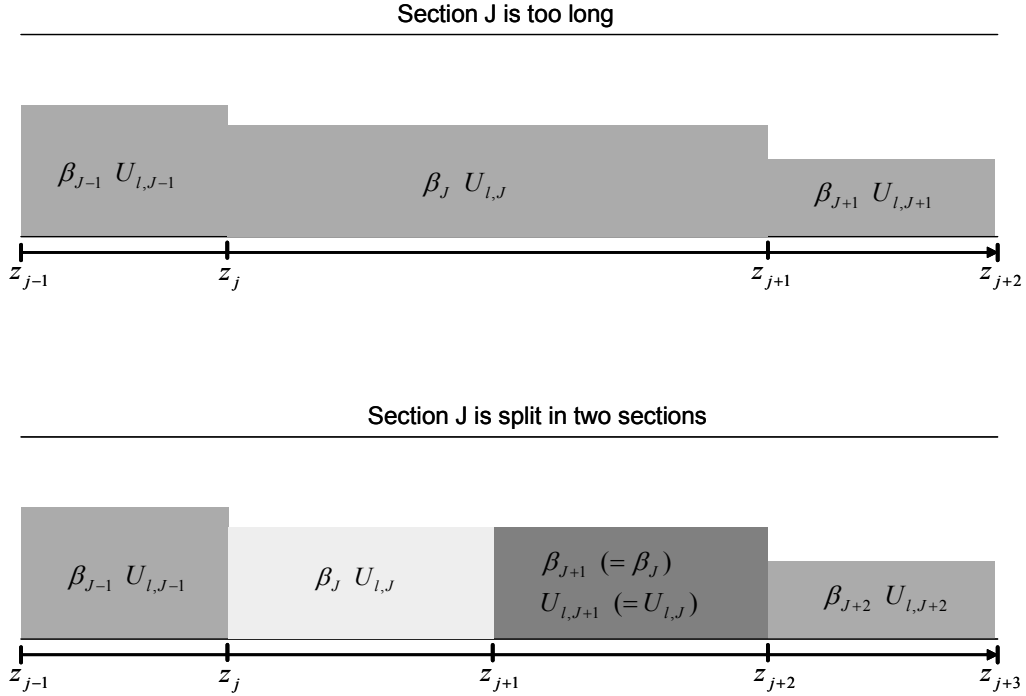


Figure 3.11: Splitting of the long sections in LASSI

Regarding the inlet treatment, it was first attempted not to use any special treatment. The first *section* within the pipe would then receive the inlet liquid flux as a source, and eventually be split into two separate *sections* when the first *section* length had reached the splitting length, just like any other *section* in the pipe. This method was initially implemented but resulted in an oscillation in the liquid holdup, as the constant inlet liquid flow was spread into a *section* whose length was varying greatly in time.

It was then decided to use a dedicated class in order to model the inlet. The *inlet* object is defined as a *bubble* characterized by a liquid velocity always equal to the inlet liquid velocity $U_{l,in}$, and a liquid holdup always equal to the ratio $\frac{U_{l,in}^S}{U_{l,in}}$. Regarding the flux calculation, the right border of the inlet bubble is considered as infinitely smooth (to be opposed to the shock approach followed on standard *section-section* borders). As the liquid velocity on the border is taken equal to the inlet velocity, the liquid mass flux between the inlet *section* and the second *section* is zero. The right border of the inlet *section* is thus moving with a velocity equal to $U_{RR} = U_{l,in}$. The sketch presented figure 3.14 shows how the void wave step is handled in the special case of the *inlet-section* border.

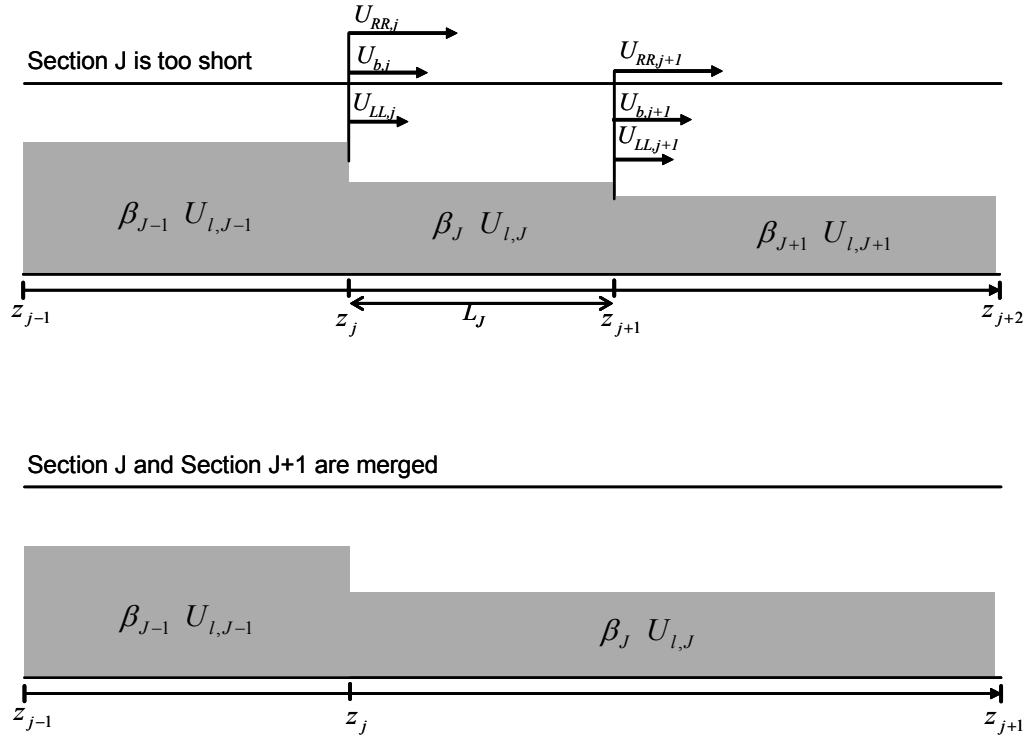


Figure 3.12: Merging of the short sections in LASSI

TargetLength is a parameter of the scheme. When the length of the *inlet* has reached twice this constant, it is split in two: the left part remains the *inlet* while the right part becomes a standard *section* object whose initial length is **TargetLength**, initial holdup is β_{in} and initial liquid velocity is $U_{l,in}$. The newly created *section* is then applied the standard void wave calculation process until it is split or merged. Figure 3.15 shows how the *inlet* is split once it has reached a sufficient length.

3.8.2 Outlet

The outlet is considered to be a separator at constant pressure. We assume that the liquid is only able to flow from the pipe into the separator, but not from the separator back into the pipe. On the other hand, we consider that the gas is able to flow both ways, allowing the pressure to remain constant at the outlet of the pipe. The holdup within the separator is assumed to be zero, as if the liquid was instantly sucked out when it exits the pipe. In the LASSI scheme, the outlet object is then defined as a *bubble* whose holdup is zero. This *object* is inserted as the last *object* of the doubly-linked *object* list and the *section-outlet border* is treated in the void wave step as any normal *section-section* border. This means that during the void wave step, the *sections*

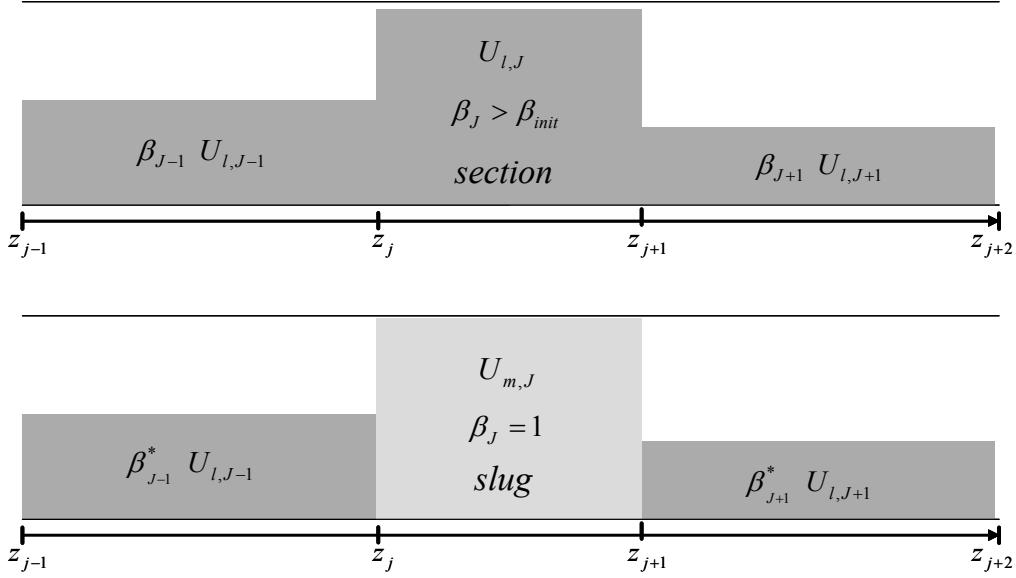


Figure 3.13: Slug initiation in LASSI

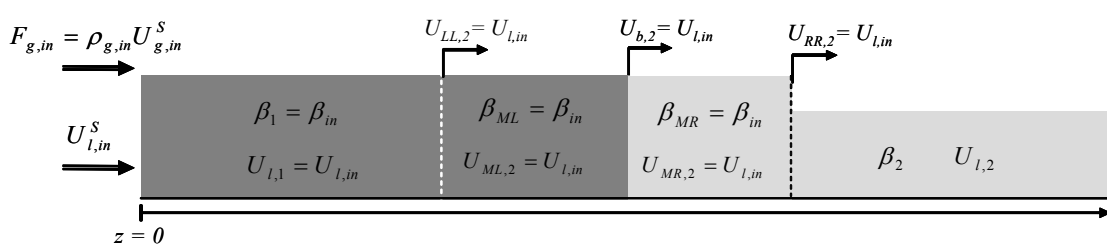


Figure 3.14: Void wave step in the inlet

are actually free to move as if the pipe was infinitely long. As the holdup within the *outlet bubble* is zero, the *section-outlet* border falls into the category of the "right dry-bed" and thus propagates at the speed $U_b = U_{l,N} + 2\sqrt{\kappa_{N+1}\beta_N}$ where $U_{l,N}$ and β_N are respectively the liquid velocity and the liquid holdup within the last *section*. At the end of the void-wave step, it is therefore likely that the newly computed position of the right border of the last *section* of the pipe (i.e. the position of the *section-outlet* border) differs from the physical length of the pipe. During the list management step, this situation is met by either "cutting" the *sections* that are partly or completely out of the pipe, (when the liquid is flowing out of the pipe), or by adding an additional empty *section* to fill the empty space between the last *section* and the pipe outlet (when the liquid in the last *section* is flowing back towards the inlet).

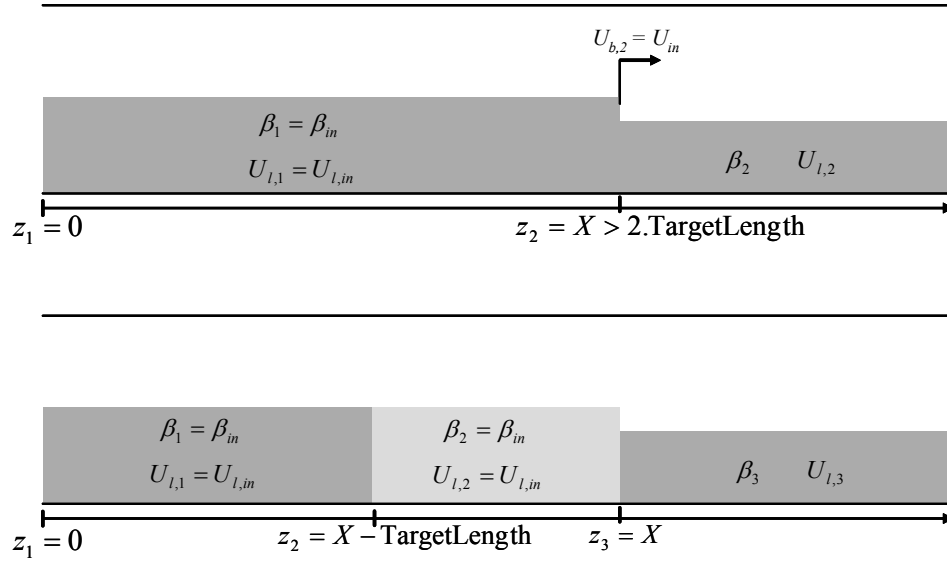


Figure 3.15: Section splitting at the inlet

The sketch on top of figure 3.16 shows how is treated the case of normal forward flow at the outlet. At the end of the void wave step, the last *section* (designated with the suffix N) has completely exited the pipe, while the previous *section* (designated with the suffix N-1) has partly exited the pipe. The last *section* is then deleted, while the previous *section* is "cut" so that its right border now matches with the physical position of the pipe outlet.

The sketch at the bottom of figure 3.16 shows what happens when there is backward flow at the outlet ($U_b = U_{l,N} + 2\sqrt{\kappa_{N+1}\beta_N} < 0$). Since the right border of the last *section* is now located inside the pipe, there is an empty gap between this position and the physical position of the pipe outlet. This gap is empty since we consider that liquid can not flow back from the separator to the pipe. We then simply create a new empty *section* and insert it within the doubly linked list of objects that represent the flow.

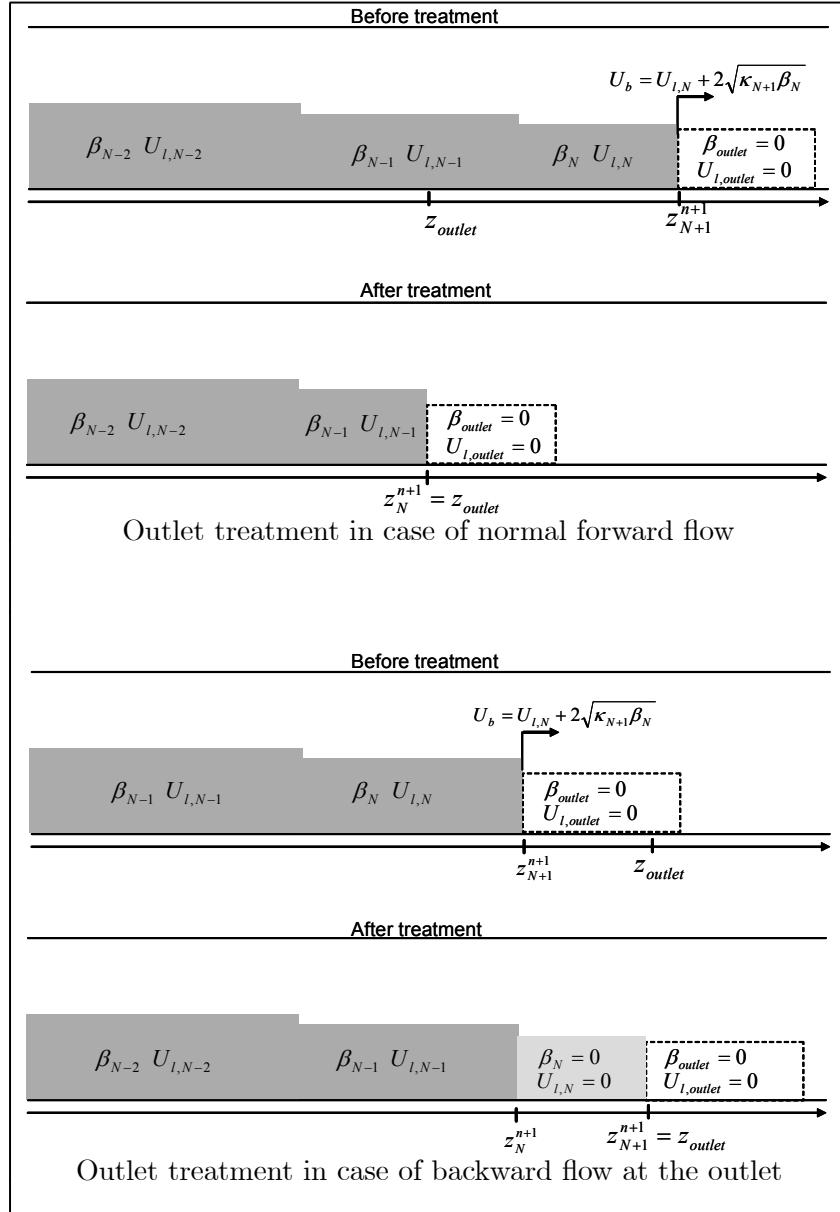


Figure 3.16: Outlet treatment in the LASSI scheme

Chapter 4

Influence of the integration parameters on the predictions

4.1 Influence of the section size on the slug length

In the second paper of this thesis, the ability of the LASSI scheme to reproduce the observed slug length distribution in a small-scale loop was investigated. Figure 4.1 recalls the pipe geometry used in the experiments and in the simulations. The inlet liquid superficial velocity $U_{l,in}^S$ was set to 0.22 m.s^{-1} and the inlet gas superficial $U_{g,in}^S$ velocity to 0.44 m.s^{-1} . Optical captors located 20, 80 and 150 diameters downstream of the bend in the upwards pipe provided the length, front velocity and tail velocity of each passing slug. More details regarding the experiments, the measurement technique and the experimental results can be found in the second paper of this thesis.

Figure 4.2 shows the computed slug length distribution obtained with the LASSI scheme using a `Targetlength` parameter of 2 cm and a time step of 2 ms. In LASSI the length of the sections varies according to border velocities calculations. The sections are created at the inlet with an initial length equal to the `Targetlength` parameter and any section whose length exceeds twice the value of this parameter is split in two sections of equal length.

The standard Moissis and Griffith (1962) correlation was used in order to model the wake effect (refer to section 2.3). As in LASSI the slug initiation process is captured automatically without using any initiation model, one can wonder if the section size used in the simulations will have a big influence on the computed slug length distribution.

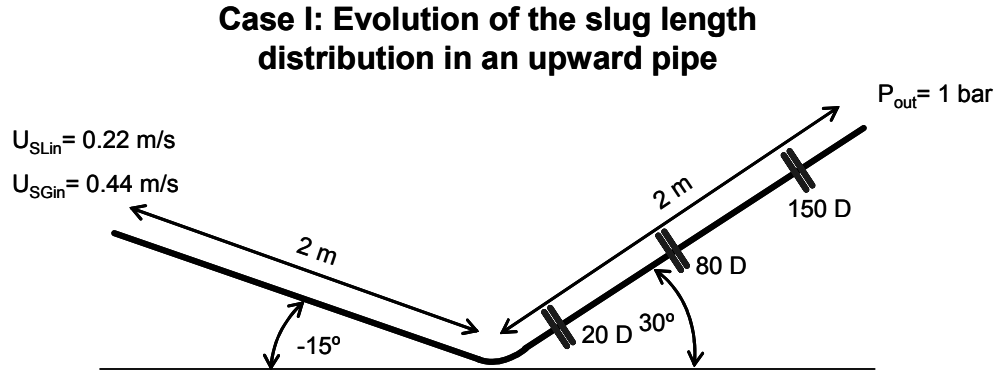


Figure 4.1: Sketch of the pipe geometry

The same case was simulated again, this time using a `Targetlength` parameter of 1 cm and a time step of 1 ms , hence maintaining the CFL ratio constant. The results are presented figure 4.3. The results obtained with a `Targetlength` parameter of 1 cm are significantly different than those obtained when this parameter was set to 2 cm . The use of a smaller section size results indeed in far many more very short slugs being observed close to the bend. After 10 diameters , 5018 slugs , in average 4.9 diameters long, were measured during a simulation time of 15 minutes for a `Targetlength` parameter of 2 cm . With a `Targetlength` parameter of 1 cm , 10116 slugs , in average 2.2 diameters long were observed at the same location and during the same period.

However, the difference between the two computations fades away as we move further downstream, towards the outlet of the pipe. After 150 diameters , the two obtained distributions are sensibly equivalent, and the average slug length is surprisingly higher in the simulations where the smaller value was used for the `Targetlength` parameter.

A comparison with the obtained experimental results is done in the second paper of this thesis. Arguably, the computations made with the bigger section length match a lot better with the experimental observations after 20 diameters . On the other hand, although the computed slug length distribution 150 diameters after the bend obtained with a `Targetlength` value of 2 cm is satisfactory, it is somehow less close to the experimental results than the slug length distribution computed with a `Targetlength` value of 1 cm which matches very well with the experiments.

Of course, the implemented wake effect model has a tremendous influence on these results, obtained here with an "uncapped" standard Griffith correlation. A sensibility study regarding the maximum value of the wake effect parameter W_{eff} is done in the

second paper of this thesis.

As a conclusion, we can say that the section length used for the LASSI simulations can have an influence on the computed average slug length. However, this influence is mainly limited to the region close to the initiation point, and the use of an adequate model for the bubble nose velocity will naturally ensure that the computed distribution will tend towards the experimentally observed slug length distribution. This is in line with Barnea and Taitel (1993) who used a wake effect model to predict the spatial evolution of an arbitrarily chosen slug length distribution at the inlet. They obtained a good match with the experimental observations and also showed that at a sufficient distance, the computed distribution was fairly insensitive to the arbitrarily chosen distribution at the inlet.

4.2 Influence of the section length and of the time step on the transition point from stratified to slug flow

In the first paper of this thesis, the LASSI predictions regarding the transition point from stratified to slug flow in a slightly downwards inclined pipe were compared with some experimental observations made by Woods et al. (2000). For a given value of the gas superficial velocity U_g^S , the lowest value of the superficial velocity U_i^S for which slug flow was observed was determined numerically with the LASSI scheme. The case of a 50 meters long pipe with an internal diameter D equal to 7.63 cm and inclined downwards with an angle of 0.5° was considered. The gas superficial velocity U_g^S was set to 3.38 m.s^{-1} and with a time step of 2 ms and a `TargetLength` value of 2 cm, transition to slug flow was observed to occur numerically when U_i^S reached a value of 0.55 m.s^{-1} . The simulations were done at given inlet superficial velocities, by starting with a pipe filled with liquid and gas at steady state. The interfacial friction factor was taken equal to the gas friction factor ($\frac{\lambda_i}{\lambda_g} = 1$). The transition was considered to have occurred if a slug had been initiated within the 50 meters of the pipe in less than a minute of simulation time.

One can wonder how important is the impact of the time step and the section length (as measured by the parameter `TargetLength`) on the transition point as predicted by the LASSI scheme. In order to evaluate this effect, different values were tried for the time step and the `TargetLength` parameter in the case presented above ($U_g^S = 3.38 \text{ m.s}^{-1}$). The results are presented in table 4.1. The first conclusion is rea-assuring

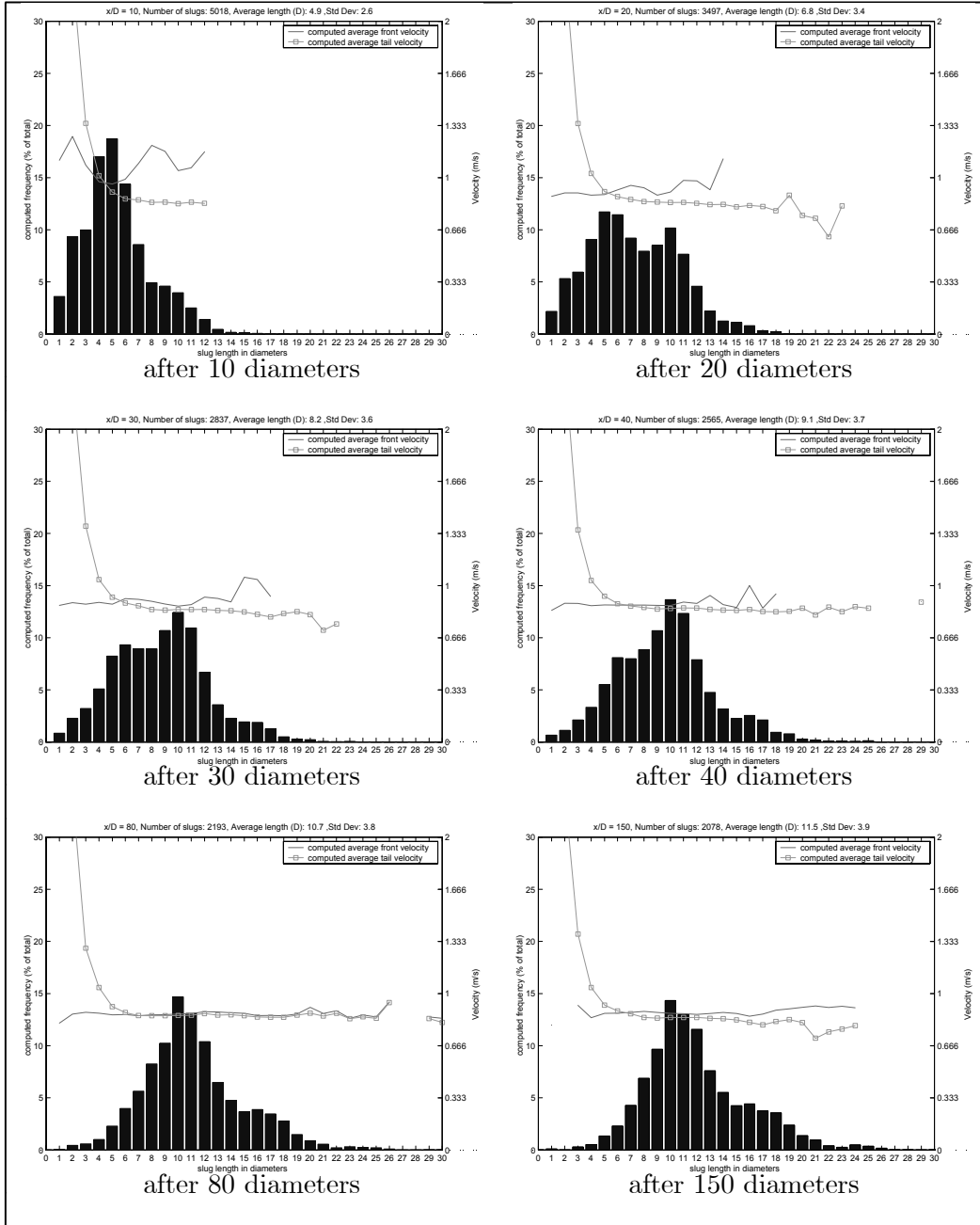


Figure 4.2: Computed slug length distribution at various locations using 2 cm long sections and a 2 ms time step

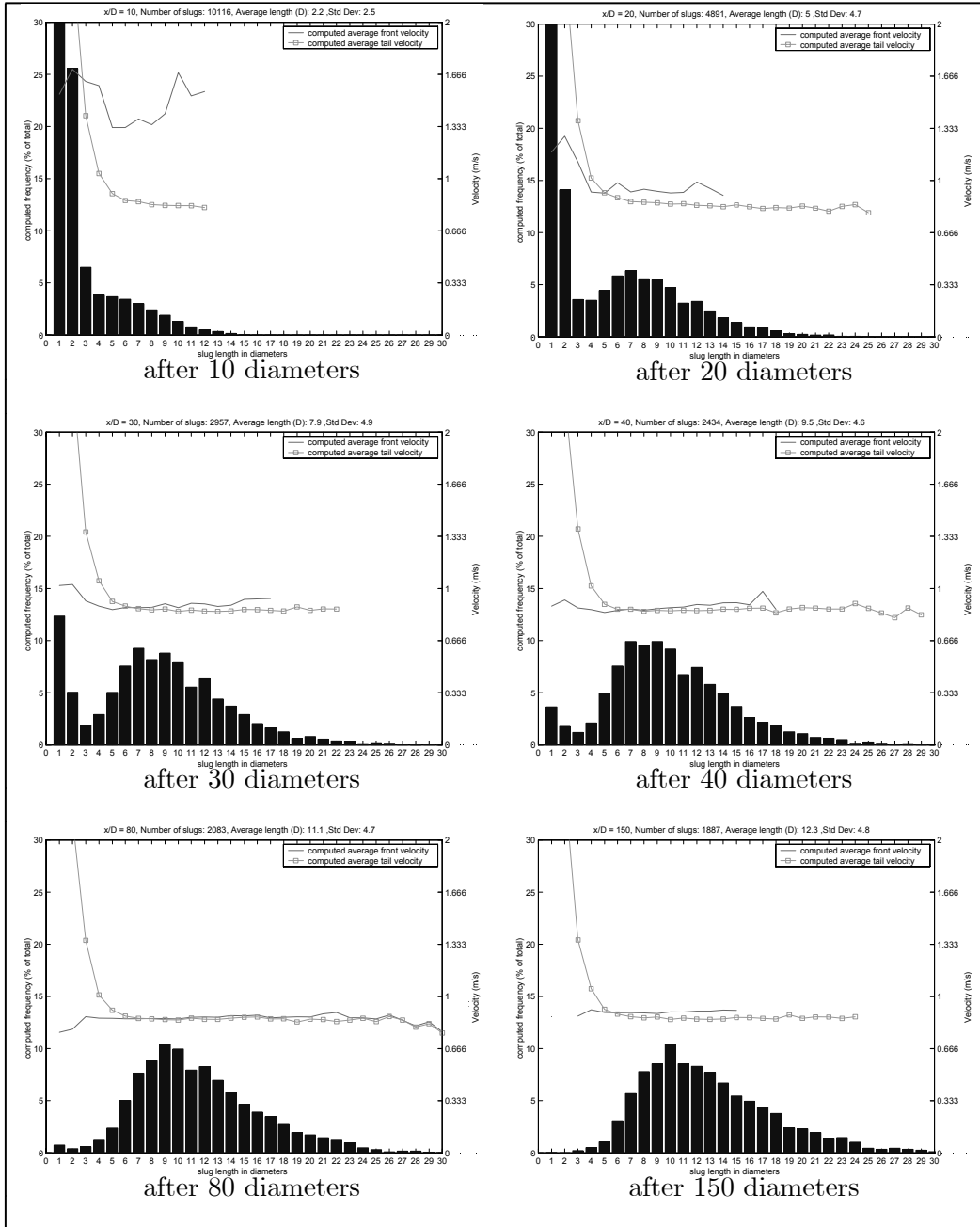


Figure 4.3: Computed slug length distribution at various locations using 1 cm long sections and a 1 ms time step

since it seems that the integration parameters do not have a sizeable importance on the critical liquid superficial velocity and thus on the numerical flowmap.

The details of the results are hard to analyse since it seems that the value of the CFL ratio does not have any importance. In an explicit scheme, it is clearly counterintuitive that for a given section length, stability increases with the time step as what happens when `TargetLength` is set to 2 *cm*. This paradox can probably be explained by the functioning of the LASSI scheme: the `TargetLength` parameter only corresponds to the section length at the inlet. As the border velocities are set according to the characteristics of the flow, the section length varies throughout the pipe and the simulation duration. The only effects that bound the length of the sections are the splitting of the sections whose length exceeds twice the `TargetLength` parameter, and the merging of the sections in which the CFL criterion would be violated. Increasing the time step thus naturally increases the minimum section length under which the sections do not comply with the CFL criterion and are merged. In other words, in LASSI for a given value of the parameter `TargetLength`, increasing the time step also increases the average section length.

Increasing the section length for a given time step tends to marginally destabilize the scheme, which might also be surprising. However, if we refer to the demonstration provided section 4.1 of the first paper of this thesis, we realize that if we used infinitely long sections, we would be exactly in the case where the area of stability of the scheme corresponds exactly to the Viscous Kelvin Helmholtz criterion. The results shown table 4.1 seem finally plausible given the characteristics of the scheme.

	TargetLength		
Value of U_l^S at the transition	1 <i>cm</i>	2 <i>cm</i>	4 <i>cm</i>
$\delta t = 1$ <i>ms</i>	0.57	0.55	0.55
$\delta t = 2$ <i>ms</i>	0.57	0.55	0.55
$\delta t = 4$ <i>ms</i>	0.57	0.57	0.55

Table 4.1: Influence of the time step and the section length on the critical liquid superficial velocity

We can conclude by pointing out the very robust predictions of LASSI regarding the transition from stratified to slug flow. Given its original, non-staggered way of implementing the Bernoulli suction force, the tests indicate that the LASSI scheme is able to accurately predict the transition from stratified to slug flow irrespectively of the time step or section length used.

Chapter 5

References

Andreussi, P., Bendiksen, K., Nydal, O., 1993. Void distribution in slug flow Int. J. Multiphase Flow, 19, 817-828.

Barre, F., 1990. The CATHARE code strategy and assessment. Nucl. Eng. Design, 124(3):257-284.

Barnea, D., Taitel Y., 1993. A model for slug length distribution in gas-liquid slug flow. Int. J. Multiphase Flow, 19, 829-838.

Barnea, D., Brauner, N., 1985. Holdup of the liquid slug in two phase intermittent flow. Int. J. Multiphase Flow, 11 43-49.

Barnea, D., Shemer, L., 1989 Void-fraction measurements in vertical slug flow: applications to slug characteristics and transition. Int. J. Multiphase Flow 15, 495-504.

Barnea, D., Taitel, Y., 1993. Kelving-Helmholtz stability criteria for stratified flow: viscous versus non-viscous (inviscid) approaches. Int. J. Multiphase Flow 19 (4), 639-649.

Bendiksen, K.H., 1984. An experimental investigation of the motion of long bubbles in inclined tubes. Int. J. Multiphase Flow 10, 467-483.

Bendiksen, K. H., Malnes, D., Straume, T., Hedne, P., 1990. A non-diffusive numerical model for transient simulation of oil-gas transportation systems. European simulation multi conference, Nuremberg, June 1990, pp. 508-515.

Bendiksen, K.H., Malnes, D., Moe, R., Nuland, S., 1991. The dynamic two-fluid model OLGA: Theory and application. SPE Production Engineering, May 1991, 171-180.

Bendiksen, K.H., Espedal, M., 1992. Onset of slugging in horizontal gas-liquid pipe flow. Int. J. Multiphase Flow 18, 234-247.

Bendiksen, K.H., Malnes, D., Nydal, O.J., 1996. On the modelling of slug flow. Chem. eng. com. 141: 71-102

Biberg, D., 1999. Two-phase stratified pipe flow modelling a new expression for the interfacial shear stress. In: Two-Phase Flow Modelling and Experimentation (1999), 99-108.

Black, P., Daniels, L., Hoyle, N., Jepson, W., 1990. Studying Multi-Phase Flow Using the Pipeline Analysis Code (PLAC). J. Energy Re. Technology. Vol. 112. March 1990.

Bonizzi, M., 2002. Transient one-dimensional modelling of multi-phase slug flows. Ph.D. Thesis, Imperial College, University of London.

Bonizzi, M., Issa, R., 2003a. A model for simulating gas bubble entrainment in two-phase horizontal slug flow. Int. J. Multiphase Flow 29, 1685-1717.

Bonizzi, M., Issa, R., 2003b. On the simulation of three-phase slug flow in nearly horizontal pipes using the multi-fluid model. Int. J. Multiphase Flow 29, 1719-1747.

Colebrook, C., 1939. Turbulent flow in pipes, with particular reference to the transition regime between smooth and rough pipe laws. Institution of Civ. Eng. Journal, 11, 133-156.

Davies, R.M., Taylor, G. I., 1949. The mechanics of large bubbles rising through extended liquids and through liquids in tubes. Proc. Roy. Soc. London 200 Am 375-390.

Fan, Z., Lusseyran, F., Hanratty, T.T., 1993. Initiation of slugs in horizontal gas-liquid flows. AIChE J. 39, 1741-1753.

Griffith, P., Wallis, G. 1961. Two-phase flow. Journal of Heat Transfer, 83, 301-320.

Haaland, S., 1983. Simple and explicit formulas for the friction factor in turbulent pipe flow. *Journal of Fluids Engineering*, 105, 89-90.

Holden, H., Risebro, N. H., 2002 *Front tracking for hyperbolic conservation laws*. Springer.

Hurlburt, E. T., Hanratty, T. J., 2002. Prediction of the transition from stratified to slug and plug flow for long pipes. *Int. J. Multiphase Flow* 28, 707–729.

Issa, R.I., Kempf, M.H.W., 2003. Simulation of slug flow in horizontal or nearly horizontal pipes with the two-fluid model. *Int. J. Multiphase Flow* 29, 69–95.

Kristiansen, O., 2004. Experiments on the transition from stratified to slug flow in multiphase pipe flow. Ph.D. Thesis, NTNU, Trondheim, Norway.

Larsen, M. Hustvedt, E., Straume, T., 1997. PeTra: A Novel Computer Code for Simulation of Slug Flow. *SPE Annual Technical Conference and Exhibition*, San Antonio, Texas, 5–8 October 1997. SPE 38841.

Lin, P.Y., Hanratty, T.J., 1986. Prediction of the initiation of slugs with linear stability theory. *Int. J. Multiphase Flow* 12, 79–98.

Manolis, I.G., 1995. High pressure gas-liquid slug flow. Ph.D. Thesis, Imperial College

Moissis, R., Griffith, P., 1962. Entrance effects in a two-phase slug flow. *Journal of Heat Transfer*, 84, 366-370.

Nicklin, D. J., Wilkes, J. O., Davidson, J. F., 1962. Two-phase flow in vertical tubes. *Trans. Inst. Chem. Eng*, 40, 61-68.

Nikuradse, J., 1932. Gesetzmäßigkeiten der turbulenten stromung in glatten rohren. *Forschungsheft 356*, volume B. VDI Verlag Berlin.

Nydal, O. J., 1998. Experiments in downwards ow on stability of slug fronts. *Third International. Conference. on Multiphase Flow*, Lyon (France).

Nydal, O.J., Pintus, S., Andreussi, P., 1992. Statistical characterization of slug flow in horizontal pipes. *Int. J. Multiphase Flow* 18, 439-453.

Nydal, O.J., Banerjee, S., 1996. Dynamic slug tracking simulations for gas-liquid flow in pipelines. *Chem. Eng. Commun.* 141–142, 13–39.

Nydal, O. J., Audibert M., Johansen, M., 2001. Experiments and modelling of gas-liquid flow in an s-shape riser. Tenth International Conference on Multiphase Technology, Cannes (France).

Pauchon, C., Dhulesia, H., Lopez, D., Fabre, J., 1993. TACITE: A comprehensive mechanistic model for two-phase flow. Multi Phase Production Conference. Cannes (France). June 1993.

Ransom, V., 1982 RELAP5/MOD1 Code Manual Volume 1: Code structure, system models, and numerical method. NUREG/CR-1826, U.S. Nuclear Regulatory Commission, 1982.

Ramshaw, J. D., Trapp, J. A., 1978. Characteristics, stability, and short-wavelength phenomena in two-phase flow equation systems. Nuclear Science and Engineering: 66, 93-102.

Ruder, Z., Hanratty, P.J., Hanratty, T.J., 1989. Necessary conditions for the existence of stable slugs. Int. J. Multiphase Flow 15, 209—226.

Shemer, L., 2003. Hydrodynamic and statistical parameters of slug flow. Int. J. Multiphase Flow 24, 334-344

Simmons, M. J., Hanratty, T. J., 2001. Transition from stratified to intermittent flows in small angle upflows. Int. J. Multiphase Flow 27, 599—616.

Soleimani, A., Hanratty, T., J., 2003. Critical liquid flows for the transition from the pseudo-slug and stratified patterns to slug flow. Int. J. Multiphase Flow 29, 51—67.

Taitel, Y., Dukler, A.E., 1976. A model for predicting flow regime transitions in horizontal and near horizontal gas-liquid flow. AIChE J 22, 47-55.

Taitel, Y., Barnea, D., 1997 Simplified transient simulation of two-phase flow using quasi-equilibrium momentum balances. Int. J. Multiphase Flow Vol. 23, No. 3, 493-501.

Taitel, Y., Barnea, D., 2000. Slug-tracking model for hilly terrain pipelines. SPE Journal 5 (1): 102-109.

Taitel, Y., 2000. Two-phase gas-liquid flow short course - Fundamentals of multiphase flow modelling. Department of Fluid Mechanics and Heat Transfer, Tel Aviv University.

Van Hout, R., Barnea, D., Shemer, L., 2001. Evolution statistical parameters of gas-liquid slug flow along vertical pipes. *International Journal of Multiphase Flow*, 27, 1579-1602.

Van Hout, R., Shemer, L., Barnea, D., 2003. Evolution of hydrodynamic and statistical parameters of gas-liquid slug flow along inclined pipelines. *Chemical Engineering Science*, 58, 115-133.

Woods, B.D., Hanratty, T.J., 1996. Relation of slug stability to shedding rate. *Int. J. Multiphase Flow* 22, No. 5, 809-828.

Woods, B.D., Hurlburt, E.T., Hanratty, T.J., 2000. Mechanism of slug formation in downwardly inclined pipes. *Int. J. Multiphase Flow* 26, 977-998

Zheng, G., Brill, J., Taitel, Y., 1994. Slug flow behavior in a hilly terrain pipeline. *Int. J. Multiphase Flow*, Vol. 20, No.1, pp. 63-79.

Zukoski, E., 1966. Influence of viscosity, surface tension, and inclination angle on motion of long bubbles in closed tubes. *Journal of Fluid Mechanics*, 25, 821-837.

Chapter 6

Nomenclature

A	Pipe section area	m^2
A_l	Pipe area occupied by the liquid phase	m^2
A_g	Pipe area occupied by the gas phase	m^2
C_0	Bubble nose velocity coefficient	–
D	Pipe diameter	m
F	Resulting volume force on the liquid phase (friction+gravity)	$N.m^{-3}$
g	Gravity acceleration	$m.s^{-2}$
h_l	Liquid height	m
H_l	Equivalent liquid height	m
H_g	Equivalent gas height	m
p	Absolute pressure	bara
U_l	Liquid velocity	$m.s^{-1}$
U_g	Gas velocity	$m.s^{-1}$
U_{ls}	Liquid velocity in the slug	$m.s^{-1}$
U_{lb}	Liquid velocity in the bubble film	$m.s^{-1}$
U_{gs}	Gas velocity in the slug	$m.s^{-1}$
U_{gb}	Gas velocity in the bubble	$m.s^{-1}$
U_l^S	Liquid superficial velocity	$m.s^{-1}$
U_g^S	Gas superficial velocity	$m.s^{-1}$
U_m	Mixture velocity	$m.s^{-1}$
U_L	Liquid velocity in the left section (Riemann problem)	$m.s^{-1}$
U_R	Liquid velocity in the right section (Riemann problem)	$m.s^{-1}$
U_M	Liquid velocity in the middle section (Riemann problem)	$m.s^{-1}$
S	Internal pipe perimeter	m
S_i	Gas-liquid interfacial perimeter	m
S_l	Liquid-wall interfacial perimeter	m
S_g	Gas-wall interfacial perimeter	m
W_{eff}	Wake effect parameter acting on the bubble nose velocity	–

α	Void fraction	—
α_b	Void fraction in the bubble	—
α_S	Void fraction in the slug	—
β	Holdup	—
β_b	Holdup in the bubble	—
β_s	Holdup in the slug	—
β_L	Holdup in the left section (Riemann problem)	—
β_R	Holdup in the right section (Riemann problem)	—
β_M	Holdup in the middle section (Riemann problem)	—
κ	Modified hydrostatic parameter (hydrostatic - Bernoulli)	$m^2.s^{-2}$
λ_l	Liquid friction factor	—
λ_i	Interfacial friction factor	—
λ_g	Gas friction factor	—
ρ_l	Liquid-phase density	$kg.m^{-3}$
ρ_g	Gas-phase density	$kg.m^{-3}$
μ_l	Liquid dynamic viscosity	$Pa.s$
μ_g	Gas dynamic viscosity	$Pa.s$
ν_l	Liquid cinematic viscosity	$m^2.s^{-1}$
ν_g	Gas cinematic viscosity	$m^2.s^{-1}$
ν_0	Drift velocity of a Taylor bubble in stagnant liquid	$m.s^{-1}$
ρ_g	Gas-phase density	$kg.m^{-3}$
τ_l	Liquid-wall shear stress	Pa
τ_g	Gas-wall shear stress	Pa
τ_i	Liquid-gas shear stress	Pa
ϕ	Oriented angle between the horizontal and the pipe (positive for an upwards pipe)	—

Appendix A

Void wave step: the different cases

A.1 Void wave variables

This annex presents in more details the calculations that take place when the void wave step is calculated in the case of a *section-section* border (see section 3.6.4).

Figure A.1 recalls the principle of the void wave step in LASSI and the different variables to be computed. We consider the case of *section J* characterized by its liquid holdup β_J^n and its liquid velocity $U_{l,J}^{n+1/2}$ (here the suffix $n+1/2$ refers to the fact the liquid velocity has been updated from the action of friction forces and gravity). *Section J* is surrounded by its neighbours *section J - 1* and *section J + 1*, respectively characterized by their liquid holdup β_{J-1}^n and β_{J+1}^n and their liquid velocity $U_{l,J-1}^{n+1/2}$ and $U_{l,J+1}^{n+1/2}$.

The Riemann problem is solved for both *Section - Section* borders j and $j + 1$, as explained in *section 3.6.4*. The variables to compute are for each of the two *section-section* borders j and $j + 1$ the intermediate states (β_{ML}, U_{ML}) and (β_{MR}, U_{MR}) , as well as the border velocities U_{LL} , U_b and U_{RR} as they are defined figure A.1.

Once the characteristics of each border have been calculated, the updated border positions, holdup and liquid velocity of the *sections* can be derived using the simple relations that follow:

$$z_{RR,j}^{n+1} = z_j^n + U_{RR,j} \delta t \quad z_j^{n+1} = z_j^n + U_{b,j} \delta t \tag{A.1}$$

$$z_{LL,j+1}^{n+1} = z_{j+1}^n + U_{LL,j} \delta t \quad z_{j+1}^{n+1} = z_{j+1}^n + U_{b,j+1} \delta t$$

$$\beta_J^{n+1} = \frac{\beta_J^n (z_{LL,j+1}^{n+1} - z_{RR,j}^{n+1}) + \beta_{ML,j+1}^n (z_{j+1}^{n+1} - z_{LL,j+1}^{n+1}) + \beta_{MR,j}^n (z_{RR,j}^{n+1} - z_j^{n+1})}{z_{j+1}^{n+1} - z_j^{n+1}} \tag{A.2}$$

$$U_J^{n+1} = \frac{\beta_J^n U_J^n (z_{LL,j+1}^{n+1} - z_{RR,j}^{n+1}) + \beta_{ML,j+1}^n U_{ML,j+1}^n (z_{j+1}^{n+1} - z_{LL,j+1}^{n+1}) + \beta_{MR,j}^n U_{MR,j}^n (z_{RR,j}^{n+1} - z_j^{n+1})}{(z_{j+1}^{n+1} - z_j^{n+1}) \beta_J^{n+1}} \quad (\text{A.3})$$

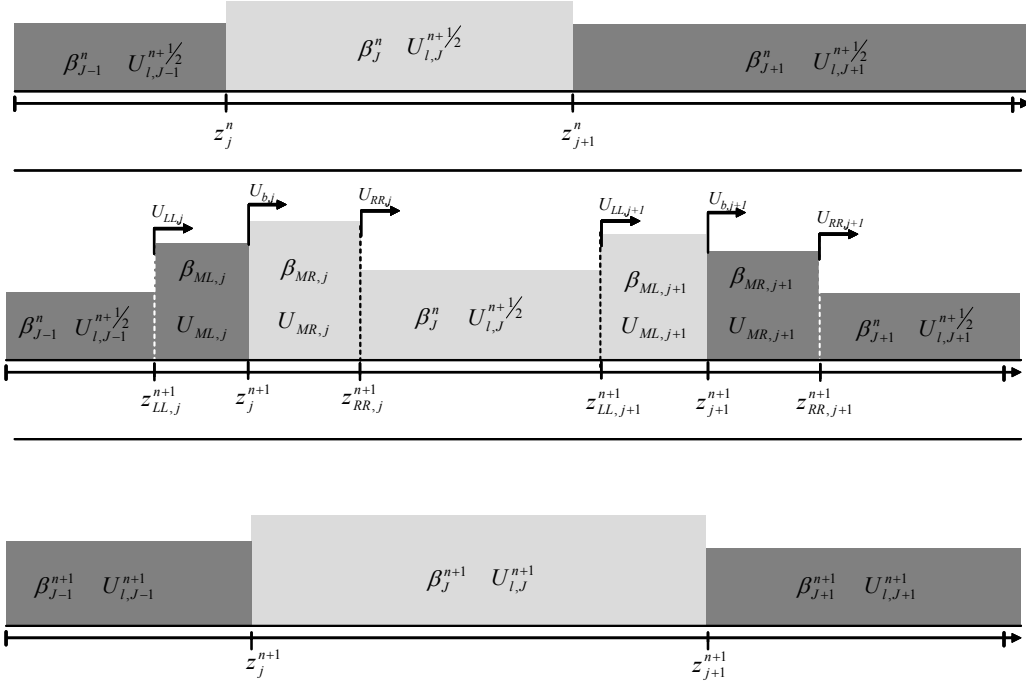


Figure A.1: Void wave calculation in LASSI

A.2 Case of β_M greater than one

When the intermediate state (β_M, U_M) solution of the Riemann problem is a state characterized by a holdup β_M greater than one, the standard Shock-Shock results (as presented table A.4) do not apply. Indeed when $\beta_M > 1$, the modified shallow water equations can not be used to represent the flow in a pipe. As a consequence, the following approach is used: β_M is set to exactly 1 and U_M is calculated from liquid mass and momentum conservation.

The value for U_M is calculated as follows.

- liquid mass conservation provides the relation:

$$U_{RR} - U_{LL} = \beta_L (U_L - U_{LL}) + \beta_R (U_{RR} - U_R) \quad (\text{A.4})$$

- liquid momentum conservation yields:

$$(U_{RR} - U_{LL}) U_M = \beta_L U_L (U_L - U_{LL}) + \beta_R U_R (U_{RR} - U_R) \quad (\text{A.5})$$

Replacing the expression of $(U_{RR} - U_{LL})$ provided by the liquid mass conservation relation into the liquid momentum conservation equation gives:

$$[\beta_L (U_L - U_{LL}) + \beta_R (U_{RR} - U_R)] U_M = \beta_L U_L (U_L - U_{LL}) + \beta_R U_R (U_{RR} - U_R) \quad (\text{A.6})$$

or

$$0 = \beta_L (U_L - U_M) (U_L - U_{LL}) + \beta_R (U_R - U_M) (U_{RR} - U_R) \quad (\text{A.7})$$

After replacing the expressions of U_{LL} and U_{RR} , the previous equation becomes:

$$\frac{\beta_R}{1 - \beta_R} (U_M - U_R)^2 = \frac{\beta_L}{1 - \beta_L} (U_L - U_M)^2 \quad (\text{A.8})$$

Since we have $U_L > U_M > U_R$ we can finally conclude:

$$U_M = \frac{1}{\sqrt{\frac{\beta_L}{1 - \beta_L}} + \sqrt{\frac{\beta_R}{1 - \beta_R}}} \left(\sqrt{\frac{\beta_R}{1 - \beta_R}} U_R + \sqrt{\frac{\beta_L}{1 - \beta_L}} U_L \right) \quad (\text{A.9})$$

The normal results for a Shock-Shock are then applied to the newly defined intermediate state.

A.3 Average holdup within a rarefaction wave

When a rarefaction wave is present (case Rarefaction-Rarefaction, Rarefaction-Shock or Shock-Rarefaction), it is necessary to calculate the average hold-up and liquid velocity within the rarefaction wave in order to proceed with the geometrical approach of calculating fluxes that has been used throughout this thesis. We take the case of a rarefaction wave between the left state (β_L, U_L) and the intermediate state (β_M, U_M) , as shown in figure A.2. The variable to compute is the average liquid hold-up within the rarefaction wave β_{rar} .

The liquid flux F_{in} entering the rarefaction wave from the left state can be expressed as:

$$F_{in} = \beta_L (U_L - U_{LL}) = \beta_L \sqrt{\kappa \beta_L} \quad (\text{A.10})$$

The liquid flux F_{out} leaving the rarefaction wave to the intermediate state can be expressed as:

$$F_{out} = \beta_M (U_M - U_{LR}) = \beta_M \sqrt{\kappa \beta_M} \quad (\text{A.11})$$

The average hold-up within the rarefaction wave β_{rar} can then be calculated from the relation:

$$\beta_{rar} = \frac{F_{in} - F_{out}}{U_{LR} - U_{LL}} = \frac{\beta_L \sqrt{\kappa \beta_L} - \beta_M \sqrt{\kappa \beta_M}}{(U_M - \sqrt{\kappa \beta_M}) - (U_L - \sqrt{\kappa \beta_L})} \quad (\text{A.12})$$

Given that $U_M = U_L - 2(\sqrt{\kappa \beta_M} - \sqrt{\kappa \beta_L})$ (see section 3.6.4), the expression can be simplified as:

$$\beta_{rar} = \frac{1}{3} \left(\beta_L + \sqrt{\beta_L \beta_M} + \beta_M \right) \quad (\text{A.13})$$

The average hold-up β_{rar} within a rarefaction wave is therefore the *Heronian mean* of the hold-ups of the two states the rarefaction wave is connected to. It is interesting to point out that the average hold-up in the rarefaction wave does not depend on the value of the liquid velocity.

The *Heronian mean* is named after the Greek engineer and geometer Heron who lived in Alexandria during the first century before our era. The Heronian mean also appears in the formula for the volume of a frustum (a frustum is the portion of a cone or pyramid which lies between two parallel planes cutting the pyramid or cone). The volume of a frustum of a pyramid (or cone) is found by multiplying the height of the frustum by the Heronian mean of the areas of the opposing parallel faces.

A.4 Tables

Tables A.1 to A.10 present how the variables (β_{ML}, U_{ML}) , (β_{MR}, U_{MR}) and the border velocities U_{LL} , U_b and U_{RR} are calculated according to the nature of the border.

- Table A.1 presents the Rarefaction-Rarefaction case
- Table A.2 presents the Rarefaction-Shock case
- Table A.3 presents the Shock-Rarefaction case

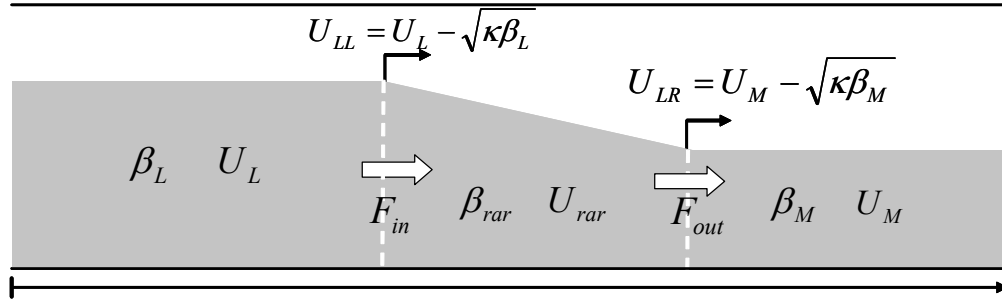


Figure A.2: Rarefaction wave between the left and intermediate state

- Table A.4 presents the Shock-Shock case
- Table A.5 deals with the Saturated Shock-Shock case which occurs when the holdup within the intermediate region reaches one
- Table A.6 introduces the Rarefaction-Void case, characterized by a dry right bed
- Table A.7 introduces the Void-Rarefaction case, characterized by a dry left bed
- Table A.8 tackles the Appearing Dry-Bed case ($\beta_M = 0$ although both the left and right bed are not dry, occurring when $U_L + 2\sqrt{\kappa\beta_L} < U_R - 2\sqrt{\kappa\beta_R}$)
- Finally table A.9 and table A.10 tackle respectively the bubble nose-*slugs* and *slugs*-bubble nose cases

Rarefaction-Rarefaction (RR)	
$U_M = U_L - 2\sqrt{\kappa}(\sqrt{\beta_M} - \sqrt{\beta_L})$ $\beta_M < \beta_L$ $U_{LL} = U_L - \sqrt{\kappa\beta_L}$ $U_{LR} = U_M - \sqrt{\kappa\beta_M}$	$U_M = U_R + 2\sqrt{\kappa}(\sqrt{\beta_M} - \sqrt{\beta_R})$ $\beta_M < \beta_R$ $U_{RL} = U_M + \sqrt{\kappa\beta_M}$ $U_{RR} = U_R + \sqrt{\kappa\beta_R}$
$U_b = \frac{1}{2}(U_{LR} + U_{RL}) = U_M$	
$\beta_{rarL} = \frac{1}{3}(\beta_L + \sqrt{\beta_L\beta_M} + \beta_M)$ $\beta_{ML} = \frac{\beta_{rarL}(U_{LR} - U_{LL}) + \beta_M(U_b - U_{LR})}{U_b - U_{LL}}$ $U_{ML} = U_L - 2\sqrt{\kappa}(\sqrt{\beta_{ML}} - \sqrt{\beta_L})$	$\beta_{rarR} = \frac{1}{3}(\beta_R + \sqrt{\beta_R\beta_M} + \beta_M)$ $\beta_{MR} = \frac{\beta_{rarR}(U_{RR} - U_{RL}) + \beta_M(U_{RL} - U_b)}{U_{RR} - U_b}$ $U_{MR} = U_R + 2\sqrt{\kappa}(\sqrt{\beta_{MR}} - \sqrt{\beta_R})$

Table A.1: Details of the void wave step in the Rarefaction-Rarefaction case

Rarefaction-Shock (RS)	
$U_M = U_L - 2\sqrt{\kappa}(\sqrt{\beta_M} - \sqrt{\beta_L})$ $\beta_M < \beta_L$ $U_{LL} = U_L - \sqrt{\kappa\beta_L}$ $U_{LR} = U_M - \sqrt{\kappa\beta_M}$	$U_M = U_R + \frac{1}{\sqrt{2}}\sqrt{\kappa}(\beta_M - \beta_R)\sqrt{\frac{1}{\beta_M} + \frac{1}{\beta_R}}$ $\beta_M > \beta_R$ $U_{RL} = \frac{\beta_M U_M - \beta_R U_R}{\beta_M - \beta_R}$ $U_{RR} = U_{RL}$
$\beta_{rarL} = \frac{1}{3}(\beta_L + \sqrt{\beta_L\beta_M} + \beta_M)$ $\beta_{ML} = \frac{\beta_{rarL}(U_{LR} - U_{LL}) + \beta_M(U_b - U_{LR})}{U_b - U_{LL}}$ $U_{ML} = U_L - 2\sqrt{\kappa}(\sqrt{\beta_{ML}} - \sqrt{\beta_L})$	$U_b = U_{RR} = U_{RL} = \frac{\beta_M U_M - \beta_R U_R}{\beta_M - \beta_R}$ $\beta_{MR} = \beta_R$ $U_{MR} = U_R$

Table A.2: Details of the void wave step in the Rarefaction-Shock case

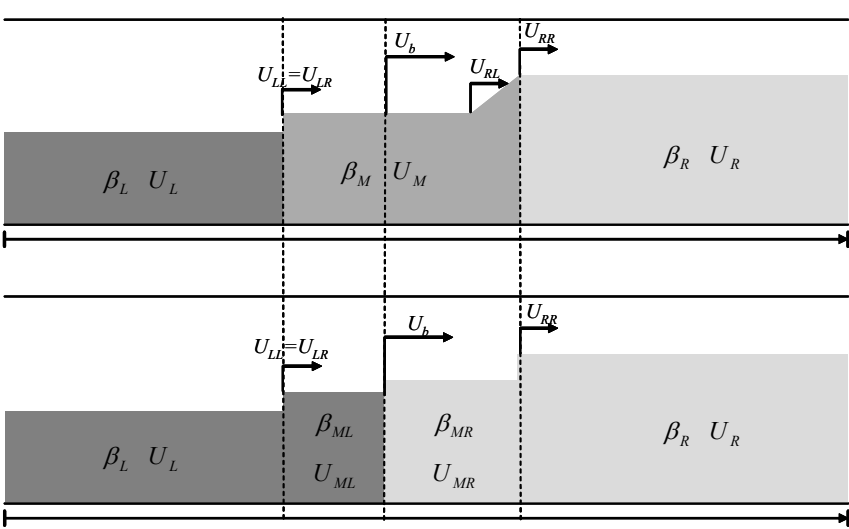
Shock-Rarefaction (SR)	
	
$U_M = U_L - \frac{1}{\sqrt{2}}\sqrt{\kappa}(\beta_M - \beta_L) \sqrt{\frac{1}{\beta_M} + \frac{1}{\beta_L}}$ $\beta_M > \beta_L$ $U_{LL} = \frac{\beta_M U_M - \beta_L U_L}{\beta_M - \beta_L}$ $U_{LR} = U_{LL}$	$U_M = U_R + 2\sqrt{\kappa}(\sqrt{\beta_M} - \sqrt{\beta_R})$ $\beta_M < \beta_R$ $U_{RL} = U_M + \sqrt{\kappa\beta_M}$ $U_{RR} = U_R + \sqrt{\kappa\beta_R}$
$U_b = \frac{1}{2}(U_{LR} + U_{RL})$	$\beta_{rarR} = \frac{1}{3}(\beta_R + \sqrt{\beta_R\beta_M} + \beta_M)$ $\beta_{MR} = \frac{\beta_{rarR}(U_{RR} - U_{RL}) + \beta_M(U_{RL} - U_b)}{U_{RR} - U_b}$ $U_{MR} = U_R + 2\sqrt{\kappa}(\sqrt{\beta_{MR}} - \sqrt{\beta_R})$
$\beta_{ML} = \beta_M$ $U_{ML} = U_M$	

Table A.3: Details of the void wave step in the Shock-Rarefaction case

Shock-Shock (SS)	
$U_M = U_L - \frac{1}{\sqrt{2}} \sqrt{\kappa} (\beta_M - \beta_L) \sqrt{\frac{1}{\beta_M} + \frac{1}{\beta_L}}$ $\beta_M > \beta_L$ $U_{LL} = \frac{\beta_M U_M - \beta_L U_L}{\beta_M - \beta_L}$ $U_{LR} = U_{LL}$	$U_M = U_R + \frac{1}{\sqrt{2}} \sqrt{\kappa} (\beta_M - \beta_R) \sqrt{\frac{1}{\beta_M} + \frac{1}{\beta_R}}$ $\beta_M > \beta_R$ $U_{RL} = \frac{\beta_M U_M - \beta_R U_R}{\beta_M - \beta_R}$ $U_{RR} = U_{RL}$
$U_b = U_{RR} = U_{RL}$	
$\beta_{ML} = \beta_M$ $U_{ML} = U_M$	$\beta_{MR} = \beta_R$ $U_{MR} = U_R$

Table A.4: Details of the void wave step in the Shock-Shock case

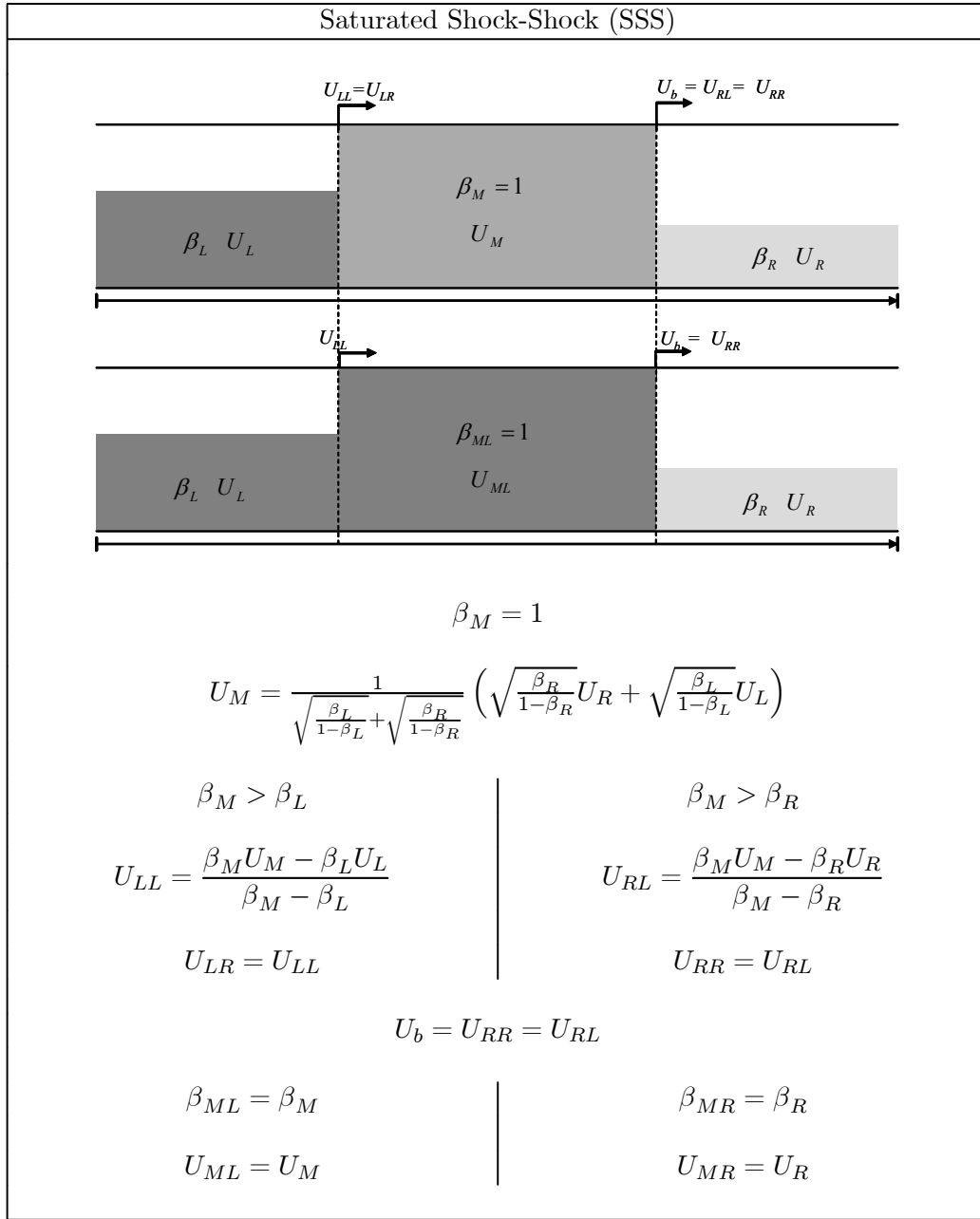


Table A.5: Details of the void wave step in the Saturated Shock-Shock case

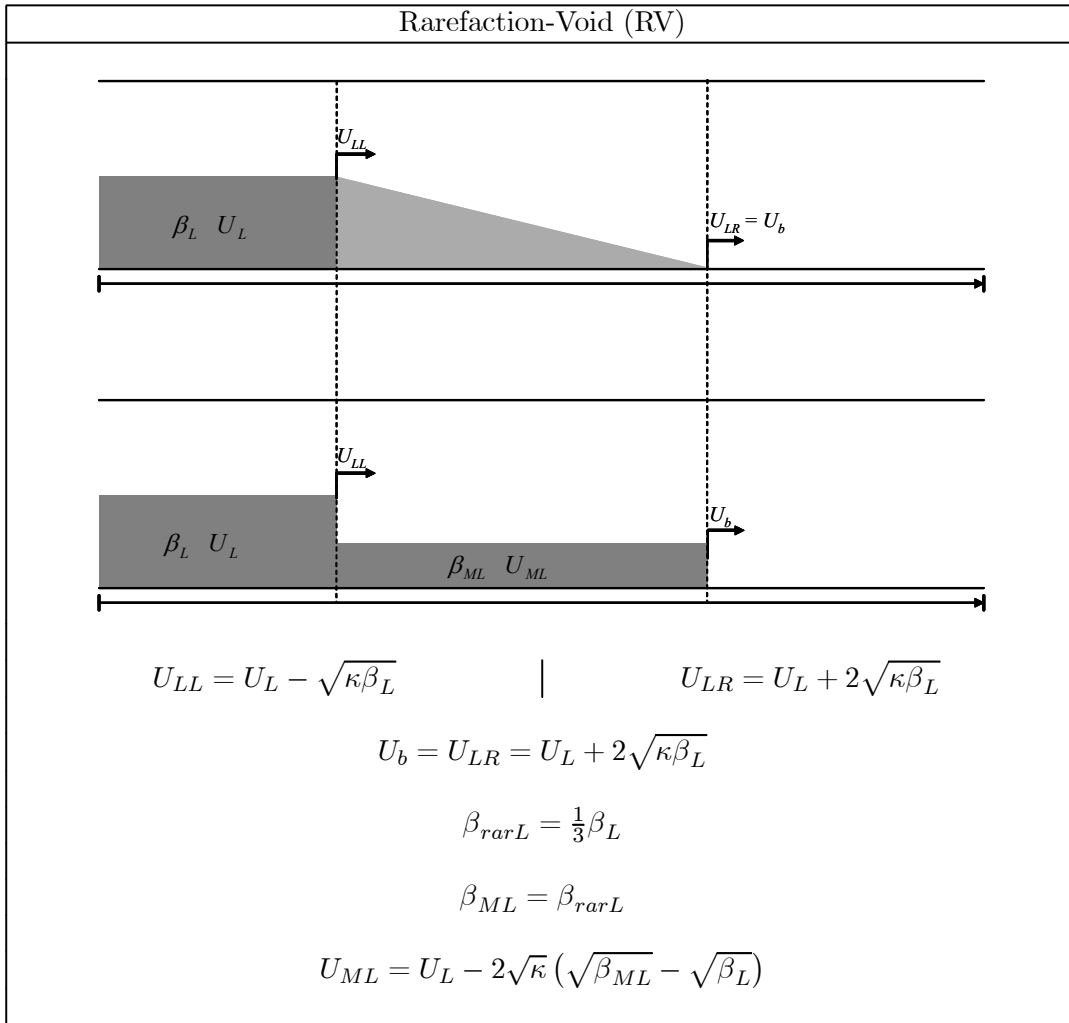


Table A.6: Details of the void wave step in the Rarefaction-Rarefaction case

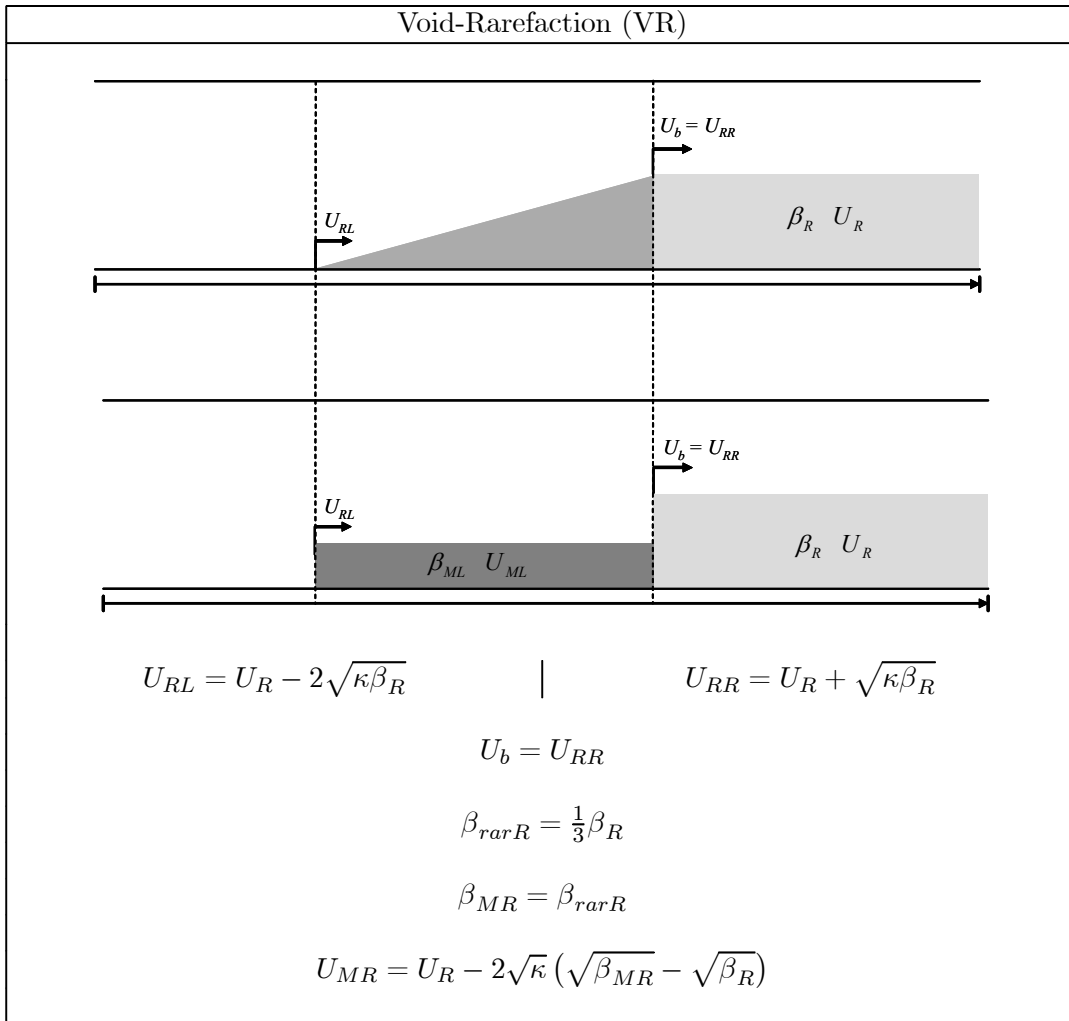


Table A.7: Details of the void wave step in the Rarefaction-Rarefaction case

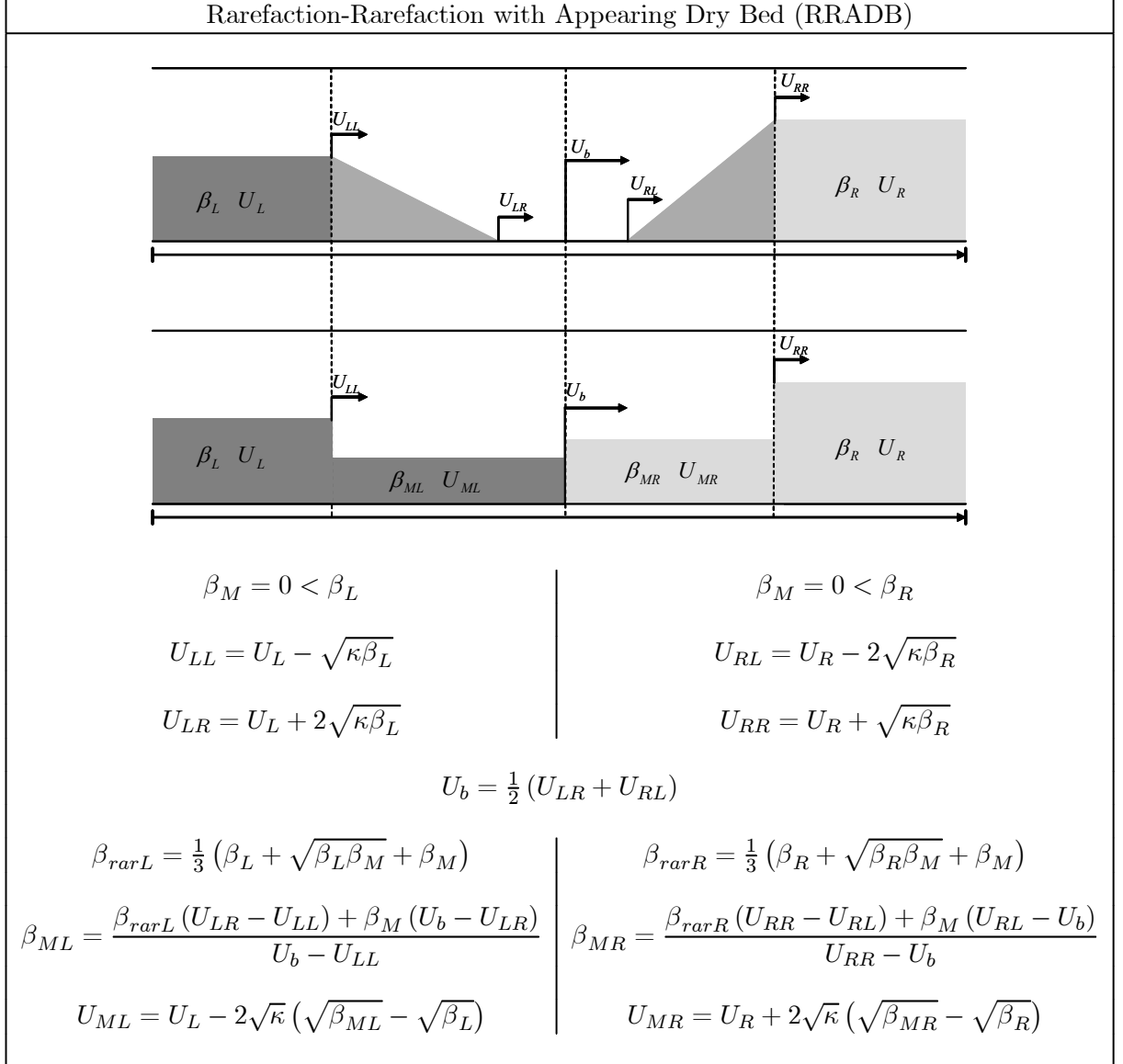


Table A.8: Details of the void wave step in the Rarefaction-Rarefaction case

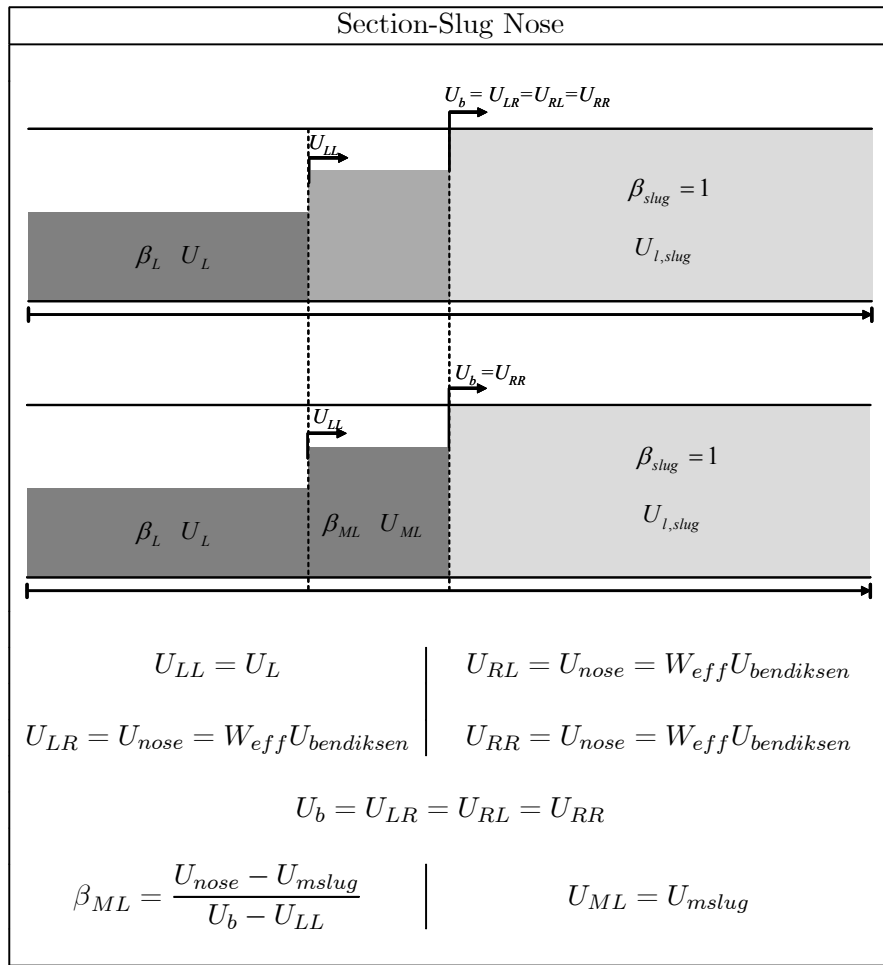


Table A.9: Details of the void wave step in the Section-Slug case

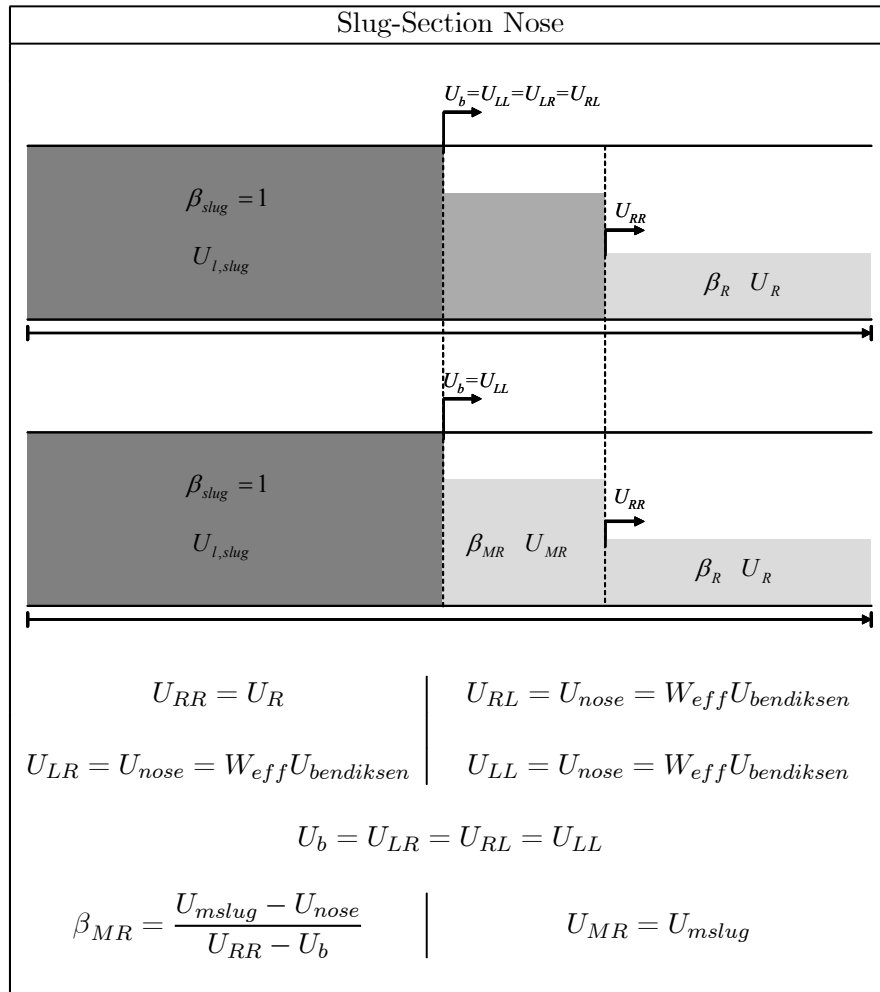


Table A.10: Details of the void wave step in the Slug-Section case

Appendix B

Stability analysis of an upwind-differentiated two-fluid model

This chapter aims to investigate the consequences of the discretized nature of the implemented equations on the stability of the two-fluid model. In other words, how close is the stability area of a standard Eulerian scheme based on the two-fluid model to the stability area of the continuous two-fluid model set of equations ? This question is especially important in the case of slug capturing schemes since the objective of those schemes is to be able to initiate slugs automatically, according to the VKH criterion, i.e. to the linear stability analysis of the continuous two-fluid model set of equations. This question, not yet answered in the literature, is tackled in the following pages.

Quantities of different schemes have been proposed for the two-fluid model, each potentially possessing a different area of stability. The scheme chosen for this analysis is a fully implicit upwind scheme. Upwind differentiation is very popular because of its simplicity and robustness, and is widely used in the industry. Some considerations regarding the ability to physically model slug initiation with an upstream scheme have been made in the first paper of this thesis. It can indeed be argued that the Bernoulli effect, which plays a great role in the slug initiation mechanism is modelled in a non-satisfactory way in an upstream scheme. It was thus natural to continue investigating the ability of the two-fluid model to tackle slug initiation, this time using the tool of stability analysis.

The scheme investigated here is fully implicit and we assume that the set of obtained non-linear discretized equations is solved numerically without any numerical error. In reality, fully implicit schemes typically require an iterative resolution of the set of discretized equations, in a way similar to the SIMPLE method used for single phase gas flow. The solution found thus conveys a small yet non null error which is dependent on the level of accuracy chosen. This approach is followed in the TRI-OMPH scheme (Bonizzi, 2002, Issa and Kempf, 2003, Bonizzi and Issa, 2003), which was the first scheme proved able to fully capture slug initiation. Another possibility is to use a semi-implicit scheme that allows for a non-iterative resolution such as OLGA

(Bendiksen et al., 1991) but introduces a discrepancy in the volume conservation equation which is corrected during the next time step.

By assuming the system of discretized equations is solved perfectly, we are able to focus our analysis on the consequences of the upstream differentiation method on the stability of the scheme. This effect is independent on the method chosen to solve the set of discretized equations and the following analysis can therefore be applied to all upwind schemes.

B.1 The two-fluid model

We use the usual (no additional terms, no surface tension) 2 fluid model cross section averaged equations as a starting point. The liquid phase is considered incompressible. The system is composed of four partial differential equations, traducing the mass and momentum conservation of each phase independently.

$$\begin{aligned} \frac{\partial}{\partial t} (\alpha_l) + \frac{\partial}{\partial x} (\alpha_l U_l) &= 0 \\ \frac{\partial}{\partial t} (\rho_g \alpha_g) + \frac{\partial}{\partial x} (\rho_g \alpha_g U_g) &= 0 \\ \frac{\partial}{\partial t} (\rho_l \alpha_l U_l) + \frac{\partial}{\partial x} (\rho_l \alpha_l U_l^2) + \alpha_l \frac{\partial}{\partial x} p &= -\frac{\tau_l S_l}{A} + \frac{\tau_i S_i}{A} - \rho_l g \alpha_l \sin \beta - \rho_l g \alpha_l \cos \beta \frac{\partial}{\partial x} h_l \\ \frac{\partial}{\partial t} (\rho_g \alpha_g U_g) + \frac{\partial}{\partial x} (\rho_g \alpha_g U_g^2) + \alpha_g \frac{\partial}{\partial x} p &= -\frac{\tau_g S_g}{A} - \frac{\tau_i S_i}{A} - \rho_g g \alpha_g \sin \beta - \rho_g g \alpha_g \cos \beta \frac{\partial}{\partial x} h_l \end{aligned}$$

The subscript l and g refer respectively to the liquid and gas phase, ρ , and U are the density and velocity of the considered phase. τ_l is the liquid-wall friction, τ_g the gas-wall friction and τ_i the gas-liquid friction. S_l and S_g are the liquid-wetted and gas-wetted perimeter and S_i is the interfacial width. p is the pressure, h_l the liquid height and ϕ the angle between the pipe and the horizontal. Finally α is the void fraction (i.e. the ratio between the gas-occupied area and the total pipe area) and β is the holdup (i.e. the ratio between the liquid-occupied area and the total pipe area).

B.2 An Eulerian scheme based on the two-fluid model

B.2.1 Grid

The scheme is based on the grid presented figure B.1. In the dots are stored the pressure, the gas density and the phase fractions while the liquid and gas velocities are stored in the arrows. The upper case subscripts will refer to the information related to the dots, while the lower case subscripts will refer to the information related to the arrows.

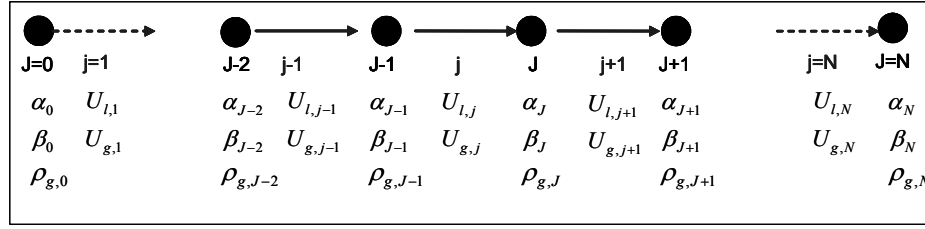


Figure B.1: Staggered grid for an upstream-differentiated two-fluid scheme

B.2.2 Notations

The following notations are used in the discretized equations:

$$\begin{aligned}
 \overleftrightarrow{\rho}_j &= \frac{1}{2} (\rho_J + \rho_{J-1}) \\
 \overleftrightarrow{\alpha}_j &= \frac{1}{2} (\alpha_J + \alpha_{J-1}) \\
 \widehat{\rho}_j &= \rho_{J-1} \text{ if } U_j > 0, \rho_J \text{ if } U_j < 0 \\
 \widehat{\alpha}_j &= \alpha_{J-1} \text{ if } U_j > 0, \alpha_J \text{ if } U_j < 0 \\
 \overleftrightarrow{\rho\alpha\hat{U}}_J &= \frac{1}{2} (\widehat{\rho}_j \widehat{\alpha}_j U_j + \widehat{\rho}_{j+1} \widehat{\alpha}_{j+1} U_{j+1}) \\
 \widehat{U}_J &= U_j \text{ if } \overleftrightarrow{\rho\alpha\hat{U}}_J > 0, U_{j+1} \text{ if } \overleftrightarrow{\rho\alpha\hat{U}}_J < 0
 \end{aligned}$$

The $\overleftrightarrow{}$ superscript refers to a centrally-averaged variable, while the $\widehat{}$ superscript refers to an upwinded variable.

In what follows, the double vertical bars refer to the maximum function, i.e. $\|a, b\| = \max(a, b) = \{a, \text{if } a \geq b, b \text{ if } b < a\}$.

B.2.3 Discretized equations

The discretized equations used in the considered implicit upwind scheme are presented in this section. Since the aim of this work is to derive the stability area of the scheme by performing a linear stability analysis around the equilibrium points of the system, we are able to simplify the problem by considering that at equilibrium, gas and liquid are flowing towards the outlet of the pipe. This simplifies the expression of the upstreamed variables. Since the gas phase is also assumed incompressible in the derivation of the VKH criterion (Barnea and Taitel, 1993), this approximation is also used here.

Liquid mass conservation

- In the general case, the liquid mass conservation equation is discretized as:

$$\frac{1}{\delta t} \left(\rho_{l,J}^{n+1} \beta_J^{n+1} - \rho_{l,J}^n \beta_J^n \right) + \frac{1}{\delta x} \left(\widehat{\rho}_{l,j+1}^{n+1} \widehat{\beta}_{j+1}^{n+1} U_{l,j+1}^{n+1} - \widehat{\rho}_{l,j}^{n+1} \widehat{\beta}_j^{n+1} U_{l,j}^{n+1} \right) = 0$$

- By considering an incompressible forward flow, we are able to simplify the expression to:

$$\frac{1}{\delta t} (\beta_J^{n+1} - \beta_J^n) + \frac{1}{\delta x} (\beta_J^{n+1} U_{l,j+1}^{n+1} - \beta_{J-1}^{n+1} U_{l,j}^{n+1}) = 0 \quad (\text{B.1})$$

Gas mass conservation

- The discretized gas mass conservation equation can be expressed as:

$$\frac{1}{\delta t} (\rho_{g,J}^{n+1} \alpha_J^{n+1} - \rho_{g,J}^n \alpha_J^n) + \frac{1}{\delta x} (\widehat{\rho}_{g,j+1}^{n+1} \widehat{\alpha}_{j+1}^{n+1} U_{g,j+1}^{n+1} - \widehat{\rho}_{g,j}^{n+1} \widehat{\alpha}_j^{n+1} U_{g,j}^{n+1}) = 0$$

- In the case of an incompressible forward flow, this expression can be simplified as:

$$\frac{1}{\delta t} (\alpha_J^{n+1} - \alpha_J^n) + \frac{1}{\delta x} (\alpha_J^{n+1} U_{g,j+1}^{n+1} - \alpha_{J-1}^{n+1} U_{g,j}^{n+1}) = 0 \quad (\text{B.2})$$

Liquid momentum conservation

- The liquid momentum conservation equation is discretized as:

$$\left(\begin{array}{l} \frac{\delta x}{\delta t} \overleftarrow{\rho}_{l,j}^{n+1} \overleftarrow{\beta}_j^{n+1} \\ + \left\| \overleftarrow{\rho}_l \beta \overleftarrow{U}_{l,J}^{n+1}, 0 \right\| \\ + \left\| -\overleftarrow{\rho}_l \beta \overleftarrow{U}_{l,J-1}^{n+1}, 0 \right\| \end{array} \right) U_{l,j}^{n+1} = \left(\begin{array}{l} + \frac{\delta x}{\delta t} \overleftarrow{\rho}_{l,j}^n \overleftarrow{\beta}_j^n U_{l,j}^n \\ + \left\| -\overleftarrow{\rho}_l \beta \overleftarrow{U}_{l,J}^{n+1}, 0 \right\| U_{l,j+1}^{n+1} \\ + \left\| \overleftarrow{\rho}_l \beta \overleftarrow{U}_{l,J-1}^{n+1}, 0 \right\| U_{l,j-1}^{n+1} \\ - \overleftarrow{\beta}_j^{n+1} (p_J^{n+1} - p_{J-1}^{n+1}) \\ - \frac{\delta x}{A} \tau_{l,j}^{n+1} S_{l,j}^{n+1} + \frac{\delta x}{A} \tau_{i,j}^{n+1} S_{i,j}^{n+1} \\ - \overleftarrow{\rho}_{l,j}^{n+1} \delta x g \overleftarrow{\beta}_j^{n+1} \sin \phi \\ - \overleftarrow{\rho}_{l,j}^{n+1} g \overleftarrow{\beta}_j^{n+1} \cos \phi (h_{l,J} - h_{l,J-1})^{n+1} \end{array} \right)$$

with $\tau_{l,j}^{n+1} = \frac{1}{8} \lambda_{l,j}^{n+1} \rho_l^{n+1} (U_{l,j}^{n+1})^2$

and $\tau_{i,j}^{n+1} = \frac{1}{8} \lambda_{i,j}^{n+1} \rho_{g,j}^{n+1} |U_{g,j} - U_{l,j}|^{n+1} (U_{g,j}^{n+1} - U_{l,j}^{n+1})$

- Simplification in the case of an incompressible forward flow provides:

$$\begin{aligned} \left\| \overleftarrow{\rho}_l \beta \overleftarrow{U}_{l,J}^{n+1}, 0 \right\| &= \frac{1}{2} \rho_l (\widehat{\beta}_j^{n+1} U_{l,j}^{n+1} + \widehat{\beta}_{j+1}^{n+1} U_{l,j+1}^{n+1}) = \frac{1}{2} \rho_l (\beta_{J-1}^{n+1} U_{l,j}^{n+1} + \beta_J^{n+1} U_{l,j+1}^{n+1}) \\ \left\| \overleftarrow{\rho}_l \beta \overleftarrow{U}_{l,J-1}^{n+1}, 0 \right\| &= \frac{1}{2} \rho_l (\widehat{\beta}_{j-1}^{n+1} U_{l,j-1}^{n+1} + \widehat{\beta}_j^{n+1} U_{l,j}^{n+1}) = \frac{1}{2} \rho_l (\beta_{J-2}^{n+1} U_{l,j-1}^{n+1} + \beta_{J-1}^{n+1} U_{l,j}^{n+1}) \end{aligned}$$

$$\left(\begin{array}{l} \frac{\delta x}{\delta t} \rho_l \frac{1}{2} (\beta_J^{n+1} + \beta_{J-1}^{n+1}) \\ \beta_{J-1}^{n+1} U_{l,j}^{n+1} \\ + \beta_J^{n+1} U_{l,j+1}^{n+1} \end{array} \right) U_{l,j}^{n+1} = \left(\begin{array}{l} \frac{\delta x}{\delta t} \rho_l \frac{1}{2} (\beta_J^n + \beta_{J-1}^n) U_{l,j}^n \\ + \frac{1}{2} \rho_l (\beta_{J-2}^{n+1} U_{l,j-1}^{n+1} + \beta_{J-1}^{n+1} U_{l,j}^{n+1}) U_{l,j-1}^{n+1} \\ - \frac{1}{2} (\beta_J^{n+1} + \beta_{J-1}^{n+1}) (p_J^{n+1} - p_{J-1}^{n+1}) \\ - \frac{\delta x}{A} \tau_{l,j}^{n+1} S_{l,j}^{n+1} + \frac{\delta x}{A} \tau_{i,j}^{n+1} S_{i,j}^{n+1} \\ - \rho_l \delta x g \frac{1}{2} (\beta_J^{n+1} + \beta_{J-1}^{n+1}) \sin \phi \\ - \rho_l g \frac{1}{2} \left(\begin{array}{l} \beta_J^{n+1} \\ + \beta_{J-1}^{n+1} \end{array} \right) \cos \phi (h_{l,J} - h_{l,J-1})^{n+1} \end{array} \right) \quad (\text{B.3})$$

Gas momentum conservation

- In the general case, the gas momentum conservation equation is discretized as:

$$\left(\begin{array}{c} \frac{\delta x}{\delta t} \overleftarrow{\rho}_{g,j}^{n+1} \overleftarrow{\alpha}_j^{n+1} \\ + \left\| \overleftarrow{\rho}_g \overleftarrow{\alpha} \overleftarrow{U}_{g,J}^{n+1}, 0 \right\| \\ + \left\| -\overleftarrow{\rho}_g \overleftarrow{\alpha} \overleftarrow{U}_{g,J-1}^{n+1}, 0 \right\| \end{array} \right) U_{g,j}^{n+1} = \left(\begin{array}{c} \frac{\delta x}{\delta t} \overleftarrow{\rho}_{g,j}^n \overleftarrow{\alpha}_j^n U_{g,j}^n \\ + \left\| -\overleftarrow{\rho}_g \overleftarrow{\alpha} \overleftarrow{U}_{g,J}^{n+1}, 0 \right\| U_{g,j+1}^{n+1} \\ + \left\| \overleftarrow{\rho}_g \overleftarrow{\alpha} \overleftarrow{U}_{g,J-1}^{n+1}, 0 \right\| U_{g,j-1}^{n+1} \\ - \overleftarrow{\alpha}_j^{n+1} (p_J^{n+1} - p_{J-1}^{n+1}) \\ - \frac{\delta x}{A} \tau_{g,j}^{n+1} S_{g,j}^{n+1} - \frac{\delta x}{A} \tau_{i,j}^{n+1} S_{i,j}^{n+1} \\ - \overleftarrow{\rho}_{g,j}^{n+1} \delta x g \overleftarrow{\alpha}_j^{n+1} \sin \beta \\ - \overleftarrow{\rho}_{g,j}^{n+1} g \overleftarrow{\alpha}_j^{n+1} \cos \beta (h_{l,J} - h_{l,J-1})^{n+1} \end{array} \right)$$

$$\text{with } \tau_{g,j}^{n+1} = \frac{1}{8} \lambda_{g,j}^{n+1} \rho_{g,j}^{n+1} \left(U_{g,j}^{n+1} \right)^2$$

$$\text{and } \tau_{i,j}^{n+1} = \frac{1}{8} \lambda_{i,j}^{n+1} \rho_{g,j}^{n+1} |U_{g,j} - U_{l,j}|^{n+1} \left(U_{g,j}^{n+1} - U_{l,j}^{n+1} \right)$$

- By considering an incompressible forward flow, we are able to simplify the expression to:

$$\begin{aligned} \left\| \overleftarrow{\rho}_g \overleftarrow{\alpha} \overleftarrow{U}_{g,J}^{n+1}, 0 \right\| &= \frac{1}{2} \rho_g \left(\widehat{\alpha}_j^{n+1} U_{g,j}^{n+1} + \widehat{\alpha}_{j+1}^{n+1} U_{g,j+1}^{n+1} \right) = \frac{1}{2} \rho_g \left(\alpha_{J-1}^{n+1} U_{g,j}^{n+1} + \alpha_J^{n+1} U_{g,j+1}^{n+1} \right) \\ \left\| \overleftarrow{\rho}_g \overleftarrow{\alpha} \overleftarrow{U}_{g,J-1}^{n+1}, 0 \right\| &= \frac{1}{2} \rho_g \left(\widehat{\alpha}_{j-1}^{n+1} U_{g,j-1}^{n+1} + \widehat{\alpha}_j^{n+1} U_{g,j}^{n+1} \right) = \frac{1}{2} \rho_l \left(\alpha_{J-2}^{n+1} U_{g,j-1}^{n+1} + \alpha_{J-1}^{n+1} U_{g,j}^{n+1} \right) \end{aligned}$$

$$\left(\begin{array}{c} \frac{\delta x}{\delta t} \rho_g \frac{1}{2} \left(\alpha_J^{n+1} + \alpha_{J-1}^{n+1} \right) \\ + \frac{1}{2} \rho_g \left(\begin{array}{c} \alpha_{J-1}^{n+1} U_{g,j}^{n+1} \\ + \alpha_J^{n+1} U_{g,j+1}^{n+1} \end{array} \right) \end{array} \right) U_{g,j}^{n+1} = \left(\begin{array}{c} \frac{\delta x}{\delta t} \rho_g \frac{1}{2} \left(\alpha_J^n + \alpha_{J-1}^n \right) U_{g,j}^n \\ + \frac{1}{2} \rho_l \left(\begin{array}{c} \alpha_{J-2}^{n+1} U_{g,j-1}^{n+1} \\ + \alpha_{J-1}^{n+1} U_{g,j}^{n+1} \end{array} \right) U_{g,j-1}^{n+1} \\ - \frac{1}{2} \left(\alpha_J^{n+1} + \alpha_{J-1}^{n+1} \right) \left(p_J^{n+1} - p_{J-1}^{n+1} \right) \\ - \frac{\delta x}{A} \tau_{g,j}^{n+1} S_{g,j}^{n+1} - \frac{\delta x}{A} \tau_{i,j}^{n+1} S_{i,j}^{n+1} \\ - \rho_g \delta x g \frac{1}{2} \left(\alpha_J^{n+1} + \alpha_{J-1}^{n+1} \right) \sin \beta \\ - \rho_g g \frac{1}{2} \left(\begin{array}{c} \alpha_J^{n+1} \\ + \alpha_{J-1}^{n+1} \end{array} \right) \cos \beta (h_{l,J} - h_{l,J-1})^{n+1} \end{array} \right) \quad (\text{B.4})$$

B.3 Stability analysis of an upwind Eulerian two-fluid model scheme

B.3.1 Combined Momentum Equation

We establish a combined momentum equation by replacing the expression of the pressure gradient in the gas momentum conservation equations into the liquid momentum conservation equation.

$$(p_J^{n+1} - p_{J-1}^{n+1}) = \frac{2}{(\alpha_J^{n+1} + \alpha_{J-1}^{n+1})} \begin{pmatrix} \frac{\delta x}{\delta t} \rho_g \frac{1}{2} (\alpha_J^n + \alpha_{J-1}^n) U_{g,j}^n \\ - \frac{\delta x}{\delta t} \rho_g \frac{1}{2} (\alpha_J^{n+1} + \alpha_{J-1}^{n+1}) U_{g,j}^{n+1} \\ + \frac{1}{2} \rho_g (\alpha_{J-2}^{n+1} U_{g,j-1}^{n+1} + \alpha_{J-1}^{n+1} U_{g,j}^{n+1}) U_{g,j-1}^{n+1} \\ - \frac{1}{2} \rho_g (\alpha_{J-1}^{n+1} U_{g,j}^{n+1} + \alpha_J^{n+1} U_{g,j+1}^{n+1}) U_{g,j}^{n+1} \\ - \frac{\delta x}{A} \tau_{g,j}^{n+1} S_{g,j}^{n+1} - \frac{\delta x}{A} \tau_{i,j}^{n+1} S_{i,j}^{n+1} \\ - \rho_g \delta x g \frac{1}{2} (\alpha_J^{n+1} + \alpha_{J-1}^{n+1}) \sin \beta \\ - \rho_g g \frac{1}{2} (\alpha_J^{n+1} + \alpha_{J-1}^{n+1}) \cos \beta (h_{l,J} - h_{l,J-1})^{n+1} \end{pmatrix}$$

Reporting into the liquid momentum conservation discretized equation, we get:

$$\begin{pmatrix} - \frac{\delta x}{\delta t} \rho_l \left(U_{l,j}^{n+1} - \frac{\beta_J^n + \beta_{J-1}^n}{\beta_J^{n+1} + \beta_{J-1}^{n+1}} U_{l,j}^n \right) \\ + \frac{\delta x}{\delta t} \rho_g \left(U_{g,j}^{n+1} - \frac{\alpha_J^n + \alpha_{J-1}^n}{\alpha_J^{n+1} + \alpha_{J-1}^{n+1}} U_{g,j}^n \right) \\ + \rho_l \frac{1}{\beta_J^{n+1} + \beta_{J-1}^{n+1}} \left(\beta_{J-2}^{n+1} U_{l,j-1}^{n+1} + \beta_{J-1}^{n+1} U_{l,j}^{n+1} \right) U_{l,j-1}^{n+1} \\ - \rho_l \frac{1}{\beta_J^{n+1} + \beta_{J-1}^{n+1}} \left(\beta_{J-1}^{n+1} U_{l,j}^{n+1} + \beta_J^{n+1} U_{l,j+1}^{n+1} \right) U_{l,j}^{n+1} \\ - \rho_g \frac{1}{\alpha_J^{n+1} + \alpha_{J-1}^{n+1}} \left(\alpha_{J-2}^{n+1} U_{g,j-1}^{n+1} + \alpha_{J-1}^{n+1} U_{g,j}^{n+1} \right) U_{g,j-1}^{n+1} \\ + \rho_g \frac{1}{\alpha_J^{n+1} + \alpha_{J-1}^{n+1}} \left(\alpha_{J-1}^{n+1} U_{g,j}^{n+1} + \alpha_J^{n+1} U_{g,j+1}^{n+1} \right) U_{g,j}^{n+1} \\ + \delta x F \left(U_{l,j}^{n+1}, U_{g,j}^{n+1}, \frac{\beta_J^{n+1} + \beta_{J-1}^{n+1}}{2} \right) \\ - (\rho_l - \rho_g) g \cos \phi (h_{l,J} - h_{l,J-1})^{n+1} \end{pmatrix} = 0 \quad (\text{B.5})$$

$$\text{with } F \left(U_{l,j}^{n+1}, U_{g,j}^{n+1}, \frac{\beta_J^{n+1} + \beta_{J-1}^{n+1}}{2} \right) = \begin{bmatrix} - \frac{2\delta x}{A(\beta_J^{n+1} + \beta_{J-1}^{n+1})} \tau_{l,j}^{n+1} S_{l,j}^{n+1} \\ + \frac{2\delta x}{A} \left(\frac{1}{\beta_J^{n+1} + \beta_{J-1}^{n+1}} + \frac{1}{\alpha_J^{n+1} + \alpha_{J-1}^{n+1}} \right) \tau_{i,j}^{n+1} S_{i,j}^{n+1} \\ + \frac{2\delta x}{A(\alpha_J^{n+1} + \alpha_{J-1}^{n+1})} \tau_{g,j}^{n+1} S_{g,j}^{n+1} \end{bmatrix}$$

F is the resulting volume force on the liquid phase.

B.3.2 The system of equations

The stability of the system composed of the 3 following discretized equations is to be investigated:

- $\frac{1}{\delta t} (\beta_J^{n+1} - \beta_J^n) + \frac{1}{\delta x} (\beta_J^{n+1} U_{l,j+1}^{n+1} - \beta_{J-1}^{n+1} U_{l,j}^{n+1}) = 0$
- $\frac{1}{\delta t} (\alpha_J^{n+1} - \alpha_J^n) + \frac{1}{\delta x} (\alpha_J^{n+1} U_{g,j+1}^{n+1} - \alpha_{J-1}^{n+1} U_{g,j}^{n+1}) = 0$
- $\begin{pmatrix} - \frac{\delta x}{\delta t} \rho_l Trans_{liq} \\ + \frac{\delta x}{\delta t} \rho_g Trans_{gas} \\ + \rho_l Conv_{liq} \\ - \rho_g Conv_{gas} \\ + \delta x Fric \\ - (\rho_l - \rho_g) Hydro \end{pmatrix} = 0$

- For the sake of clarity, the following notations were introduced in the combined momentum conservation equation:

$$\begin{aligned}
 Trans_{liq} &= U_{l,j}^{n+1} - \frac{\beta_J^n + \beta_{J-1}^n}{\beta_J^{n+1} + \beta_{J-1}^{n+1}} U_{l,j}^n \\
 Trans_{gas} &= U_{g,j}^{n+1} - \frac{\alpha_J^n + \alpha_{J-1}^n}{\alpha_J^{n+1} + \alpha_{J-1}^{n+1}} U_{g,j}^n \\
 Conv_{liq} &= \begin{bmatrix} \frac{1}{\beta_J^{n+1} + \beta_{J-1}^{n+1}} \left(\beta_{J-2}^{n+1} U_{l,j-1}^{n+1} + \beta_{J-1}^{n+1} U_{l,j}^{n+1} \right) U_{l,j-1}^{n+1} \\ -\frac{1}{\beta_J^{n+1} + \beta_{J-1}^{n+1}} \left(\beta_{J-1}^{n+1} U_{l,j}^{n+1} + \beta_J^{n+1} U_{l,j+1}^{n+1} \right) U_{l,j}^{n+1} \end{bmatrix} \\
 Conv_{gas} &= \begin{bmatrix} \frac{1}{\alpha_J^{n+1} + \alpha_{J-1}^{n+1}} \left(\alpha_{J-1}^{n+1} U_{g,j}^{n+1} + \alpha_J^{n+1} U_{g,j+1}^{n+1} \right) U_{g,j}^{n+1} \\ -\frac{1}{\alpha_J^{n+1} + \alpha_{J-1}^{n+1}} \left(\alpha_{J-2}^{n+1} U_{g,j-1}^{n+1} + \alpha_{J-1}^{n+1} U_{g,j}^{n+1} \right) U_{g,j-1}^{n+1} \end{bmatrix} \\
 Fric &= F \left(U_{l,j}^{n+1}, U_{g,j}^{n+1}, \frac{\beta_J^{n+1} + \beta_{J-1}^{n+1}}{2} \right) \\
 Hydro &= g \cos \phi (h_{l,J} - h_{l,J-1})^{n+1}
 \end{aligned}$$

B.3.3 Stability analysis of the system

Notations

Starting from an equilibrium point characterized by a holdup $\bar{\beta}$, a liquid velocity \bar{U}_l and a gas velocity \bar{U}_g , we investigate the effects of a small perturbation on the system. The complex variable ρ is the growth rate of the perturbation and the real variable θ is its wave number. $\tilde{\beta}$, \tilde{U}_l and \tilde{U}_g are the respective amplitudes of the perturbation affecting respectively the liquid holdup, the liquid velocity and the gas velocity. Using those notations, we can express each flow variable as follows:

$$\begin{aligned}
 \beta_J^n &= \bar{\beta} + \tilde{\beta} \rho^n e^{iJ\theta} \\
 \alpha_J^n &= \bar{\alpha} + \tilde{\alpha} \rho^n e^{iJ\theta} = \bar{\alpha} - \tilde{\beta} \rho^n e^{iJ\theta} \\
 U_{l,j}^n &= \bar{U}_l + \tilde{U}_l \rho^n e^{ij\theta} = \bar{U}_l + \tilde{U}_l \rho^n e^{i(J-\frac{1}{2})\theta} \\
 U_{g,j}^n &= \bar{U}_g + \tilde{U}_g \rho^n e^{ij\theta} = \bar{U}_g + \tilde{U}_g \rho^n e^{i(J-\frac{1}{2})\theta} \\
 F_j^n &= \bar{F} + \tilde{F} \rho^n e^{ij\theta} = \bar{F} + \tilde{F} \rho^n e^{i(J-\frac{1}{2})\theta} = \tilde{F} \rho^n e^{i(J-\frac{1}{2})\theta}
 \end{aligned}$$

In the last equation we used the fact that at the equilibrium point $(\bar{\beta}, \bar{U}_l, \bar{U}_g)$ the total resulting force on the liquid is zero.

Discretized liquid mass conservation equation

Using the discretized liquid mass conservation equation (equation B.1):

$$\frac{1}{\delta t} (\beta_J^{n+1} - \beta_J^n) + \frac{1}{\delta x} \left(\beta_J^{n+1} U_{l,j+1}^{n+1} - \beta_{J-1}^{n+1} U_{l,j}^{n+1} \right) = 0$$

we are able to express the amplitude of the perturbation on the liquid velocity \tilde{U}_l as a function of the amplitude of the perturbation on the liquid holdup $\tilde{\beta}$. After simplification we obtain:

$$\tilde{U}_l = \left[i \frac{1}{2 \sin\left(\frac{1}{2}\theta\right)} \frac{\delta x}{\delta t} \frac{\rho - 1}{\rho} - \overline{U}_l e^{-\frac{1}{2}i\theta} \right] \frac{\tilde{\beta}}{\overline{\beta}} \quad (\text{B.6})$$

Discretized gas mass conservation equation

Similarly, starting with the discretized gas mass conservation equation (equation B.2):

$$\frac{1}{\delta t} (\alpha_J^{n+1} - \alpha_J^n) + \frac{1}{\delta x} \left(\alpha_J^{n+1} U_{g,j+1}^{n+1} - \alpha_{J-1}^{n+1} U_{g,j}^{n+1} \right) = 0$$

we can express the amplitude of the perturbation on the liquid velocity \tilde{U}_g as a function of the amplitude of the perturbation on the liquid holdup $\tilde{\beta}$. After simplification we obtain:

$$\tilde{U}_g = \left[\overline{U}_g e^{-\frac{1}{2}i\theta} - i \frac{1}{2 \sin\left(\frac{1}{2}\theta\right)} \frac{\delta x}{\delta t} \frac{\rho - 1}{\rho} \right] \frac{\tilde{\beta}}{\overline{\alpha}} \quad (\text{B.7})$$

Combined momentum conservation equation

We now have to express each of the terms within the underneath combined momentum conservation equation as a function of $\tilde{\beta}$, \tilde{U}_l and \tilde{U}_g .

$$\begin{pmatrix} -\frac{\delta x}{\delta t} \rho_l Trans_{liq} \\ +\frac{\delta x}{\delta t} \rho_g Trans_{gas} \\ +\rho_l Conv_{liq} \\ -\rho_g Conv_{gas} \\ +\delta x Fric \\ -(\rho_l - \rho_g) Hydro \end{pmatrix} = 0 \quad (\text{B.8})$$

Transient liquid term

We start with the transient liquid term $Trans_{liq} = U_{l,j}^{n+1} - \frac{\beta_J^n + \beta_{J-1}^n}{\beta_J^{n+1} + \beta_{J-1}^{n+1}} U_{l,j}^n$

After simplification we obtain:

$$Trans_{liq} = (\rho - 1) \left[\tilde{U}_l + \cos\left(\frac{1}{2}\theta\right) \frac{\overline{U}_l}{\overline{\beta}} \tilde{\beta} \right] \rho^n e^{i(J-\frac{1}{2})\theta} \quad (\text{B.9})$$

Transient gas term

Similarly, differentiating the transient gas term $Trans_{gas} = U_{g,j}^{n+1} - \frac{\alpha_J^n + \alpha_{J-1}^n}{\alpha_J^{n+1} + \alpha_{J-1}^{n+1}} U_{g,j}^n$ leads after simplification to:

$$Trans_{gas} = (\rho - 1) \left[\tilde{U}_g - \cos\left(\frac{1}{2}\theta\right) \frac{\overline{U}_g}{\overline{\alpha}} \tilde{\beta} \right] \rho^n e^{i(J-\frac{1}{2})\theta} \quad (\text{B.10})$$

Liquid convective term

The liquid convective term $Conv_{liq} = \frac{1}{\beta_J^{n+1} + \beta_{J-1}^{n+1}} \left[\begin{array}{c} \left(\beta_{J-2}^{n+1} U_{l,j-1}^{n+1} + \beta_{J-1}^{n+1} U_{l,j}^{n+1} \right) U_{l,j-1}^{n+1} \\ - \left(\beta_{J-1}^{n+1} U_{l,j}^{n+1} + \beta_J^{n+1} U_{l,j+1}^{n+1} \right) U_{l,j}^{n+1} \end{array} \right]$ becomes:

$$Conv_{liq} = \left(\begin{array}{c} -i\rho \frac{\overline{U}_l^2}{\beta} e^{-i\frac{1}{2}\theta} \sin(\theta) \left(\tilde{\beta} \rho^n e^{i(J-\frac{1}{2})\theta} \right) \\ -i\rho \left[\sin(\theta) + 2e^{-i\frac{1}{2}\theta} \sin\left(\frac{1}{2}\theta\right) \right] \overline{U}_l \left(\tilde{U}_l \rho^n e^{i(J-\frac{1}{2})\theta} \right) \end{array} \right) \quad (\text{B.11})$$

Gas convective term

Applying the same treatment to the gas convective term

$$Conv_{gas} = \frac{1}{\alpha_J^{n+1} + \alpha_{J-1}^{n+1}} \left[\begin{array}{c} \left(\alpha_{J-2}^{n+1} U_{g,j-1}^{n+1} + \alpha_{J-1}^{n+1} U_{g,j}^{n+1} \right) U_{g,j-1}^{n+1} \\ - \left(\alpha_{J-1}^{n+1} U_{g,j}^{n+1} + \alpha_J^{n+1} U_{g,j+1}^{n+1} \right) U_{g,j}^{n+1} \end{array} \right] \text{ yields:}$$

$$Conv_{gas} = \left(\begin{array}{c} i\rho \frac{\overline{U}_g^2}{\alpha} e^{-i\frac{1}{2}\theta} \sin(\theta) \left(\tilde{\beta} \rho^n e^{i(J-\frac{1}{2})\theta} \right) \\ -i\rho \left[\sin(\theta) + 2e^{-i\frac{1}{2}\theta} \sin\left(\frac{1}{2}\theta\right) \right] \overline{U}_g \left(\tilde{U}_g \rho^n e^{i(J-\frac{1}{2})\theta} \right) \end{array} \right) \quad (\text{B.12})$$

Resulting volumic force on the liquid phase

The resulting force on the liquid phase F is a function of the three variables β , U_l and U_g . We are therefore able to express the variations of F around its equilibrium value of 0 as a function of the variations of β , U_l and U_g . Although the partial derivatives of F $\left[\frac{\partial F}{\partial U_l} \right]_{U_g, \beta}$, $\left[\frac{\partial F}{\partial U_g} \right]_{U_l, \beta}$ and $\left[\frac{\partial F}{\partial \beta} \right]_{U_l, U_g}$ can be expressed analytically if we have an explicit expression for the friction factors, such derivation is unnecessary and cumbersome. We therefore choose not to explicitly derive the derivatives of F and evaluate them numerically when needed.

$$Fric = F \left(U_{l,j}^{n+1}, U_{g,j}^{n+1}, \frac{\beta_J^{n+1} + \beta_{J-1}^{n+1}}{2} \right) = \left(\begin{array}{c} \overline{F} + \\ \left[\frac{\partial F}{\partial U_l} \right]_{U_g, \beta} \tilde{U}_l \rho^{n+1} e^{i(J-\frac{1}{2})\theta} \\ + \left[\frac{\partial F}{\partial U_g} \right]_{U_l, \beta} \tilde{U}_g \rho^{n+1} e^{i(J-\frac{1}{2})\theta} \\ + \left[\frac{\partial F}{\partial \beta} \right]_{U_l, U_g} \cos\left(\frac{1}{2}\theta\right) \tilde{\beta} \rho^{n+1} e^{i(J-\frac{1}{2})\theta} \end{array} \right) \quad (\text{B.13})$$

with $\overline{F} = 0$, as at equilibrium, the resulting force on the liquid is null.

Hydrostatic term

Finally the hydrostatic term $Hydro = g \cos \phi (h_{l,J} - h_{l,J-1})^{n+1}$ gives after simplification:

$$Hydro = 2ig \cos \phi \frac{A}{\left[\frac{dA_l}{dh_l}\right]} \sin\left(\frac{1}{2}\theta\right) \rho \left(\tilde{\beta} \rho^n e^{i(J-\frac{1}{2})\theta}\right) \quad (\text{B.14})$$

Expressing the discretized combined momentum equation

Now we have an expression for all the terms of the discretized combined momentum equation.

$$\begin{pmatrix} -\frac{\delta x}{\delta t} \rho_l Trans_{liq} \\ +\frac{\delta x}{\delta t} \rho_g Trans_{gas} \\ +\rho_l Conv_{liq} \\ -\rho_g Conv_{gas} \\ +\delta x Fric \\ -(\rho_l - \rho_g) Hydro \end{pmatrix} = 0 \quad (\text{B.15})$$

After some simplification, we can express the discretized combined momentum equation as a linear equation of the three amplitudes $\tilde{\beta}$, \tilde{U}_l and \tilde{U}_g .

$$\begin{bmatrix} \begin{pmatrix} -\frac{\delta x}{\delta t} \rho_l \left(\frac{\rho-1}{\rho}\right) \\ -2 \left[i \sin(\theta) + \sin^2\left(\frac{1}{2}\theta\right) \right] \rho_l \overline{U}_l \\ +\delta x \left[\frac{\partial F}{\partial U_l} \right]_{U_g, \beta} \end{pmatrix} \tilde{U}_l \\ + \begin{pmatrix} +\frac{\delta x}{\delta t} \rho_g \left(\frac{\rho-1}{\rho}\right) \\ +2 \left[i \sin(\theta) + \sin^2\left(\frac{1}{2}\theta\right) \right] \rho_g \overline{U}_g \\ +\delta x \left[\frac{\partial F}{\partial U_g} \right]_{U_l, \beta} \end{pmatrix} \tilde{U}_g \\ + \begin{pmatrix} -\frac{\delta x}{\delta t} \left(\frac{\rho-1}{\rho}\right) \cos\left(\frac{1}{2}\theta\right) \left(\rho_l \frac{\overline{U}_l}{\beta} + \rho_g \frac{\overline{U}_g}{\alpha}\right) \\ -i \left(\frac{\rho_l \overline{U}_l^2}{\beta} + \frac{\rho_g \overline{U}_g^2}{\alpha}\right) e^{-i\frac{1}{2}\theta} \sin(\theta) \\ +\delta x \left[\frac{\partial F}{\partial \beta} \right]_{U_l, U_g} \cos\left(\frac{1}{2}\theta\right) \\ -2i(\rho_l - \rho_g) g \cos \phi \frac{A}{\left[\frac{dA_l}{dh_l}\right]} \sin\left(\frac{1}{2}\theta\right) \end{pmatrix} \tilde{\beta} \end{bmatrix} = 0 \quad (\text{B.16})$$

B.3.4 Dispersion Equation

The system of three discretized equations (liquid mass conservation, gas mass conservation and combined momentum conservation equation) can now be translated into a linear system of equations for the three variables $\tilde{\beta}$, \tilde{U}_l and \tilde{U}_g .

$$\begin{aligned}
& \bullet \tilde{U}_l = \left[i \frac{1}{2 \sin(\frac{1}{2}\theta)} \frac{\delta x}{\delta t} \frac{\rho-1}{\rho} - \overline{U}_l e^{-\frac{1}{2}i\theta} \right] \frac{\tilde{\beta}}{\beta} \\
& \bullet \tilde{U}_g = \left[\overline{U}_g e^{-\frac{1}{2}i\theta} - i \frac{1}{2 \sin(\frac{1}{2}\theta)} \frac{\delta x}{\delta t} \frac{\rho-1}{\rho} \right] \frac{\tilde{\beta}}{\alpha} \\
& \bullet \begin{pmatrix} -\frac{\delta x}{\delta t} \rho_l \left(\frac{\rho-1}{\rho} \right) \\ -2 \left[i \sin(\theta) + \sin^2\left(\frac{1}{2}\theta\right) \right] \rho_l \overline{U}_l \\ + \delta x \left[\frac{\partial F}{\partial U_l} \right]_{U_g, \beta} \end{pmatrix} \tilde{U}_l + \begin{pmatrix} +\frac{\delta x}{\delta t} \rho_g \left(\frac{\rho-1}{\rho} \right) \\ +2 \left[i \sin(\theta) + \sin^2\left(\frac{1}{2}\theta\right) \right] \rho_g \overline{U}_g \\ + \delta x \left[\frac{\partial F}{\partial U_g} \right]_{U_l, \beta} \end{pmatrix} \tilde{U}_g + \\
& \begin{pmatrix} -\frac{\delta x}{\delta t} \left(\frac{\rho-1}{\rho} \right) \cos\left(\frac{1}{2}\theta\right) \left(\rho_l \frac{\overline{U}_l}{\beta} + \rho_g \frac{\overline{U}_g}{\alpha} \right) \\ -i \left(\frac{\rho_l \overline{U}_l^2}{\beta} + \frac{\rho_g \overline{U}_g^2}{\alpha} \right) e^{-i\frac{1}{2}\theta} \sin(\theta) \\ + \delta x \left[\frac{\partial F}{\partial \beta} \right]_{U_l, U_g} \cos\left(\frac{1}{2}\theta\right) \\ -2i (\rho_l - \rho_g) g \cos \phi \frac{A}{\left[\frac{dA_l}{dh_l} \right]} \sin\left(\frac{1}{2}\theta\right) \end{pmatrix} \tilde{\beta} = 0
\end{aligned}$$

After replacing the expressions of \tilde{U}_l and \tilde{U}_g in the first two equations into the last equation, we find:

$$\begin{aligned}
& -i \left(\frac{\rho_l}{\beta} + \frac{\rho_g}{\alpha} \right) \frac{1}{2 \sin(\frac{1}{2}\theta)} \left(\frac{\delta x}{\delta t} \right)^2 \left(\frac{\rho-1}{\rho} \right)^2 \\
& + \left[\begin{aligned} & \left(\frac{\rho_l \overline{U}_l}{\beta} + \frac{\rho_g \overline{U}_g}{\alpha} \right) e^{-\frac{1}{2}i\theta} \\ & - \frac{2}{2 \sin(\frac{1}{2}\theta)} i \left[i \sin(\theta) + \sin^2\left(\frac{1}{2}\theta\right) \right] \left(\frac{\rho_l \overline{U}_l}{\beta} + \frac{\rho_g \overline{U}_g}{\alpha} \right) \frac{\delta x}{\delta t} \left(\frac{\rho-1}{\rho} \right) \\ & i \delta x \frac{1}{2 \sin(\frac{1}{2}\theta)} \left(\frac{1}{\beta} \left[\frac{\partial F}{\partial U_l} \right]_{U_g, \beta} - \frac{1}{\alpha} \left[\frac{\partial F}{\partial U_g} \right]_{U_l, \beta} \right) \\ & - \cos\left(\frac{1}{2}\theta\right) \left(\rho_l \frac{\overline{U}_l}{\beta} + \rho_g \frac{\overline{U}_g}{\alpha} \right) \end{aligned} \right] \\
& + \left(\begin{aligned} & 2 \left[i \sin(\theta) + \sin^2\left(\frac{1}{2}\theta\right) \right] e^{-\frac{1}{2}i\theta} \left(\frac{\rho_l \overline{U}_l^2}{\beta} + \frac{\rho_g \overline{U}_g^2}{\alpha} \right) \\ & - \delta x \left[\frac{\partial F}{\partial U_l} \right]_{U_g, \beta} \frac{\overline{U}_l}{\beta} e^{-\frac{1}{2}i\theta} + \delta x \left[\frac{\partial F}{\partial U_g} \right]_{U_l, \beta} \frac{\overline{U}_g}{\alpha} e^{-\frac{1}{2}i\theta} + \delta x \left[\frac{\partial F}{\partial \beta} \right]_{U_l, U_g} \cos\left(\frac{1}{2}\theta\right) \\ & -i \left(\frac{\rho_l \overline{U}_l^2}{\beta} + \frac{\rho_g \overline{U}_g^2}{\alpha} \right) e^{-i\frac{1}{2}\theta} \sin(\theta) \\ & -2i (\rho_l - \rho_g) g \cos \phi \frac{A}{\left[\frac{dA_l}{dh_l} \right]} \sin\left(\frac{1}{2}\theta\right) \end{aligned} \right) = 0
\end{aligned}$$

By reorganizing the terms, we are able to highlight the similarity between the linear stability analysis of the continuous equations and of the discretized equations:

$$\begin{aligned}
 & \left[\frac{\rho_l}{\beta} + \frac{\rho_g}{\alpha} \right] \left(\frac{\rho-1}{\rho\delta t} \right)^2 + \\
 & + \left[- \left(\left[\frac{\partial F}{\partial U_l^S} \right]_{U_g^S, \beta} - \left[\frac{\partial F}{\partial U_g^S} \right]_{U_l^S, \beta} \right) + \right. \\
 & \quad \left. 2i \left(\frac{\rho_l \bar{U}_l}{\beta} + \frac{\rho_g \bar{U}_g}{\alpha} \right) \left(\frac{2 \sin(\frac{1}{2}\theta)}{\delta x} \right) \right] \left(\frac{\rho-1}{\rho\delta t} \right) \\
 & + i \left[\frac{\partial F}{\partial \beta} \right]_{U_l^S, U_g^S} \left(\frac{2 \sin(\frac{1}{2}\theta)}{|\delta x|} \right) \\
 & + \left(- \left(\frac{\rho_l \bar{U}_l^2}{\beta} + \frac{\rho_g \bar{U}_g^2}{\alpha} \right) \right. \\
 & \quad \left. + (\rho_l - \rho_g) g \cos \phi \frac{A}{\left[\frac{dA_l}{dh_l} \right]} \right) \left(\frac{2 \sin(\frac{1}{2}\theta)}{\delta x} \right)^2 \\
 & - i \left[\frac{\partial F}{\partial \beta} \right]_{U_l^S, U_g^S} (1 - \cos(\frac{1}{2}\theta)) \left(\frac{2 \sin(\frac{1}{2}\theta)}{|\delta x|} \right) \\
 & + 2i (\cos(\frac{1}{2}\theta) - 1) \left(\frac{\rho_l \bar{U}_l}{\beta} + \frac{\rho_g \bar{U}_g}{\alpha} \right) \left(\frac{2 \sin(\frac{1}{2}\theta)}{\delta x} \right) \\
 & + (1 - e^{-i\theta}) \left(\frac{\rho_l \bar{U}_l^2}{\beta} + \frac{\rho_g \bar{U}_g^2}{\alpha} \right) \left(\frac{2 \sin(\frac{1}{2}\theta)}{\delta x} \right)^2 \\
 & + i \left[+ \left[\frac{\partial F}{\partial U_l^S} \right]_{U_g^S, \beta} \bar{U}_l i \sin(\frac{1}{2}\theta) \right. \\
 & \quad \left. - \left[\frac{\partial F}{\partial U_g^S} \right]_{U_l^S, \beta} \bar{U}_g i \sin(\frac{1}{2}\theta) \right] \left(\frac{2 \sin(\frac{1}{2}\theta)}{|\delta x|} \right) \\
 & + 2 \sin(\frac{1}{2}\theta) \left(\frac{\rho_l \bar{U}_l}{\beta} + \frac{\rho_g \bar{U}_g}{\alpha} \right) \left(\frac{2 \sin(\frac{1}{2}\theta)}{\delta x} \right) \left(\frac{\rho-1}{\rho\delta t} \right) = 0
 \end{aligned}$$

In order to highlight furthermore the correspondence between the linear stability analysis of the continuous equations and of the discretized equations, we can replace ρ and θ , traditionally used for discrete stability analysis by the wave number k and the pulsation w . We have then $\rho = e^{iw\delta t}$ and $\theta = -k\delta x$. For small enough δt the term $\left(\frac{\rho-1}{\rho\delta t} \right)$ can be replaced by iw . A second order development in $k\delta x$ gives the following relations:

$$\begin{aligned}
 \left(\frac{2 \sin(\frac{1}{2}\theta)}{\delta x} \right) & \approx -k & 2 \sin(\frac{1}{2}\theta) & \approx -k\delta x \\
 1 - \cos(\frac{1}{2}\theta) & \approx \frac{1}{8}k^2\delta x^2 & 1 - e^{-i\theta} & \approx -ik\delta x + \frac{1}{2}k^2\delta x^2
 \end{aligned} \tag{B.17}$$

We now introduce the standard parameters ρ , a , b , c and e as presented by Barnea and Taitel (1993) for the linear stability analysis of the two-fluid model equations. We also introduce the additional parameters r , h and m in order to account for the extra terms deriving from the discretized nature of the starting equations.

$$\begin{aligned}
 \rho &= \frac{\rho_l}{\beta} + \frac{\rho_g}{\alpha} \\
 a &= \frac{1}{\rho} \left(\frac{\rho_l \overline{U}_l}{\beta} + \frac{\rho_g \overline{U}_g}{\alpha} \right) \\
 b &= \frac{1}{2\rho} \left(\left[\frac{\partial F}{\partial U_l^S} \right]_{U_g^S, \beta} - \left[\frac{\partial F}{\partial U_g^S} \right]_{U_l^S, \beta} \right) \\
 c &= \frac{1}{\rho} \left(\frac{\rho_l \overline{U}_l^2}{\beta} + \frac{\rho_g \overline{U}_g^2}{\alpha} - (\rho_l - \rho_g) g \cos \phi \frac{A}{\left[\frac{dA_l}{dh_l} \right]} \right) \\
 e &= -\frac{1}{\rho} \left[\frac{\partial F}{\partial \beta} \right]_{U_l^S, U_g^S} \\
 r &= \frac{1}{\rho} \left(\frac{\rho_l \overline{U}_l^2}{\beta} + \frac{\rho_g \overline{U}_g^2}{\alpha} \right) \\
 h &= \frac{1}{\rho} \frac{1}{2} \left(\left[\frac{\partial F}{\partial U_l^S} \right]_{U_g^S, \beta} \overline{U}_l - \left[\frac{\partial F}{\partial U_g^S} \right]_{U_l^S, \beta} \overline{U}_g \right) \\
 m &= \frac{1}{\rho} \frac{1}{8} \left[\frac{\partial F}{\partial \beta} \right]_{U_l^S, U_g^S} + \frac{1}{\rho} \frac{1}{4} \left(\frac{\rho_l \overline{U}_l}{\beta} + \frac{\rho_g \overline{U}_g}{\alpha} \right)
 \end{aligned}$$

We can now write the dispersion equation of the discretized two-fluid model equations as:

$$w^2 - 2[ak - bi]w + (c + h\delta x)k^2 - iek - imk^3\delta x^2 - \frac{1}{2}rk^4\delta x^2 + ir\delta xk^3 - iawk^2\delta x = 0 \quad (\text{B.18})$$

If we let δx tend towards zero, we encounter the usual standard VKH criterion deriving from the linear stability analysis of the continuous two-fluid model (Barnea and Taitel, 1993):

$$w^2 - 2[ak - bi]w + ck^2 - iek = 0 \quad (\text{B.19})$$

B.3.5 Stability criterion

Going back to the dispersion equation of the discretized two-fluid model, we look for the point of neutral stability by writing that at neutral stability the imaginary part of w is null. We can now replace the complex equation by two real equations by taking the real and the imaginary part of the dispersion equations.

$$\begin{aligned}
 w_R^2 - 2akw_R + (c + h\delta x)k^2 - \frac{1}{2}rk^4\delta x^2 &= 0 \text{ for the real part} \\
 2bw_R - ek - mk^3\delta x^2 + r\delta xk^3 - awk^2\delta x &= 0 \text{ for the imaginary part}
 \end{aligned}$$

$$\text{Yielding } w_R = \frac{e + (m\delta x^2 - r\delta x)k^2}{2b - ak^2\delta x}k = C_k k$$

Of course, if we let δx tend towards zero, we find the well-known expression for the wave speed in the continuous two-fluid model system of equations: $\frac{e}{2b}$.

Going back to the real part of the equation, we replace w_R by its expression $C_k k$. The equation then becomes:

$$C_k^2 k^2 - 2aC_k k^2 + (c + h\delta x) k^2 - \frac{1}{2} r k^4 \delta x^2 = 0 \quad (\text{B.20})$$

We are now able to express the stability criterion for the discretized two-fluid model equations:

$$\text{stable} \Leftrightarrow \left(\begin{array}{l} \forall k \ (C_k - a)^2 + (c - a^2 + h\delta x) - \frac{1}{2} r k^2 \delta x^2 < 0 \\ \text{where } C_k = \frac{e + (m\delta x^2 - r\delta x) k^2}{2b - ak^2 \delta x} \end{array} \right) \quad (\text{B.21})$$

If surface tension is inserted within the equations, we get:

$$\text{stable} \Leftrightarrow \left(\begin{array}{l} \forall k \ (C_k - a)^2 + (c - a^2 + h\delta x) - (\frac{1}{2} r \delta x^2 + d) k^2 < 0 \\ \text{where } C_k = \frac{e + (m\delta x^2 - r\delta x) k^2}{2b - ak^2 \delta x} \end{array} \right) \quad (\text{B.22})$$

Parameter d is defined by the relation $d = \frac{\sigma}{\rho} \frac{A}{\frac{dA_l}{dh_l}}$ where σ is the surface tension between the gas and the liquid phase.

We can compare this result with the stability criterion for the continuous two-fluid model equations with surface tension, as obtained by Barnea and Taitel (1993):

$$\text{stable} \Leftrightarrow \left(\begin{array}{l} \forall k \ (C - a)^2 + (c - a^2) - dk^2 < 0 \\ \text{where } C = \frac{e}{2b} \end{array} \right) \quad (\text{B.23})$$

which is equivalent to :

$$\text{stable} \Leftrightarrow \left(\begin{array}{l} (C - a)^2 + (c - a^2) < 0 \\ \text{where } C = \frac{e}{2b} \end{array} \right) \quad (\text{B.24})$$

The discretized nature of the equations has had three consequences on the stability criterion:

- A numerical extra stabilizing term $h\delta x$ proportional to the grid size has appeared. It is here important to notice that h is negative. This extra-term is independent of the wave number k .

- A numerical surface tension term $\frac{1}{2}r\delta x^2$ proportional to the square of the grid size has appeared. Its effect is similar to the one of the surface tension. It is important to note that the parameter r takes here only positive values.
- The wave speed C is dependent on the wave number k in the discretized equations stability analysis. In the VKH analysis, C is constant for all low amplitude waves. If we consider the effect of surface tension, which tends to dampen short-wavelength waves, we can conclude that in the VKH analysis, the most unstable wavelength will always be infinite. On the other hand we have a priori no such certitude for the discretized equations stability analysis.

Given that b is negative and a positive, the function $f : k \rightarrow C_k = \frac{e + (m\delta x^2 - r\delta x) k^2}{2b - ak^2\delta x}$ is defined for all values of k . The function f is homographic thus monotonic and therefore increases (or decreases) from $\frac{e}{2b}$ (which is a positive number since both e and b are negative reals) to $\frac{r - m\delta x}{a}$ (where r , m and a are all positive).

The obtained stability criterion for the discretized two-fluid model was implemented in a MATLAB code able to create numerical flowmaps from any chosen stability criterion (such as Taitel and Dukler's, Minimum Holdup or VKH). It appeared

that for reasonable values of δx , $\frac{r - m\delta x}{a} \approx \frac{r}{a} \approx \frac{\frac{\rho_l \overline{U}_l^2}{\beta} + \frac{\rho_g \overline{U}_g^2}{\alpha}}{\frac{\rho_l \overline{U}_l}{\beta} + \frac{\rho_g \overline{U}_g}{\alpha}} \approx \overline{U}_l + \frac{\overline{\beta} \rho_g \overline{U}_g^2}{\overline{\alpha} \rho_l \overline{U}_l}$. We can

therefore conclude that for short wavelength waves, the wave velocity tends towards the liquid velocity. Moreover, as numerical trials show that $\frac{e}{2b} > \overline{U}_l$ and bearing in

mind that $a = \frac{1}{\rho} \left(\frac{\rho_l \overline{U}_l}{\beta} + \frac{\rho_g \overline{U}_g}{\alpha} \right) \approx \overline{U}_l$ we can conclude that the destabilizing contribution of the term $(C_k - a)^2$ will simply decrease from its long wavelength limit of $\left(\frac{e}{2b} - a\right)^2$ to its small wavelength limit of nearly zero.

Since the other terms depending on k , $(\frac{1}{2}r\delta x^2 + d) k^2$ have a stabilizing effect on the flow, we can conclude that the most dangerous wavelength for the discretized two-fluid model will be infinite, as in the continuous case. This simple analysis now allows us to re-write the stability condition for the discretized two-fluid model as:

$$stable \Leftrightarrow \left(\begin{array}{l} (C - a)^2 + (c - a^2 + h\delta x) < 0 \\ \text{where } C = \frac{e}{2b} \end{array} \right) \quad (\text{B.25})$$

Finally, only the extra-term in $h\delta x$ plays a role in the stability of the discretized equations.

Fluids	U_l^S [$m.s^{-1}$]	U_g^S [$m.s^{-1}$]	D [cm]	$\frac{\bar{h}_l}{D}$	$d \times 10^6$	$\frac{1}{2}r$	δx ensuring $\frac{1}{2}r\delta x^2 = d$ [mm]
Air-water	0.09	0.5	2.5	0.67	1.07	0.013	9
Air-water	0.09	3.34	2.5	0.4	0.54	0.041	3.6
Air-water	0.16	0.5	10	0.74	0.51	0.036	3.7
Air-water	0.20	3.34	10	0.51	2.94	0.108	5
Air-ExxsolD80	0.09	0.5	2.5	0.67	0.48	0.014	6
Air-ExxsolD80	0.09	3.34	2.5	0.39	0.24	0.042	2.4

Table B.1: Relative importance of the numerical and physical surface tension in various conditions

B.3.6 Importance of the numerical surface tension

Although the extra-surface tension term $\frac{1}{2}r\delta x^2$ does not affect the stability of the flow at long wavelength, it can possibly modify the behaviour of the flow at smaller scales. Table B.1 attempts to quantify the relative importance of the numerical surface tension term $\frac{1}{2}r\delta x^2$ compared to the physical surface tension term d . The grid cell size at which the contribution of the numerical surface tension is as important as the contribution of the physical surface tension (i.e. the value of δx ensuring $\frac{1}{2}r\delta x^2 = d$) is evaluated at neutral stability point (i.e. the point of transition between stratified to slug flow according to the VKH criterion). Several flow conditions (flow rates, fluids and pipe diameter) were tested. A surface tension of $\sigma = 0.072 N.m^{-1}$ was taken for air and water and a surface tension of $\sigma = 0.026 N.m^{-1}$ was taken for air and ExxsolD80 (as measured in Kristiansen, 2004).

Table B.1 shows that in order to be able to accurately model the effect of surface tension with an upwind-averaged two-fluid model scheme, it is necessary to use a grid cell size no bigger than $1 mm$. It might however be possible to work with bigger grid cells by subtracting the calculated numerical surface tension from the physical surface tension which could mean in some cases using a negative input value for σ . Although feasible, this would be cumbersome as the right input value for σ would depend not only on δx and on the pipe diameter but also on other variable flow parameters such as the holdup and the liquid and gas velocities. Finally, although this effect does not in practice seem to bring excessive problems to the simulation of slug initiation with an upwind two-fluid model (Issa and Kempf, 2003), it has to be kept in mind as a limitation of the upstream differentiation of the two-fluid model.

B.3.7 Importance of the numerical extra-stabilizing term

The effect of the extra-term in $h\delta x$ was numerically quantified for several values of δx and several types of flows. Figure B.2 represent the stability flowmaps computed for

both the continuous two-fluid model equations (VKH criterion) and for the discretized two-fluid model equations, in the case of an air-water flow, and for three different pipe diameters ($\delta x = 0.1$ m, $\delta x = 0.2$ m and $\delta x = 0.5$ m). The stability area is plotted on a $(U_l^S - U_g^S)$ flowmap on the left-hand side and on a $(U_l^S - \frac{h_l}{D})$ on the right-hand side.

It appears that the discretized nature of the equations has a moderate impact in terms of stability area. Quite predictably, the smaller the pipe diameter, the smaller should be the grid size in order not to introduce an excessive stabilizing effect. In all cases however, a 1 cm grid was enough to obtain a neutral stability line undiscernibly close to the VKH neutral stability line.

As the h parameter is defined from partial derivatives of the friction fictions, it seemed logical to evaluate the influence of the viscosity by investigating a different set of fluids. The same computations presented for air-water flow was performed in the case of an Air-ExxsolD80 (see figure B.2). No significant difference in the influence of the grid cell size was observed. The same conclusion also applies to higher viscosity oils.

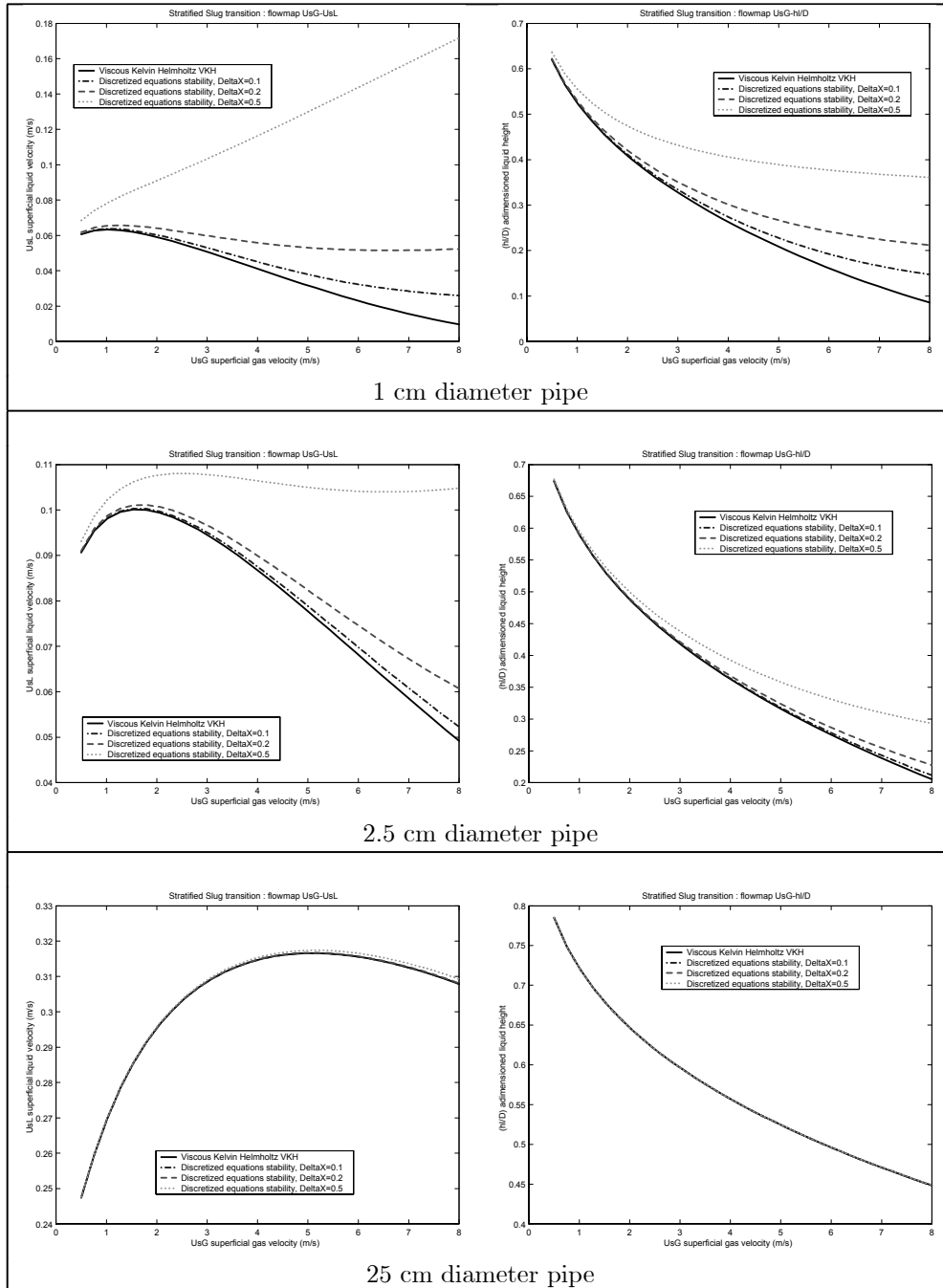


Figure B.2: Numerical flowmaps for water and air

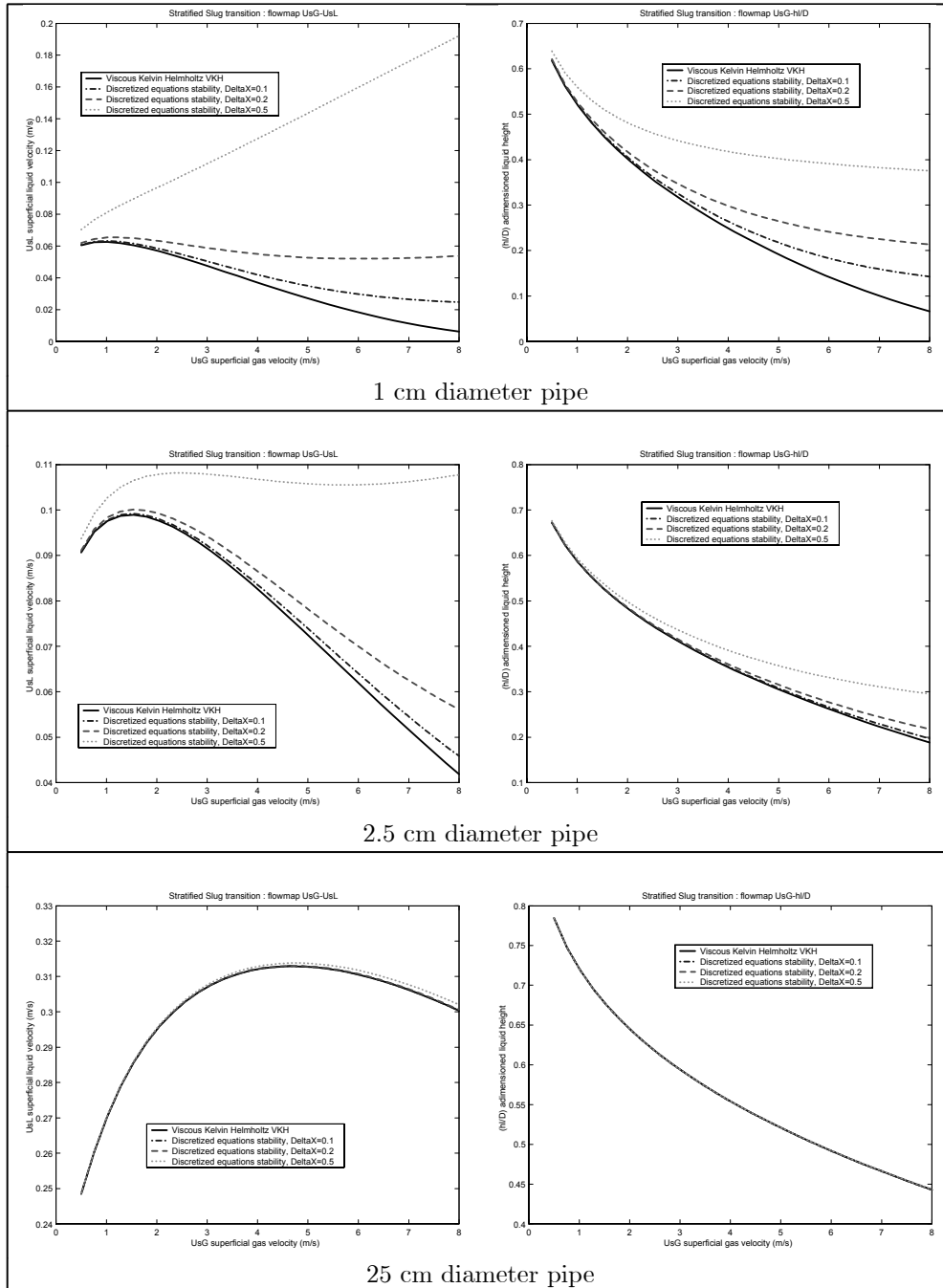


Table B.2: Numerical flowmaps for Exxsold80 and air

Appendix C

Influence of high order terms on the initiation process

C.1 Principle

In the fourth paper of this thesis, *Influence of dynamic pressure terms on stratified two-phase flow stability*, some additional high order terms were included in the two-fluid model set of four partial differential equations. The motivation behind the derivation of these high order terms was the thought that these terms could be used to improve the slug capturing ability of the two-fluid model.

Indeed, Issa and Kempf (2003) first showed that the two-fluid model was able to automatically capture the development of slugs from established stratified flow. However, as noted by Issa and Kempf and documented by Bonizzi (2002), this approach is limited to the well-posed region of stratified flow. As high order differential terms (such as surface tension or the terms derived in the fourth paper of this thesis) ensure that the problem remains constantly mathematically well-posed as a hyperbolic problem, it was believed worthwhile to investigate whether these terms could in practice have a beneficial effect on the slug initiation process.

Another important consideration is the wavelength of the perturbation responsible for slug initiation. In the absence of surface tension, linear stability analysis of the stratified two-fluid model predicts that in given flow conditions either all wavelengths will be unstable, or all wavelengths will be stable. When surface tension is included, linear stability analysis predicts that the "most dangerous wavelength" at the transition point, the one leading to slug initiation will be infinity. However, this is seldom observed experimentally and many experimentators such as Woods (1998), Fan et al. (1993) and Espedal (1998) report critical wavelengths ranging from 8 to 20 cm in small diameter pipes (refer to the fourth paper of this thesis for further description of these works).

As demonstrated in the fourth paper of this thesis, including some additional high order differential terms can theoretically change the "most dangerous wavelength" and shift it towards more physical lengths. It was then considered worth investigating if

in practice, in a slug capturing scheme, the addition of high order differential terms could have an influence on the wavelength leading to the transition.

C.2 The dynamic pressure terms

In the two-fluid model, the liquid momentum conservation equation can be written as:

$$\frac{\partial}{\partial t} (\rho_l A_l U_l) + \frac{\partial}{\partial x} (\rho_l A_l U_l^2) = -\tau_l S_l + \tau_i S_i - \rho_l g A_l \sin \beta + p_{il} \frac{\partial}{\partial x} A_l - \frac{\partial}{\partial x} (A_l P_l) \quad (\text{C.1})$$

where the pressure at the interface p_{il} is *a priori* distinct from the cross-sectional averaged pressure within the liquid phase P_l . In the fourth paper of this thesis the consideration of a transverse momentum balance instead of the usual hydrostatic approximation in the two-fluid model provided the following closure, after several drastic approximations:

$$p_{il} \frac{\partial}{\partial x} A_l - \frac{\partial}{\partial x} (A_l P_l) = -A_l \frac{\partial}{\partial x} p_{il} - I_1 - I_2 - I_3 \quad (\text{C.2})$$

Where the terms I_1 , I_2 and I_3 are defined as follows:

$$I_1 = \rho_l A_l \frac{\partial h_l}{\partial x} g \cos \beta \quad (\text{C.3})$$

$$I_2 = \rho_l A_l \frac{\partial h_l}{\partial x} \left[\frac{\partial}{\partial t} + U(x) \frac{\partial}{\partial x} \right]^2 (h_l) \quad (\text{C.4})$$

$$I_3 = -\rho_l h_l^2 A_l \eta \left[\frac{\partial}{\partial t} + U_l \frac{\partial}{\partial x} - \frac{\partial U_l}{\partial x} - \nu_l^* \frac{\partial^2}{\partial x^2} \right] \left(\frac{\partial^2}{\partial x^2} U_l \right) \quad (\text{C.5})$$

$$\eta = \frac{1}{2} \left[1 - \frac{1}{\pi} \frac{A}{A_l} \sin\left(\frac{\pi h_l}{4R}\right) \right] \quad (\text{C.6})$$

In the above expression of I_3 , ν_l^* represents a sort of turbulent dynamic viscosity, whose value is not easy to evaluate. The term I_1 is nothing but the hydrostatic term without which it was found that the two-fluid model was unconditionally ill-posed under all flow conditions (Ramshaw and Trapp, 1978). I_1 is therefore now included in all two-fluid model schemes. Replacing I_1 by its expression, the liquid momentum conservation equation then becomes:

$$\frac{\partial}{\partial t} (\rho_l A_l U_l) + \frac{\partial}{\partial x} (\rho_l A_l U_l^2) = \left(\begin{array}{c} -\tau_l S_l + \tau_i S_i - \rho_l g A_l \sin \beta - A_l \frac{\partial}{\partial x} p_{il} \\ -\rho_l A_l \frac{\partial h_l}{\partial x} g \cos \beta - I_2 - I_3 \end{array} \right) \quad (\text{C.7})$$

Compared to a standard two-fluid model, the high order differential terms I_2 and I_3 have been added.

C.3 Effect of the derived high order terms on slug initiation: a numerical experimentation

C.3.1 Scheme used

The scheme used for the simulation is based on the TRIOMPH code of Issa et al. (Issa and Kempf, 2003, Bonizzi and Issa, 2003). For the purpose of this experimentation a TRIOMPH code was thus re-constructed on the basis of the description made in Bonizzi (2002)¹.

C.3.2 Well-posed case (case 1)

Air-water flow was simulated in a horizontal one inch diameter pipe at atmospheric pressure. The length of the simulated pipe was taken equal to 2.5 m . The inlet gas superficial velocity was set to $U_g^S = 0.75 \text{ m.s}^{-1}$ and the inlet liquid superficial velocity was taken equal to $U_l^S = 0.5 \text{ m.s}^{-1}$. For the simulation, the interfacial friction factor λ_i was taken equal to the gas friction factor λ_g . The parameter ν_l^* was set to ν_l in the results presented. At these flow rates, steady stratified flow is extremely close to the ill-posedness limit (Inviscous Kelvin Helmholtz criterion) as shown in figure C.1 where case 1 is represented by a square, the ill-posedness limit is represented by a solid line and stratified flow stability is represented by an interrupted line. The simulation is started from established stratified flow. A cell length of 1 mm , and a time step of 0.1 ms were used for the simulations.

As no slug initiation was obtained initially, a punctual perturbation of very small amplitude was added. In a single section ($x = 0.5 \text{ m}$) and for a single time step ($t = 0.5 \text{ s}$) the gas-liquid friction was increased, giving a "kick" to the liquid velocity at this position.

This case was simulated twice, without the extra differential terms (case 1A) and with the extra terms (case 1B).

The results obtained without the additional terms are presented figure C.2 where the simulated holdup profiles are presented after 0.65 s , 0.7 s , 0.75 s , 0.8 s and 1 s .

¹This was done in good faith by following as much as possible the documentation available. However, as all the subtleties present in the TRIOMPH code might not have been fully described in Bonizzi (2002) and as the author of those lines might have overlooked some of the potentially missing details, no guaranty is given to the reader that the implementation of the two-fluid model effectively used for this numerical experiment is strictly equivalent to the original version of the TRIOMPH code. Moreover, the only objective of this numerical experimentation was to investigate the potential consequences of the use of the derived high order terms. Only the influence of the terms, i.e. the difference between the results obtained with and without the added terms is to be looked at.

A small perturbation can be noticed at the interface after 0.65 *s*. The perturbation grows and bridges the pipe after 0.7 *s*. The newly formed slug scoops the liquid in front of it and propagates quickly towards the exit of the pipe.

The results obtained with the derived high order terms (case 1B) are presented figure C.3. There is no significant difference between the results obtained in case 1A and in case 1B. After 0.7 *s* however, it appears that the slug is bigger in case 1B than it is in case 1A which suggests that slug initiation occurs faster with the additional terms.

In order to investigate the impact of the extra terms on the wavelength of the perturbation, a spatial Fourier analysis was performed on the holdup profiles after 0.55 *s*, 0.6 *s*, 0.65 *s*, 0.7 *s*, 0.75 *s* and 1 *s*. The results are presented figure C.4, which shows the obtained power spectrum as a function of the inverse of the wavelength (the contribution of the infinite wavelength has been taken out). The power spectrum obtained without the additional terms (case 1A) is shown as a solid line while the power spectrum obtained with the high order terms is shown as squares. After 0.55 *s* the dominant wavelength is $\lambda = 4$ *cm*, it seems to halve and reaches 2 *cm* after 0.65 *s*. Once the slug has been initiated (after time 0.75 *s* and 1 *s*), the power spectrum is dominated by very long wavelengths. Only after 0.7 *s* can we notice some difference between cases 1A and 1B: the power profile in case 1B is closer to what it is in the case of a slug. This is consistent with our observation that the additional high order terms led in this case to a somehow faster slug initiation.

C.3.3 Ill-posed case (case 2)

We still simulate an air-water flow within a horizontal one inch diameter pipe at atmospheric pressure. This time, the length of the pipe was taken equal to 20 *m*. The inlet water superficial velocity was set to $U_g^S = 2$ *m.s*⁻¹ and the inlet gas superficial velocity was taken equal to $U_l^S = 0.5$ *m.s*⁻¹. The simulation was started from steady state stratified flow. A cell length of 1 *cm*, and a time step of 1 *ms* were used. At those low velocities, the interface can be considered as smooth and the interfacial friction factor λ_i was taken equal to the gas friction factor λ_g . The simulated case is well over the ill-posedness limit (Inviscous Kelvin Helmholtz criterion) as shown in figure C.1 where case 2 is represented by a circle, the ill-posedness limit is represented by a solid line and stratified flow stability is represented by an interrupted line. The simulation is started from established stratified flow. In this case, slugging appeared naturally and it was not necessary to introduce any artificial perturbation.

The results obtained without the additional terms are presented in figure C.5 where the simulated holdup profiles are presented after 2.3 *s*, 2.4 *s*, 2.5 *s*, 2.6 *s* and 4 *s*. A small perturbation grows at the interface and bridges the pipe between 2.5 and 2.6 seconds after the start of the simulation. The newly formed slug grows very fast given the very high level of liquid in front of it and its length exceeds 5 meters, 4 seconds after the start of the simulation.

The results obtained with the derived high order terms are presented in figure C.6. The addition of the derived high order differential terms has not had any visible effect on the simulated holdup profiles.

In order to investigate further the impact of the extra terms on the wavelength of the perturbation leading to slug initiation, a spatial Fourier analysis was performed on the holdup profiles after 0.9 s, 1.3 s, 1.9 s, 2.4 s, 2.5 s and 2.9 s. The results are presented figure C.7, which shows the obtained power spectrum as a function of the inverse of the wavelength (the contribution of the infinite wavelength has been taken out). The power spectrum obtained without the additional terms is shown as a solid line while the power spectrum obtained with the high order terms is shown as squares. Very long waves are dominating at the beginning of the simulation, with 20 cm wavelength appearing after 1.9 s. The dominating wave seems to interact with its harmonics and after 2.5 s we can observe three peaks in the power spectrum, corresponding to the wavelengths 7, 14 and 40 cm.

Once the slug has been initiated the power spectrum is dominated by very long wavelengths. No difference whatsoever can be observed between case 2A (without the extra terms) and case 2B (with the extra terms).

C.4 Conclusions

The simulations performed with the help of a slug capturing scheme based on the two-fluid model showed that the high order differential terms derived in the fourth paper of this thesis did not have in practice the property to influence significantly the wavelength of the perturbation responsible for slug initiation. Several values were tried for ν_i^* , without more success.

Furthermore, it was observed in other simulations that the integration parameters (time step and grid size) could have a much bigger influence on the wavelength of the critical wave than the inclusion of the derived high order differential terms.

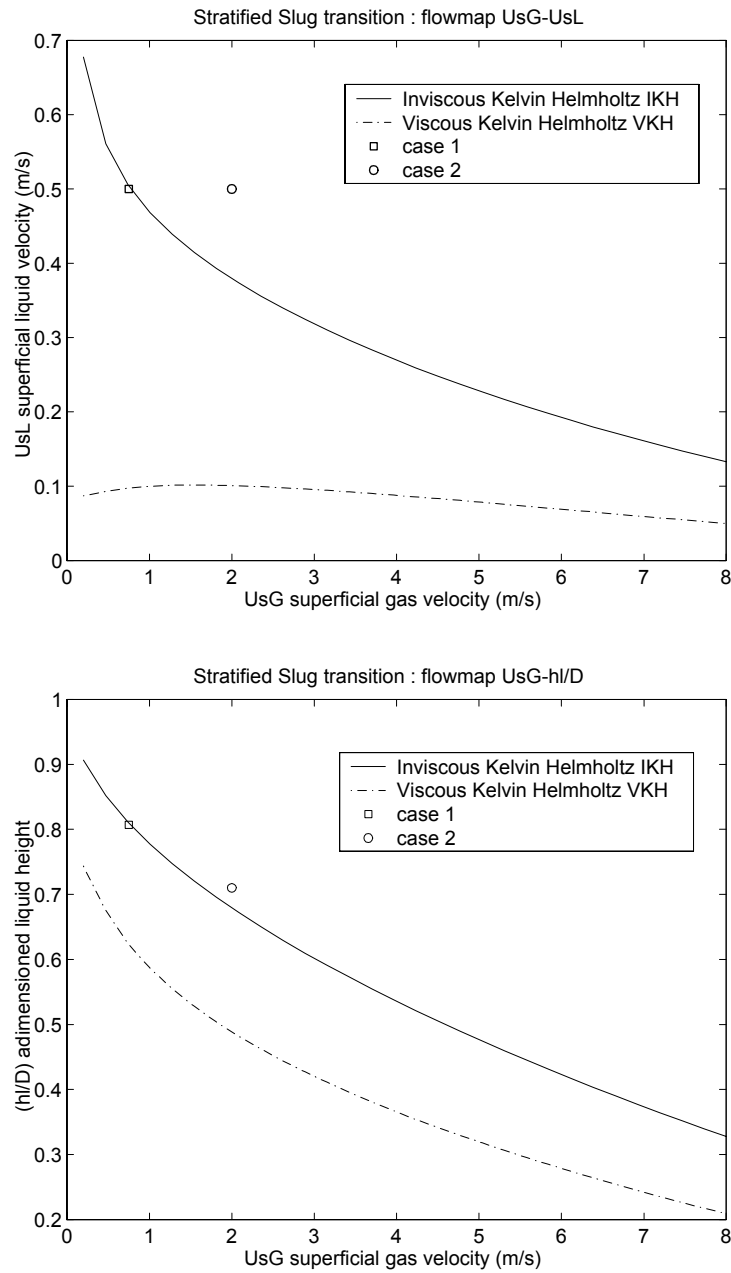


Figure C.1: Stratified-slug transition for an air-water flow in a one inch pipe

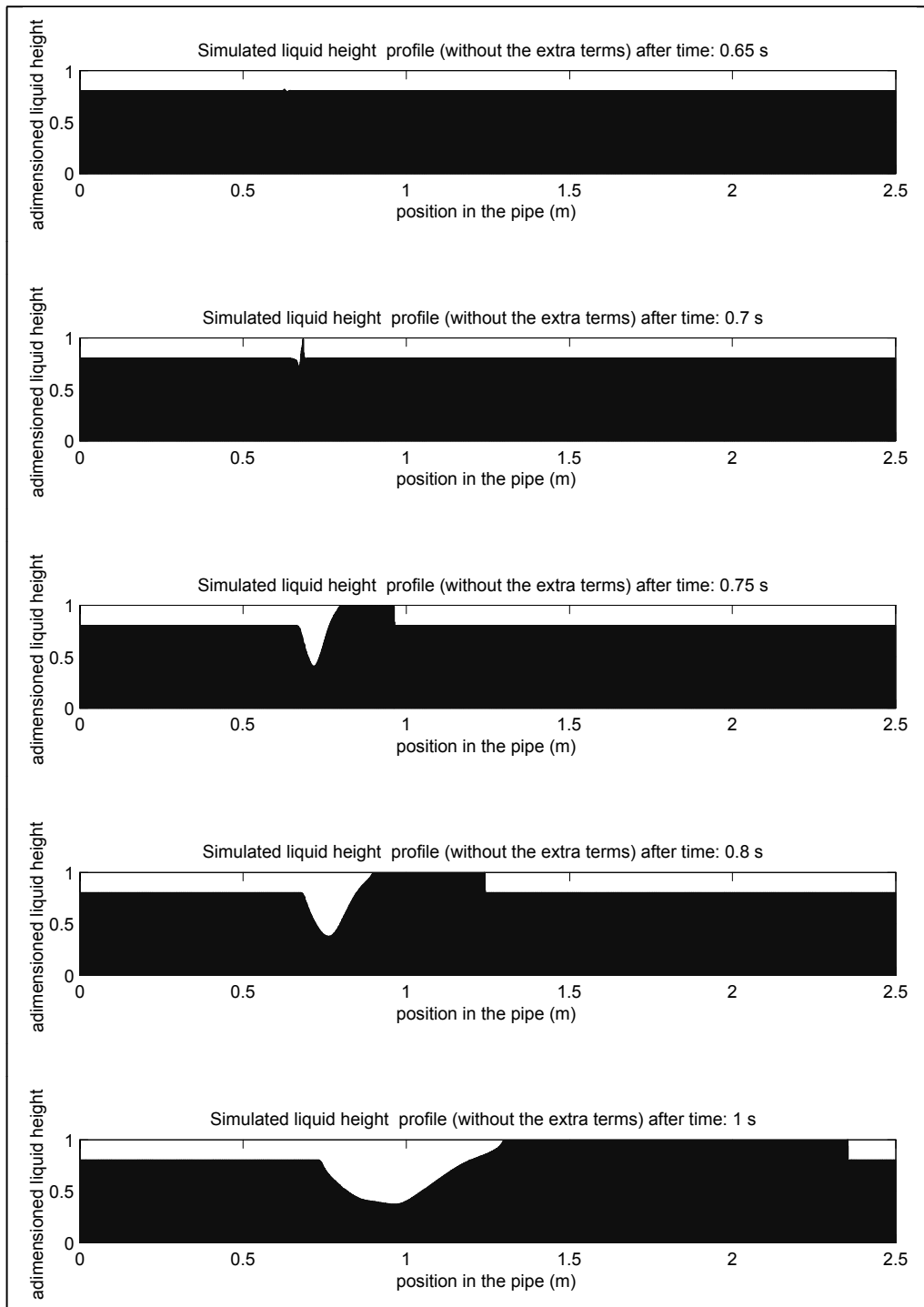


Figure C.2: Holdup profiles computed in the well-posed case, without the derived high order terms (Case 1A)

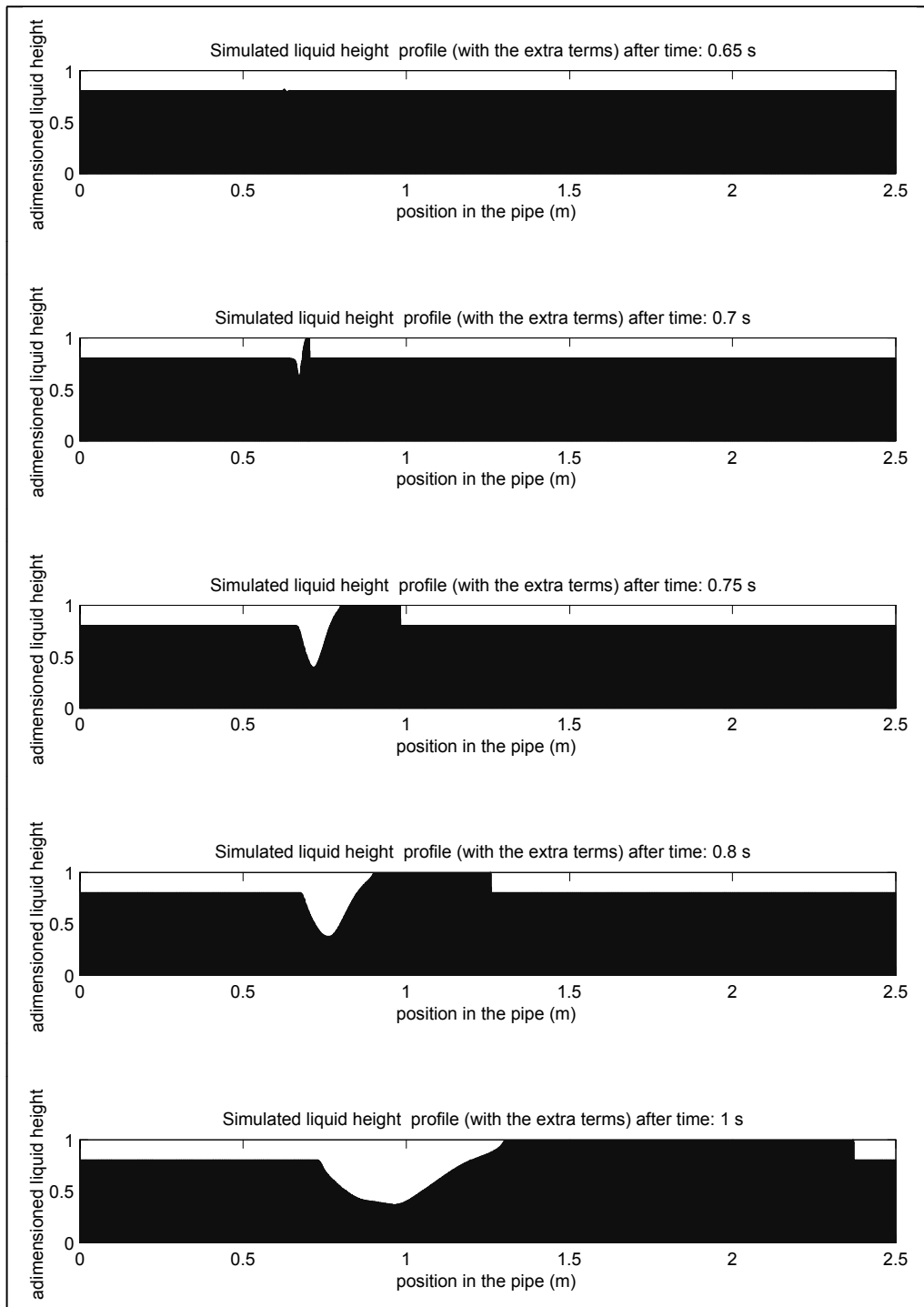


Figure C.3: Holdup profiles computed in the well-posed case, with the derived high order terms (Case 1B)

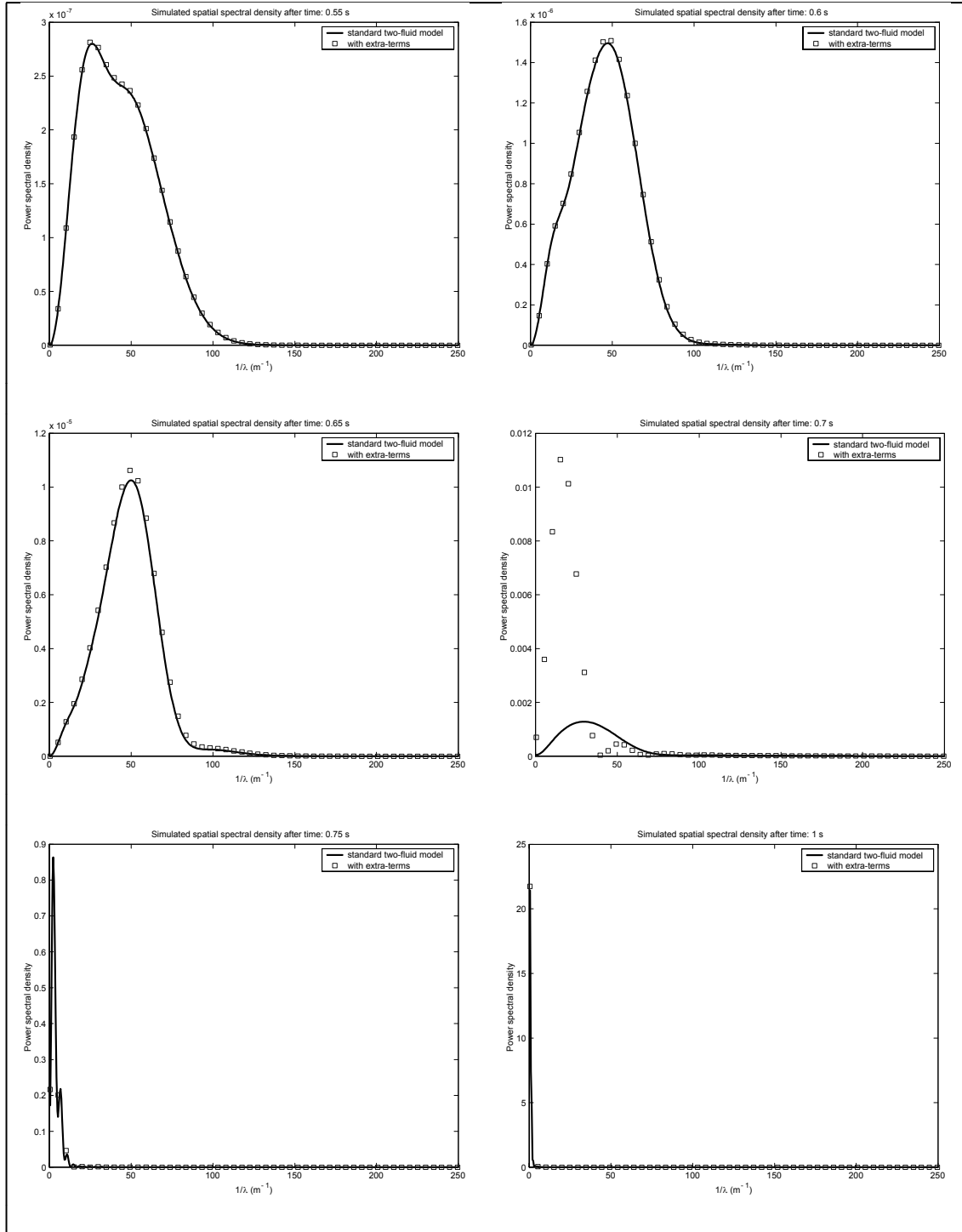


Figure C.4: Fourier analysis of the holdup profiles obtained in the well-posed case with (case 1B, shown as squares) and without (case 1A, shown as a solid line) the derived high-order differential terms

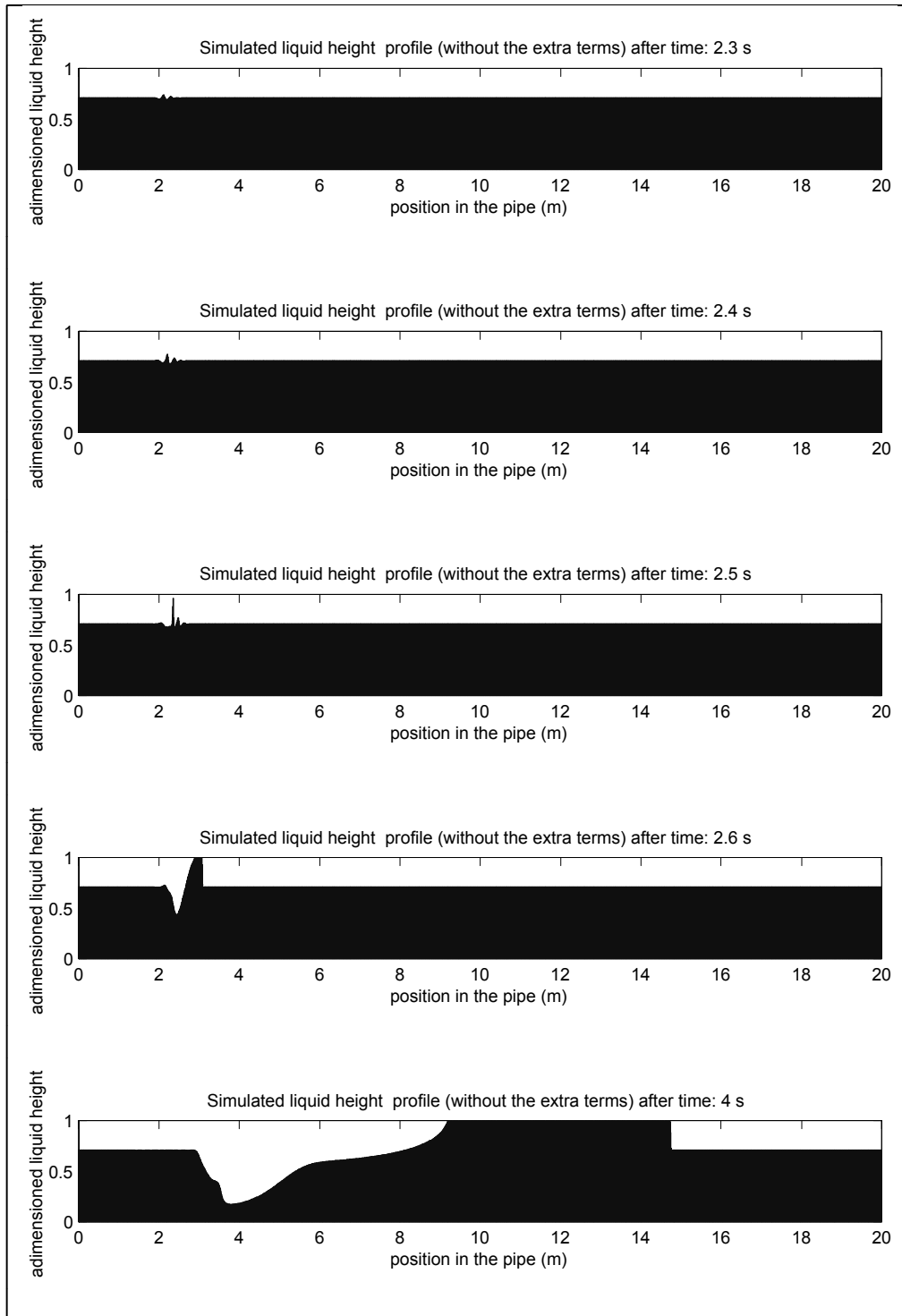


Figure C.5: Holdup profiles computed in the ill-posed case, without the derived high order terms (Case 2A)

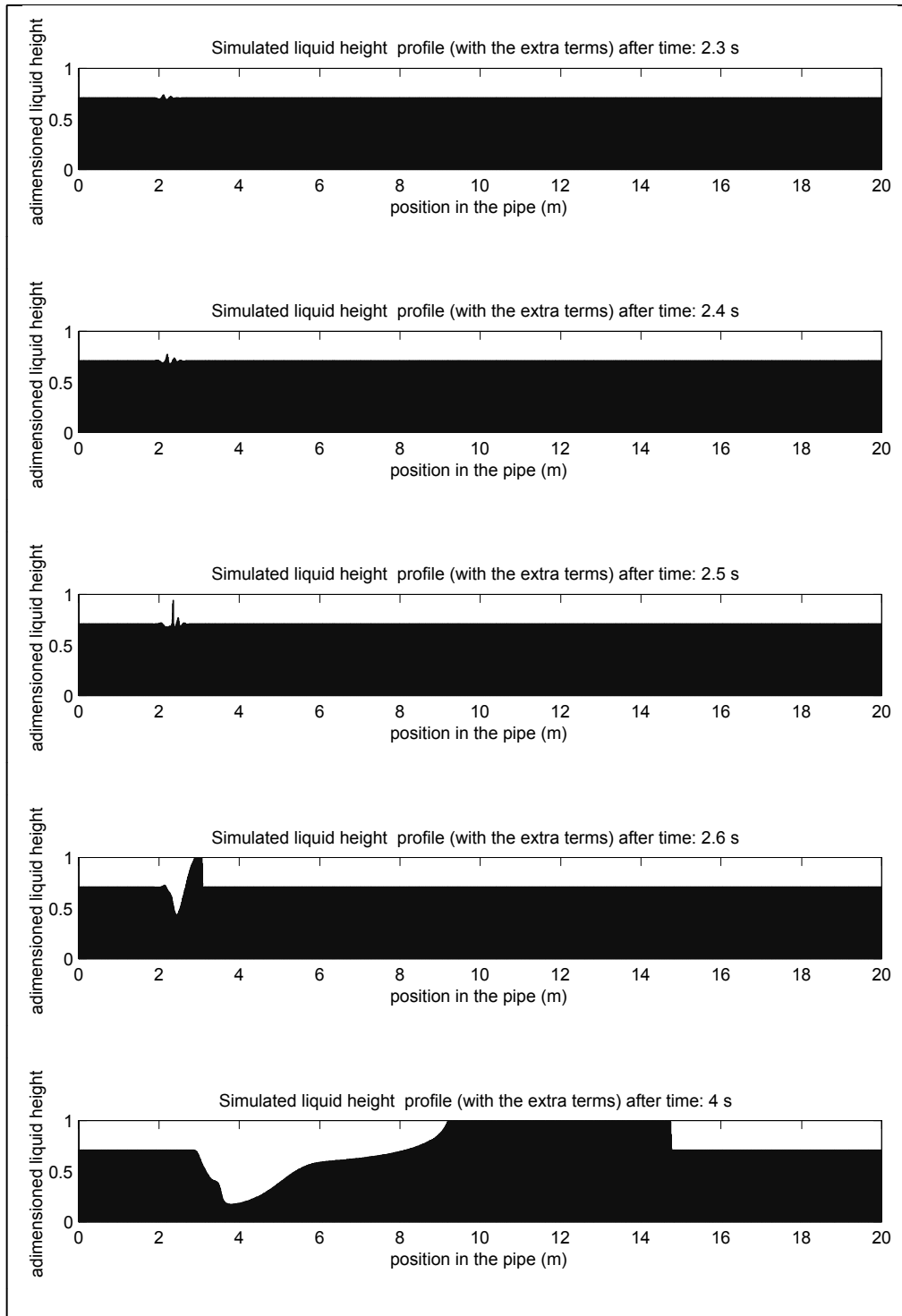


Figure C.6: Holdup profiles computed in the ill-posed case, with the derived high order terms (Case 2B)

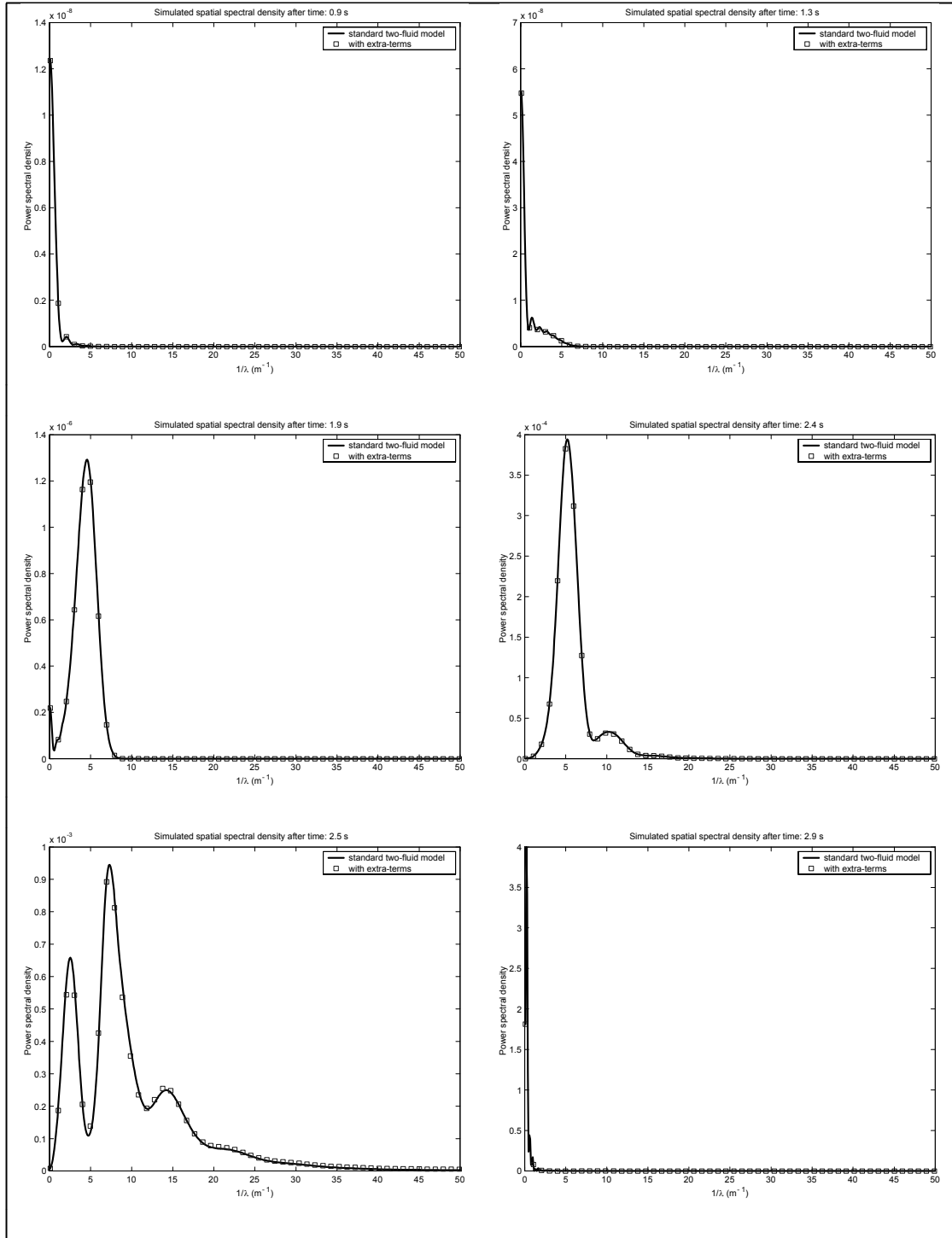


Figure C.7: Fourier analysis of the holdup profiles obtained in the ill-posed case with (case 2B, shown as squares) and without (case 2A, shown as a solid line) the derived high-order differential terms

Appendix D

Geometrical relations within the pipe

D.1 The geometrical variables of two-phase flow in a circular pipe

This very short appendix recalls the geometrical relations of interest in the field of two-phase flow modelling. The sketch presented figure D.1 shows a section of a circular pipe of radius R and introduces the liquid-wetted perimeter S_l , the gas-wetted perimeter S_g and the interfacial width S_i . The liquid holdup β is defined as the ratio between the liquid-occupied area A_l and the total pipe section area, while h_l is the liquid height from the bottom of the pipe to the liquid surface. The angle θ shown on the sketch is called the wetted half-angle. Finally D_{hl} and D_{hg} are respectively the liquid and gas hydraulic diameters.

D.2 Resolution of a pipe

Knowing the pipe radius and any one of the variables of interest is sufficient to calculate all the other relevant variables. Table D.1 shows how all variables can be explicitly determined from θ and $\frac{h_l}{R}$.

When only the holdup β is known, there is no available explicit exact expression providing the liquid height h_l or the half-wetted angle θ . The non-linear equation $\beta = \frac{1}{\pi} (\theta - \frac{1}{2} \sin 2\theta)$ can be solved for θ when β is known but as this task has to be performed a great number of times in a single simulation, an approximate explicit formula is often used instead. The following expression proposed by Biberg (1999), provides the half-wetted angle with a great accuracy and is used throughout the LASSI code:

$$\theta \approx \pi\beta + \left(\frac{3\pi}{2}\right)^{\frac{1}{3}} \left[1 - 2\beta + \beta^{\frac{1}{3}} - (1 - \beta)^{\frac{1}{3}}\right] \quad (\text{D.1})$$

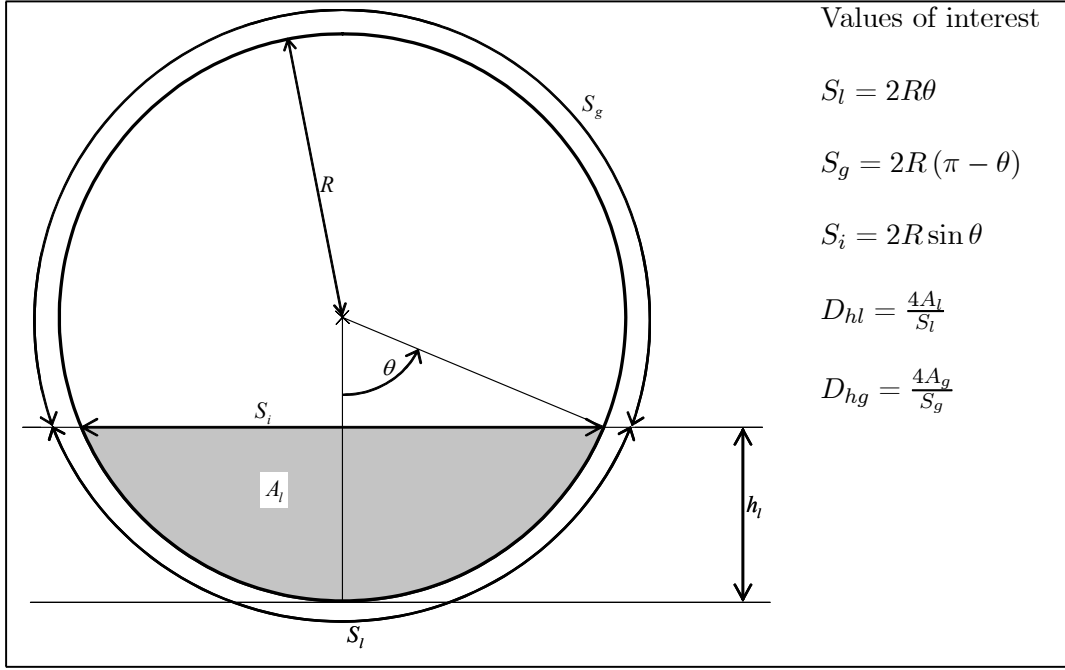


Figure D.1: Circular pipe geometry

In practice in the LASSI scheme, β is used as the primary variable, as conserving β is basically ensuring liquid mass conservation when the liquid is considered incompressible. As other variables are needed for the dynamics, such as for example $\frac{dA_l}{dh_l}$ (to evaluate the parameter κ) and S_l , S_g and S_i (to evaluate the action of the friction forces), Biberg's approximation is used, every section and every time step, to determine θ from β . The other variables are then derived from the relations presented in tables D.1 and D.1.

known variable: θ	known variable: $\frac{h_l}{R}$
$h_l = R(1 - \cos \theta)$	$\theta = \arccos\left(1 - \frac{h_l}{R}\right)$
$A_l = R^2\left(\theta - \frac{1}{2}\sin 2\theta\right)$	$A_l = R^2\left[\arccos\left(1 - \frac{h_l}{R}\right) - \left(1 - \frac{h_l}{R}\right)\sqrt{1 - \left(1 - \frac{h_l}{R}\right)^2}\right]$
$\beta = \frac{1}{\pi}\left(\theta - \frac{1}{2}\sin 2\theta\right)$	$\beta = \frac{1}{\pi}\left[\arccos\left(1 - \frac{h_l}{R}\right) - \left(1 - \frac{h_l}{R}\right)\sqrt{1 - \left(1 - \frac{h_l}{R}\right)^2}\right]$
$\frac{dA_l}{dh_l} = 2R \sin \theta$	$\frac{dA_l}{dh_l} = 2R\sqrt{1 - \left(1 - \frac{h_l}{R}\right)^2}$

Table D.1: Relations of interest in a circular pipe

First Paper

A simple slug capturing and slug tracking
scheme for gas-liquid pipe flow.
Part 1: Presentation of the scheme

Fabien Renault and Ole Jørgen Nydal

Preprint

A simple slug capturing and slug tracking scheme for gas-liquid pipe flow. Part 1: Presentation of the scheme

Fabien Renault ^{a,*} Ole-Jorgen Nydal ^b

^a*Department of Energy and Process Technology, University of NTNU, Trondheim, Norway*

^b*Department of Energy and Process Technology, University of NTNU, Trondheim, Norway*

Abstract

This paper presents an original slug capturing and slug tracking scheme, named LASSI (Lagrangian Approximate Scheme for Slug Initiation) for transient simulations of gas-liquid flow in pipes. The scheme is based on the two criteria that govern the transition from stratified to slug flow: the stratified stability criterion or Viscous Kelvin Helmholtz and the slug stability criterion or Minimum Holdup. The presented scheme is able to automatically capture the slug initiation phenomenon without the use of any closure, and to track the initiated slugs along the pipe, as they propagate according to Bendiksen's bubble nose velocity closure. The details of the scheme are presented and the scheme is successfully validated against experiments in its ability to predict the correct flowmap. In addition, a new derivation of the VKH criterion is presented, and some concerns regarding the modelling of the Bernoulli suction force with an upwind-differentiated two-fluid model are raised.

Key words: two-phase flow, two-fluid model, slug flow, slug initiation

1 Introduction

The study of gas-liquid flow in pipelines is of special importance for the transport of hydrocarbons in the oil industry and liquid-vapour mixture in power plants. Gas-liquid flow is characterized by the variety of flow patterns that can occur, depending on the gas and liquid flow rates as well as other physical

* Corresponding author: fabien.a.renault@ntnu.no

parameters such as the pipe inclination or the gas density. The list of possible flow patterns includes stratified flow where gas flows on top of a liquid layer and slug flow, an inherently unsteady flow regime where gas bubbles and liquid slugs alternately surge along the pipe. One of the greatest challenges of two-phase flow computations lies in the modelling of flow regime transitions, especially the transition between stratified and slug flow, because of its chaotic nature, and because of the great variety of slug initiation mechanisms. Slugs can indeed be initiated due to liquid accumulation at the low points of the pipe until the liquid bridges the pipe and forms a blockade which will either travel down the pipe as a slug or, if the upstream gas compressibility is high enough, form a severe slug, which can be seen as the most extreme case of slug flow. Another mechanism is the sometimes quite slow growth of small perturbations at the gas-liquid interface due to the hydrodynamic instability of stratified flow at those conditions. Fast variations of the gas velocity, due to operational transients or to system-dependent effects such as the departure of a previous slug, can also trigger slug initiation.

While some semi-empirical criteria such as the Taitel and Dukler (1976) criterion have long been proposed to predict slug initiation, one can doubt that a criterion-based approach could be able to cope with the most complicated pipe geometries or gas transient effects. More practically, the implementation of those criteria into standard transport models like the two-fluid model (which consists of one mass and one momentum conservation equation for each phase) is tedious and subject to some numerical difficulties. Moreover this approach requires further closures in addition to the transition criterion itself, like the initiation position and the initiation frequency. No matter how difficult it is, this criterion-based approach is necessary if the underlying code is not able to capture the physics of slug initiation.

It was indeed early seen that the two-fluid model, used in many industrial codes such as OLGA (Bendiksen et al., 1991) becomes ill-posed as a hyperbolic problem when the Bernoulli suction overcomes the hydrostatic force (Ramshaw and Trapp, 1978), raising doubts about the ability of such models to initiate slugs. However, it was also shown (Lin and Hanratty, 1986, Barnea and Taitel, 1993) that the linear stability analysis of the two-fluid model yielded a criterion, denoted as Viscous Kelvin Helmholtz or VKH that successfully predicts the transition from stable stratified flow to non-stratified flow (which can be roll waves regime or slug flow according to the conditions). Hence a faithful implementation of the two-fluid model (numerically stable whenever the two-fluid model is stable, and numerically unstable whenever the two-fluid model is unstable) can be expected to predict accurately this transition.

The other problem consists in the transport of the slugs after their initiation: as still grids diffuse the slug fronts dramatically, they seemed ill-suited for the modelling of hydrodynamic slugs which are typically in the order of ten diame-

ters long only. To overcome this problem, two different approaches have arisen: the "unit cell model", in which slugs are treated statistically by considering an average cell unit consisting of a bubble followed by a liquid slug (Bendiksen et al., 1996) and slug tracking schemes. In slug tracking schemes (Nydal and Banerjee, 1996, Taitel and Barnea, 2000), each individual slug is followed by a special moving grid, allowing its accurate transport along the pipe. However, those schemes cannot be considered as slug capturing schemes as slugs are "inserted" at an arbitrary location and with an arbitrary frequency whenever a transition criterion, such as the Taitel and Dukler criterion is fulfilled. Slug tracking schemes are often based on Bendiksen's correlation (Bendiksen, K.H., 1984) which links the bubble nose velocity to the mixture velocity within the slug. This correlation also provides a criterion for slug stability: liquid slugs die whenever their tail goes faster than their front, and survive otherwise. This criterion, denoted as the Minimum Holdup (MH) or slug stability criterion was shown to successfully predict transition from unstable stratified flow to slug flow (Ruder et al., 1989, Bendiksen and Espedal, 1992, Woods and Hanratty, 1996). Hence a gas-liquid transport code using Bendiksen's correlation as a closure can be expected to predict accurately this transition.

Issa and Kempf (2003) first demonstrated the ability of the two-fluid model to automatically capture the initiation of slugs and follow their development as they travel along the pipe. Slugs are not tracked by a special moving grid like in slug tracking schemes, but simply transported over a regular still grid. However, the use of a fine grid with an iterative code is computationally very demanding, which makes any field-scale application difficult. The aim of this paper is to present a non-iterative fast and robust slug capturing and slug tracking scheme. Slug initiations are automatically captured by the code without relying on any initiation criterion or parameter, other than the grid size or the time step. Once initiated, slugs are tracked as individual objects using Bendiksen's correlation in a way similar as in Nydal and Banerjee (1996). A Lagrangian approach is used throughout the whole scheme, and the implementation relies on object-oriented programming.

2 Transition criteria

2.1 Stratified flow stability: the Viscous Kelvin-Helmholtz criterion (VKH)

First introduced by Lin and Hanratty (1986) and Barnea and Taitel (1993), this criterion is based on the linear stability analysis of the two fluid-model which consists of the four equations (liquid mass conservation, gas mass conservation, liquid momentum conservation, gas momentum conservation) that follow:

$$\begin{aligned}
\frac{\partial}{\partial t} (\rho_l A_l) + \frac{\partial}{\partial x} (\rho_l A_l U_l) &= 0 \\
\frac{\partial}{\partial t} (\rho_g A_g) + \frac{\partial}{\partial x} (\rho_g A_g U_g) &= 0 \\
\frac{\partial}{\partial t} (\rho_l A_l U_l) + \frac{\partial}{\partial x} (\rho_l A_l U_l^2) &= -\tau_l S_l + \tau_i S_i - \rho_l g A_l \sin \phi - A_l \frac{\partial}{\partial x} p - \rho_l g A_l \cos \phi \frac{\partial}{\partial x} h_l \\
\frac{\partial}{\partial t} (\rho_g A_g U_g) + \frac{\partial}{\partial x} (\rho_g A_g U_g^2) &= -\tau_g S_g - \tau_i S_i - \rho_g g A_g \sin \phi - A_g \frac{\partial}{\partial x} p - \rho_g g A_g \cos \phi \frac{\partial}{\partial x} h_l
\end{aligned}$$

The subscripts l and g refer respectively to the liquid and gas phase. ρ , A and U are the density, occupied area and cross-area averaged velocity of the considered phase. τ_l is the liquid-wall friction, τ_g the gas-wall friction and τ_i the gas-liquid friction. S_l and S_g are the liquid-wetted and gas-wetted perimeter and S_i is the interfacial width. p is the pressure, h_l the liquid height and ϕ the angle between the pipe and the horizontal. Using the same notations as Barnea and Taitel, the equations are rewritten in a non-conservative form and the pressure gradient is eliminated from the two momentum balances to form a transient holdup equation. The system then becomes:

$$\begin{aligned}
(1) \quad \frac{\partial}{\partial t} h_l + H_l \frac{\partial U_l}{\partial x} + U_l \frac{\partial}{\partial x} h_l &= 0 \\
(2) \quad \frac{\partial}{\partial t} h_l - H_g \frac{\partial U_g}{\partial x} + U_g \frac{\partial}{\partial x} h_l &= 0 \\
(3) \quad \rho_l \frac{\partial U_l}{\partial t} - \rho_g \frac{\partial U_g}{\partial t} + \rho_l U_l \frac{\partial U_l}{\partial x} - \rho_g U_g \frac{\partial U_g}{\partial x} + (\rho_l - \rho_g) g \cos \phi \frac{\partial}{\partial x} h_l &= F
\end{aligned}$$

introducing $H_l = \frac{A_l}{\frac{dA_l}{dh_l}}$ the equivalent liquid height, $H_g = \frac{A_g}{\frac{dA_g}{dh_g}}$ the equivalent gas height and F the resultant volume force acting on the liquid phase, defined as:

$$F = -\frac{\tau_l S_l}{A_l} + \frac{\tau_g S_g}{A_g} + \tau_i S_i \left(\frac{1}{A_l} + \frac{1}{A_g} \right) - (\rho_l - \rho_g) g \sin \phi$$

Starting from equilibrium (all time derivatives and all spatial derivatives but the one of the pressure are null), we introduce a small sinusoidal perturbation of pulsation ω , wave number k and amplitudes (\tilde{h}_l , \tilde{U}_l , \tilde{U}_g) in the flow variables around the equilibrium values (\bar{h}_l , \bar{U}_l , \bar{U}_g):

$$h_l = \bar{h}_l + \tilde{h}_l e^{i(\omega t - kx)} \quad U_l = \bar{U}_l + \tilde{U}_l e^{i(\omega t - kx)} \quad U_g = \bar{U}_g + \tilde{U}_g e^{i(\omega t - kx)}$$

Reporting in the first equation (liquid conservation) yields:

$$\tilde{U}_l = \left[\frac{\omega}{k} - \bar{U}_l \right] \frac{\tilde{h}_l}{\bar{H}_l}$$

While the second equation (gas conservation) gives:

$$\tilde{U}_g = \left[\bar{U}_g - \frac{\omega}{k} \right] \frac{\tilde{h}_l}{\bar{H}_g}$$

The source term F is a function of 3 variables (the holdup $\beta = \frac{A_l}{A}$, the liquid local superficial velocity $U_l^S = \beta U_l$ and the gas local superficial velocity $U_g^S = (1 - \beta) U_g$). Hence

$$\tilde{F} = \left(\frac{\partial F}{\partial \beta} \right)_{U_l^S, U_g^S} \tilde{\beta} + \left(\frac{\partial F}{\partial U_l^S} \right)_{\beta, U_g^S} \widetilde{U}_l^S + \left(\frac{\partial F}{\partial U_g^S} \right)_{\beta, U_l^S} \widetilde{U}_g^S$$

Reporting the values of \widetilde{U}_l , \widetilde{U}_g and \tilde{F} inside the third equation (dynamic holdup equation) provides the dispersion equation

$$\omega^2 - 2[ak - ib]\omega + ck^2 - iek = 0$$

Introducing the following Barnea and Taitel's (1993) notations:

$$\begin{aligned} \rho &= \frac{\rho_l}{\beta} + \frac{\rho_g}{\alpha} \\ a &= \frac{1}{\rho} \left(\frac{\rho_l \overline{U}_l}{\beta} + \frac{\rho_g \overline{U}_g}{\alpha} \right) \\ b &= \frac{1}{2\rho} \left[\left(\frac{\partial F}{\partial U_l^S} \right)_{\beta, U_g^S} - \left(\frac{\partial F}{\partial U_g^S} \right)_{\beta, U_l^S} \right] \\ c &= \frac{1}{\rho} \left[\frac{\rho_l \overline{U}_l^2}{\beta} + \frac{\rho_g \overline{U}_g^2}{\alpha} - (\rho_l - \rho_g) g \cos \phi \frac{\overline{H}_l}{\alpha} \right] \\ e &= -\frac{1}{\rho} \left(\frac{\partial F}{\partial \beta} \right)_{U_l^S, U_g^S} \end{aligned}$$

The dispersion equation is a second degree complex equation in ω . The model will predict that stratified flow is stable if both roots of this equation have a negative imaginary part. We can find the neutral stability condition ($\omega_i = 0$) by letting $\omega = \omega_R + i\omega_i = \omega_R$ in the dispersion equation. We can then calculate the wave velocity C_F :

$$C_F = \frac{\omega}{k} = \frac{e}{2b} = -\frac{\left(\frac{\partial F}{\partial \beta} \right)_{U_l^S, U_g^S}}{\left[\left(\frac{\partial F}{\partial U_l^S} \right)_{\beta, U_g^S} - \left(\frac{\partial F}{\partial U_g^S} \right)_{\beta, U_l^S} \right]}$$

The stability criterion is then:

$$(C_F - a)^2 + (c - a^2) < 0$$

Based on the linear stability analysis of a perfectly smooth stratified flow, this simple criterion gives a hint at whether or not, smooth stratified flow is a possible solution. As a consequence, an unstable VKH criterion does only mean that a smooth stratified flow regime can not be established, and does not necessarily mean that slug flow can be established at those conditions. Clearly, a roll waves solution or an unsteady pseudo-slug regime are also possible solutions.

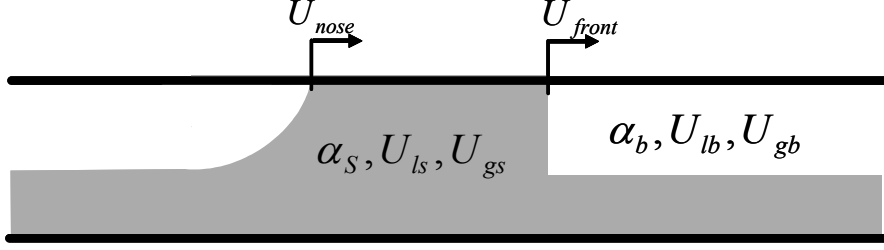


Fig. 1. Minimum Holdup criterion: sketch of a slug unit

2.2 Slug flow stability: the Minimum Holdup criterion (MH)

First Ruder et al. (1989), then Bendiksen and Espedal (1992) followed by Woods and Hanratty (1996) developed a criterion based this time on slug stability. The idea is to consider slug flow as a succession of slug units as the one shown figure 1, consisting of a slug region followed by a bubble region where the flow is stratified. α_S , U_{ls} and U_{gs} are respectively the void fraction, liquid velocity and gas velocity within the slug, and α_b , U_{lb} and U_{gb} are respectively the void fraction, liquid velocity and gas velocity within the bubble. U_{nose} and U_{front} are the bubble nose (or slug tail) velocity and the slug front velocity.

Steady state slug flow, defined by its inlet superficial velocities U_l^S and U_g^S , is at neutral stability ($U_{nose} = U_{front}$) a system characterized by seven unknowns (α_S , U_{ls} , U_{gs} , α_b , U_{lb} , U_{gb} , U_{nose}).

- (1) The void in slug α_S can be determined by experimental closure laws.
- (2) The slip velocity within the slug $U_{gs} - U_{ls}$ can be determined by experimental closure laws.
- (3) Volume conservation ensures that $U_m = U_l^S + U_g^S = (1 - \alpha_S)U_{ls} + \alpha_S U_{gs}$
- (4) Bendiksen's closure law can be used for the bubble nose velocity, hence providing the relation $U_{nose} = C_0 U_m + \nu_0$ where C_0 and ν_0 are known.
- (5) Liquid conservation across the front gives $U_{front} = \frac{(1 - \alpha_S)U_{ls} - (1 - \alpha_b)U_{lb}}{\alpha_b - \alpha_S}$
- (6) Gas conservation across the front gives $U_{front} = \frac{\alpha_S U_{gs} - \alpha_b U_{gb}}{\alpha_S - \alpha_b}$
- (7) A momentum balance in the bubble yields $F(\alpha_b, U_{lb}, U_{gb}) = 0$

This set of equations can be solved iteratively but provides a physical solution (with a positive slug fraction) only as long as the predicted average holdup within the slug unit (slug and bubble region) is below the one in plain stratified flow. Hence this criterion is usually labelled as the Minimum Holdup criterion, for it predicts the prevalence of the flow regime with the lower holdup. It is important to stress out that this criterion only answers the question of whether or not an already initiated slug will survive (in other terms will U_{front} exceeds U_{nose} ?). Should the answer be yes, it does not necessarily mean that slug flow will be the established flow regime within the pipe, for this criterion says

nothing about slug initiation. Should the answer be no, stratified flow is not the unique possibility, a roll waves or pseudo-slug regime can also arise.

2.3 Interest of a slug capturing/tracking scheme

The literature clearly stresses the importance of both the Viscous Kelvin-Helmholtz and the Minimum Holdup criteria. The VKH criterion dominates the transition from stratified to slug flow for low pressure systems with moderate velocities. For high pressure systems, the Minimum Holdup criterion defines the transition.

More recently, more complex effects have been shown, clearly demonstrating the role of each of those criteria. When stratified flow is present at the inlet of the pipe, the flow regime will remain stratified along the pipe as long as the flow is stable according to the VKH criterion. However, if slug flow is to be present at the inlet, then slug flow will remain the established flow regime all along the pipe if the flow is stable according to the MH criterion (Kristiansen, 2004). This defines a "hysteresis zone" in the traditional $(U_t^S - U_g^S)$ flowmap: in this area the flow regime is dependent on both the spatial and time history of the flow. This phenomenon clearly shows the interest of transient slug tracking schemes in opposition to steady-state or statistical approaches.

For high pressures and high velocities, there is an area where both criteria predict instability. As observed experimentally, this zone corresponds to roll waves and unstable flow (neither stratified nor slug flow). Figure 2, shows an indicative computed numerical flowmap corresponding to an horizontal 1 inch pipe with an air-water flow at 10 bars.

3 Structure of the scheme

3.1 Principle

The objective is to create a simple and fast transient two-phase code that would use the presented criteria (VKH and MH) to automatically initiate and track each individual slug within the pipe. The code is both "slug capturing" (the slugs are automatically initiated in the sense that they occur naturally as liquid blockades), and "slug tracking" because each slug is then followed by the mean of a moving grid, preventing numerical diffusion. The presented scheme, called LASSI (Lagrangian Approximate Scheme for Slug Initiation) can be seen as an intermediary between an usual two-fluid model where the

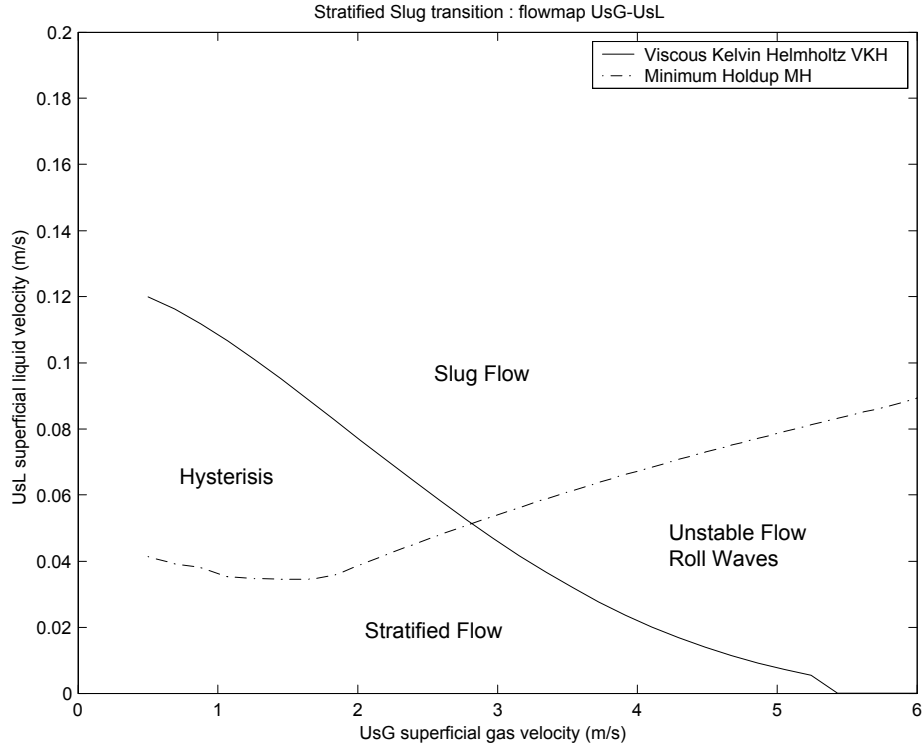


Fig. 2. Numerical flowmap showing the VKH and MH criteria

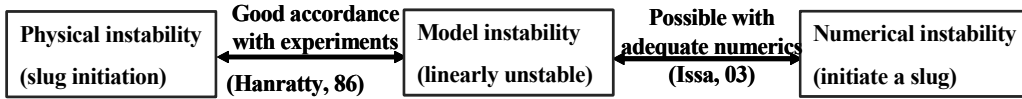


Fig. 3. Slug initiation principle in the LASSI scheme.

equations are solved in full (OLGA in Bendiksen et al., 1991, TRIOMPH in Issa et al., 2003) and a more simplified slug tracking scheme (SLUGGIT in Nydal et al., 1996). As in SLUGGIT and other slug tracking schemes, Bendiksen's closure law is used to calculate the bubble nose velocity, and a simplified "step front" model is used to depict the behaviour of slug fronts, using the same relations that are used in the Minimum Holdup criterion. However a simplified two-fluid model, the very basis of the VKH criterion, is used to compute the evolution of the flow within the bubble regions, which allows the scheme to automatically initiate the slugs according to the stratified stability criterion. Figure 3 explains the idea behind slug capturing based on the two fluid-model.

Although it is fully possible to use a gas entrainment model into the liquid slugs, the present paper will only treat the unaerated slugs case, for the sake of simplicity. The liquid is always considered incompressible, while the gas compressibility is determined using a simple gas law.

3.2 A Shortcoming of upwind schemes

Solving the two-fluid model in full is relatively complex and becomes computationally expensive for the small section sizes required to have slug capturing. Some simplified models (Taitel et al., 1997, Nydal, 1996) have been proposed but they can not be used for slug capturing for their area of stability is different from the one of the original two-fluid model. When it comes to slug capturing methods, the first published code TRIOMPH (Issa et al., 2003) solves the two-fluid model in an iterative manner and is thus very time-consuming. Furthermore, all the two-fluid codes relying on the upwind method of differentiation face the problem explained below.

α and β are the gas and liquid volume fraction. A staggered grid as used in OLGA or TRIOMPH is shown in figure 4.

The gas mass conservation equation $\frac{\partial}{\partial t}(\rho_g \alpha) + \frac{\partial}{\partial x}(\rho_g \alpha U_g) = 0$ is discretised as:

$$\frac{\delta x}{\delta t} (\rho_{g,J}^{n+1} \alpha_J^{n+1} - \rho_{g,J}^n \alpha_J^n) + (\widehat{\rho}_{g,j+1}^{n+1} \widehat{\alpha}_{j+1}^{n+1} U_{g,j+1}^{n+1} - \widehat{\rho}_{g,j}^{n+1} \widehat{\alpha}_j^{n+1} U_{g,j}^{n+1}) = 0$$

where the upwinded values $\widehat{\alpha}_j$ and $\widehat{\rho}_{g,j}$ are defined by the relation:

$$\widehat{\alpha}_j = \alpha_{J-1} \text{ if } U_{g,j} > 0, \quad \alpha_J \text{ if } U_{g,j} < 0$$

Assuming steady-state and positive velocities, the upwind-differentiated gas mass conservation equation in the J mass control volume gives:

$$\rho_{g,J+1} \alpha_{g,J+1} U_{g,j+2} = \rho_{g,J} \alpha_{g,J} U_{g,j+1} = \rho_{g,J-1} \alpha_{g,J-1} U_{g,j} = \rho_g U_g^S$$

Then, at steady state, neglecting the friction forces, the upwind-differentiated gas momentum conservation equation in the j momentum control volume gives:

$$\widetilde{\rho_g \alpha U}_{g,J} U_{g,j} = \widetilde{\rho_g \alpha U}_{g,J-1} U_{g,j-1} - \widetilde{\alpha}_j (p_J - p_{J-1})$$

with $\widetilde{\rho_g \alpha U}_{g,J} = \frac{1}{2} (\widehat{\rho}_{g,j} \widehat{\alpha}_j U_j + \widehat{\rho}_{g,j+1} \widehat{\alpha}_{j+1} U_{j+1}) = \rho_g U_g^S = \widetilde{\rho_g \alpha U}_{g,J-1}$
and $\widetilde{\alpha}_j = \frac{1}{2} (\alpha_J + \alpha_{J-1})$. We can then deduct $p_J = p_{J-1}$ as $U_{g,j} = U_{g,j-1}$

Now, under the same assumptions, the gas momentum conservation in the $j+1$ momentum control volume yields:

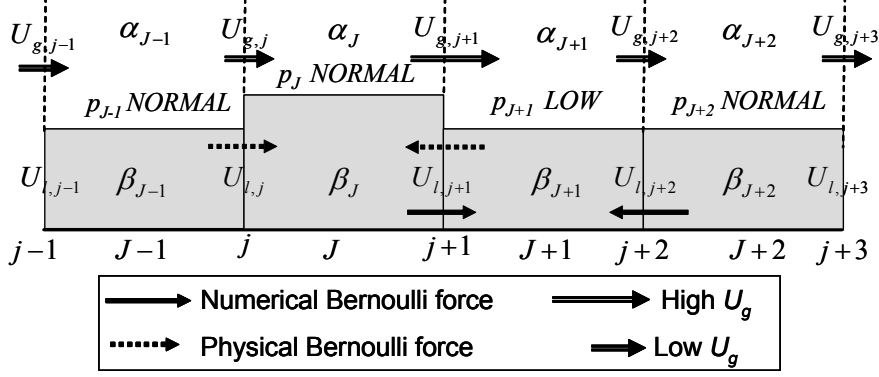


Fig. 4. Bernoulli effect with an upwind-differentiated scheme

$$\widetilde{\rho_g \alpha_g U_{g,J+1} U_{g,j+1}} = \widetilde{\rho_g \alpha_g U_{g,J} U_{g,j}} - \tilde{\alpha}_{g,j+1} (p_{J+1} - p_J)$$

$$\text{or } \rho_g U_g^S U_{g,j+1} = \rho_g U_g^S U_{g,j} - \tilde{\alpha}_{g,j+1} (p_{J+1} - p_J)$$

so $p_{J+1} < p_J$ because $U_{g,j+1} > U_{g,j}$

The consequence is that the decrease in pressure that comes with the increase of the gas velocity due to the bump, appears numerically in the next grid cell, and not in the grid cell where the bump actually is. The Bernoulli effect, which normally "sucks" the liquid towards the bump, will then "suck" the liquid towards the next grid cell, as shown by the arrows in figure 4. Though this may not be a problem for sufficiently long waves, the fact that the hydrostatic force, which tends to kill the bump, and the Bernoulli effect which tends to make it grow, are not in phase might have an influence on the transition process, especially in its last time steps, when the holdup in the bump has reached the critical value when the Bernoulli force overtakes the hydrostatic force.

3.3 Simplification of the two-fluid model

As the competition between the hydrostatic force and the Bernoulli suction force is, together with the destabilizing effect of the friction forces, the key to the slug initiation mechanism, one can think of a scheme where the Bernoulli effect would be treated like the hydrostatic force, as a force acting directly on the liquid momentum equation, independently of the gas dynamics.

Combining the gas and liquid momentum equations yields:

$$\frac{1}{\beta} \left[\frac{\partial}{\partial t} (\beta U_l) + \frac{\partial}{\partial x} (\beta U_l^2) \right] = \frac{1}{\alpha \rho_l} \left(\frac{\partial}{\partial t} (\alpha \rho_g U_g) + \frac{\partial}{\partial x} (\alpha \rho_g U_g^2) \right) + \frac{1}{\rho_l} F - \frac{\rho_l - \rho_g}{\rho_l} g \cos \phi \frac{\partial}{\partial x} h_l$$

Under the assumption that the local gas density ρ_g is slowly varying in space

and time:

$$\frac{1}{\alpha \rho_l} \left(\frac{\partial}{\partial t} (\alpha \rho_g U_g) + \frac{\partial}{\partial x} (\alpha \rho_g U_g^2) \right) \approx \frac{1}{\alpha} \frac{\rho_g}{\rho_l} \left[\frac{\partial}{\partial t} (U_g^S) + \frac{\partial}{\partial x} \left(\frac{1}{\alpha} (U_g^S)^2 \right) \right]$$

If we neglect the term in $\frac{\partial}{\partial t} (U_m)$ and use the liquid mass conservation equation $\frac{\partial}{\partial t} \beta + \frac{\partial}{\partial x} (\beta U_l) = 0$, developing $\frac{\partial}{\partial t} (U_g^S)$ gives:

$$\frac{\partial}{\partial t} (U_g^S) \approx -\frac{\partial}{\partial t} (\beta U_l) \approx -\beta \frac{\partial}{\partial t} U_l + U_l \frac{\partial}{\partial x} (\beta U_l)$$

Neglecting the term in $2U_g \frac{\partial}{\partial x} (U_m)$ we obtain:

$$\frac{\partial}{\partial x} \left(\frac{1}{\alpha} (U_g^S)^2 \right) \approx (U_g)^2 \frac{\partial}{\partial x} (\beta) - 2U_g \frac{\partial}{\partial x} (\beta U_l)$$

Then replacing the expression for:

$$\left[\frac{\partial}{\partial t} (U_g^S) + \frac{\partial}{\partial x} \left(\frac{1}{\alpha} (U_g^S)^2 \right) \right] \approx (U_g - U_l)^2 \frac{\partial}{\partial x} (\beta) - \beta \frac{\partial}{\partial t} U_l + \beta (U_l - 2U_g) \frac{\partial}{\partial x} (U_l)$$

into the combined gas and liquid momentum equation provides the relation:

$$\frac{\partial}{\partial t} (\beta U_l) + \frac{\partial}{\partial x} (\beta U_l^2) = \left[\frac{\beta \rho_g}{\alpha \rho_l} (U_g - U_l)^2 - \frac{\rho_l - \rho_g}{\rho_l} g \cos \phi \frac{A_l}{dh_l} \right] \frac{\partial}{\partial x} (\beta) + \frac{\beta}{\rho_l} F + \frac{\beta \rho_g}{\alpha \rho_l} \left[-\beta \frac{\partial}{\partial t} U_l + \beta (U_l - 2U_g) \frac{\partial}{\partial x} (U_l) \right]$$

Under the assumption that $\rho_l U_l \gg \rho_g U_g$ the terms in $\frac{\partial}{\partial t} U_l$ and $\frac{\partial}{\partial x} (U_l)$ in the right-hand side can be neglected compared to the left hand-side, hence yielding:

$$\frac{\partial}{\partial t} (\beta U_l) + \frac{\partial}{\partial x} (\beta U_l^2) \approx -\kappa \beta \frac{\partial}{\partial x} (\beta) + \frac{\beta}{\rho_l} F$$

with:

$$\kappa = \frac{\rho_l - \rho_g}{\rho_l} g \cos \phi \frac{A}{dh_l} - \frac{1}{\alpha} \frac{\rho_g}{\rho_l} (U_g - U_l)^2$$

Under the reasonable assumptions that U_m and ρ_g (both constants in incompressible flows) are only slowly varying in time and space and that $\rho_l U_l \gg \rho_g U_g$ the liquid momentum equation can be uncoupled from the gas momentum equation to yield a modified shallow-water equation in which a Bernoulli suction term $\frac{1}{\alpha} \frac{\rho_g}{\rho_l} (U_g - U_l)^2$ is subtracted from the traditional hydrostatic term

$\frac{\rho_l - \rho_g}{\rho_l} g \cos \phi \frac{A}{dh_l}$. It is important to note that the simplified system:

$$\frac{\partial}{\partial t} (\beta) + \frac{\partial}{\partial x} (\beta U_l) = 0$$

$$\frac{\partial}{\partial t} (\beta U_l) + \frac{\partial}{\partial x} \left(\beta U_l^2 + \frac{1}{2} \kappa \beta^2 \right) = \frac{\beta}{\rho_l} F(U_l, \beta, U_g^S)$$

has the same area of well-posedness as the full two-fluid model and becomes ill-posed when the coefficient κ becomes negative. The well-posedness condition yields the well-known Inviscid Kelvin-Helmholtz (IKH) criterion:

$$\text{well-posed} \Leftrightarrow (U_g - U_l)^2 < \frac{\rho_l - \rho_g}{\rho_g} g \cos \phi \frac{A_g}{dh_l} \Leftrightarrow \kappa > 0$$

The fact that the two-fluid model becomes ill-posed as a hyperbolic problem when this criterion is no longer fulfilled has long raised concerns among authors in the literature (Ramshaw and Trapp, 1978). However it is clear that, as stated by Issa et al. (2003) and Taitel and Barnea (1995), the initiation process relies also on the destabilizing effect of the friction forces, and that ill-posedness is not a requirement for slug initiation. As it is theoretically impossible to solve an ill-posed problem and as ill-posedness presents numerical problems in practice (Bonizzi, 2002), the approach proposed in this article is to simply prevent κ from becoming negative by assigning it a strictly positive minimum value.

3.4 Solving Procedure

Figure 5 shows LASSI's solving procedure. The grid used is shown in figure 6. The pipe is divided in grid cells, which are either *sections* or *slugs* according to whether or not the liquid bridges the pipe within them. The first step is the Pressure-Momentum implicit computation where the pressure p and the gas superficial velocity U_g^S within the *sections* and the mixture velocity U_m within the *slugs* are calculated implicitly, using a simple and fast tridiagonal algorithm detailed later. Using the bubble turning criterion to be explained in the following pages, the nature of each of the *section-slug* and *slug-section* is set to either Front or Nose.

Using the newly determined local mixture velocity, the liquid velocity within the section J is then updated with the relation:

$$U_{l,J}^{n+1/2} = U_{l,J}^n + \frac{\delta t}{\rho_l} F(\beta_J^n, U_{l,J}^n, U_{m,J}^{n+1})$$

In the void wave step, liquid mass and momentum fluxes are evaluated using a Lagrangian modified shallow water scheme, hence for each *section* β_J^{n+1} , $U_{l,J}^{n+1}$ as well as the *section* border velocities are calculated from $(\beta_J^n, U_{l,J}^{n+1/2})$, $(\beta_{J-1}^n, U_{l,J-1}^{n+1/2})$ and $(\beta_{J+1}^n, U_{l,J+1}^{n+1/2})$. For *section–slug* and *slug–section* borders, Bendiksen’s correlation is used when the border has been detected a bubble nose, while an iterative steep front model (which allows the slug to "eat" completely several sections in a single time step, while ensuring liquid mass conservation) is used if a front has been detected.

Since the length of the *sections* is varying, some list management is needed, in order to prevent the appearance of very large or very short *sections*. List management is invoked a first time in the void wave step when the CFL criterion is checked: if the fast wave from the left border of a section is able to take over the slow wave from the right border of this section in a time inferior to the chosen time step, than this section is merged with one of its neighbours. If this happens, the border velocities and liquid fluxes are recalculated between the newly merged *section* and its neighbours. Finally, list management also occurs when a *section* that has exceeded a critical length, has to be cut in two.

3.5 Pressure-Momentum Step

This paragraph presents the details of the pressure-momentum step used in LASSI.

3.5.1 Gas Mass conservation

Considering gas mass conservation within the pressure control volume j provides the relation:

$$V_{g,j} \frac{d\rho_{g,j}}{dt} = \frac{dm_{g,j}}{dt} - \rho_{g,j} \frac{dV_{g,j}}{dt}$$

where $V_{g,j}$ and $m_{g,j}$ are respectively the gas volume and the gas mass within the control volume j , and $\rho_{g,j}$ is the gas density at this control volume.

We then have : $\frac{dm_{g,j}}{dt} = (\rho_g U_g^S)_{J-1} - (\rho_g U_g^S)_J - \alpha_{J-1} \rho_{g,J-1} U_{b,J-1} + \alpha_J \rho_{g,J} U_{b,J}$ and $\frac{dV_{g,j}}{dt} = \alpha_J U_{b,J} - \alpha_{J-1} U_{b,J-1} + \beta_J U_{l,J} - \beta_{J-1} U_{l,J-1}$ where $U_{b,J}$ is the velocity

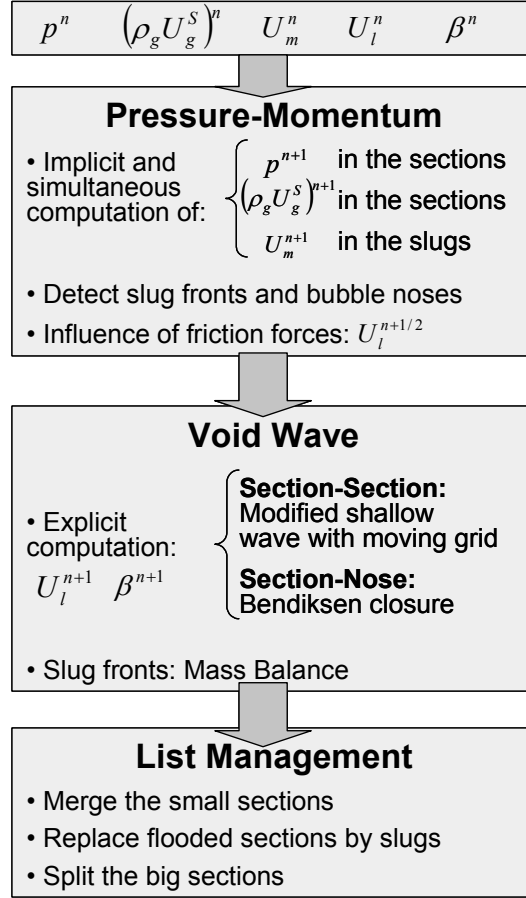


Fig. 5. The LASSI scheme computation procedure

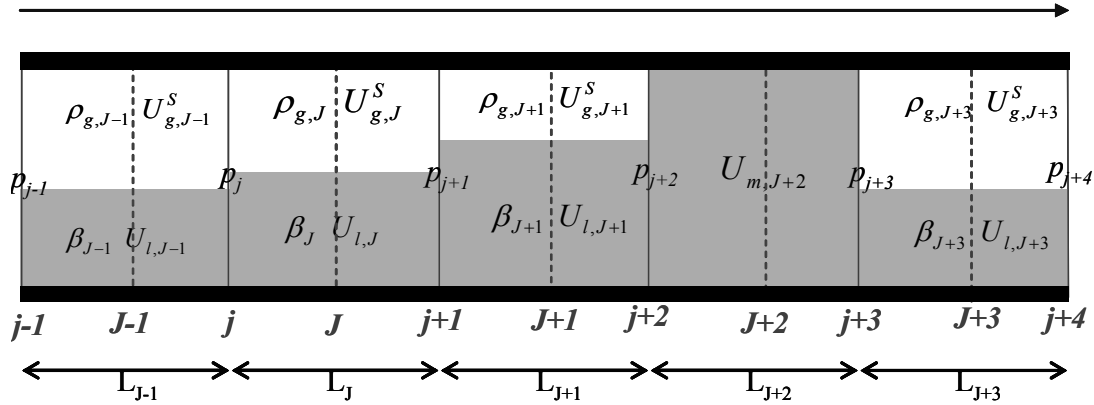


Fig. 6. Lassi scheme grid

of the J border.

We can then write, with $V_{g,j}^n = \frac{1}{2} (\alpha_{J-1} L_{J-1} + \alpha_J L_J)$:

$$p_j^{n+1} = \varkappa_j^n \left[(\rho_g U_g^S)_{J-1}^{n+1} - (\rho_g U_g^S)_J^{n+1} \right] + \varrho_j^n$$

introducing:

$$\mathcal{X}_j^n = \frac{\delta t}{V_{g,j}^n \left[\frac{\partial \rho_g}{\partial p} \right]_j^n}$$

$$\varrho_j^n = p_j^n + \frac{\delta t}{V_{g,j}^n \left[\frac{\partial \rho_g}{\partial p} \right]_j^n} \rho_{g,j}^n \left[(\beta U_l)_{J-1}^n - (\beta U_l)_J^n \right] + \frac{\delta t}{V_{g,j}^n \left[\frac{\partial \rho_g}{\partial p} \right]_j^n} \left(\alpha_{J-1}^n U_{b,J-1}^n (\rho_{g,j}^n - \rho_{g,J-1}^n) + \alpha_J^n U_{b,J}^n (\rho_{g,j}^n - \rho_{g,J}^n) \right)$$

The *section-slug* pressure control volume $j + 2$ is discretized as:

$$p_{j+2}^{n+1} = \mathcal{X}_{j+2}^n \left[(\rho_g U_g^S)_{J+1}^{n+1} - \rho_{g,j+2}^n U_{m,J+2}^{n+1} \right] + \varrho_{j+2}^n$$

with:

$$\mathcal{X}_{j+2}^n = \frac{\delta t}{V_{g,j+2}^n \left[\frac{\partial \rho_g}{\partial p} \right]_{j+2}^n}$$

$$\varrho_{j+2}^n = p_{j+2}^n + \frac{\delta t}{V_{g,j+2}^n \left[\frac{\partial \rho_g}{\partial p} \right]_{j+2}^n} \rho_{g,j+2}^n (\beta U_l)_{J+1}^n + \frac{\delta t}{V_{g,j+2}^n \left[\frac{\partial \rho_g}{\partial p} \right]_{j+2}^n} \left(\alpha_{J+1}^n U_{b,J+1}^n (\rho_{g,j+2}^n - \rho_{g,J+1}^n) \right)$$

3.5.2 Gas momentum conservation

The gas momentum conservation equation:

$$\frac{\partial}{\partial t} (\rho_g U_g^S) + \frac{\partial}{\partial x} (\rho_g U_g^S U_g) + \alpha \frac{\partial}{\partial x} p = -\frac{\tau_g S_g}{A} - \frac{\tau_i S_i}{A} - \rho_g g \alpha \sin \phi$$

discretized around the J control volume gives, after replacing p_{j+1}^{n+1} and p_j^{n+1} in the pressure gradient term $\frac{\alpha_J^n}{L_J^n} (p_{j+1}^{n+1} - p_j^{n+1})$ by their expression above:

$$a_J^n (\rho_g U_g^S)_J^{n+1} = b_J^n (\rho_g U_g^S)_{J+1}^{n+1} + c_J^n (\rho_g U_g^S)_{J-1}^{n+1} + d_J^n$$

where:

- $a_J^n = \frac{1}{\delta t} + b_J^n + c_J^n + \frac{1}{8} \left(\frac{S_g}{A_g} \lambda_g |U_g| \right)_J^n + \frac{1}{8} \left(\frac{S_i}{A_g} \lambda_i |U_g - U_l| \right)_J^n$
- $b_J^n = -\frac{1}{L_J^n} \min(U_{g,j+1}^n - U_{b,j+1}^n, 0) + \frac{\alpha_J^n}{L_J^n} \mathcal{X}_{j+1}^n$
- $c_J^n = \frac{1}{L_J^n} \max(U_{g,j}^n - U_{b,j}^n, 0) + \frac{\alpha_J^n}{L_J^n} \mathcal{X}_j^n$
- $d_J^n = \frac{1}{\delta t} (\rho_g U_g^S)_J^n + \frac{\alpha_J^n}{L_J^n} (\varrho_j^n - \varrho_{j+1}^n) + \frac{1}{8} \left(\frac{S_i}{A} \lambda_i \rho_g U_l |U_g - U_l| \right)_J^n - \rho_{g,J}^n g \alpha_J^n \sin \phi$

3.5.3 Slug momentum conservation

The $J + 2$ slug, considered incompressible, is subject to the pressure difference across it, the gravity and the friction at the wall. It also loses some momentum

by ingressing low velocity liquid at its front and shedding high velocity liquid at its tail. The equation is here discretized for a slug with a front on its right and a bubble nose on its left, as an example:

$$\rho_l \frac{L_{J+2}^{n+1} U_{m,J+2}^{n+1} - L_{J+2}^n U_{m,J+2}^n}{\delta t} = \left[\begin{array}{l} -p_{j+3}^{n+1} + p_{j+2}^{n+1} - g\rho_l (h_R^n - h_L^n) - \frac{\lambda\rho_l}{2D} L_s^n U_{m,J+2}^{n+1} \left| U_{m,J+2}^n \right| \\ + \rho_l (U_f^n - U_{m,J+2}^n) U_{l,J+3}^n - \rho_l (U_b^n - U_{m,J+2}^n) U_{m,J+2}^{n+1} \end{array} \right]$$

where h_R^n and h_L^n are the liquid heights respectively at the right and at the left of the slug, U_f^n is the front velocity at the right and U_b^n is the bubble nose velocity at the left. This equation can be re-written as:

$$a_{J+2}^n U_{m,J+2}^{n+1} = b_{J+2}^n (\rho_g U_g^S)_{J+3}^{n+1} + c_{J+2}^n (\rho_g U_g^S)_{J+1}^{n+1} + d_{J+2}^n$$

with:

- $a_{J+2}^n = \frac{\rho_l L_{J+2}^n}{\delta t} + \rho_l \frac{\beta_{J+3}^n}{1-\beta_{J+3}^n} (U_{m,J+2}^n - U_{l,J+3}^n) + \frac{\lambda\rho_l}{2D} L_{J+2}^n \left| U_{m,J+2}^n \right| + \rho_{g,j+3}^n \mathcal{Z}_{j+3}^n + \rho_{g,j+2}^n \mathcal{Z}_{j+2}^n$
- $b_{J+2}^n = \mathcal{Z}_{j+3}^n$
- $c_{J+2}^n = \mathcal{Z}_{j+2}^n$
- $d_{J+2}^n = \varrho_{j+2}^n - \varrho_{j+3}^n - g\rho_l (h_R - h_L) + \frac{\rho_l L_{J+2}^n}{\delta t} U_{m,J+2}^n + \rho_l \frac{\beta_{J+3}^n}{1-\beta_{J+3}^n} (U_{m,J+2}^n - U_{l,J+3}^n) U_{l,J+3}^n$

There is therefore only a tridiagonal system $a_j^n X_j^{n+1} = b_j^n X_j^{n+1} + c_j^n X_j^{n+1} + d_j^n$ to solve using the Thomas algorithm in order to evaluate the mixture velocity within the slugs, the pressure along the pipe, and the gas velocity. The resolution is therefore extremely fast. In order to ensure full gas mass conservation, a correction is needed. It is done at the unit level (a unit consists of all the sections between two slugs), since the exact gas mass within one unit can be tracked easily. The amount of correction needed is however extremely small.

3.6 Void-Wave step

3.6.1 Solving the Riemann problem

Thanks to the simplifications presented earlier, the gas and the liquid dynamics have been uncoupled. The void wave step of the scheme is therefore nothing more than a shallow water equations system, modified in the sense that the Bernoulli effect is subtracted from the hydrostatic term. However, it

is important to note that compared to the shallow water equations for channel flow, the presented system is only pseudo-conservative because of both the Bernoulli effect and the circular shape of the pipe. The presented scheme being non-staggered and first-order, the objective is to solve the Riemann problem between a left state (U_L, β_L) characterized by its liquid velocity U_L and its holdup β_L and a right state (U_R, β_R) of liquid velocity U_R and holdup β_R . It is done explicitly. The equations to be solved consist of the liquid mass conservation differential equation and the liquid momentum conservation differential equation:

$$\frac{\partial}{\partial t} (\beta) + \frac{\partial}{\partial x} (\beta U) = 0$$

$$\frac{\partial}{\partial t} (\beta U) + \frac{\partial}{\partial x} \left(\beta U^2 + \frac{1}{2} \kappa \beta^2 \right) = 0$$

This system has an exact solution that can be determined numerically. Indeed, the solution of this two-variables Riemann problem consists in one intermediate state (U_M, β_M) which is connected to both the left state (U_L, β_L) and the right state (U_R, β_R) by either a shock or a rarefaction wave (Holden et al., 2002), depending on the conditions. A shock is characterized by the Rankine-Hugoniot condition which gives mass and momentum conservation across a front travelling at a constant velocity s . For a shock between (U_L, β_L) and (U_M, β_M) (slow shock), this condition can be written as the system:

$$\begin{aligned} s(\beta_M - \beta_L) &= \beta_M U_M - \beta_L U_L \\ s(\beta_M U_M - \beta_L U_L) &= \left(\beta_M U_M^2 + \frac{1}{2} \kappa \beta_M^2 \right) - \left(\beta_L U_L^2 + \frac{1}{2} \kappa \beta_L^2 \right) \end{aligned}$$

This system has only one entropy-conserving solution which consists of:

$$\beta_M > \beta_L \text{ and } U_M = U_L - \frac{1}{\sqrt{2}} \sqrt{\kappa} (\beta_M - \beta_L) \sqrt{\frac{1}{\beta_M} + \frac{1}{\beta_L}} \text{ (LeftShock: LS)}$$

For a shock between (U_M, β_M) and (U_R, β_R) (fast shock) the entropy-conserving solution will be:

$$\beta_M > \beta_R \text{ and } U_M = U_R + \frac{1}{\sqrt{2}} \sqrt{\kappa} (\beta_M - \beta_R) \sqrt{\frac{1}{\beta_M} + \frac{1}{\beta_R}} \text{ (RightShock: RS)}$$

Rarefaction waves are structures travelling with the system's characteristic speed $U - \sqrt{\kappa\beta}$ (slow wave) and $U + \sqrt{\kappa\beta}$ (fast wave) within which the flow variables β and U vary smoothly from one state to another. It can be shown that within a rarefaction wave, the Riemann invariant ($U + 2\sqrt{\kappa\beta}$ for a slow wave and $U - 2\sqrt{\kappa\beta}$ for a fast wave) is a constant of the flow. It follows that

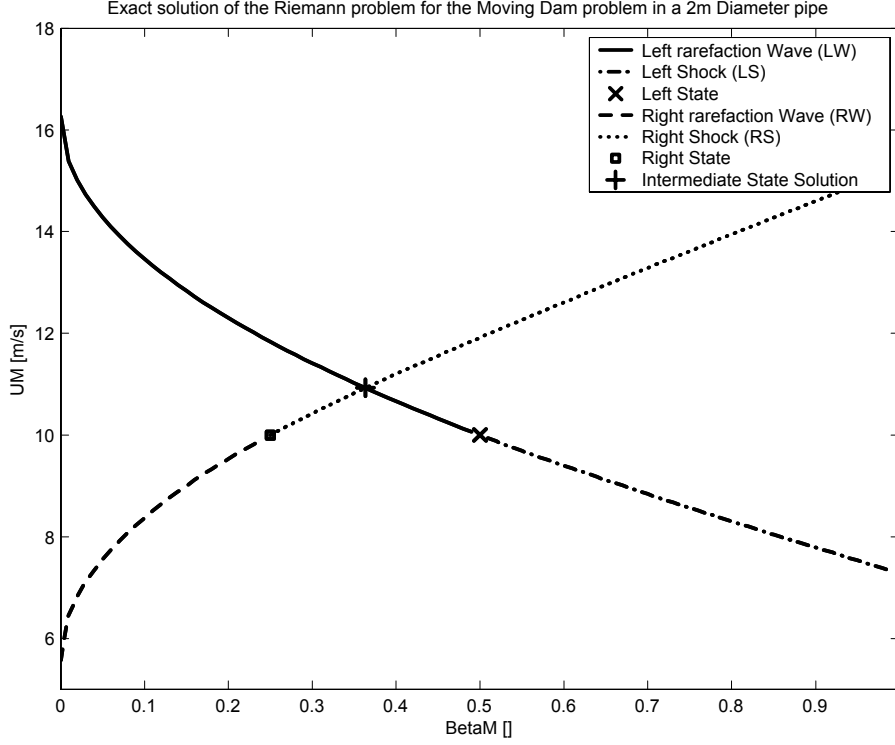


Fig. 7. Determination of the intermediate state (β_M, U_M) in the Riemann Problem the (U_L, β_L) state can be connected to the (U_M, β_M) state by a slow wave provided that:

$$\beta_M < \beta_L \text{ and } U_M = U_L - 2\sqrt{\kappa} \left(\sqrt{\beta_M} - \sqrt{\beta_L} \right) \text{ (LeftWave: LW)}$$

Similarly one can connect the intermediate state (U_M, β_M) to the right state (U_R, β_R) by a fast wave provided that:

$$\beta_M < \beta_R \text{ and } U_M = U_R + 2\sqrt{\kappa} \left(\sqrt{\beta_M} - \sqrt{\beta_R} \right) \text{ (RightWave: RW)}$$

The two states (U_L, β_L) and (U_R, β_R) being known, the intermediate state (U_M, β_M) can be determined as the intersection of the four curves (Left Shock LS, Left Wave LW, Right Shock RS, Right Wave RW) $U_M = f(\beta_M)$ detailed above. Due to the monotonous nature of those four functions, only a few iterations are needed to calculate U_M and β_M with great accuracy. The graph presented figure 7 shows the four curves and the calculated intermediate state in the moving dam case (represented figure 11).

The so-called left and right dry-bed cases (respectively β_L and β_R equals zero) and the appearing dry-bed case ($\beta_M = 0$, occurring when $U_L + 2\sqrt{\kappa\beta_L} < U_R - 2\sqrt{\kappa\beta_R}$) are special cases that do not present any particular difficulties to implement and are therefore not detailed here.

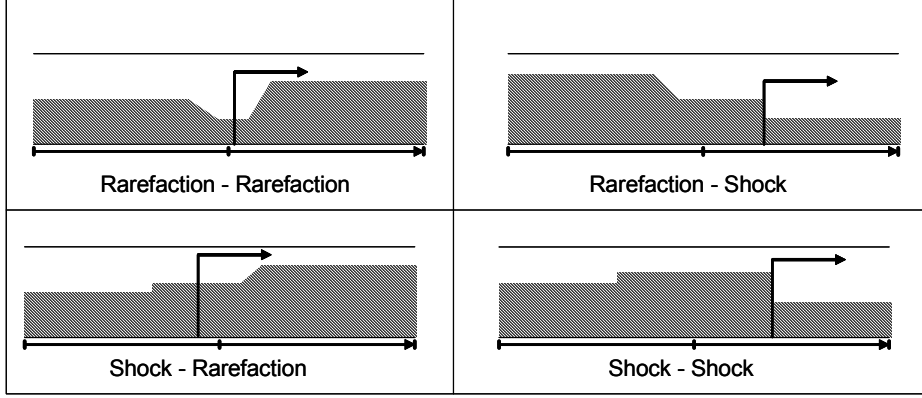


Fig. 8. Interface tracking in the LASSI scheme

3.6.2 Border velocities and front tracking

Once the Riemann problem is solved and the intermediate state is found, the boundary velocities and the liquid mass and momentum fluxes are evaluated between the sections. It is natural to take profit of the power of the Lagrangian approach to make the most of the information provided by the exact solution of the Riemann problem. It is decided to focus on the propagation of the fast fronts, as they are of special interest when it comes to modelling the transition, as will be shown later, in paragraph 4.1. Modelling correctly the fast fronts allows also to follow ripples and roll-waves with limited diffusion. As a consequence, the border velocities and liquid fluxes are evaluated in the LASSI scheme as presented in figure 8. If a fast front is detected (case Rarefaction-Shock and Shock-Shock), the border velocity will be set to the fast front velocity in order to follow it. If no fast front is present (case Rarefaction-Rarefaction and Shock-Rarefaction), the border velocity will be set to follow the middle of the intermediate state. Liquid mass and liquid momentum fluxes follow automatically from conservation laws, once the border velocity has been chosen. The reason for this dissymmetric treatment lies on the ambition to model as correctly as possible a wave composed by a smooth tail and a sharp fast front.

3.7 Slug closures

As explained previously, some closures are used to calculate the slug transport. A *section-slug* or a *slug-section* border can be either a nose or a front. The critical velocity for the turning of the bubble is taken as the velocity that balances friction and gravity forces within the slug:

$$\frac{1}{2}\lambda_l\rho_l U_{crit}^2 S = \rho_l g \sin \varphi A$$

Should the mixture velocity within the slug exceed this critical velocity, then the slug-bubble border will be considered as a perfectly steep front, whose velocity can be determined by simple liquid conservation in the "no void in slug" case:

$$U_{front} = \frac{U_{ls} - (1 - \alpha_b)U_{lb}}{\alpha_b}$$

U_{ls} and U_{lb} are respectively the liquid velocity within the slug and within the liquid film ahead of it and α_b is the void fraction within the bubble section in front of the slug.

In the opposite situation, the slug-bubble border will be considered as a bubble nose, and calculated using Bendiksen's closure law (Bendiksen et al., 1984). For low Froude numbers ($Fr = \frac{U_m}{\sqrt{gD}} < 3.5$), the slug bubble nose is located close to the top of the tube where the local liquid velocity is moderate, while for higher Froude numbers, the tip of the bubble moves down towards the centre of the pipe, where the liquid velocity is highest. The bubble nose velocity U_b is then calculated as $U_b = C_0 U_m + \nu_0$ where C_0 and ν_0 are given by:

$$\begin{aligned} C_0 &= 1.05 + 0.15 \sin^2 \varphi & \nu_0 &= (0.35 \sin \varphi + 0.54 \cos \varphi) \sqrt{gD} & \text{for } Fr < 3.5 \\ C_0 &= 1.2 + 0.15 \sin^2 \varphi & \nu_0 &= 0.35 \sin \varphi \sqrt{gD} & \text{for } Fr > 3.5 \end{aligned}$$

In practice C_0 and ν_0 are chosen in order to maximize U_b rather than using the Froude number, to ensure a continuous transition of the bubble nose velocity when the Froude number increases.

3.8 Implementation

The great power given by the adaptive grid comes with some implementation challenges: some grid cells become too small and the CFL criterion is no longer verified within them at the chosen timestep (the fast wave from their left border takes over the slow wave from their right border). Some other grid cells become too large and have to be split in order to maintain the wanted spatial accuracy. Those difficulties are met by the use of an object oriented programming method in C++. The pipe is represented as a doubly-linked list of objects which can be either slugs or bubbles. Those objects can be taken away and deleted (if a slug dies for example, or if a section becomes too short), and new objects can be inserted (if the holdup in a bubble reaches one, than a slug is inserted). Figure 9 represents the different classes used in LASSI.

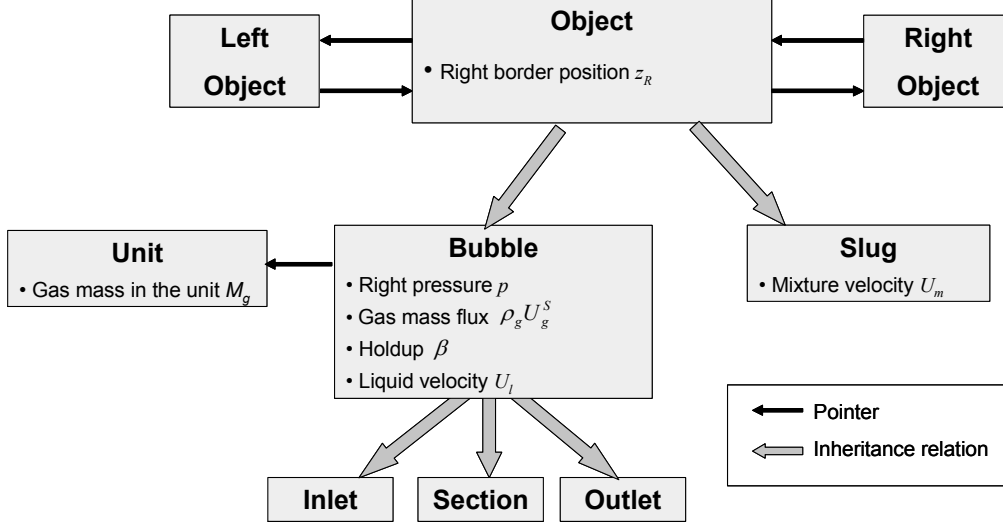


Fig. 9. Object-Oriented implementation of the LASSI scheme

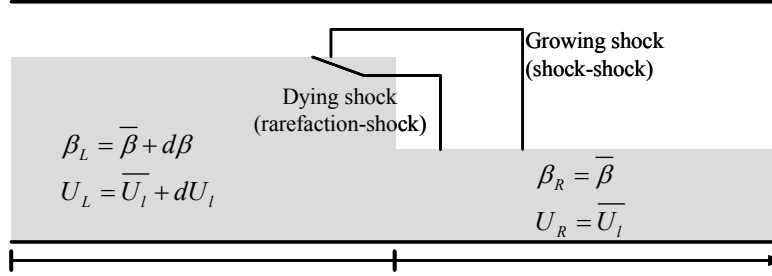


Fig. 10. LASSI and the VKH criterion

4 Evaluation of the scheme

4.1 The stability of stratified flow

The somehow tedious derivation of the VKH criterion from the linear stability analysis presented in section 2.1 should not conceal the physics of the destabilizing effects of the friction forces on the interfacial waves, leading to a growing perturbation and eventually, if the conditions are fulfilled, to a slug. As this effect lies in the very core of the presented scheme, and is essential to the correct modelling of the transition from stratified to slug flow, a new derivation of the VKH criterion is presented.

We consider that the flow, defined by its liquid and gas superficial velocities U_l^s and U_g^s , is at its steady state. The equilibrium holdup and liquid velocity $\bar{\beta}$ and \bar{U}_l will verify the dynamic equilibrium equation $F(\bar{\beta}, \bar{U}_l, U_m) = 0$ where the mixture velocity U_m verifies $U_m = U_l^s + U_g^s$. We suppose that an infinitely small disturbance in the holdup on the left part of the pipe meets a section where the holdup is at its equilibrium value. Now if the left section is long

enough (long wave approximation), its holdup and liquid velocity will also be at dynamic equilibrium, i.e. $F(\beta_L, U_L, U_m) = 0$.

From this relation we can derive the liquid velocity in the left section:

$$F(\beta_L, U_L, U_m) = F(\bar{\beta}, \bar{U}_l, U_m) + d\beta \left(\frac{\partial F}{\partial \beta} \right)_{U_l, U_m} + dU_l \left(\frac{\partial F}{\partial U_l} \right)_{\beta, U_m}$$

and therefore:

$$dU_l = - \frac{\left(\frac{\partial F}{\partial \beta} \right)_{U_l, U_m}}{\left(\frac{\partial F}{\partial U_l} \right)_{\beta, U_m}} d\beta$$

Now it is clear from the sketch presented figure 10 that the perturbation will grow if we are in the "growing shock case" (that is to say if we are in the shock-shock case) and will eventually vanish if we are in the "dying shock case" (that is to say if we are in the rarefaction-shock case). The condition for a "neutral shock" which propagates without growing nor dying, is simply for the intermediate (β_M, U_M) to be equal to the left state (β_L, U_L) .

We then have $U_L = U_R + \frac{1}{\sqrt{2}}\sqrt{\kappa}(\beta_L - \beta_R) \sqrt{\frac{1}{\beta_L} + \frac{1}{\beta_R}}$ and after differentiating:

$$dU_l = \sqrt{\frac{\kappa}{\beta}} d\beta$$

The condition for a growing shock is then clearly: $dU_l > \sqrt{\frac{\kappa}{\beta}} d\beta$. Replacing the expression for dU_l within this inequation yields the stability criterion:

$$\text{stable} \Leftrightarrow - \frac{\left(\frac{\partial F}{\partial \beta} \right)_{U_l, U_m}}{\left(\frac{\partial F}{\partial U_l} \right)_{\beta, U_m}} < \sqrt{\frac{\kappa}{\beta}}$$

This expression can of course be rewritten in the traditional form of the VKH, after noticing that:

$$- \frac{\left(\frac{\partial F}{\partial \beta} \right)_{U_l, U_m}}{\left(\frac{\partial F}{\partial U_l} \right)_{\beta, U_m}} = - \frac{\left(\frac{\partial F}{\partial \beta} \right)_{U_l^S, U_g^S} + U_l \left(\frac{\partial F}{\partial U_l^S} \right)_{\beta, U_g^S} - U_l \left(\frac{\partial F}{\partial U_g^S} \right)_{\beta, U_l^S}}{\bar{\beta} \left[\left(\frac{\partial F}{\partial U_l^S} \right)_{\beta, U_g^S} - \left(\frac{\partial F}{\partial U_g^S} \right)_{\beta, U_l^S} \right]} = \frac{1}{\bar{\beta}} [C_F - U_l]$$

where $C_F = - \frac{\left(\frac{\partial F}{\partial \beta} \right)_{U_l^S, U_g^S}}{\left[\left(\frac{\partial F}{\partial U_l^S} \right)_{\beta, U_g^S} - \left(\frac{\partial F}{\partial U_g^S} \right)_{\beta, U_l^S} \right]}$ is the wave velocity of the perturbation

in the VKH analysis, as introduced in Barnea and Taitel (1993).

The stability criterion can then be written as:

$$stable \Leftrightarrow \frac{1}{\beta} [C_F - U_l] < \sqrt{\frac{\kappa}{\beta}} \Leftrightarrow [C_F - U_l]^2 + (c - a^2) < 0$$

Keeping in mind that $U_l \approx a$ when $\rho_l U_l \gg \rho_g U_g$, we are able to find back the stability criterion of stratified flow as derived by Lin and Hanratty (1986) and Barnea and Taitel (1993). Whenever holds the assumption $\rho_l U_l \gg \rho_g U_g$ made in section 3.3 when the derivation of the scheme was presented, the LASSI scheme has therefore exactly the same area of stability as the two-fluid model continuous equations. The approximations made in the derivation of the scheme have therefore had no impact on its area of stability.

Moreover, this alternative derivation of the Viscous Kelvin Helmholtz criterion clearly shows the importance of friction forces, the hydrostatic force, and the Bernoulli effect. If the friction forces accelerate the liquid within the bump fast enough to create a growing shock between the bump and the low speed liquid bed ahead of it, then the bump will grow and the flow is unstable. The speed difference between the bump and the liquid bed needed to let the growing shock appear is directly dependant on the competition between the hydrostatic force and the Bernoulli effect.

4.2 Front tracking abilities

As explained, the slug fronts are tracked by the scheme under the assumption that they remain perfectly sharp. Therefore, slugs are tracked along the pipe without any diffusion.

The previous chapter stressed the importance of front tracking to obtain the right transition from stratified to slug flow. A small perturbation with a growing front will become bigger, while a small perturbation with a dying front will eventually disappear. For this reason, the border velocities between the sections were chosen as explained in section 3.6.2.

To illustrate the front tracking properties of the scheme, the "moving dam case" is introduced. At $t = 0$ s, the liquid height and velocity distribution in an infinitely long channel is as described by figure 11. Friction is neglected hence the shallow water model is used, and the problem is reduced to solving the Riemann problem between the left state ($h_L = 1$ m, $U_L = 10$ m.s⁻¹) and the right state ($h_R = 0.5$ m, $U_L = 10$ m.s⁻¹).

The LASSI scheme is compared with an usual explicit, non-staggered first-order upwind scheme for the shallow water equations, and the same scheme

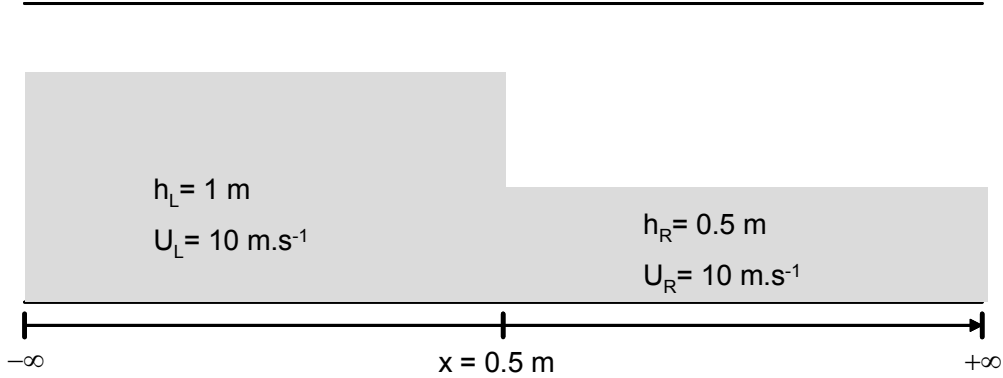


Fig. 11. Sketch introducing the moving dam case

applied with a moving grid which travels at a velocity of 10 m.s^{-1} . A grid size of 1 cm and a time step of 0.1 ms were used for all schemes. The results are shown figure 12. The analytical solution is shown as a solid line, while the results obtained with the first-order upwind schemes are represented by a dashed line (when no moving grid is used) and a dotted line (when a grid moving at 10 m.s^{-1} is used). As a flexible grid is used in Lassi, the section length is not constant across the pipe at $t = 0.06 \text{ s}$ (although it was the case at the start of the simulation). The holdup profile obtained with the LASSI scheme is therefore shown as solid grey bars.

The results clearly show the ability of the LASSI scheme to follow perfectly the fast front on the right. Part of this performance can be explained by the Lagrangian character of the scheme (illustrated by the difference between the upwind scheme with a moving grid and the traditional upwind scheme), the other part is due to the adaptiveness of the grid which focuses on following the fast shock (illustrated by the difference between the LASSI scheme and the upwind scheme with a moving grid: the perfect capturing of the right front is done to the expense of a slight deterioration in the rarefaction wave).

To illustrate the power of the Lagrangian methods, a modified version of the scheme, here labelled LASSI Slow, has been tried on this case. LASSI Slow follows the slow rarefaction wave instead of the fast shock like the standard LASSI scheme. Figure 13 clearly shows that in this case, the left rarefaction wave is correctly followed at the expense of the right front.

4.3 Numerical flowmap

The prerequisite of the use of a slug capturing model for two-phase flow problems lies in its ability to predict correctly the transition from stratified to slug flow, that is to say, its ability to produce a numerical flowmap consistent with the experimental observations. Following the idea expressed by figure 3,

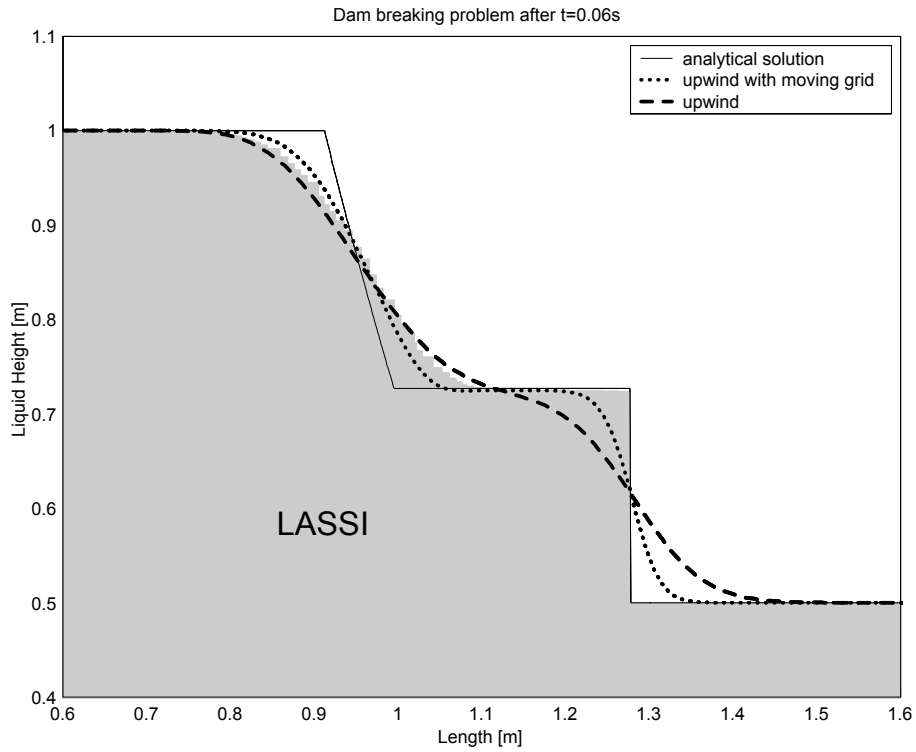


Fig. 12. Simulation of the moving dam case, normal LASSI scheme

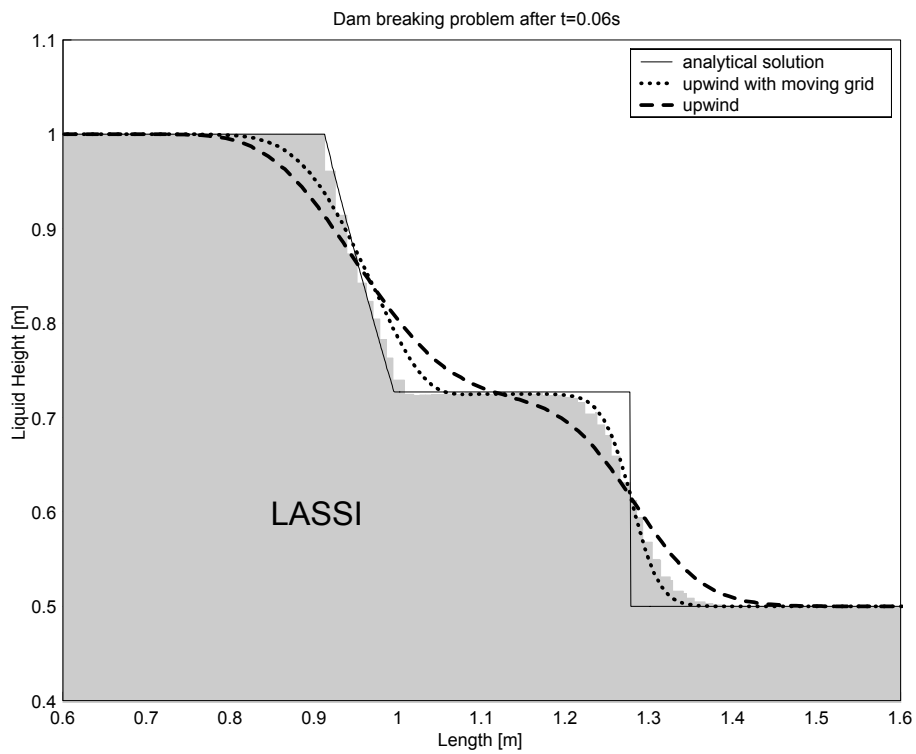


Fig. 13. Simulation of the moving dam case, LASSI SLOW scheme

the numerical scheme is compared both to some experimental results and to the VKH model predictions. In this paper are presented results for both a downwards inclined pipe and a horizontal pipe.

4.3.1 Downwards inclined pipe

This case is taken from Woods (2000), referring to some experiments presented in Lin et al. (1986). Lin conducted experiments with air and water in a 7.63 cm downwards inclined pipe (-0.5°) at atmospheric pressure. As in Woods (2000), the experimental results are compared to the predictions of the VKH criterion, used with the usual Blasius friction factors, and an interfacial friction factor equal to the gas-wall friction factor. In addition, some numerical simulations have been made with the LASSI scheme: a 50 meters pipe is simulated with an average 2 cm section length and a 2 ms time step. For a given gas superficial velocity U_g^S , the critical liquid superficial velocity U_l^S defining the numerical transition from stratified to slug flow is determined with an accuracy equal to 0.01 m.s^{-1} . The results are shown both in terms of the adimensioned liquid height against the gas superficial velocity (figure 14) and in terms of the liquid superficial velocity against the gas superficial velocity (figure 15). There is a very good match between the experimental observations and the predictions of the VKH criterion in the $(\frac{h_l}{D} - U_g^S)$ plot, and although less accurate than the VKH itself, the LASSI predictions are very satisfactory. As already mentioned in Fan et al. (1993), a small error in the predicted critical liquid height can produce a much larger error in the predicted critical superficial liquid velocity. This statement indeed applies here. In addition, the results obtained by Woods suggest a problem in the modelling of the friction factors, especially for $U_g^S = 1.48$, where the experimentally observed interfacial friction factor λ_i was actually smaller than the gas-wall friction factor λ_g .

4.3.2 Horizontal pipe

The same work was conducted again, this time based on some experiments made by Manolis (1995) with air and water in a horizontal 7.8 cm diameter pipe at atmospheric pressure and used by Issa et al. for slug capturing validation (2003). Some numerical simulations were run with LASSI, using a time step of 5 ms and an average section length of 1 cm. The critical liquid superficial velocity U_l^S is determined with an accuracy of 0.01 m.s^{-1} . A long pipe (200 m) was used in the simulations, in order to be able to compare more efficiently the scheme against the VKH criterion, derived for an infinitely long pipe. The results are shown both in terms of the adimensioned liquid height against the gas superficial velocity (figure 16) and in terms of the liquid superficial velocity against the gas superficial velocity (figure 17). There is a particularly good match between the numerical predictions and both the experiments and the

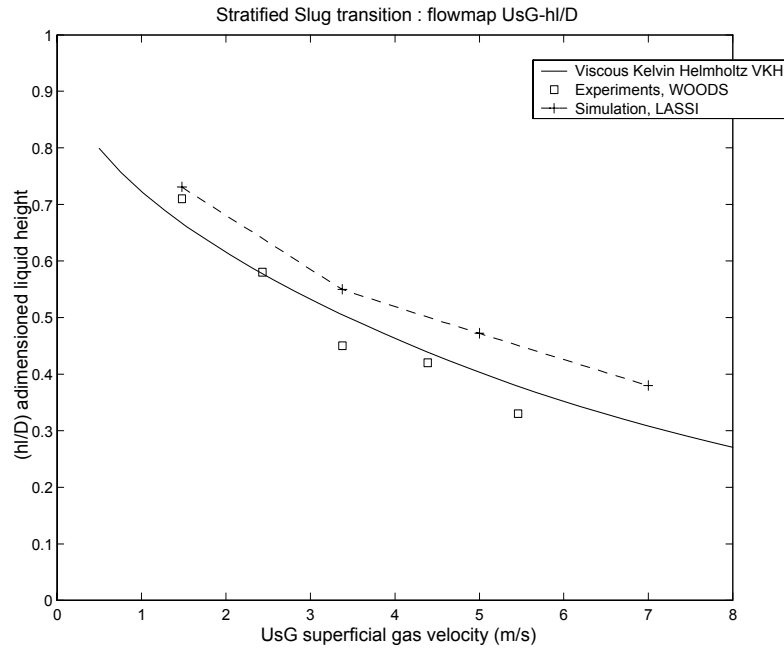


Fig. 14. Comparison between experimental, model-based and numerical transition: liquid height against gas superficial velocity ($D=7.63$ cm, -0.5° , air-water, 1 bar)

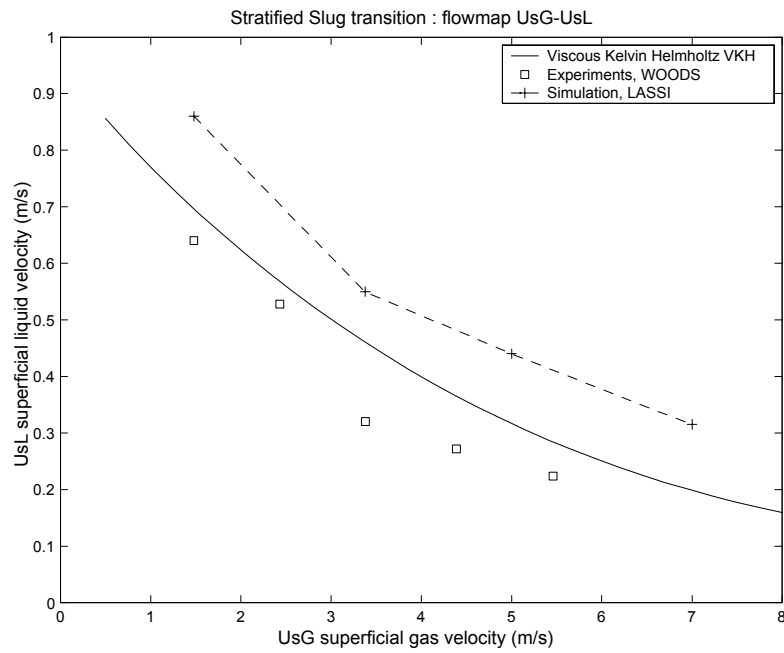


Fig. 15. Comparison between experimental, model-based and numerical transition: liquid superficial velocity against gas superficial velocity ($D=7.63$ cm, -0.5° , air-water, 1 bar)

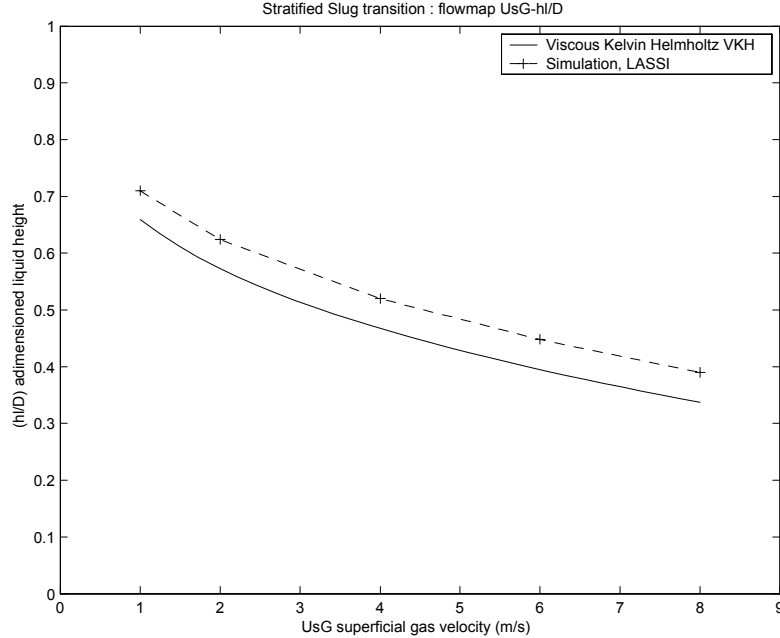


Fig. 16. Comparison between experimental, model-based and numerical transition: liquid height against gas superficial velocity ($D=7.8$ cm, horizontal, air-water, 1 bar)

model predictions, with an average error of around one twentieth of a diameter in the predicted critical liquid height. However it should be noted that at the transition point, the slugs were initiated much farther in the pipe in the simulations than in the experiments.

4.4 Initiation example

A typical profile of the pipe at initiation is shown figure 18. A 20 meters long, 1 inch diameter, air-water pipe is simulated at atmospheric pressure. The time step is 0.01 s and the average section length is around 1 cm. Simulating 5 minutes takes only a few minutes on a standard PC, thanks to the explicit nature of the scheme. One can clearly see a travelling wave, breaking and finally bridging the pipe, giving birth to a slug.

4.5 Roll waves example

Though it is not the main objective of this paper, an example of what happens in the "unstable flow" region, as defined by figure 2, is shown. A simulation is run in a horizontal pipe with a gas density of 50 kg.m^{-3} , a gas superficial velocity of $U_g^S = 3.5 \text{ m.s}^{-1}$ and a liquid superficial velocity of $U_l^S = 0.35 \text{ m.s}^{-1}$. Due to the high gas density, the flow is clearly unstable according to

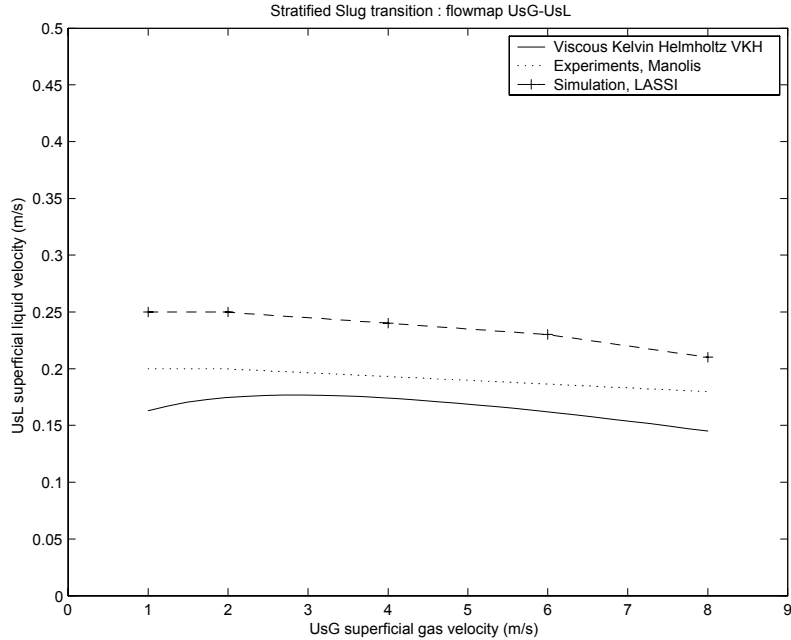


Fig. 17. Comparison between experimental, model-based and numerical transition: liquid superficial velocity against gas superficial velocity ($D=7.8$ cm, horizontal, air-water, 1 bar)

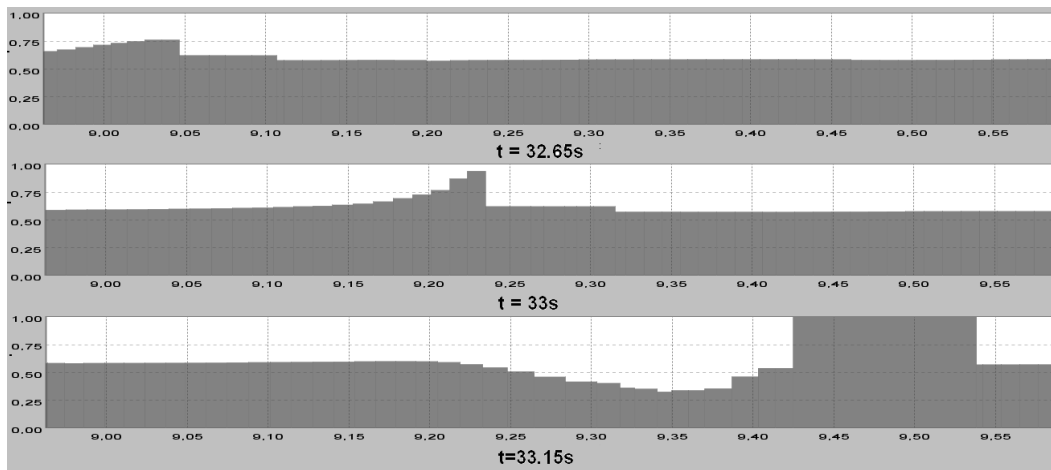


Fig. 18. Slug initiation with LASSI.

the VKH criterion. However the liquid holdup is not sufficient to sustain slug flow. An interesting regime of ripples, growing into roll-waves that overtake each other to grow appears, as shown by the profile in figure 19.

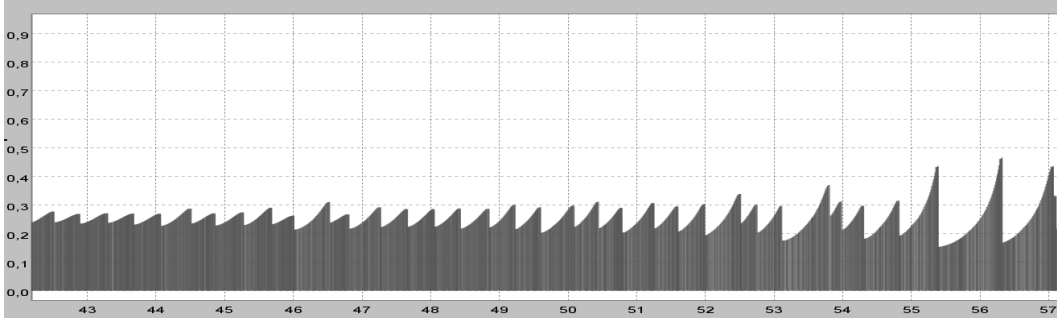


Fig. 19. Roll-wave regime simulated with the LASSI scheme.

5 Conclusion

A new transient scheme for the simulation of two-phase flow, based on the decoupling of the gas and liquid momentum equations, as well as on a Lagrangian and adaptive approach, has been presented. By incorporating both the Viscous Kelvin Helmholtz criterion, and the Minimum Holdup criterion, this scheme aims at reproducing the correct flowmap automatically. The scheme is demonstrated to possess the same area of stability as the VKH criterion provided that the gas momentum is negligible compared to the liquid momentum. Incidentally, this demonstration provides a new derivation of the VKH criterion, less cumbersome and more intuitive, which could be of interest for the other researchers in the area.

In this paper, the followed approach was tested against experimental and theoretical results and the scheme was shown to predict the transition from stratified to slug flow in near-horizontal pipes with a very good accuracy. At the transition between stratified and slug flow, the slugs can require a notably longer pipe length to be initiated than in the experiments. This is due to the fact that at neutral stability, the theoretical growth rate of the perturbations is zero, and probably, also to an inevitable amount of numerical diffusion. Should a closer agreement with the experiments, which always involve a fair amount of destabilizing effects, such as unwanted variations in the pipe inclination and in the flow rates, be wanted, some counter-measures could be investigated, such as the arbitrary reduction of the κ coefficient, mechanically shifting the numerical flowmap in favor of slug flow.

Some concerns raised on the ability of the upwind-differentiated schemes to correctly model the Bernoulli suction force could also be of interest for the other researchers in the area.

References

- Barnea, D., Taitel, Y., 1993. Kelving-Helmholtz stability criteria for stratified flow: viscous versus non-viscous (inviscid) approaches. *Int. J. Multiphase Flow* 19 (4), 639-649.
- Bendiksen, K.H., 1984. An experimental investigation of the motion of long bubbles in inclined tubes. *Int. J. Multiphase Flow* 10, 467-483.
- Bendiksen, K.H., Malnes, D., Moe, R., Nuland, S., 1991. The dynamic two-fluid model OLGA: Theory and application. *SPE Production Engineering*, May 1991, 171-180.
- Bendiksen, K.H., Espedal, M., 1992. Onset of slugging in horizontal gas-liquid pipe flow. *Int. J. Multiphase Flow* 18, 234-247.
- Bendiksen, K.H., Malnes, D., Nydal, O.J., 1996. On the modelling of slug flow. *Chem. eng. com.* 141: 71-102
- Bonizzi, M., 2002. Transient one-dimensional modelling of multi-phase slug flows. Ph.D. Thesis, Imperial College, University of London.
- Fan, Z., Lusseyran, F., Hanratty, T.T, 1993. Initiation of slugs in horizontal gas-liquid flows. *AIChE J.* 39, 1741-1753.
- Holden, H., Risebro, N. H., 2002 *Front tracking for hyperbolic conservation laws.* Springer.
- Issa, R.I., Kempf, M.H.W., 2003. Simulation of slug flow in horizontal or nearly horizontal pipes with the two-fluid model. *Int. J. Multiphase Flow* 29, 69-95.
- Kristiansen, O., 2004. Experiments on the transition from stratified to slug flow in multiphase pipe flow. Ph.D. Thesis, NTNU, Trondheim, Norway.
- Lin, P.Y., Hanratty, T.J, 1986. Prediction of the initiation of slugs with linear stability theory. *Int. J. Multiphase Flow* 12, 79-98.
- Manolis, I.G., 1995. High pressure gas-liquid slug flow. Ph.D. Thesis, Imperial College
- Nydal, O.J., Banerjee, S., 1996. Dynamic slug tracking simulations for gas-liquid flow in pipelines. *Chem. Eng. Commun.* 141-142, 13-39.
- Ramshaw, J. D., Trapp, J. A., 1978. Characteristics, stability, and short-wavelength phenomena in two-phase flow equation systems. *Nuclear Science and Engineering*: 66, 93-102.

Ruder, Z., Hanratty, P.J., Hanratty, T.J., 1989. Necessary conditions for the existence of stable slugs. *Int. J. Multiphase Flow* 15, 209–226.

Taitel, Y., Dukler, A.E., 1976. A model for predicting flow regime transitions in horizontal and near horizontal gas–liquid flow. *AIChE J* 22, 47–55.

Taitel, Y., Barnea, D., 1997 Simplified transient simulation of two-phase flow using quasi-equilibrium momentum balances. *Int. J. Multiphase Flow* Vol. 23, No. 3, 493-501.

Taitel, Y., Barnea, D., 2000. Slug-tracking model for hilly terrain pipelines. *SPE Journal* 5 (1): 102-109.

Woods, B.D., Hanratty, T.J., 1996. Relation of slug stability to shedding rate. *Int. J. Multiphase Flow* 22, No. 5, 809-828.

Woods, B.D., Hurlburt, E.T., Hanratty, T.J., 2000. Mechanism of slug formation in downwardly inclined pipes. *Int. J. Multiphase Flow* 26, 977-998

Second Paper

A simple slug capturing and slug tracking
scheme for gas-liquid pipe flow.
Part 2: Application to slug length
determination in a small scale loop.

Fabien Renault and Ole Jørgen Nydal

Preprint

A simple slug capturing and slug tracking scheme for gas-liquid pipe flow. Part 2: Application to slug length determination in a small scale loop

Fabien Renault ^{a,*} Ole-Jorgen Nydal ^b Vincent Gruez ^c
Pierre Luquet ^d

^a*Department of Energy and Process Technology, University of NTNU, Trondheim, Norway*

^b*Department of Energy and Process Technology, University of NTNU, Trondheim, Norway*

^c*ENSAM, Paris*

^d*ENSAM, Paris*

Abstract

The hydrodynamical characteristics of slug flow in a small scale V-shaped loop were investigated experimentally and numerically. Using optical sensors, the length, front velocity and tail velocity of each individual slug were measured at various locations along the pipe. The experiments clearly show that for the shorter slugs the slug tail velocity exceeds the slug front velocity hence leading to the disappearing of small slugs and to an increase of the average slug length. The influence of the upstream flow regime (stratified or slug flow) is also investigated and shown to be negligible at sufficient distances from the bend. In addition, the transition between normal slug flow and severe slugging is studied by gradually increasing the upstream gas volume. The experimental observations were compared to the predictions of a Lagrangian slug capturing model and there is a fair agreement on the slug length distribution between the numerical predictions and the experimental results.

Key words: two-phase flow, slug flow, severe slugging, slug initiation

* Corresponding author: fabien.a.renault@ntnu.no

1 Introduction

Gas liquid slug flow is an intermittent flow regime occurring in many engineering applications such as oil and gas transport in pipelines. It is characterized by a sequence of liquid slugs travelling downstream the pipe and separated by large gas regions called Taylor bubbles. The study of the hydrodynamics of slug flow, and specially the determination of parameters such as the average and maximum slug length, is of special interest for the design of separators and slug catchers after oil and gas pipelines. Considerable theoretical and experimental work has therefore been conducted in this area.

The average slug length has been observed to be between 10 to 60 diameters in horizontal pipes (Dukler and Hubbard, 1975, Barnea and Braumer, 1985, Nydal et al., 1992, Andreussi et al., 1993) and between 10 to 25 diameters in vertical pipes (Griffith and Wallis, 1961, Barnea and Shemer, 1989, van Hout et al., 1992). In addition, both Brill et al. (1981) on the basis of some field observations and Nydal et al. (1992) based on lab experiments, were able to show that the probability density function of the measured slug lengths is close to a log-normal distribution.

Moisis and Griffith (1962) first observed that the nose velocity of a Taylor bubble increased as the length of the liquid slug ahead of it decreased. This was explained by the fact that the liquid "eaten" by the slug is only fully assimilated after a given minimum length. In slugs whose length is inferior to that critical minimum length, the velocity profile at the slug tail has not yet reached its equilibrium value and induces some disturbances on the propagation of the Taylor bubble behind the slug (Taitel et al. 1980, Barnea and Braumer 1985, Dukler et al. 1985).

Correct modelling of this "wake effect" is of course critical to the prediction of the evolution of the slug length distribution throughout the pipe. Since the tail velocity of the shorter slugs is higher, the shortest slugs eventually vanish which leads to the growth in length of the remaining slugs. It then appears that only remain the slugs whose length is over a certain minimum stable length. This minimum stable length is an important parameter for slug length predictions and is generally comprised between a few diameters and 10 diameters. However, this parameter is system dependent and the correct modelling of the wake effect is still an open question.

Using a simple kinematic slug tracking model, Barnea and Taitel (1993) were able to predict the slug length distribution at various locations of the pipe. They used an arbitrary slug length distribution consisting of very short slugs at the entrance of the pipe and let it evolve according to a wake effect model similar to the one proposed by Griffith. Not only was the predicted slug length

distribution similar to the experimental observations at a sufficient distance, but it was also shown that the predicted slug length distribution far from the inlet was fairly insensitive to the arbitrary slug length distribution used to generate the slugs at the inlet. Slug length distributions were also computed by Nydal (1996) with a dynamic slug tracking model.

Van Hout et al. (2001, 2003), and Shemer (2003) conducted extensive slug length measurements in two 10 meters long pipe with internal diameters of 2.4 and 5.4 cm. Using optical probes to detect slugs passing by and measure their speed and their length, they were able to observe the slug length distribution at various locations of the pipe. Finally they ran Barnea and Taitel's slug tracking model for slug length determination using a wake effect model fitted to their observations as an input. The predictions obtained with this model compared fairly well with the experimental observations.

Issa and Kempf (2003) first presented a two-fluid model named TRIOMPH capable of slug capturing, meaning that the numerics are able to automatically capture the initiation of slugs without using any arbitrary closure law. For various flow conditions, Issa and Kempf compared the predicted slug frequencies with the available experimental data from the literature and a good agreement was obtained between the predictions and the experiments.

Renault et al. (2007) proposed a new combined slug capturing and slug tracking scheme called LASSI. It is an extension of a simplified slug tracking scheme (Nydal and Banerjee, 1996). In the simplified scheme, a slug initiation model was required in the stratified flow regime. In the LASSI scheme, slugs are generated automatically from a dynamic two fluid model in the stratified region. After their initiation, the slugs are tracked along the pipe with the help of a moving grid. Bendiksen's (1984) correlation is used as a closure for the slug tail velocity while the slug front velocity is calculated from a mass conservation balance. In this respect the LASSI scheme is therefore both slug capturing and slug tracking. As no experimental closure providing either the slug frequency, initial length or the initiation point is used for slug insertion, there is no intrinsic guarantee that the slug capturing mechanism of the LASSI scheme will be able to correctly reproduce the characteristics of slug flow. The aim of this paper is to validate the slug capturing and slug tracking approach by comparing the experimental results with the LASSI scheme predictions.

This paper is structured as follows. First the experimental set-up is briefly introduced, then three different experimental cases are presented, and for each of the cases, the experimental results are compared with the predictions from the LASSI scheme. The first case consists in simply monitoring the evolution of the slug length distribution after a bend in an upwardly inclined pipe. In the second case, the influence of the flow regime (stratified or slug flow) upstream of the bend is investigated. This question is of special interest because it tackles

the issue of the spatial memory of gas-liquid flow. Finally, in the third case the upstream compressibility is increased until the system reaches the severe slugging conditions. The effect of this transition on the slug length distribution in the downstream pipe is studied.

2 Experimental set-up

2.1 *Small-scale flow loop*

The experiments were carried out in a small-scale plexiglas flow loop with an internal diameter of 12 mm. The fluids used were air and water. The loop consisted of two transparent straight pipes fixed in an aluminium structure. The pipes were joined with a flexible hose of the same internal diameter, allowing easy reconfiguration of the loop. Water was circulated by a pump and air was provided by the central supply. Figure 1 shows a sketch of the system. Figure 2 provides a representation of the loop and the structure that supports it.

A gas buffer tank could optionally be used at the inlet, in order to increase the upstream compressibility of the system and thus operate in the severe slugging region, as if there were a very long upstream pipe. The water and gas flowmeters allowed accurate measurements of the water and air inlet flow rates for values of U_l^S comprised between 0.07 and 0.37 $m.s^{-1}$ and values of U_g^S comprised between 0.15 and 0.65 $m.s^{-1}$. A slug catcher had to be specially designed in PVC and installed at the outlet of the pipe to cope with the long slugs encountered in the severe slugging region.

2.2 *Data acquisition*

Optical sensors were used to detect the presence of slugs at various locations in the loop and calculate their propagation velocity. Each sensor consisted of a commercially available optical sensor (E3X-DA51-N, manufactured by OMRON) and two optical fibres, one sender and one receiver. A plexiglas device shown on figure 3 was specially designed to perfectly maintain the two optical probes on the same axis, perpendicular to the pipe. The sender fibre was constantly emitting a red light beam crossing the transparent plexiglas pipe towards the receiver fibre. When the phase present at the center of the

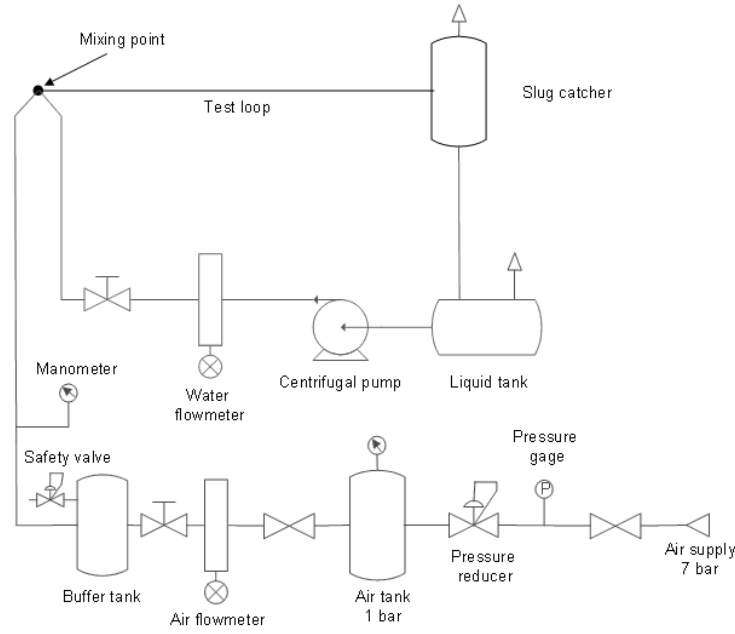


Fig 1: The experimental set-up

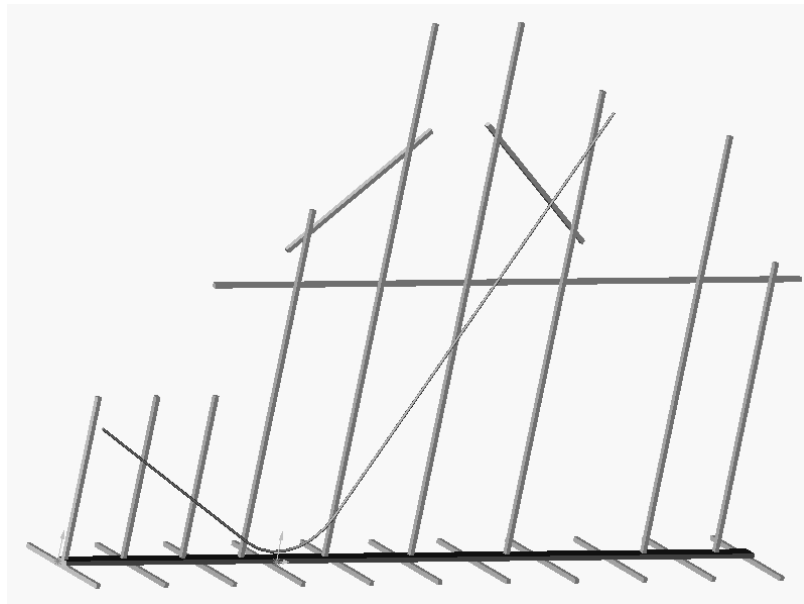


Fig 2: The small-scale loop

pipe was air, the light beam was able to travel through the pipe from the sender fiber to the receiver fiber. On the contrary, when a liquid slug was present, the liquid phase absorbed the light beam and thus no signal was received. Given the straightforward characteristics of the flow in this small diameter upward pipe (unaerated slugs followed by low holdup Taylor bubbles), the detection of the phase present in the center of the pipe was enough to determine if a slug or a bubble was present at this given location. In order to increase the absorption of the liquid phase and therefore to improve the performance of our optical

probes, a blue colorant (Vulcanosol blue 6840, manufactured by BASF) was added to the water. In total, 6 optical probes were used, and arranged in 3 optical units (see figure 4) of 2 closely positionned probes. The data provided by the probes were sampled at a rate of 500 Hz and logged in a laptop PC with the help of a DAQCard-6036E (National Instruments).

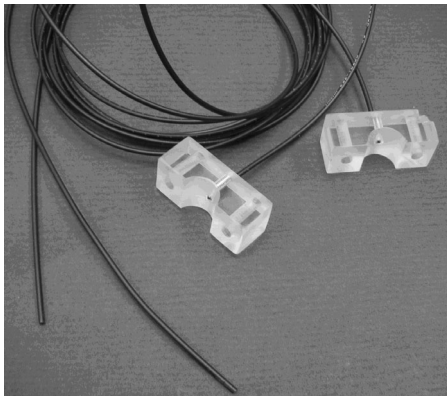


Fig 3: The optical sensors

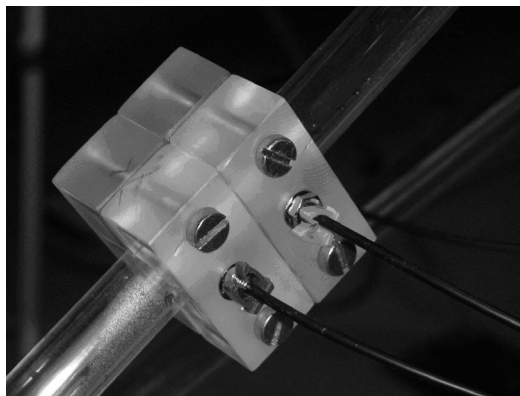


Fig 4: An optical unit

Simple signal processing in MATLAB was used to identify slug fronts and bubble noses in the time series provided by each of the probes. For each of the three optical units, the time needed by the bubble nose and the slug front to travel from one sensor to the other allowed to calculate the bubble nose and the slug front velocity. Finally, the length of a slug was evaluated as the product of its residence time in the optical unit by the average between its front velocity and its tail velocity. This corresponds to the length of the slug when its center crosses the first sensor. Figure 5 provides insight on the calculations done. For a small fraction of the slugs, the computed front or bubble nose velocity reached unphysical values, possibly due to the merging of two bubbles occurring between the two probes of one unit. These abnormal results were thus discarded.

3 Bubble nose velocity

The slug capturing scheme presented in this paper uses a closure law to evaluate the bubble nose velocity from the mixture velocity within the slug:

$$U_{nose} = C_0 U_m + \nu_0$$

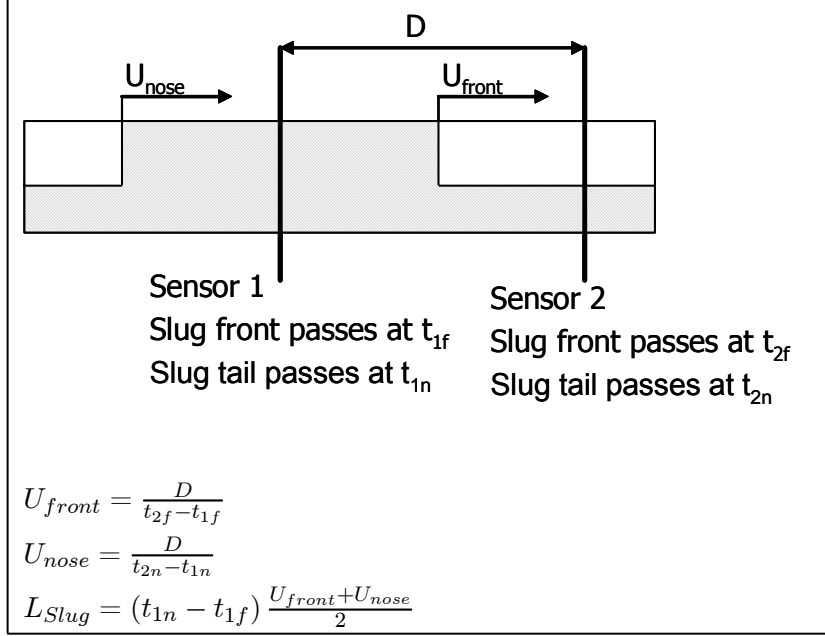


Fig 5: Data processing in an optical unit

where ν_0 stands for the bubble drift velocity in stagnant liquid, i.e. the speed at which a bubble rises in a pipe full of stagnant liquid.

Many experimentators have investigated the issue and proposed semi-empirical correlations for C_0 and ν_0 , depending on the pipe inclination, the pipe diameter and various other parameters such as fluid viscosities and surface tension. Davies and Taylor (1949) studied experimentally and theoretically the rise of bubbles in stagnant liquid in vertical pipes and showed that in those conditions the value of ν_0 was given by $0.35\sqrt{gD}$. Nicklin et al. (1962) then first presented the relation $U_{nose} = C_0U_m + \nu_0$ for vertical pipes, using Davies and Taylor's expression of ν_0 and a coefficient C_0 ranging between 1.2 for fully developed turbulent flow to 2.0 for laminar flows. Zukoski (1966) measured the velocity of large bubbles in horizontal pipes of stagnant liquid and found a value of $0.54\sqrt{gD}$ for ν_0 .

Finally Bendiksen et al. (1984) provided correlations for C_0 and ν_0 for all pipe inclinations based on both experimental and theoretical considerations. In the LASSI scheme, the correlation proposed by Bendiksen et al., which proved accurate for long pipes is normally used on a standard basis. Bendiksen's correlation gives the following expression for the drift velocity in a stagnant liquid:

$$\nu_0 = (0.35 \sin \varphi + 0.54 \cos \varphi) \sqrt{gD}$$

However, this value of ν_0 is not valid for very small diameter loops in which the capillary effects are not negligible and contribute to greatly reducing the

value of the drift velocity. The correct modelling of the bubble nose velocity being of primary importance for the accuracy of the model, it was therefore necessary to use a different closure to reproduce this set of experiments.

Zukoski (1966) studied experimentally the influence of viscosity, surface tension and pipe inclination angle on ν_0 and provided a chart giving the non-dimensional drift velocity $\frac{\nu_0}{\sqrt{\frac{\Delta\rho}{\rho}g\frac{D}{2}}}$ as a function of the inclination angle φ and the parameter $\Sigma = \frac{4\sigma}{gD^2\Delta\rho}$. With air and water and a pipe diameter equal to 1.2 cm, we find a value of 0.206 for Σ which finally gives for an inclination angle of 30° a predicted drift velocity of 0.116 m.s⁻¹. As a comparison, Bendiksen's closure law gives a value of 0.22 m.s⁻¹ for the drift velocity.

In order to validate the experimental set-up and verify the result provided by Zukoski, the drift velocity was measured experimentally for an inclination of 30° by injecting an air bubble right after the bend, the small-scale loop being entirely filled with water. The observed value of ν_0 was then 0.12 m.s⁻¹. This result being close to the prediction of Zukoski, a new closure for the drift velocity in the small scale loop was derived from Zukoski's predictions for horizontal and vertical pipes and implemented in the LASSI code:

$$\nu_0 = (0.28 \sin \varphi + 0.23 \cos \varphi) \sqrt{gD}$$

For the value of C_0 , Bendiksen's standard correlation was used as usual i.e. :

$$\begin{aligned} C_0 &= 1.05 + 0.15 \sin^2 \varphi & \text{for } Fr < 3.5 \\ C_0 &= 1.2 & \text{for } Fr > 3.5 \end{aligned}$$

4 Evolution of the slug length distribution in an upwards inclined pipe

4.1 Experimental results

For this experiment the small-scale loop was arranged as follows: the 2 meter long upstream pipe was inclined downwards with an inclination of 15° while the 2 meter downstream pipe was inclined upwards with an inclination of 30°. The two pipes were connected with a 5 cm long flexible plastic pipe. The three optical units were positioned respectively 20, 80 and 150 diameters downstream of the bend and provided for each recorded slug, its length, its front velocity and its tail velocity. A sketch of the experimental geometry is presented figure 6. The inlet liquid superficial velocity was maintained constant

at $U_{lin}^S = 0.22 \text{ m.s}^{-1}$ and the inlet gas superficial velocity was set to $U_{gin}^S = 0.44 \text{ m.s}^{-1}$. Due to the small scale of the loop, a recording time of 15 minutes was sufficient to record more than 2000 slugs and produce valuable statistical information.

Case I: Evolution of the slug length distribution in an upwards inclined pipe

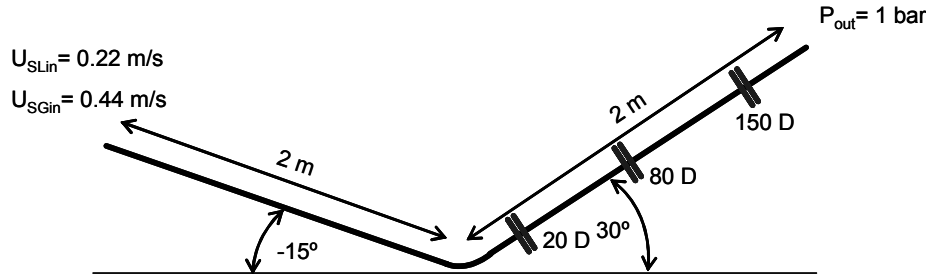


Fig 6: Case 1, sketch of the pipe geometry

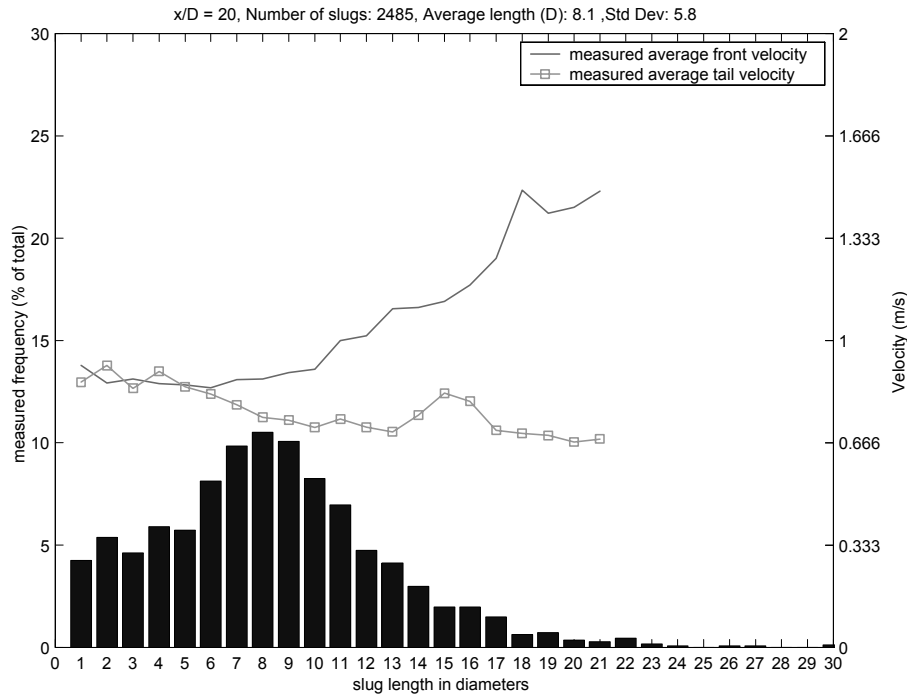


Fig 7: Observed slug length distribution after 20 diameters, case 1.

The observed slug length distribution after 20, 80 and 150 diameters are respectively shown figures 7, 8 and 9. In addition, the average front and tail velocities observed for a given class of slug length are plotted on the same graph. The experimental results clearly show an increase in the average slug length along the pipe, accompanied by a decrease in the number of slugs observed. Indeed, 20 diameters after the bend, nearly 2500 slugs were observed, with an average length close to 8 diameters. After 150 diameters, there were only 1250 slugs left, but their average length had increased up to 15 diameters.

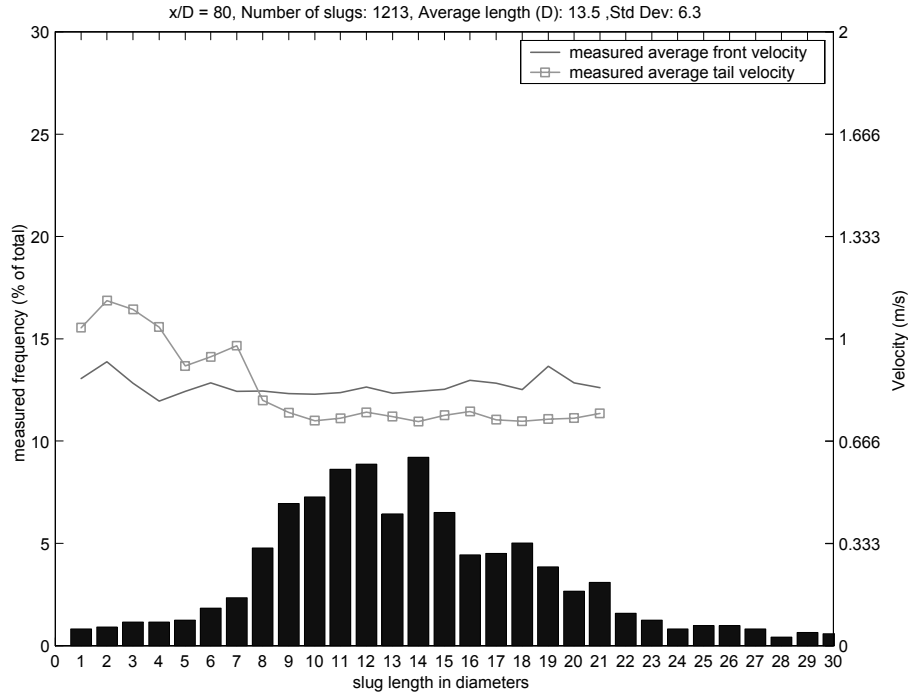


Fig 8: Observed slug length distribution after 80 diameters, case 1.

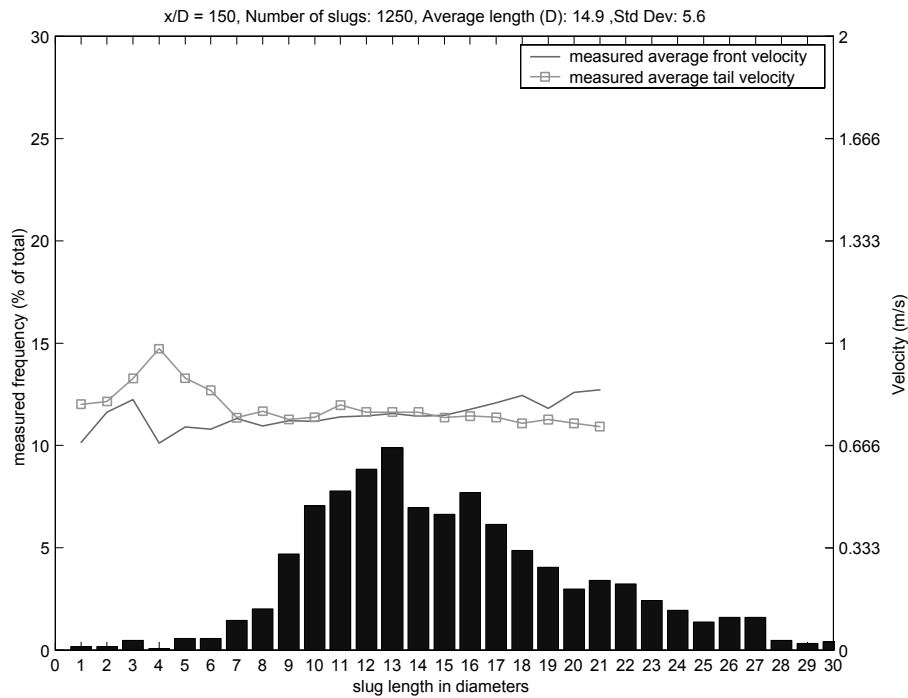


Fig 9: Observed slug length distribution after 150 diameters, case 1.

This increase in the average slug length along the pipe can be explained by the observed velocity profiles: the graph clearly shows that for the shortest slugs, the tail velocity tends to exceed the front velocity, causing the slug to eventually disappear. On the opposite, the slug front velocity is higher than the bubble nose velocity for the longest slugs, especially close to the bend. As

a consequence these long slugs will grow longer, picking up the liquid shed by the disappearing shortest slugs.

We can also observe that the slug length distribution has evolved much less between 80 and 150 diameters than between 20 and 80 diameters. Once the smallest slugs, whose length is inferior to 7 or 8 diameters have disappeared, the slug length distribution seems to evolve at a much slower rate.

4.2 Modelling of the wake effect

In order to capture the evolution of the slug length distribution along the pipe, it is crucial to model correctly the wake effect, i.e. the increase in the bubble nose velocity for the small slugs. Physically, this phenomenon can be explained by the fact that for very small slugs, the liquid velocity distribution at the tail has not yet reached its equilibrium value and is still influenced by the disturbances induced at the front of the slug. This results in a higher tail velocity for small slugs. The bubble nose velocity can then be expressed as:

$$U_{nose} = W_{eff}.U_{bubble}$$

where $U_{bubble} = C_0U_m + \nu_0$ is the expression of the bubble nose velocity for an infinitely long slug.

Several authors have investigated the phenomenon since Moissis and Griffith (1962) and proposed several correlations. The original Moissis and Griffith correlation was used for this paper, as in Nydal and Banerjee (1996). The expression used for W_{eff} was then, for a slug of length L_S :

$$W_{eff} = 1 + 8e^{-1.06\frac{L_S}{D}}$$

4.3 Simulation results

The case was simulated using the LASSI scheme, using a time step of 0.002 s and a targeted section length of 2 cm. Standard Blasius' friction factors were used to represent the liquid-wall, gas-wall and the liquid-gas friction. The standard Moissis and Griffith expression for W_{eff} was used for the modelling of the wake effect. The slug length, front velocity and tail velocity of all the passing slugs were extracted at six different locations of the downstream pipe (10, 20, 30, 40, 80 and 150 diameters after the bend).

The computed slug length distributions obtained in 15 minutes of simulation time are presented figure 10. Either after 20, 80 or 150 diameters, the computed slug length distributions look reasonably close to the ones observed in the experiments. However, it seems that the model underestimates the frequency of the "extreme slugs", i.e. more very short and very long slugs were observed in the experiments than in the simulations. The average slug length is thus slightly underestimated in the simulations (the average slug was 13.5 diameters long after 80 diameters in the experiments, while it was only 10.7 diameters long in the simulations).

Moreover, the total number of observed slugs is much higher in the simulations than in the experiments. This could be explained by a poor modelling of the holdup and liquid velocity in the bubbles. However, this is not necessarily a modelling problem: since it was sometimes difficult to capture tiny bubbles and very short slugs with the optical probes, some of the shortest slugs might have been simply missed by the sensors. Some of the shortest objects were also discarded later at the data processing stage, for example when a slug passed by the first of the two optical probes of one optical unit and had disappeared before it had reached the second probe located 2 cm away.

The slug tail velocity for the longest slugs seems to be slightly lower in the experiments than in the simulations, although the drift velocity used in the computations was calibrated from experimental measurements. For the shortest slugs where the wake effect is the dominating effect, the difference between experiments and simulation is however much bigger. It seems that the wake effect, defined as the ratio between the tail velocity of the shortest slugs and the tail velocity of the longest slugs, never exceeded 1.5 in the experiments. On the other hand, the wake effect model used in the simulations yielded some extremely high bubble nose velocities for the shortest slugs. This constatation motivated the study presented in the next section.

4.4 On the importance of the wake effect on the simulations

The results presented figure 10 clearly showed that Griffith's correlation, used in the scheme to model the wake effect, had a clear tendency to overestimate the tail velocity of the shortest slugs. Indeed, it was experimentally observed that even for the shortest slugs, the tail velocity never exceeded the value predicted by Bendiksen's correlation by more than 30 to 50%. It was then thought that the wake effect coefficient W_{eff} should be capped to prevent the tail velocity of the short slugs from reaching excessive values. Two additional simulations were then carried out in which the wake effect coefficient W_{eff}

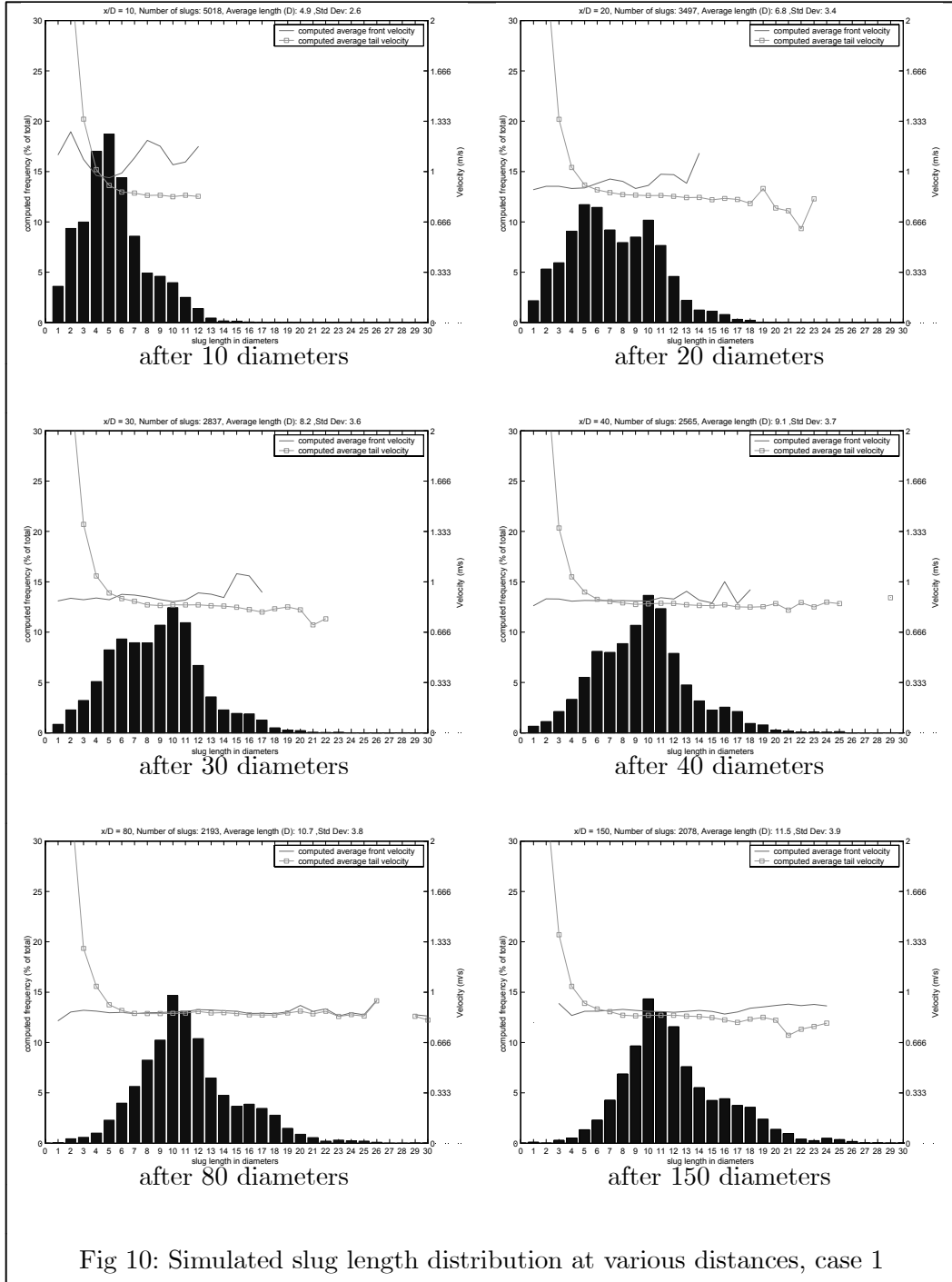


Fig 10: Simulated slug length distribution at various distances, case 1

was capped respectively by 2 and by 1.5. The obtained slug length distributions after 20 and 80 diameters are shown figure 11. The experimental results and the results obtained in the previous section with the uncapped Griffith correlation are recalled for comparison.

The numerical results are clearly not improved by the implementation of a cap in the wake effect. Although the use of a cap helps to reproduce the slug tail

velocities observed for the shortest slugs, it prevents the slug length distribution to evolve rapidly enough to match the experiments. There is therefore an apparent paradox in the fact that it is necessary to overestimate the bubble nose velocity for the shortest slugs in order to correctly predict the evolution of the slug length distribution. However, the experimental set-up did not allow very precise measurements for very short slugs and other experimentators such as van Hout et al. (2001) observed in similar conditions tail velocities in the order of twice the value given by Bendiksen's correlation.

Given those considerations, it was concluded that Griffith's correlation for the wake effect coefficient was adequate. In the rest of the paper, the coefficient W_{eff} will then be set to $W_{Griffith}$.

5 Influence of the upstream flow regime on the downstream slug length distribution

5.1 Principle

For case 2, a shorter upstream pipe is used. In case 2A, the upstream pipe is also inclined upwards, with an inclination angle of 2 degrees (see figure 12). A slug flow regime, characterized by short slugs, will then be established in the upstream pipe. The downstream pipe is still inclined 30° upwards. The aim of case 2A is to monitor how the slug length distribution established in the first pipe will evolve after the bend. Another interesting point is to compare the slug length distribution observed at the end of the downstream pipe when slug flow is established in the upstream pipe (case 2A) and when stratified flow is established in the upstream pipe (case 2B).

The first optical unit was positioned at the end of the first pipe, 10 diameters upstream of the bend. Two additional optical units were placed in the second pipe, respectively 50 and 120 diameters downstream of the bend. Figure 12 presents a sketch of the experimental set-up. The inlet liquid superficial velocity was maintained constant to $0.27 \text{ m}\cdot\text{s}^{-1}$ and the inlet gas superficial velocity was set to $0.44 \text{ m}\cdot\text{s}^{-1}$.

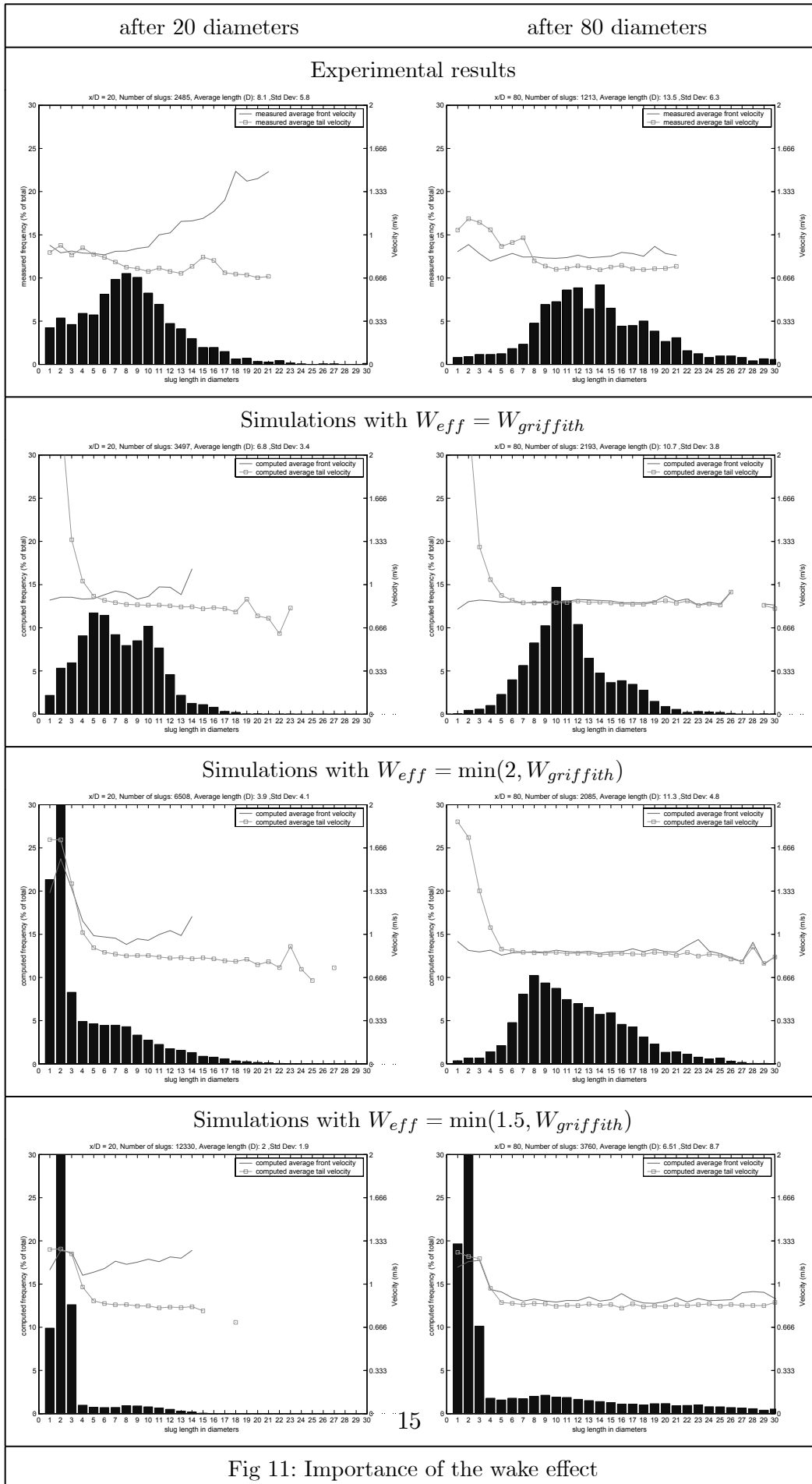


Fig 11: Importance of the wake effect

Case II: Evolution of the slug length distribution in an upwards inclined pipe

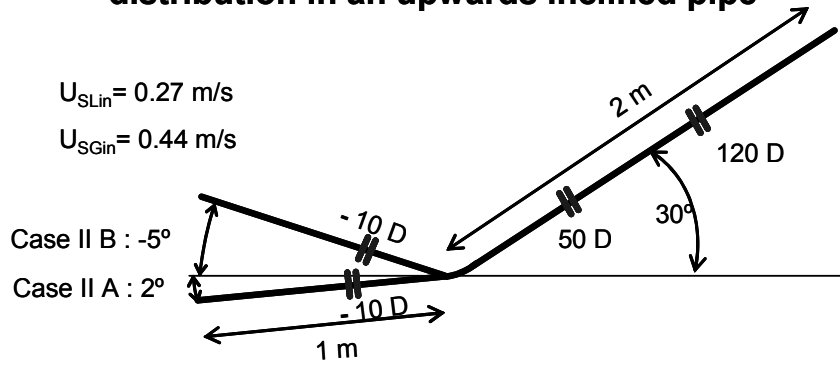


Fig 12: Case 2, sketch of the pipe geometry

5.2 Experimental results

Experimental results for case 2A are shown figures 13 to 15. The flow regime in the upstream pipe (figure 13) is characterized by very short slugs, averaging 3.5 diameters in length. The slug length distribution changes drastically in the downstream pipe where the average slug length reaches 11 diameters 50 diameters after the bend and 13 diameters 120 diameters downstream of the bend.

As a comparison figure 16 shows the experimental slug length distribution observed when the upstream pipe is inclined downwards with an inclination angle equal to 5° (case 2B). The flow regime established in the upstream pipe is then stratified flow. The slug length distribution observed 120 diameters downstream of the bend in those conditions (case 2B) is extremely similar to the one observed with a slug flow regime established in the upstream pipe (case 2A). We can then conclude that in this small scale loop, the flow regime in the upstream pipe does not seem to have any strong influence on the flow characteristics in the downstream pipe.

5.3 Simulation results

Case 2 was simulated with the LASSI scheme using a time step of 1 ms and a section size of 1 cm. Griffith's standard "uncapped" correlation was used to model the wake effect. Figures 17 to 19 show the slug length distributions recorded in 15 minutes of simulation time, 10 diameters upstream of the bend and 50 and 120 diameters downstream of the bend for the different values of the upstream gas volume. Regarding the slug length distributions, the scheme

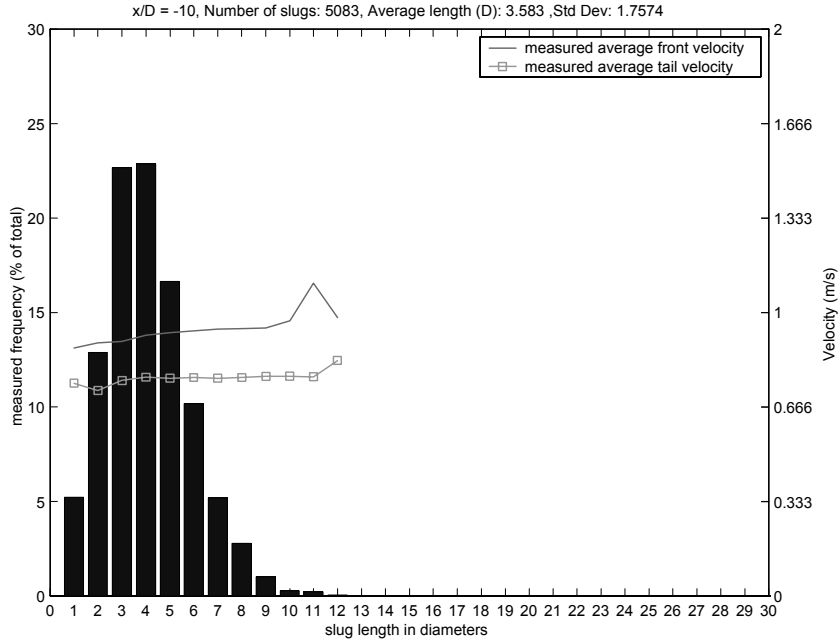


Fig 13: Observed slug length distribution 10 D before the bend (Case 2A)

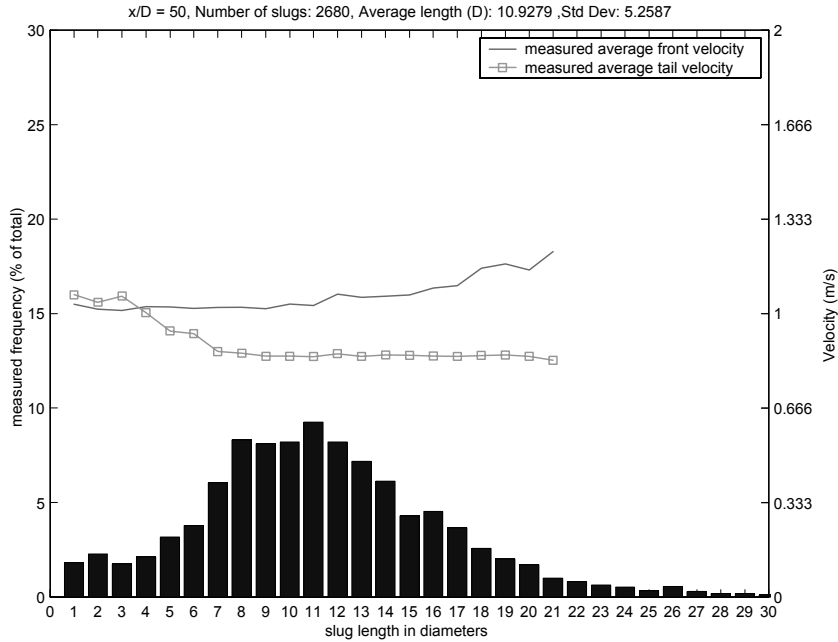


Fig 14: Observed slug length distribution 50 D after the bend (Case 2A)

predictions show a very good match with the experimental observations. It looks on the other hand that the front velocity of the long slugs is underestimated by the model, while the tail velocity of the smallest slugs is as observed before, highly overestimated.

Figure 20 shows the results obtained 120 diameters downstream of the bend when simulating case 2B with the LASSI scheme. As what was observed experimentally, the simulations predict only little difference between cases 2A

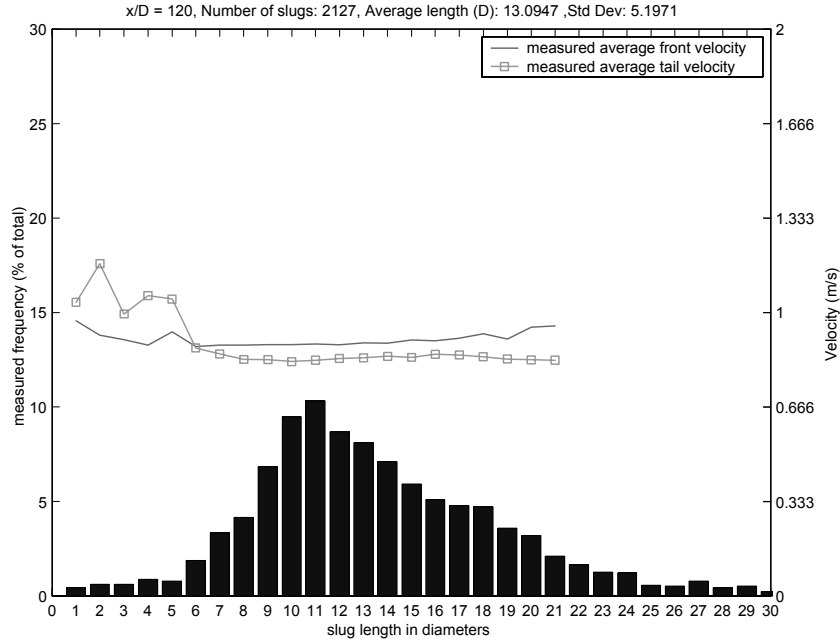


Fig 15: Observed slug length distribution 120 D after the bend (Case 2A)

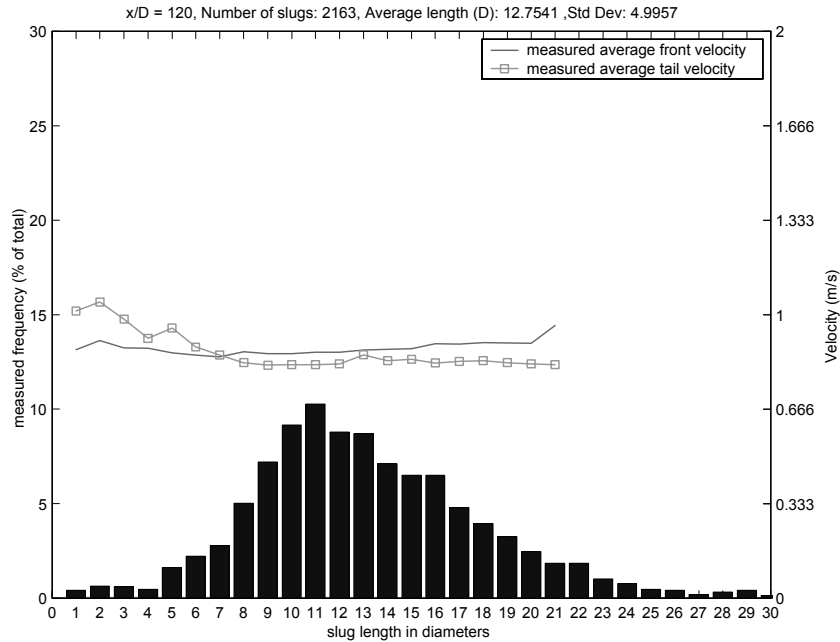


Fig 16: Observed slug length distribution 120 D after the bend (Case 2B)

and 2B. Figure 21 shows snapshots of the LASSI scheme for case 2A and 2B, which clearly show that the upstream flow regime has little influence on the situation far enough in the downstream pipe.

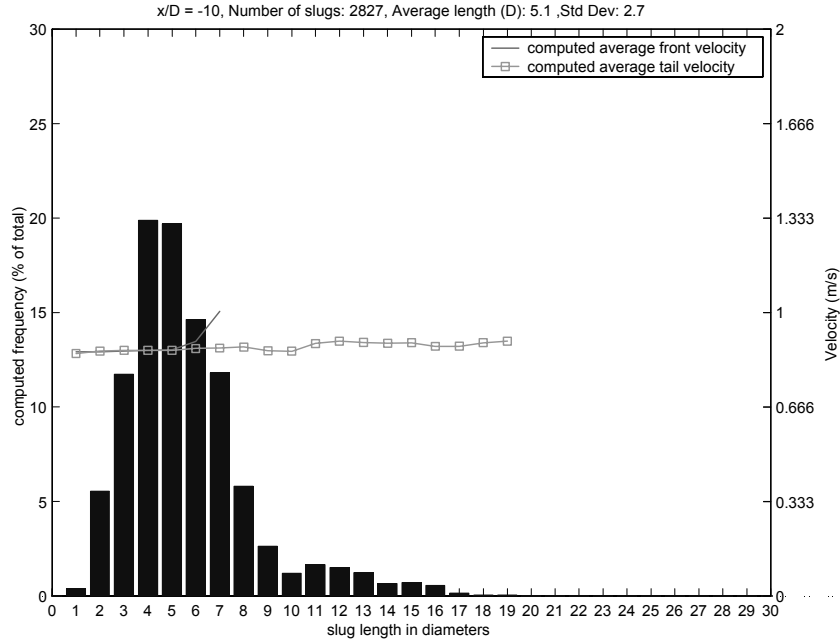


Fig 17: Computed slug length distribution 10 D before the bend (Case 2A)

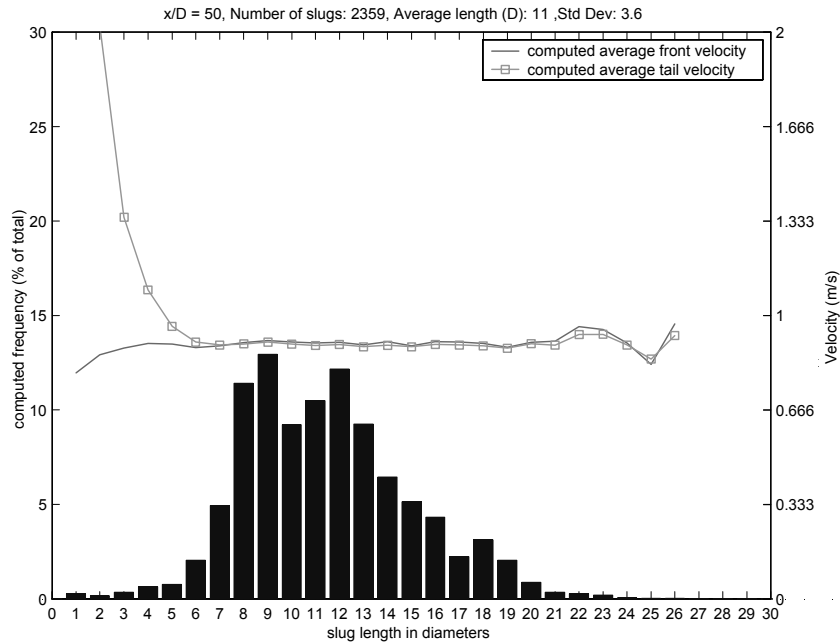


Fig 18: Computed slug length distribution 50 D after the bend (Case 2A)

6 Transition from slug flow to severe slugging

6.1 Principle

The idea is to observe the transition from normal slug flow to severe slugging within a V-shaped pipe. The small scale loop is set-up as shown in figure 22.

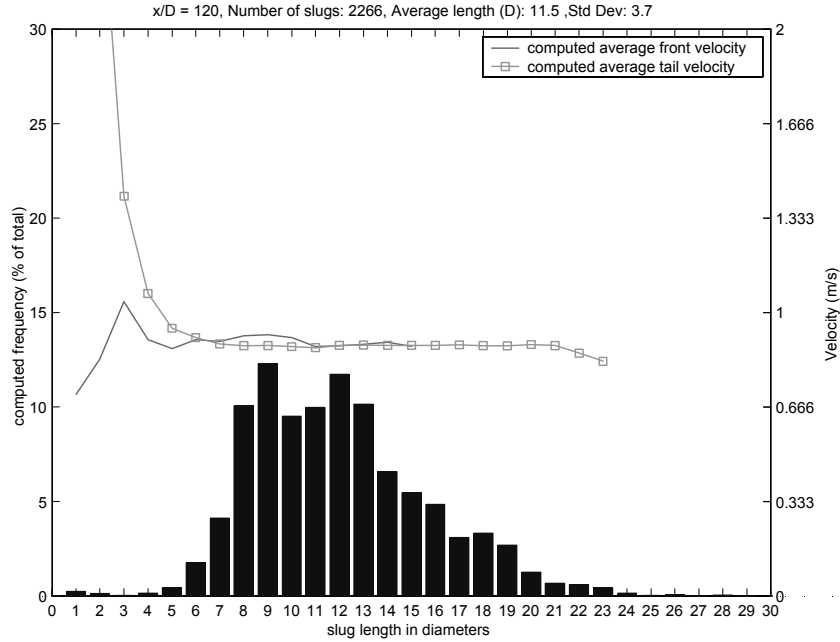


Fig 19: Computed slug length distribution 120 D after the bend (Case 2A)

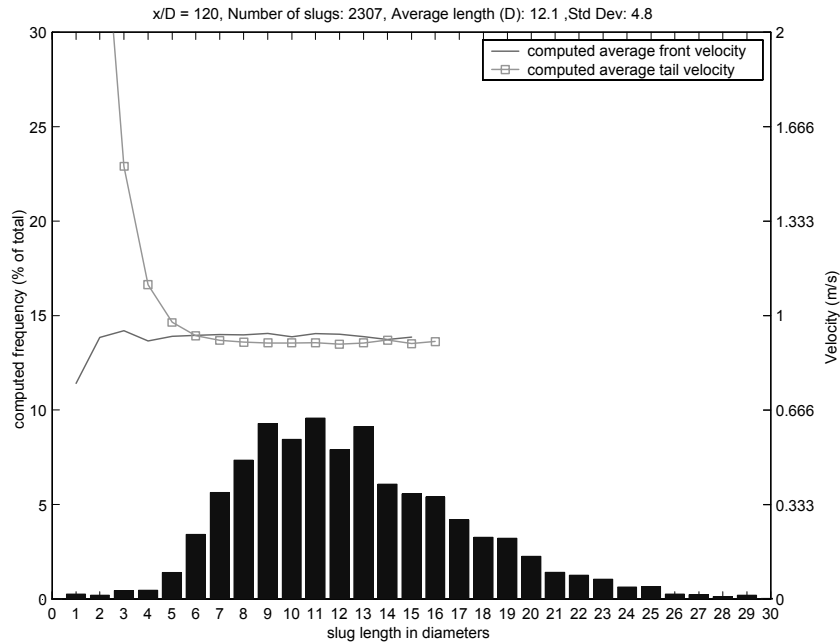
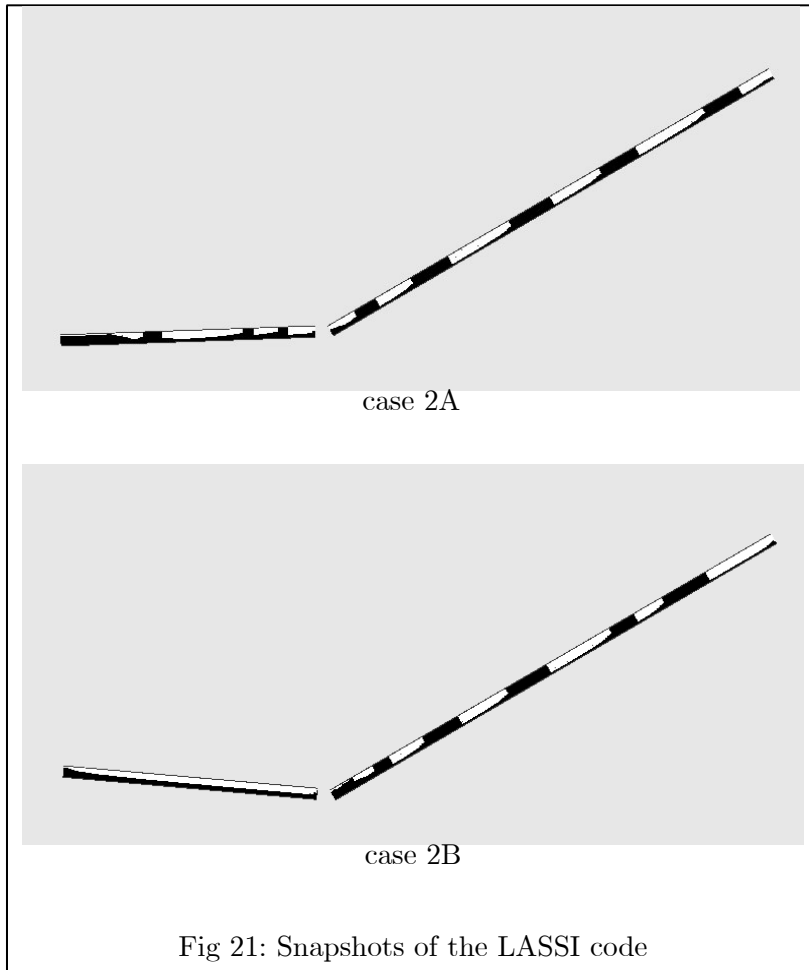


Fig 20: Computed slug length distribution 120 D after the bend (Case 2B)

Both the upstream and downstream pipe are inclined with an angle of 30° . A gas tank with a total volume equivalent to 23.8 meters of empty pipe, is added at the inlet to add compressibility to the system. The inlet tank can be partly filled with water, hence reducing the inlet gas volume, so that it is possible to run experiments with any upstream gas volume equivalent to between 0 and 23.8 meters of empty pipe length.

On the downstream pipe, a sensor is installed 80 diameters downstream of



the pipe. The slug length distribution is recorded at this location for various values of the upstream gas tank. The objective of this experiment is to observe how the bell-shaped length distribution characteristic of normal slug flow will evolve when the upstream compressibility is increased.

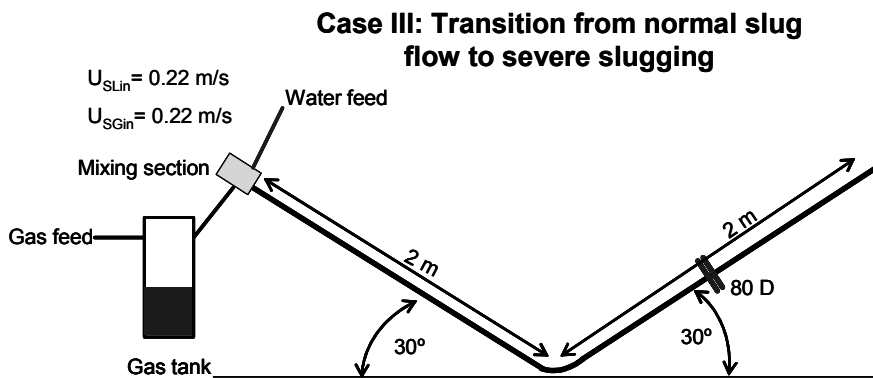


Fig 22: Case 3, sketch of the pipe geometry

6.2 *Experimental results*

Figure 23 presents the observed slug length distribution 80 diameters downstream of the bend, for upstream gas volumes of 0%, 20%, 40%, 60%, 80% and 100 %. A value of 100% corresponds to a tank volume equivalent to 23.8 meters of empty pipe.

For no upstream gas tank (0% gas volume), the slug length distribution is similar to the one observed in case 1. In particular the slug front velocity exceeds the bubble nose velocity for the longest slugs while the opposite is true for the smaller slugs.

The slug length distribution does not evolve significantly when the upstream gas volume is increased from 0% to 60%, and the average slug length stays constant at 11.3 diameters.

When the upstream gas volume reaches 80%, the system enters severe slugging and we notice the appearance of very long slugs filling all of the downstream pipe. The blow out is in the form of slug flow, and it is interesting to see that the slug length distribution during the blow out is quite similar to the distribution in steady slug flow. However, the slug front and nose velocities appear much more irregular in severe slugging, this is probably due to the somehow extreme instabilities that occur during the blow out phase of the severe slugging cycle.

6.3 *Numerical results*

The case has been simulated with LASSI using a time step of 2 ms and a section size of 2 cm. Griffith's standard model was used for the wake effect and Blasius friction factors were used in the simulation. Figure 24 shows the slug length distributions predicted by the simulations 80 diameters downstream of the bend for the different values of the upstream gas volume.

When the available inlet gas volume amounts to 0%, 20% and 40% of the total inlet tank volume, the simulation results are very similar to the experimentally observed distributions, with a predicted average slug length of around 10 diameters. However, when the upstream gas tank volume is increased to 60%, the predicted distribution changes significantly and appears as a double "bell" curve. This phenomenon corresponds to a normal slug flow regime with periodic eruptions of larger slugs and an unstable upstream pressure. This state can be seen as an intermediary between normal slug flow and severe slugging,

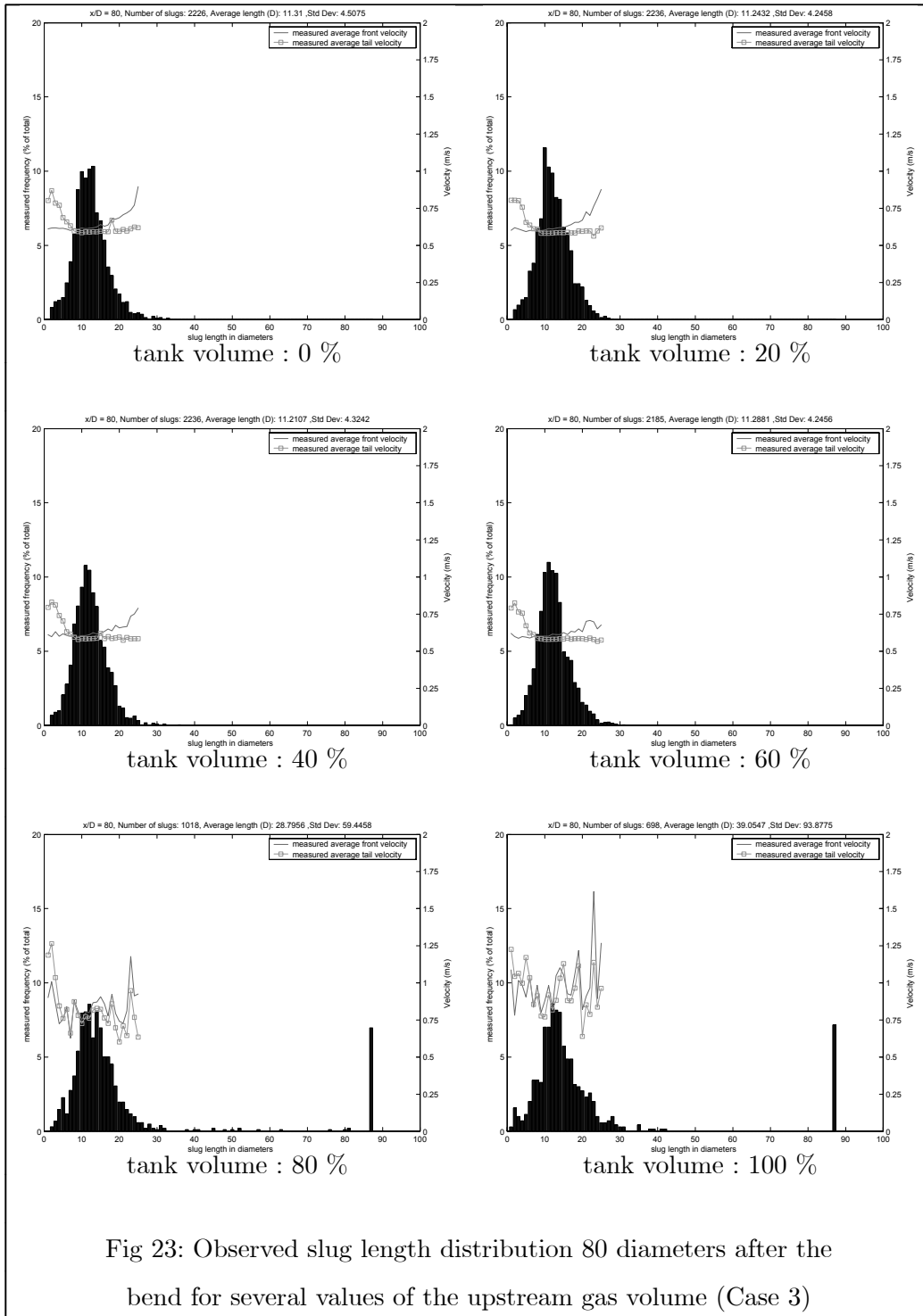


Fig 23: Observed slug length distribution 80 diameters after the bend for several values of the upstream gas volume (Case 3)

thus transition from normal slug flow to severe slugging seems to occur in a smoother way in the simulations than experimentally.

For higher tank volumes (80% and 100%), although the computed distributions are close to the observations, some questions are raised by the large discrepancy between the computed tail and front velocities of the short slugs

and the observed tail and front velocities. The simple model used by LASSI can not be expected to resolve all the details of the flow during the blow-out, but it seems that the blow-out phase occurs at a much faster mixture velocity in the computations than in the experiments.

In addition, it appears that the LASSI scheme predicts both fewer and shorter slugs than what was observed experimentally. This leads us to think that the holdup and liquid velocity within the bubbles were incorrectly reproduced in the model. This is probably due to an underestimation of the momentum loss that occurs at the tail of the slugs. As the slugs shed some liquid at their tail, it is indeed important to know how much momentum this high velocity liquid loses when it exits the slug and mixes with the liquid film that follows. If this momentum loss is underestimated, the liquid velocity within the bubbles will be overestimated, potentially leading to a decreased slug fraction.

Finally, as an illustration, figure 25 and 26 represent the computed holdup profile, pressure profile and inlet pressure time series when the inlet gas volume is set to respectively 0 and 100% of its total maximum value.

7 Conclusion

Using affordable and easily available optical devices, a study on the evolution of the slug length distribution along a small diameter pipe was conducted. The experimental set-up was able to clearly show that the tail velocity of the shorter slugs exceeded the velocity of their front, leading eventually to their disappearance. For our experimental conditions, all slugs shorter than a minimum length of around five diameters eventually disappeared and the slug length distribution evolved towards an average slug length of 12 diameters. In addition, it was shown that 100 diameters after a bend, the slug length distribution had reached a nearly stationary form.

For our gravity dominated flows, the upstream flow regime was shown to have little influence on the flow conditions within the downstream pipe. The flow characteristics 100 diameters downstream of the bend did not appear to depend on the flow regime (stratified or slug flow) in the upstream pipe.

As the upstream gas volume was increased the transition to severe slugging was observed. The liquid blow-out was in the form of gas-liquid slug flow and the statistical slug length distribution during the blow-out was similar to the steady state distribution.

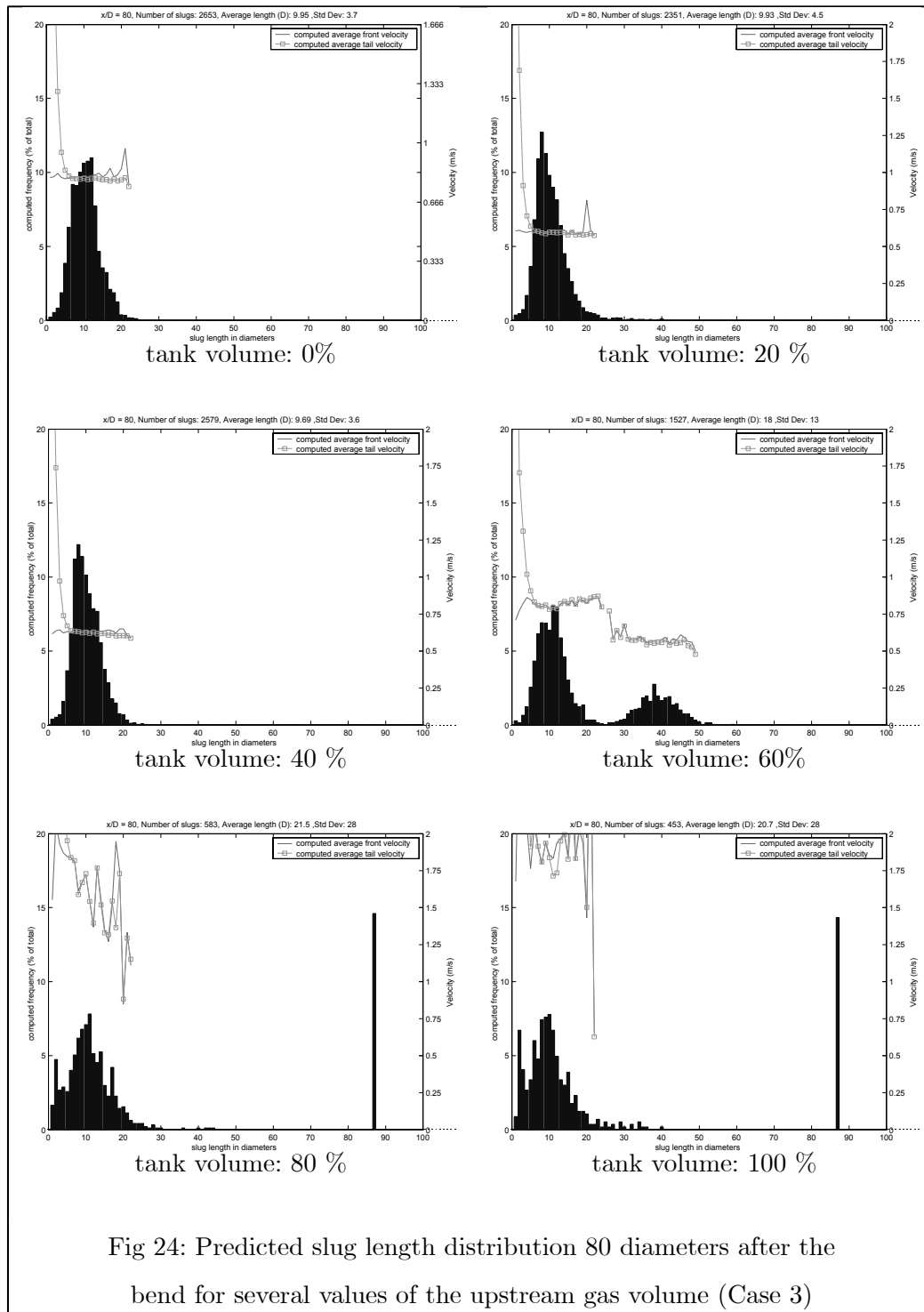


Fig 24: Predicted slug length distribution 80 diameters after the bend for several values of the upstream gas volume (Case 3)

The LASSI code presented in Renault et al. (2007) is both slug capturing and slug tracking: the slug generation phenomenon is captured automatically by the numerical scheme without using any slug initiation criterion. Each generated slug is then tracked individually as it propagates along the pipe: the slug fronts are modelled as propagating shocks and the slug tails are supposed to propagate according to a given relation for bubble propagation.

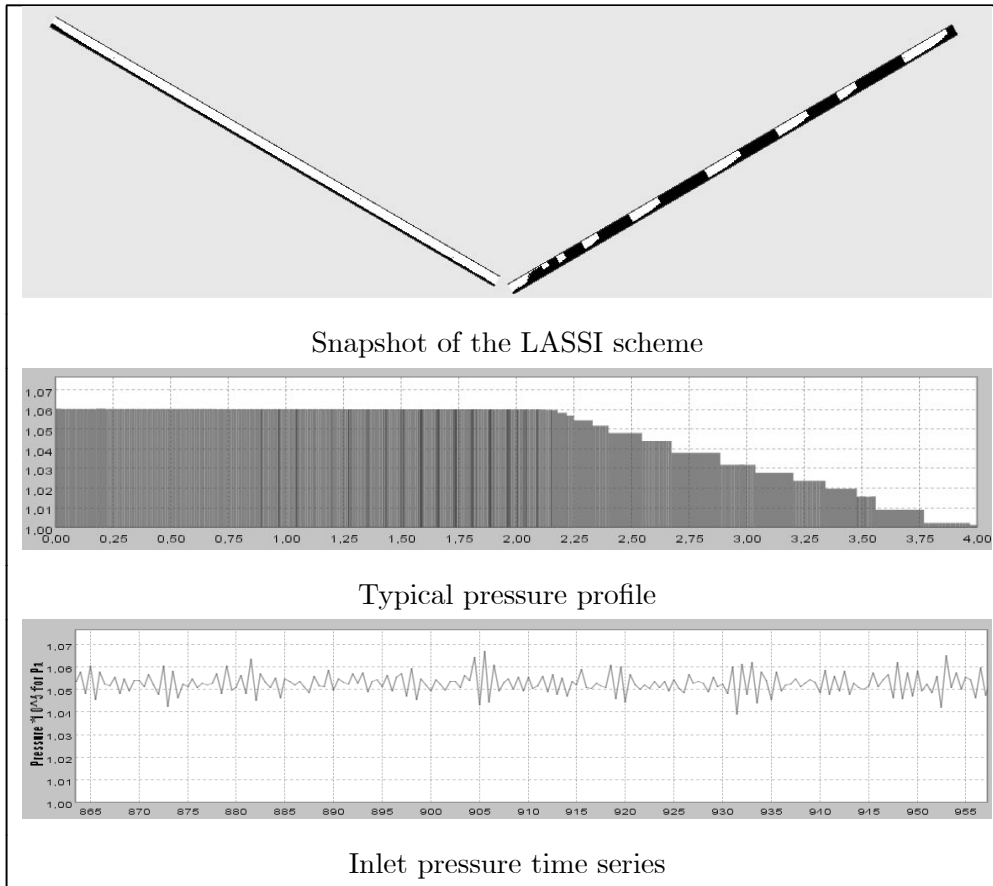


Fig 25: Case 3, LASSI predictions with no inlet gas volume (0%)

All the experimental observations on slug length distributions were compared to simulations run with the LASSI code. On the whole, a fair match was observed between the numerical predictions and the observations. As expected, a proper modelling of the wake effect is crucial to a correct prediction of the slug length distribution. Given this prerequisite, the slug capturing method used in the LASSI code was shown to be able to generate slugs in an adequate way allowing the code to correctly reproduce the evolution of the slug length distribution.

The well-known importance of the wake effect for the modelling of slug flow was confirmed by this study. In this respect, the slug tracking character of the LASSI scheme, which allows any closure for the slug tail velocity to be implemented directly into the scheme, gives the scheme a great flexibility that does not exist in direct simulation schemes in which the slugs are not tracked as individual objects but are propagated according to the equations of the two-fluid model.

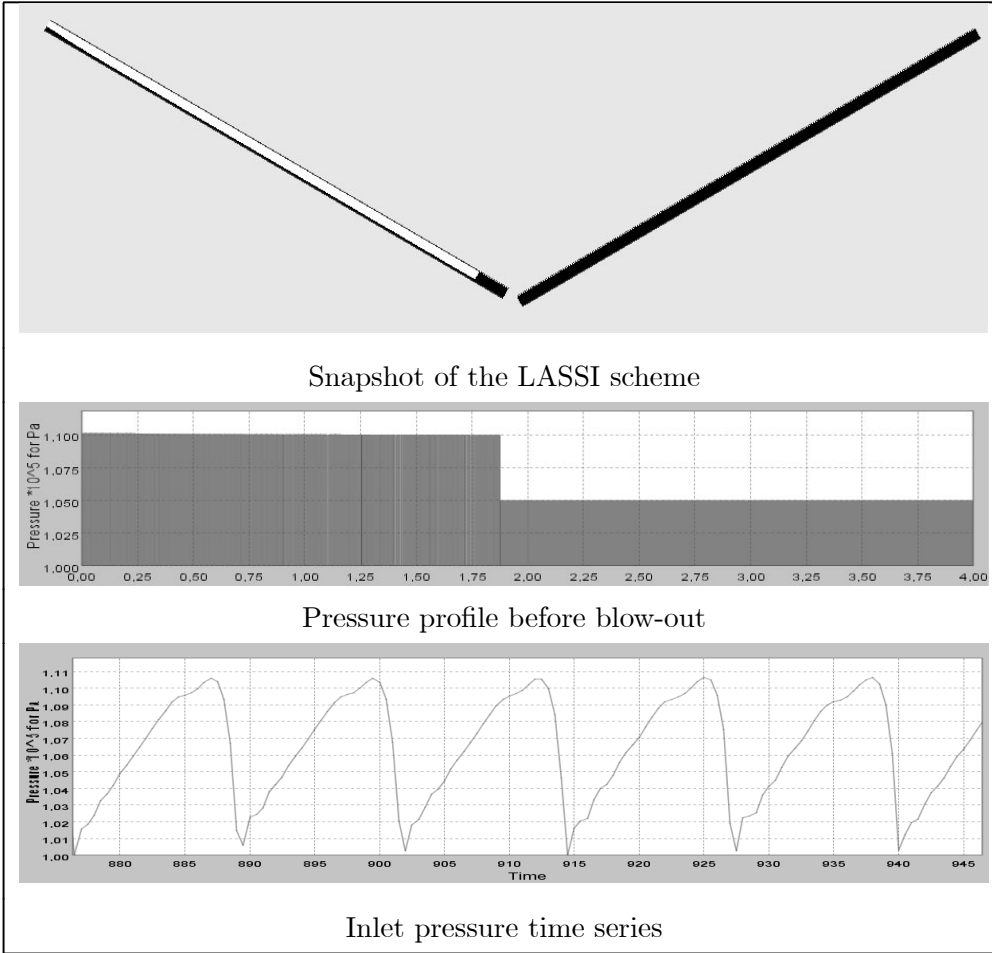


Fig 26: Case 3, LASSI predictions with full inlet gas volume (100%)

References

- Andreussi, P., Bendiksen, K., Nydal, O., 1993. Void distribution in slug flow. *Int. J. Multiphase Flow*, 19, 817-828.
- Barnea, D., Taitel Y., 1993. A model for slug length distribution in gas-liquid slug flow. *Int. J. Multiphase Flow*, 19, 829-838.
- Barnea, D., Brauner, N., 1985. Holdup of the liquid slug in two phase intermittent flow. *Int. J. Multiphase Flow*, 11 43-49.
- Barnea, D., Shemer, L., 1989 Void-fraction measurements in vertical slug flow: applications to slug characteristics and transition. *Int. J. Multiphase Flow* 15, 495-504.
- Bendiksen, K.H., 1984. An experimental investigation of the motion of long bubbles in inclined tubes. *Int. J. Multiphase Flow* 10, 467-483.
- Bendiksen, K. H., Malnes, D., Moe, R., Nuland, S., 1991. The dynamic two-fluid model OLGA: Theory and application. *SPE production engineering* May 1991, 171-180
- Davies, R.M., Taylor, G. I., 1949. The mechanics of large bubbles rising through extended liquids and through liquids in tubes. *Proc. Roy. Soc. London* 200 Am 375-390.
- Griffith, P., Wallis, G. 1961. Two-phase flow. *Journal of Heat Transfer* 83, 301-320.
- Issa, R.I., Kempf, M.H.W., 2003. Simulation of slug flow in horizontal or nearly horizontal pipes with the two-fluid model. *Int. J. Multiphase Flow* 29, 69-95.
- Moissis, R., Griffith, P., 1962. Entrance effects in a two-phase slug flow. *Journal of Heat Transfer*, 84, 366-370.
- Nicklin, D. J., Wilkes, J. O., Davidson, J. F, 1962. Two-phase flow in vertical tubes. *Trans. Inst. Chem. Eng*, 40, 61-68.
- Nydal, O.J., Pintus, S., Andreussi, P., 1992. Statistical characterization of slug flow in horizontal pipes. *Int. J. Multiphase Flow* 18, 439-453.
- Nydal, O.J., Banerjee, S., 1996. Dynamic slug tracking simulations for gas-liquid flow in pipelines. *Chem. Eng. Commun.* 141-142, 13-39.
- Renault, F., Nydal, O. J., 2007 A simple slug capturing and slug tracking scheme for gas-liquid pipe flow. Part 1: presentation of the scheme, Preprint.

Shemer, L., 2003. Hydrodynamic and statistical parameters of slug flow. *Int. J. Multiphase Flow* 24, 334-344

Taitel, Y., Barnea, D., 1997 Simplified transient simulation of two-phase flow using quasi-equilibrium momentum balances. *Int. J. Multiphase Flow* Vol. 23, No. 3, 493-501.

Taitel, Y., Barnea, D., 2000. Slug-tracking model for hilly terrain pipelines. *SPE Journal* 5 (1): 102-109.

Van Hout, R., Barnea, D., Shemer, L., 2001. Evolution statistical parameters of gas-liquid slug flow along vertical pipes. *International Journal of Multiphase Flow*, 27, 1579-1602.

Van Hout, R., Shemer, L., Barnea, D., 2003. Evolution of hydrodynamic and statistical parameters of gas-liquid slug flow along inclined pipelines. *Chemical Engineering Science*, 58, 115-133.

Zukoski, E., 1966. Influence of viscosity, surface tension, and inclination angle on motion of long bubbles in closed tubes. *Journal of Fluid Mechanics*, 25, 821-837.

Third Paper

An experimental and numerical study of flow regime transitions associated with fast flowrate changes in gas-liquid pipe flow.

Fabien Renault, Monika Johansen and Ole Jørgen Nydal

Preprint

An experimental and numerical study of flow regime transitions associated with fast flow rate changes in gas-liquid pipe flow

Fabien Renault ^{a,*} Monika Johansen ^a Ole-Jorgen Nydal ^a

^a*Department of Energy and Process Technology, University of NTNU, Trondheim, Norway*

Abstract

Flow regime transitions associated with fast changes in the inlet gas flow rate were investigated both experimentally in a 6 cm air-water pipe, and numerically with a Lagrangian slug capturing and slug tracking scheme. As liquid transport occurs at a much slower speed than the fast pressure wave associated with a change in the inlet gas velocity, a fast increase or decrease in the inlet gas flow rate creates an intermediate state characterized by the liquid holdup of the previous equilibrium state and the new gas flow rate. Experimentally, while a steady stratified flow regime was established in the pipe, a sudden increase in the inlet gas flow rate resulted in a short episode of slug flow. Similarly, when the gas flow rate at the inlet was suddenly decreased, a short period of stratified flow was observed between two periods of established slug flow. Numerical predictions from the LASSI scheme were shown to be in good agreement with the experimental observations. The LASSI scheme was also used to reproduce the severe slugging regime observed experimentally in a S-shaped riser.

Key words: two-phase flow, slug flow, flow rate transients, slug initiation

1 Introduction

The study of gas-liquid flow in pipes has many industrial applications, such as the transport of hydrocarbons in the oil industry or water-vapour mixture in power plants. One of the most fascinating aspects of gas-liquid pipe flow is the great diversity that exists in the different flow patterns that can arise depending on the flow rates and other conditions such as densities and pipe

* Corresponding author: fabien.a.renault@ntnu.no

inclination. Thus the determination of the correct flow regime is often a prerequisite to the calculation of the other flow parameters. In this aim, experimental flowmaps were first made, followed by semi-empirical transition criteria. Both of these approaches were well suited to make steady state predictions.

However two-phase flow is intrinsically unsteady in its very nature, and should probably be modelled as such. In this aim, transient two-phase codes such as OLGA (Bendiksen et al., 1991) were developed to capture more of the physics involved. Transient two-phase flow schemes soon raised the question of the modelling of the flow regime transitions, one of the biggest challenges of two-phase flow computations. In particular, the transition from stratified to slug flow presents a great complexity because of its chaotic nature, and because of the great diversity of the slug initiation mechanisms. Slugs can indeed be initiated due to liquid accumulation at the low points of the pipe until the liquid bridges the pipe and forms a blockade which will either travel down the pipe as a slug or, if the upstream gas compressibility is high enough, form a severe slug, which can be seen as the most extreme case of slug flow. Another mechanism is the sometimes quite slow growth of small perturbations at the gas-liquid interface due to the hydrodynamic instability of stratified flow at those conditions. Fast variations of the gas velocity, due to operational transients or to system-dependent effects such as the departure of a previous slug, can also trigger slug initiation.

Issa et al. (2003) first introduced a scheme called TRIOMPH capable to automatically capture the transition from stratified to slug flow. The scheme proved able to predict the stratified to slug flow transition in good accordance with the experimental observations.

The LASSI (Lagrangian Approximate Scheme for Slug Initiation) scheme is a slug capturing and slug tracking scheme specially designed to tackle the stratified-slug flow transition. In LASSI, the initiation of slugs is automatically captured by the scheme, without using any arbitrary insertion criterion providing either the slug frequency or the insertion position. After its initiation, each individual slug is tracked by the scheme as it propagates downstream according to Bendiksen's closure for the propagation of Taylor bubbles (Bendiksen et al., 1984). This is not the case in Issa et al. (2003) where no closure is used for the Taylor bubble velocity and where the slug propagation relies only on solving the two-fluid model. The LASSI scheme can then be seen as an intermediary between a full two-fluid model such as TRIOMPH or OLGA and an approximate slug tracking scheme such as Nydal et al. (1996) or Taitel et al. (2000).

In a first paper (Renault et al., 2007, [1]) the ability of the scheme to reproduce accurately an experimental flowmap in horizontal and near-horizontal flow was investigated. Transition from smooth stratified flow at the inlet of

the pipe to slug flow occurred by the slow growth of tiny waves that evolved into slugs when they eventually bridged the pipe. The predicted transition points were found in good agreement with the VKH criterion (Viscous Kelvin Helmholtz) and the experimental literature. In a second paper (Renault et al., 2007, [2]), the LASSI scheme was used to predict the slug length distribution in an upwardly inclined small diameter pipe in various conditions. The predictions compared well to the experimental observations, provided that an adequate wake effect model was used to calculate the slug tail velocity. The slug tracking nature of the LASSI scheme, which makes the use of any experimental closure for the slug tail velocity very convenient, proved in this respect very useful.

In this present paper, the slug capturing ability of the LASSI scheme is used to investigate flow regime transitions associated with fast changes in the gas inlet flow rate. The predictions from the LASSI scheme are then compared with selected experiments conducted in a 6 cm horizontal pipe. The study of those phenomena is important in an industrial context, for example in the oil industry where fast changes in production within the wells can have important consequences on the downstream flow conditions. In addition, these flow regime transitions associated to fast transients make the most of transient slug capturing schemes and provide interesting test cases to assess their accuracy.

The effects of flow rate transients on the flow regime have been studied experimentally, theoretically and numerically for a long period. Taitel et al. (1978) used a simplified semi-steady two-fluid model in order to predict the appearance of an episode of stratified flow in-between an initial state of annular flow and a final state of slug flow. The predictions matched well with the experiments conducted in a 3.8 cm pipe. Minami (1991) used a very long pipe (420 m) to conduct experiments investigating the effects of a sudden increase in the inlet gas flow rate on the inlet pressure.

King et al. (1998) probably conducted the most comprehensive experimental study on flow rate transients in a 3 inch diameter 36 meters long pipe. Every possible type of variation in the inlet flow rates ("up-gas", "down-gas", "up-liquid", "down-liquid") was experimented. When the inlet gas flow rate was increased suddenly while stratified flow was established in the pipe, a temporary period of intense slugging was observed. In addition, the inlet pressure was found to peak above the new steady state value before recovering. Similarly, a sudden decrease in the inlet gas flow rate in a slug flow regime, caused a period of stratified flow to appear before slug flow was re-established. On the contrary, fast changes in the inlet liquid flow rate had limited impact on the flow.

The main objective of this work is to test the LASSI scheme ability to capture flow regime transitions associated with those sudden changes in the gas inlet

flow rates. "Up-gas" and "down-gas" experiments were conducted in a 16 m long, 6 cm diameter pipe in the NTNU multiphase flow laboratory in Trondheim, Norway. Compared to the experiments conducted by King et al.(1998), the flow rates used were significantly lower.

The first chapter of this paper is devoted to recalling the two criteria governing the flow regime transition between stratified and slug flow : the Viscous Kelvin Helmholtz criterion and the Minimum Holdup criterion. They are intrinsically embedded within the LASSI scheme. Then the LASSI scheme itself is briefly introduced, more details can be found in (Renault et al., 2007, [1]). The first case presented is an "up-gas" case: the LASSI scheme is used to investigate the effect of a fast increase in the inlet gas superficial velocity on a smooth stratified flow in a horizontal pipe. The numerical predictions are then compared with the experimental results. Similarly, the effects of a sudden decrease in the inlet gas flow rate on an established slug flow regime are investigated both numerically and experimentally in the "down-gas" case. Finally, the LASSI scheme is used to simulate a severe slugging regime in a S-shaped riser built in the NTNU laboratory in order to reproduce the phenomena observed in offshore oil risers.

2 Transition criteria

2.1 Stratified flow stability: the Viscous Kelvin-Helmholtz criterion (VKH)

First introduced by Lin and Hanratty (1986) and Barnea and Taitel (1993), this criterion is based on the linear stability analysis of the two fluid-model which consists of the four equations (liquid mass conservation, gas mass conservation, liquid momentum balance, gas momentum balance) that follow:

$$\begin{aligned} \frac{\partial}{\partial t} (\rho_l A_l) + \frac{\partial}{\partial x} (\rho_l A_l U_l) &= 0 \\ \frac{\partial}{\partial t} (\rho_g A_g) + \frac{\partial}{\partial x} (\rho_g A_g U_g) &= 0 \\ \frac{\partial}{\partial t} (\rho_l A_l U_l) + \frac{\partial}{\partial x} (\rho_l A_l U_l^2) &= -\tau_l S_l + \tau_i S_i - \rho_l g A_l \sin \phi - A_l \frac{\partial}{\partial x} p - \rho_l g A_l \cos \phi \frac{\partial}{\partial x} h_l \\ \frac{\partial}{\partial t} (\rho_g A_g U_g) + \frac{\partial}{\partial x} (\rho_g A_g U_g^2) &= -\tau_g S_g - \tau_i S_i - \rho_g g A_g \sin \phi - A_g \frac{\partial}{\partial x} p - \rho_g g A_g \cos \phi \frac{\partial}{\partial x} h_l \end{aligned}$$

The subscript l and g refer respectively to the liquid and gas phase, ρ , A and U are the density, occupied area and velocity of the considered phase. τ_l is the liquid-wall friction, τ_g the gas-wall friction and τ_i the gas-liquid friction. S_l and S_g are the liquid-wetted and gas-wetted perimeter and S_i is the interfacial width. p is the pressure, h_l the liquid height and ϕ the angle between the pipe and the horizontal. Using the same notations as Barnea and Taitel, the equations are rewritten in a non-conservative form and the pressure gradient is eliminated from the two momentum balances to form a transient

holdup equation.

$$\begin{aligned}
(1) \quad & \frac{\partial}{\partial t} h_l + H_l \frac{\partial U_l}{\partial x} + U_l \frac{\partial}{\partial x} h_l = 0 \\
(2) \quad & \frac{\partial}{\partial t} h_l - H_g \frac{\partial U_g}{\partial x} + U_g \frac{\partial}{\partial x} h_l = 0 \\
(3) \quad & \rho_l \frac{\partial U_l}{\partial t} - \rho_g \frac{\partial U_g}{\partial t} + \rho_l U_l \frac{\partial U_l}{\partial x} - \rho_g U_g \frac{\partial U_g}{\partial x} + (\rho_l - \rho_g) g \cos \phi \frac{\partial}{\partial x} h_l = F
\end{aligned}$$

introducing $H_l = \frac{A_l}{dh_l}$ the equivalent liquid height, $H_g = \frac{A_g}{dh_g}$ the equivalent gas height and F the resultant friction force acting on the liquid phase, defined as:

$$F = -\frac{\tau_l S_l}{A_l} + \frac{\tau_g S_g}{A_g} + \tau_i S_i \left(\frac{1}{A_l} + \frac{1}{A_g} \right) - (\rho_l - \rho_g) g \sin \phi$$

Starting from equilibrium (all time derivatives and all spatial derivatives but the one of the pressure are null), we introduce a small sinusoidal perturbation of pulsation ω , wave number k and amplitudes ($\tilde{h}_l, \tilde{U}_l, \tilde{U}_g$) in the flow variables around the equilibrium values ($\bar{h}_l, \bar{U}_l, \bar{U}_g$).

$$h_l = \bar{h}_l + \tilde{h}_l e^{i(\omega t - kx)} \quad U_l = \bar{U}_l + \tilde{U}_l e^{i(\omega t - kx)} \quad U_g = \bar{U}_g + \tilde{U}_g e^{i(\omega t - kx)}$$

Reporting in the first equation (liquid conservation) yields:

$$\tilde{U}_l = \left[\frac{\omega}{k} - \bar{U}_l \right] \frac{\tilde{h}_l}{\bar{H}_l}$$

While the second equation (gas conservation) gives:

$$\tilde{U}_g = \left[\bar{U}_g - \frac{\omega}{k} \right] \frac{\tilde{h}_l}{\bar{H}_g}$$

The source term F is a function of 3 variables (the holdup $\beta = \frac{A_l}{A}$, the liquid local superficial velocity $U_l^S = \beta U_l$ and the gas local superficial velocity $U_g^S = (1 - \beta) U_g$). Hence:

$$\tilde{F} = \left(\frac{\partial F}{\partial \beta} \right)_{U_l^S, U_g^S} \tilde{\beta} + \left(\frac{\partial F}{\partial U_l^S} \right)_{\beta, U_g^S} \tilde{U}_l^S + \left(\frac{\partial F}{\partial U_g^S} \right)_{\beta, U_l^S} \tilde{U}_g^S$$

Reporting the values of \tilde{U}_l , \tilde{U}_g and \tilde{F} inside the third equation (dynamic holdup equation) provides the dispersion equation:

$$\omega^2 - 2[ak - ib]\omega + ck^2 - iek = 0$$

With the following Barnea and Taitel's (1993) notations:

$$\begin{aligned}\rho &= \frac{\rho_l}{\beta} + \frac{\rho_g}{\alpha} \\ a &= \frac{1}{\rho} \left(\frac{\rho_l \overline{U}_l}{\beta} + \frac{\rho_g \overline{U}_g}{\alpha} \right) \\ b &= \frac{1}{2\rho} \left[\left(\frac{\partial F}{\partial U_l^S} \right)_{\beta, U_g^S} - \left(\frac{\partial F}{\partial U_g^S} \right)_{\beta, U_l^S} \right] \\ c &= \frac{1}{\rho} \left[\frac{\rho_l \overline{U}_l^2}{\beta} + \frac{\rho_g \overline{U}_g^2}{\alpha} - (\rho_l - \rho_g) g \cos \phi \frac{\overline{H}_l}{\alpha} \right] \\ e &= -\frac{1}{\rho} \left(\frac{\partial F}{\partial \beta} \right)_{U_l^S, U_g^S}\end{aligned}$$

The dispersion equation is a second degree complex equation in ω . The model will predict that stratified flow is stable if both roots of this equation have a negative imaginary part. We can find the neutral stability condition ($\omega_i = 0$) by letting $\omega = \omega_R + i\omega_i = \omega_R$ in the dispersion equation. We can then calculate the wave velocity C_F :

$$C_F = \frac{e}{2b} = -\frac{\left(\frac{\partial F}{\partial \beta} \right)_{U_l^S, U_g^S}}{\left[\left(\frac{\partial F}{\partial U_l^S} \right)_{\beta, U_g^S} - \left(\frac{\partial F}{\partial U_g^S} \right)_{\beta, U_l^S} \right]} = \frac{\omega}{k}$$

The stability criterion is then:

$$(C_F - a)^2 + (c - a^2) < 0$$

Based on the linear stability analysis of a perfectly smooth stratified flow, this simple criterion gives a hint at whether or not, smooth stratified flow is a possible solution. As a consequence, an unstable VKH criterion does only mean that a smooth stratified flow regime can not be established, and does not necessarily mean that slug flow can be established at those conditions. Clearly, a roll waves solution or an unsteady pseudo-slug regime are also possible solutions.

2.2 Slug flow stability: the Minimum Holdup criterion (MH)

Ruder et al. (1989), Bendiksen and Espedal (1992) followed by Woods and Hanratty (1996) developed a criterion based this time on slug stability. The idea is to consider slug flow as a succession of slug units as the one shown in figure 1, consisting of a slug region followed by a bubble region where the flow is stratified. α_S , U_{ls} and U_{gs} are respectively the void fraction, liquid velocity and gas velocity within the slug, and α_b , U_{lb} and U_{gb} are respectively the void fraction, liquid velocity and gas velocity within the bubble. U_{nose} and U_{front} are respectively the bubble nose (or slug tail) velocity and the slug front

velocity.

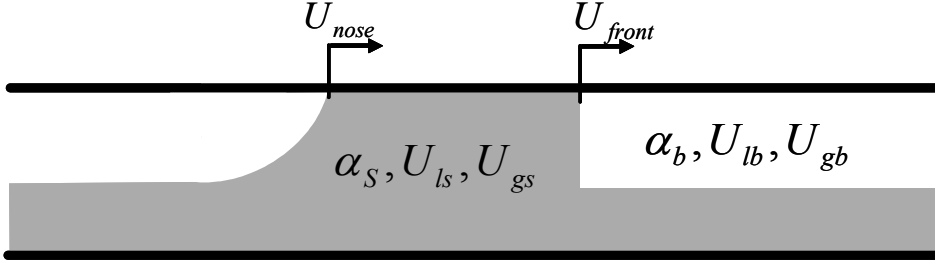


Fig 1: Minimum Holdup, sketch of a slug unit

Steady state slug flow, defined by its inlet superficial velocities U_l^S and U_g^S , is at neutral stability ($U_{nose} = U_{front}$) a system characterized by seven unknowns ($\alpha_S, U_{ls}, U_{gs}, \alpha_b, U_{lb}, U_{gb}, U_{nose}$).

- (1) The void in slug α_S can be determined by experimental closure laws.
- (2) The slip velocity within the slug $U_{gs} - U_{ls}$ can be determined by experimental closure laws.
- (3) Volume conservation ensures that $U_m = U_l^S + U_g^S = (1 - \alpha_S)U_{ls} + \alpha_S U_{gs}$
- (4) Bendiksen's closure law can be used for the bubble nose velocity, hence providing the relation $U_{nose} = C_0 U_m + \nu_0$ where C_0 and ν_0 are known.
- (5) Liquid conservation across the front gives $U_{front} = \frac{(1 - \alpha_S)U_{ls} - (1 - \alpha_b)U_{lb}}{\alpha_b - \alpha_S}$
- (6) Gas conservation across the front gives $U_{front} = \frac{\alpha_S U_{gs} - \alpha_b U_{gb}}{\alpha_S - \alpha_b}$
- (7) A momentum balance in the bubble area: $F(\alpha_b, U_{lb}, U_{gb}) = 0$

This set of equations can be solved iteratively but provides a physical solution (with a positive slug fraction) only as long as the predicted average holdup within the slug unit (slug and bubble region) is below the one in plain stratified flow. Hence this criterion is usually labelled as the Minimum Holdup criterion, for it predicts the prevalence of the flow regime with the lower holdup. It is important to stress out that this criterion only answers the question of whether or not an already initiated slug will survive (in other terms will U_{front} exceeds U_{nose} ?). Should the answer be yes, it does not necessarily mean that slug flow will be the established flow regime within the pipe, for this criterion says nothing about slug initiation. Should the answer be no, stratified flow is not the unique possibility, a roll waves or pseudo-slug regime can also arise.

2.3 Interest of a slug capturing/tracking scheme

The literature clearly stresses the importance of both the Viscous Kelvin-Helmholtz and the Minimum Holdup criteria. The VKH criterion dominates

the transition from stratified to slug flow for low pressure systems with moderate velocities. For high pressure systems, the Minimum Holdup criterion defines the transition.

More recently, more complex effects have been shown, clearly demonstrating the role of each of those criteria. When stratified flow is present at the inlet of the pipe, the flow regime will remain stratified along the pipe as long as the flow is stable according to the VKH criterion. However if slug flow is to be present at the inlet, then slug flow will remain the flow regime along the pipe if the flow is stable according to the MH criterion (Kristiansen, 2004). This defines a "hysteresis zone" in the traditional $(U_l^S - U_g^S)$ flowmap: in this area the flow regime is dependent on both the spatial and time history of the flow. This phenomenon clearly shows the interest of transient slug tracking schemes in opposition to steady-state or statistical approaches.

For high pressures and high velocities, there is an area where both criteria predict instability. As observed experimentally, this zone corresponds to roll waves and unstable flow (neither stratified nor slug flow). Figure 2 shows an indicative computed numerical flowmap corresponding to an horizontal 1 inch pipe with an air-water flow at 10 bars.

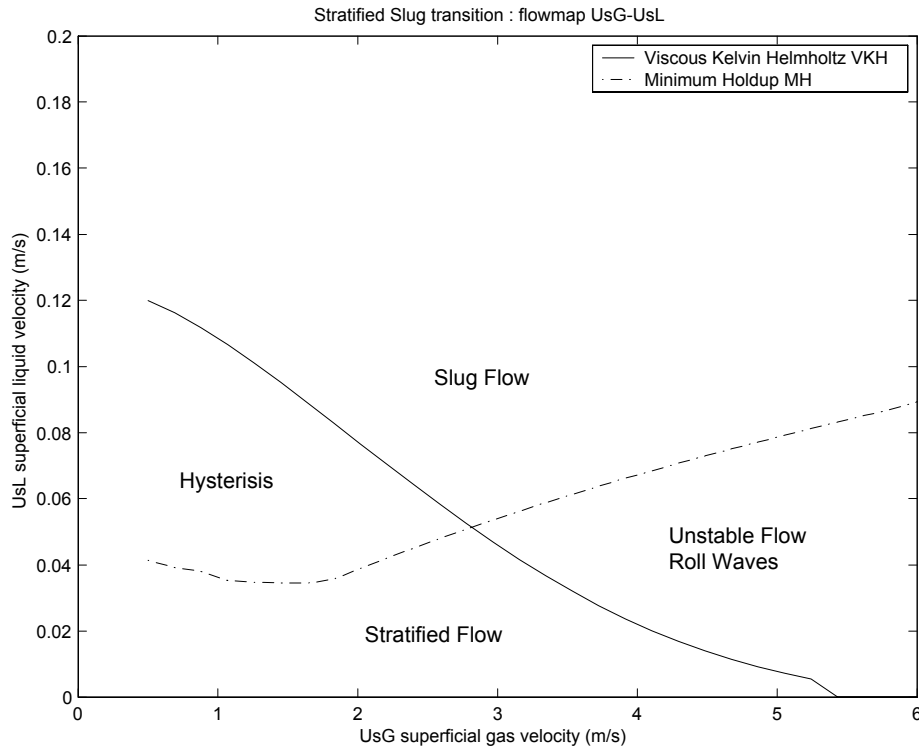


Fig 2: Numerical flowmap showing the VKH and MH criteria

3 The LASSI scheme

The LASSI (Lagrangian Approximate Scheme for Slug Initiation) scheme is a slug capturing and slug tracking Lagrangian scheme. Its principle is presented in more details in Renault et al. (2007, [1]).

The LASSI scheme can be seen as an intermediary between a traditional two-fluid model code such as OLGA (Bendiksen et al., 1991) or TRIUMPH (Issa and Kempf, 2003) and a simplified slug tracking scheme as in Nydal and Banerjee (1996) or Taitel and Barnea (1997, 2000). In LASSI the slugs are generated automatically by the numerical scheme, without using any arbitrary slug insertion criterion providing either the initial length, the slugging frequency or the initiation point. After their initiation, the slugs are transported along the pipe using Bendiksen’s correlation (Bendiksen et al., 1984) as a closure for the slug tail velocity, meaning that the slug tail velocity U_b is given in the LASSI scheme by the relation $U_b = C_0 U_m + \nu_0$ where U_m is the mixture velocity within the slug and C_0 and ν_0 are parameters whose value depend on the Froude number.

Because Bendiksen’s correlation is embedded within the code, the LASSI scheme is able to predict the flow regime transition according to the Minimum Holdup criterion, that is to say that if slug flow is predicted unstable according to the Minimum Holdup criterion, the slugs tracked in the LASSI scheme will eventually disappear.

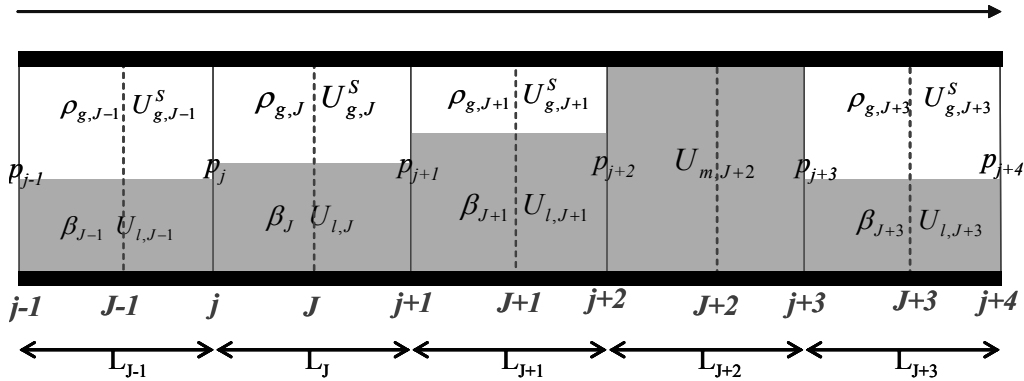


Fig 3: LASSI scheme grid

Figure 3 shows a sketch of the grid used in LASSI. The pipe is divided in *sections* (where the gas flows on top of the liquid) and *slugs*. An object oriented programming in C++ used throughout the code allows much flexibility in terms of front tracking. Each individual slug generated is followed by the adaptative grid and a Lagrangian approach is used as well in the sections.

Starting from the usual two-fluid model four differential equations, some ap-

proximations ($\rho_l U_l \gg \rho_g U_g$, U_m and ρ_g slowly varying in time and space) are made in order to uncouple the liquid film transport from the pressure wave. The system can then be solved efficiently in 3 steps. First, the gas massic flow rate and the pressure within each section and the mixture velocity within each slug are calculated simultaneously based on gas mass conservation and a dynamic momentum balance in the slugs. The liquid layer within the sections is considered to have no influence on the fast pressure and slug momentum dynamics. Thanks to this approximation, a simple tridiagonal algorithm is sufficient to solve the system.

Second, a modified shallow water algorithm is used to solve the liquid transport within the sections independently of the gas dynamics. This actually consists in solving a modified shallow-water system where friction is used as a source term and where the Bernoulli suction force is subtracted from the opposed hydrostatic effect.

The liquid transport equations of the two-fluid model then become in the LASSI scheme :

$$\begin{aligned} \frac{\partial}{\partial t} (\beta) + \frac{\partial}{\partial x} (\beta U_l) &= 0 \\ \frac{\partial}{\partial t} (\beta U_l) + \frac{\partial}{\partial x} \left(\beta U_l^2 + \frac{1}{2} \kappa \beta \right) &= \frac{\beta}{\rho_l} F (U_l, \beta, U_m) \end{aligned}$$

where the parameter κ is defined as:

$$\kappa = \frac{\rho_l - \rho_g}{\rho_l} g \cos \phi \frac{A}{\frac{dA_l}{dh_l}} - \frac{1}{\alpha} \frac{\rho_g}{\rho_l} (U_g - U_l)^2$$

Where β is the liquid holdup, α is the void fraction, U_l and U_g are respectively the liquid and gas velocity, U_m is the mixture velocity, ρ_l and ρ_g are respectively the liquid and gas densities, A is the pipe cross-sectional area, A_l is the area occupied by the liquid phase, h_l is the liquid height and ϕ is the pipe inclination from the horizontal. F is the resulting volumic force (sum of the contributions of the friction and gravitational forces) acting on the liquid phase. Standard Blasius' friction factors were used to calculate the expressions of the liquid, gas and interfacial friction throughout all the simulations presented in this paper.

The borders between the sections can be moved arbitrarily thanks to the Lagrangian nature of the scheme. The border velocities are actually chosen in

order to try and follow ripples and roll waves, based on the consideration of the exact solution of the associated Riemann problem.

Finally, a list management step deals with section splitting or merging. Indeed, some sections might become too big and have to be splitted. On the opposite, some sections might become too small in respect to the CFL criterion and have to be merged. Those operations can be done simply as the pipe is modelled as a doubly-linked list of sections and slugs. Figure 4 shows the computational sequence of the LASSI scheme.

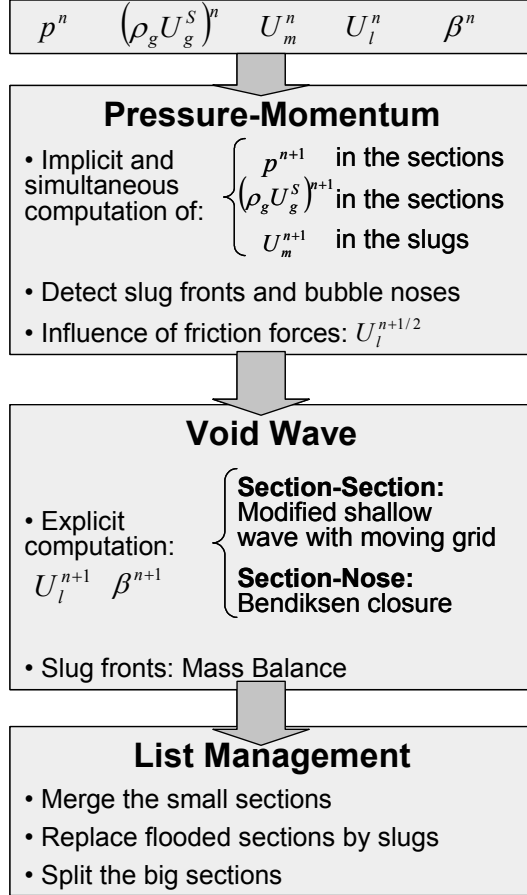


Fig 4: The LASSI scheme computation procedure

It is important to note that the simplified system has the same area of well-posedness as the full two-fluid model and becomes ill-posed when the coefficient κ becomes negative. The well-posedness condition yields the well-known Inviscid Kelvin-Helmholtz (IKH) criterion which can be written as:

$$\text{well-posed} \Leftrightarrow (U_g - U_l)^2 < \frac{\rho_l - \rho_g}{\rho_g} g \cos \phi \frac{A_g}{\frac{dA_l}{dh_l}} \Leftrightarrow \kappa > 0$$

Although some approximations are actually made to uncouple the liquid transport from the pressure dynamics, it has been demonstrated (Renault et al., 2007, [1]) that the simplified shallow-water equations used for the liquid transport has exactly the same area of stability as the standard initial two-fluid model, provided that $\rho_l U_l \gg \rho_g U_g$. Due to a careful discretization and to a front-tracking approach, the growth of small instabilities into slugs is well captured by the LASSI scheme meaning that whenever stratified flow is predicted unstable by the VKH criterion, the LASSI code will automatically capture the apparition of slugs. A typical example of slug initiation in the LASSI scheme is presented figure 5. A 20 meters long, 1 inch diameter, air-water pipe is simulated at atmospheric pressure. The time step is 0.01s and the average section length is around 1 cm. Simulating 5 minutes takes only a few minutes on a standard PC, thanks to the explicit nature of the scheme. One can clearly see a travelling wave, breaking and finally bridging the pipe, giving birth to a slug.

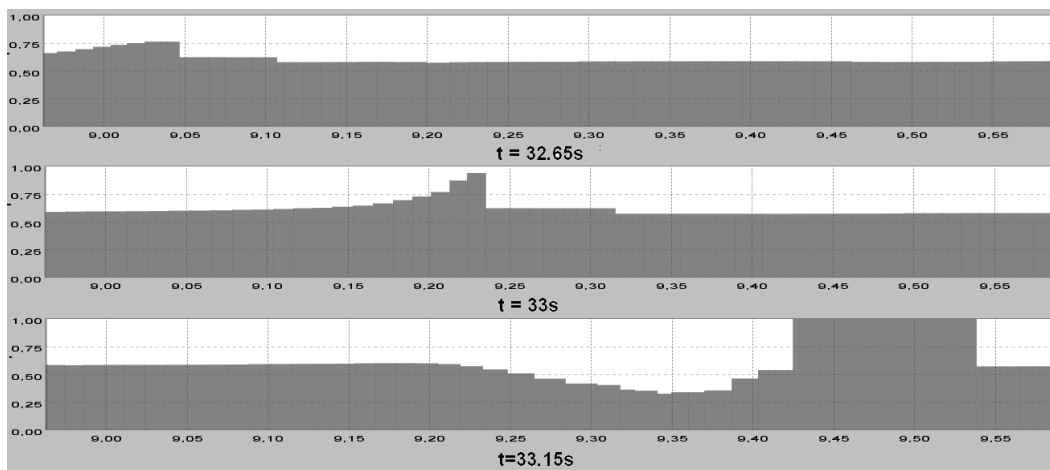


Fig 5: Slug initiation with LASSI.

4 Up gas experiment

4.1 Principle

Air-water flow is run through a horizontal 6-cm diameter pipe. With a gas superficial velocity set at $U_g^S = 0.5 \text{ m.s}^{-1}$ and a liquid superficial velocity set at $U_l^S = 0.08 \text{ m.s}^{-1}$, the established flow regime within the pipe is stratified flow. At some time, the gas superficial velocity is suddenly increased to $U_g^S = 2.0 \text{ m.s}^{-1}$. The equilibrium flow regime observed at those new conditions is still stratified flow.

The initial and final states of this experiment are plotted both on a $(U_L^S - U_G^S)$ flowmap figure 6 and on a $(\frac{h_L}{D} - U_G^S)$ flowmap figure 7. In addition, the transition line between stratified and slug flow, computed according to the Viscous Kelvin Helmholtz criterion, is drawn on each of those flowmaps.

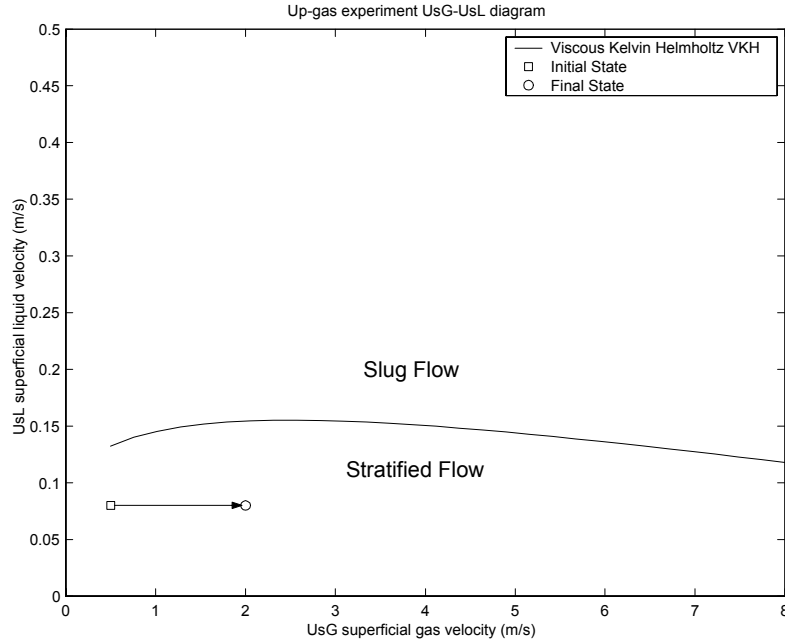


Fig 6: Up-Gas experiment, $(U_L^S - U_G^S)$ flowmap

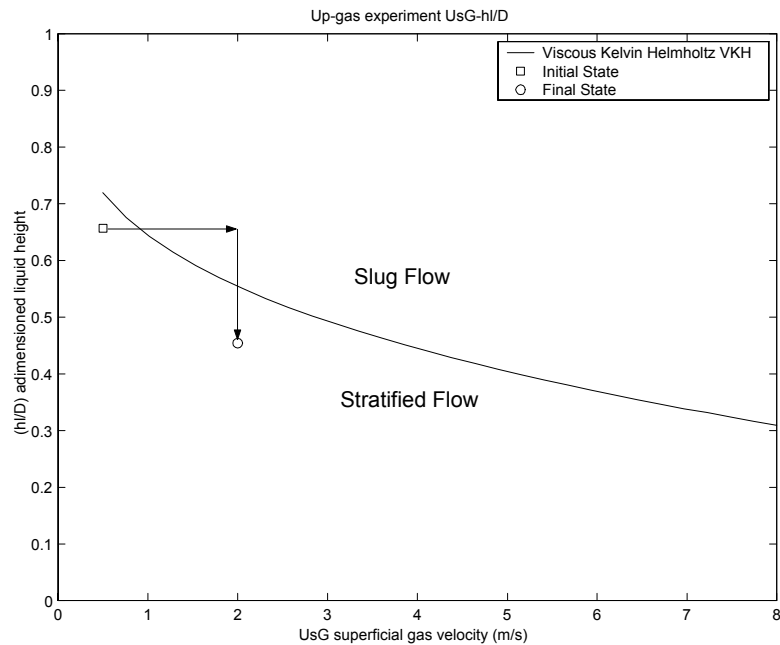


Fig 7: Up-Gas experiment, $(\frac{h_L}{D} - U_G^S)$ flowmap

Liquid transport occurs at a much slower speed than the pressure wave asso-

ciated with the fast increase in gas velocity at the inlet. As a consequence, it takes time before the liquid level decreases from its initial to its final level. During the first seconds after the gas flow rate has been increased at the inlet, the system possesses both the liquid level of the initial state and the gas superficial velocity of the final state. The path followed by the system in the flowmap is shown figure 7.

During this fast transient, stratified flow is therefore no longer stable according to the Viscous Kelvin Helmholtz criterion. Given the high level of liquid available, a transitory period of slug flow is therefore to be expected during this fast transient.

4.2 Experimental set-up

A schematic diagram of the 0.06 m diameter test section used in the “up gas” and “down gas” experiments is given in figure 8. The horizontal 16.4 m long test section is made from acrylic to allow visual observation. The fluids applied were air and filtered tap water, which gave a surface tension equal to 0.075 N.m^{-1} .

The fluids flowed to the test section in separate feed lines. The single phase air and water flow rates were measured upstream of the test section by means of a mass and a volume flow meter, respectively. The fluids entered the test section in layers according to their densities. Air was supplied from a central line, and vented to the atmosphere at the test section outlet. The liquid phase was recycled back to the test section via a separator and a centrifugal pump.

The experiments were conducted at ambient conditions, with an outlet pressure set to 1 bara. Four flush mounted conductance probes were calibrated to return the water holdup. The conductivity meter applied was found to be linear with respect to voltage output for the measured conductance. By measuring between rings located a few centimeters apart, the relation between the measured voltage (conductance) and the corresponding water level in the test section was approximately linear. A one-point calibration for water filled test section was performed twice a day to keep track of any possible drift in the electronics. The pressure was monitored at the gas feed line, the gas inlet section and immediately upstream of the first conductance ring probe. Imaging for visualisation purposes, using digital cameras, was performed upstream of the conductance probes.

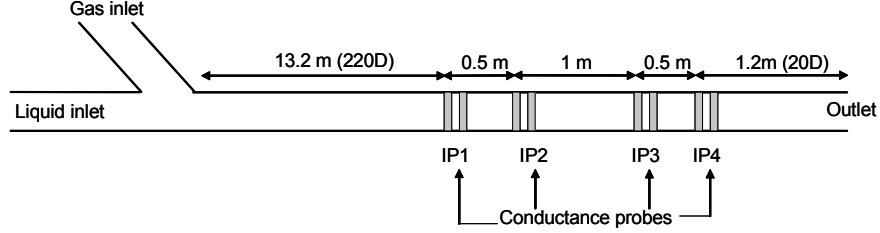


Fig 8: Schematic diagram of the test section used in the Up gas and Down gas experiments.

4.3 Results

The "up-gas" scenario has been both tested and simulated in a 6 cm diameter air-water pipe. The inlet gas flow rate was increased after 600 seconds. Four impedance probes were used to measure the holdup at different positions along the pipe (IP1: 13.25 m, IP2: 13.75 m, IP3: 14.25 m, IP4: 14.75 m). On figure 9 are plotted the time series of the experimentally observed holdup and the holdup computed by the LASSI scheme at the outlet (IP4).

There is a significant discrepancy between the computed and the observed initial equilibrium liquid level. This might come either from inappropriate interfacial friction factors in the two-fluid model or from poor calibration of the impedance probes. As expected, some slugs are triggered shortly after the gas inlet flow rate is increased. This effect is captured correctly by the scheme.

Experimentally though, the slugging episode seems to last longer, with a final slug leaving the 16 meters pipe more than 15 seconds after the gas increase.

Finally, the slow increase of the liquid level towards the new equilibrium is well captured by the simulation.

5 Down gas experiment

5.1 Principle

Air-water flow is run through the same 6-cm diameter pipe. With a gas superficial velocity set at $U_g^S = 2.0 \text{ m.s}^{-1}$ and a liquid superficial velocity set at $U_l^S = 0.3 \text{ m.s}^{-1}$, the established flow regime within the pipe is this time slug flow. Suddenly, the gas superficial velocity is decreased to $U_g^S = 1.0 \text{ m.s}^{-1}$. The equilibrium flow regime observed at those new conditions is still slug flow.

The initial and final states of this experiment are plotted both on a $(U_l^S - U_g^S)$

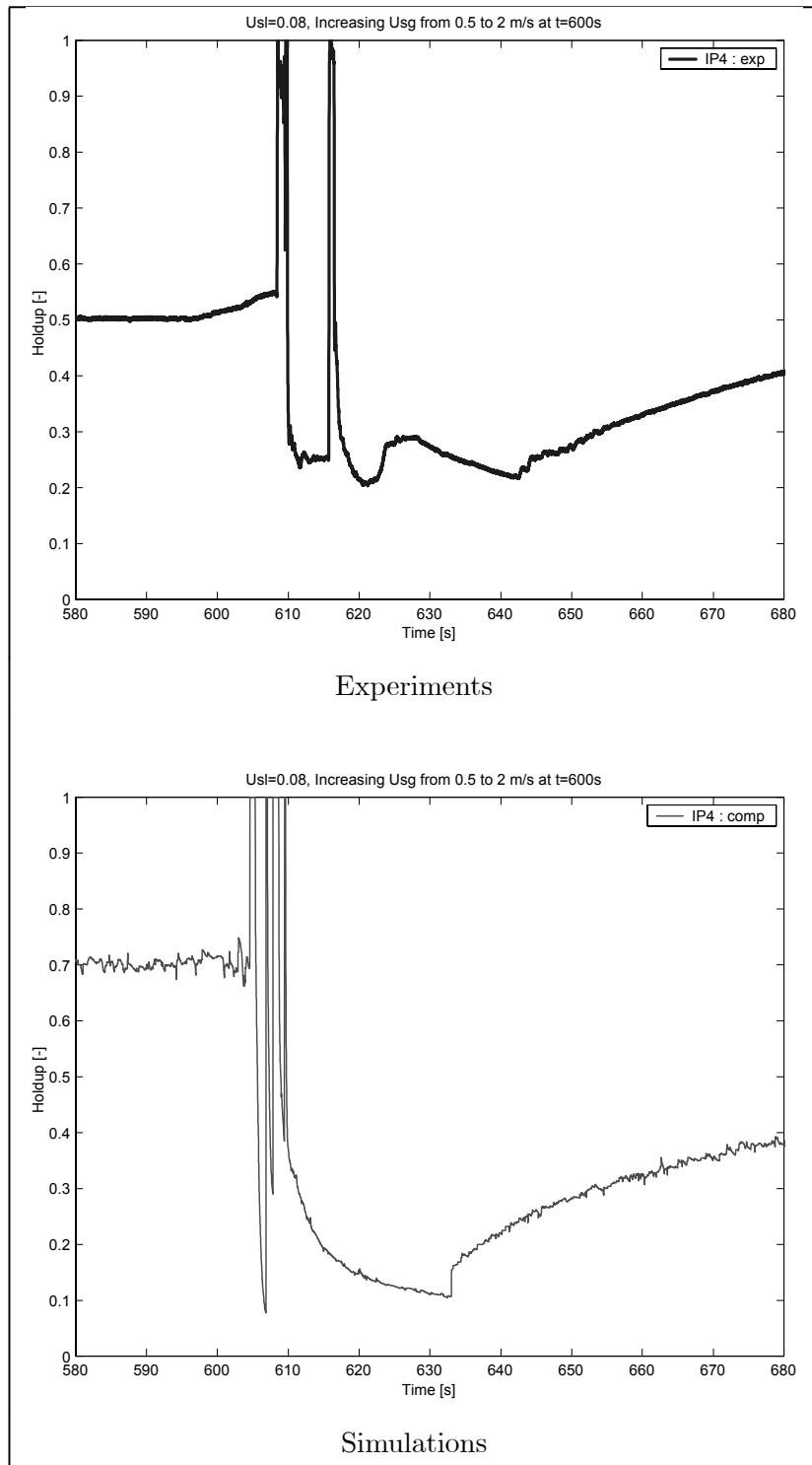


Fig 9: Up gas case : holdup at the outlet (IP4)

flowmap figure 10 and on a $\left(\frac{h_l}{D} - U_g^S\right)$ flowmap figure 11. In addition, the transition line between stratified and slug flow, computed according to both the Viscous Kelvin Helmholtz criterion, and the Minimum Holdup criterion, are drawn on each of those flowmaps.

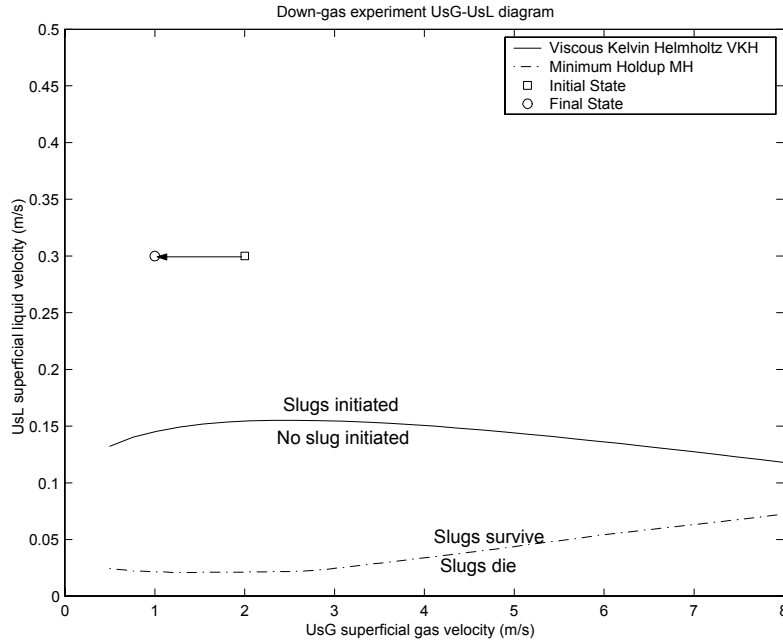


Fig 10: Down-Gas experiment: situation on a $(U_l^S - U_g^S)$ flowmap

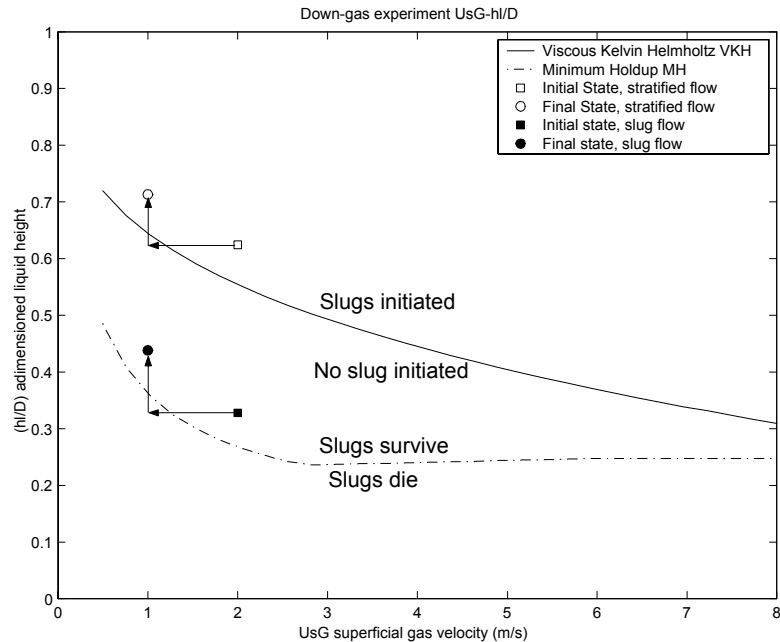


Fig 11: Down-Gas experiment: situation on a $\left(\frac{h_l}{D} - U_g^S\right)$ flowmap

Two distinct criteria govern the transition from stratified to slug flow: the Viscous Kelvin Helmholtz criterion assesses the stability of stratified flow while

the Minimum Holdup criterion predicts the stability of established slug flow. In this experiment, both approaches are of interest: indeed the pipe is composed of a short length of stratified flow close to the inlet, and then a slug flow region. In the initial conditions, the stratified region close to the inlet is not stable according to the VKH criterion, slugs are therefore initiated before they propagate downstream of the pipe.

As already mentioned in the "up-gas" case, liquid transport takes place at a much slower pace than pressure waves. Thus for a short period of time the system can be considered as characterized by the initial state holdup and the final state gas superficial velocity.

Figure 11 teaches us that the sudden decrease in the gas inlet flow rate will have two effects on the flow : the inlet stratified region will become stable thus no more slugs will be generated, and the already initiated slugs that propagate through the pipe will die. A short period of stratified flow can then be foreseen, before the liquid holdup finally increases towards its new equilibrium level, and slug flow is observed again.

5.2 Results

This scenario has been both tested and simulated in a 6 cm diameter air-water pipe. The inlet gas flow rate was decreased after 600 seconds. The same four impedance probes were used to measure the holdup at different positions along the pipe. On figure 6 are plotted the time series of both the experimentally observed holdup and the holdup computed by the LASSI scheme at the outlet (IP4).

The initial holdup and slug frequency seem to be predicted correctly by the scheme. The duration of the stratified period is also reproduced in a satisfactory manner. However in the experiments, what seems to be a roll wave is observed shortly after the decrease in the gas flow rate. This roll wave might result from the death of a previous slug, but is not observed at the end of the pipe in the simulations.

Finally the slug frequency in the final state seems to be underestimated by a factor 2. As the holdup in the bubbles seems to be correct, it appears that this is due to higher slug lengths in the simulation. That could be explained by an incorrect modelling of the "wake effect" which controls the length of the slugs.

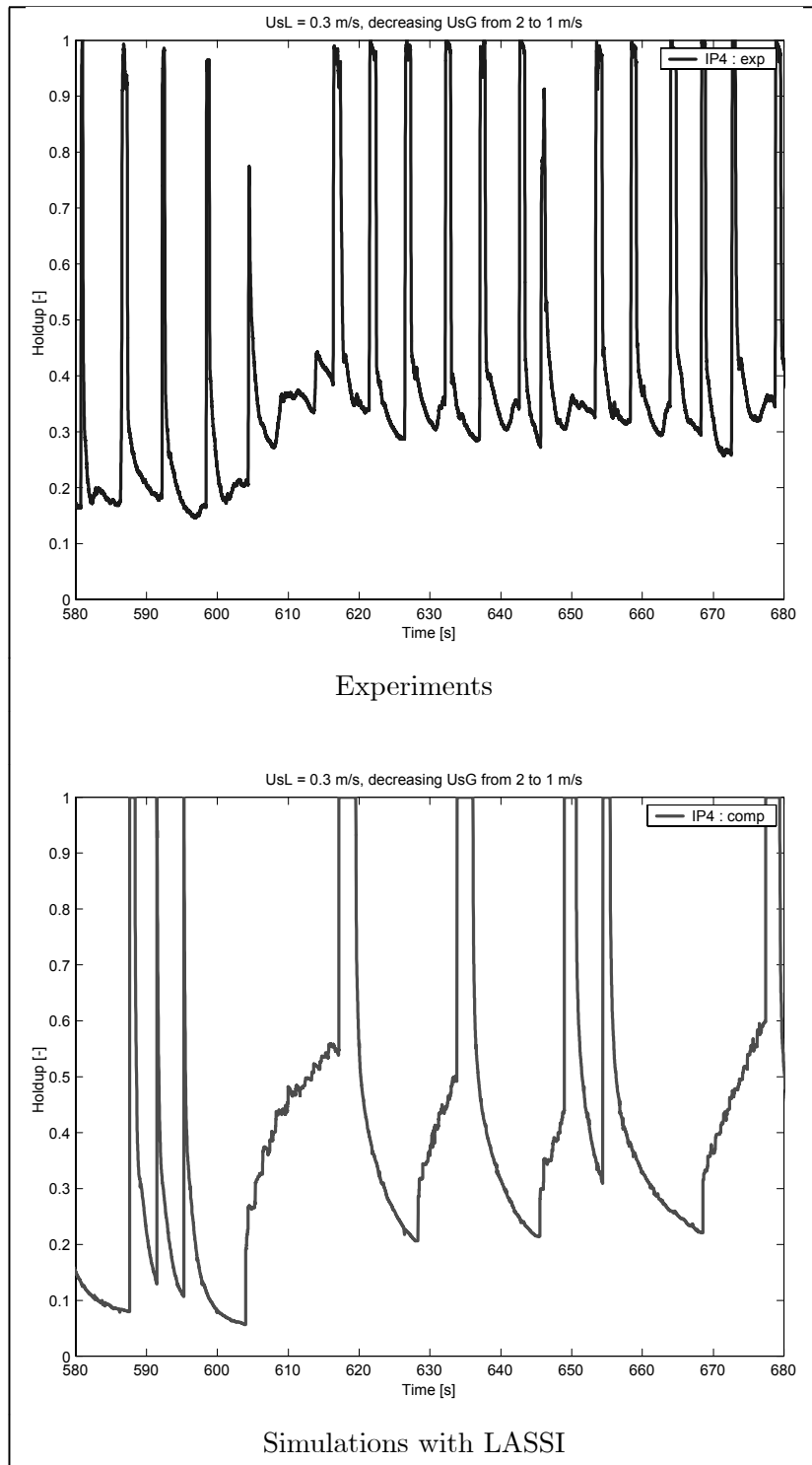


Fig 12: Down gas case : holdup at the outlet (IP4)

6 Severe slugging in a S-shaped riser

6.1 Principle

Some experiments have been made to explore the phenomenon of severe slugging within a S-shaped riser. The experimental results are presented and compared with simulations carried out with the presented code.

6.2 Experimental setup

Figure 13 shows a schematic diagram of the 0.05 m diameter test section used in the “S-riser” experiments. The test section length was approximately 18 m, with a height from the riser base to the outlet of 7 m. The pipe was made from acrylic to allow visual observation. The fluids applied were air and filtered tap water. I and P indicate respectively the impedance probe and pressure transmitter positions.

The fluids flowed to the test section in separate feed lines. The single phase air and water flow rates were measured upstream of the test section by means of a mass and a volume flow meter, respectively. The fluids entered the test section in layers according to their densities. Air was supplied from a central line, and vented to the atmosphere at the test section outlet. The liquid phase was recycled back to the test section via a separator and a centrifugal pump. The experiments were conducted at ambient conditions: the pressure was set to 1 bara at the test section outlet and the temperature was kept at around 20°C.

A gas volume corresponding to approximately 165 m of additional pipe length was installed upstream of the test section inlet. This added compressibility to the system so that severe terrain slugging could be achieved. Three flush mounted conductance probes were used for monitoring the local water content at pre-selected positions downstream of the test section. The signals were normalised based on air filled and water filled cross sections, yielding approximate holdup values between 0 and 1. The pressure was measured at the test section inlet, at the riser base, near the dip between the “first” and the “second” riser leg, and close to the riser outlet.

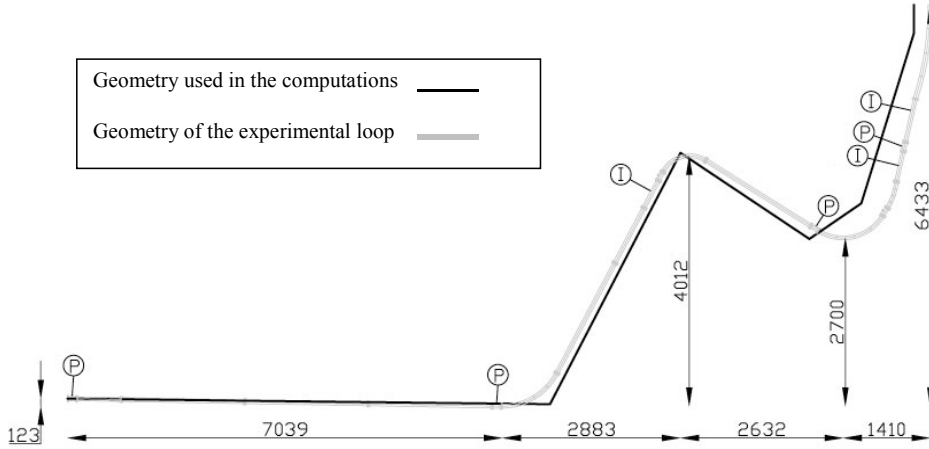


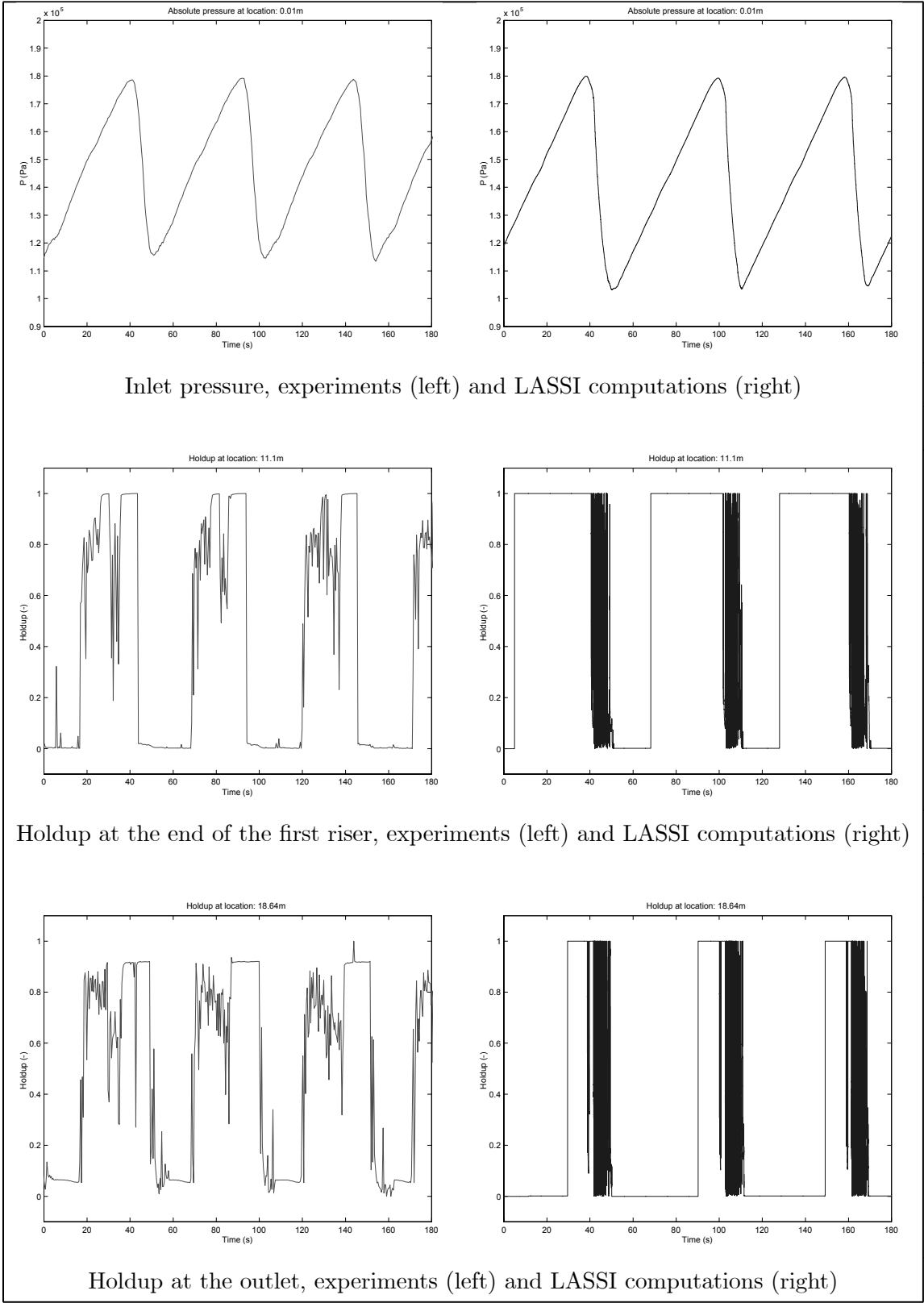
Fig 13: Geometry of the S-riser pipe

6.3 Experimental results

The left column of figure 14 contains the experimental results obtained for an inlet liquid superficial velocity $U_L^S = 0.32 \text{ m.s}^{-1}$, and an inlet gas superficial velocity $U_G^S = 2.23 \text{ m.s}^{-1}$. A gas reservoir with a volume equivalent to a 165 m long pipe with the same 5 cm diameter was used at the inlet to allow the system to operate within the severe slugging region. The inlet pressure, the holdup at the end of the first riser, and the holdup at the end of the pipe are presented. The results are of course typical of severe slugging, with large oscillations of the upstream pressure and periodic very long slugs at the outlet. The observed slugging frequency was around 50 seconds.

6.4 Simulations with the LASSI code

A constant timestep of 1 millisecond was used to simulate 200 seconds of the experiment, starting from an empty pipe. A grid size of 1 cm was used for the simulations (as the grid size is not constant in LASSI this value is only an average). The right column of figure 14 shows the computed inlet pressure time series as well as the computed holdup time series both at the end of the first riser and at the outlet. The code successfully captures the severe slugging phenomenon that occurs in the pipe and triggers large oscillations in the inlet pressure. The frequency of the oscillations is obtained with an acceptable precision. The small discrepancy between the oscillation period observed experimentally (around 50 seconds) and the computed one (around 60 seconds) can be explained by the fact that the inlet pressure never falls much



Inlet pressure, experiments (left) and LASSI computations (right)

Holdup at the end of the first riser, experiments (left) and LASSI computations (right)

Holdup at the outlet, experiments (left) and LASSI computations (right)

Figure 14 : S-Riser case, experimental results and simulations

below 1.2 bar in the experiments whereas the inlet pressure nearly reaches 1 bar in the computations. In the computations, the amount of gas present in the pipe at the beginning of the severe slugging cycle is thus underestimated, and as a consequence, the time needed for the inlet pressure to build up to the blow-out pressure is overestimated. It is therefore likely that the blow out phase, characterized by a very high gas velocity is not perfectly modelled.

Regarding the holdup time series, the results are less satisfactory, with a much higher time averaged holdup in the simulations than in the experiments. Part of the explanation could be that given that the model overestimates the oscillation period, the liquid has more time to accumulate in the simulations than in the experiments, thus filling more rapidly and more completely the pipe.

Figures 15 to 17 are aimed at providing a more detailed insight of the quality of the information provided by the simulations. 6 specific time points labelled A, B, C, D, E and F are plotted on the computed inlet pressure time series shown figure 15. The corresponding holdup profiles at those 6 distinct time points are then presented figures 16 and 17. The simulation is started with an empty pipe.

Point A represents the beginning of the severe slugging cycle: a liquid blockade has appeared at the low point of the first riser and the pressure is building up at the inlet. At point B, the liquid has completely filled the first riser and starts to fill the second riser. A small gas bubble is travelling towards the outlet through the stagnant liquid slug that fills the second riser.

Point C shows the pipe right before the blow out: the second riser is now completely filled and some liquid is flowing out of the pipe. A bubble nose is travelling downwards the fourth pipe towards the outlet.

The blow out process is shown at D: the horizontal pipe has already been cleared out of the liquid but the pressure is still high at the inlet since the two risers are still filled with water. The outlet flow rate is increasing very fast as the long remaining slug is accelerated towards the outlet.

Most of the liquid has already been blown out at point E: the remaining liquid is being carried at high speed by the gas exiting the pipe. This is probably the most difficult part to model since neither stratified nor slug flow is stable at this high gas velocity regime. The code predicts many small unstable waves travelling towards the outlet at high velocity, sometimes coalescing and bridging the pipe to form a slug that does not survive.

When the inlet pressure is low enough, the gas slows down within the pipe and is no longer able to convey the liquid that accumulates in the low points and forms some blockades.

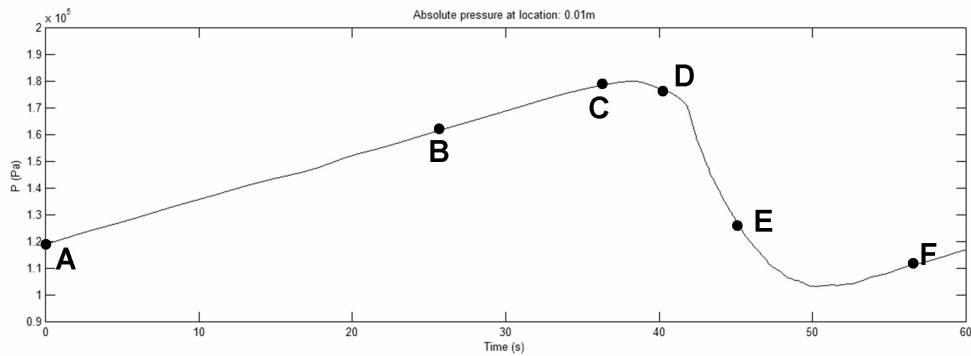


Fig 15: Simulated inlet pressure time series

7 Conclusion

Flow regime transitions associated with fast changes in the inlet gas flow rate were investigated in a 6 cm air-water pipe. Experiments showed that while a steady stratified flow regime was established in the pipe, a sudden increase in the inlet gas flow rate could trigger a short period of slug flow. Symmetrically, starting from an established slug flow regime, a fast decrease in the inlet gas flow rate resulted in a short episode of stratified flow before slug flow was established again. Those observations are in line with the experimental and theoretical works conducted before by Taitel et al. (1978) and King et al. (1998) and stress once more the importance of transient effects in gas-liquid flows.

The numerical predictions obtained with the LASSI scheme were in good agreement with the experimental observations. The slug capturing approach used in the LASSI scheme was shown to adequately capture the changes in the flow regime associated with sudden changes in the gas velocity. This approach presents the advantage to offer a common modelling framework for all the mechanisms leading to slug flow, from slugs created from the growth of small perturbations in horizontal pipes as in Renault et al. (2007, [1]) and bend-initiated slugs as in Renault et al. (2007, [2]) to slugs generated from fast transients and severe slugs.

The LASSI code was indeed also used to reproduce the severe slugging regime observed experimentally in a S-shaped riser. The results are qualitatively good, yet a probably poor modelling of the blow-out phase leads to an underestimation of the amount of gas and liquid remaining in the pipe after the blow-out phase and therefore to an overestimation of the slugging frequency.

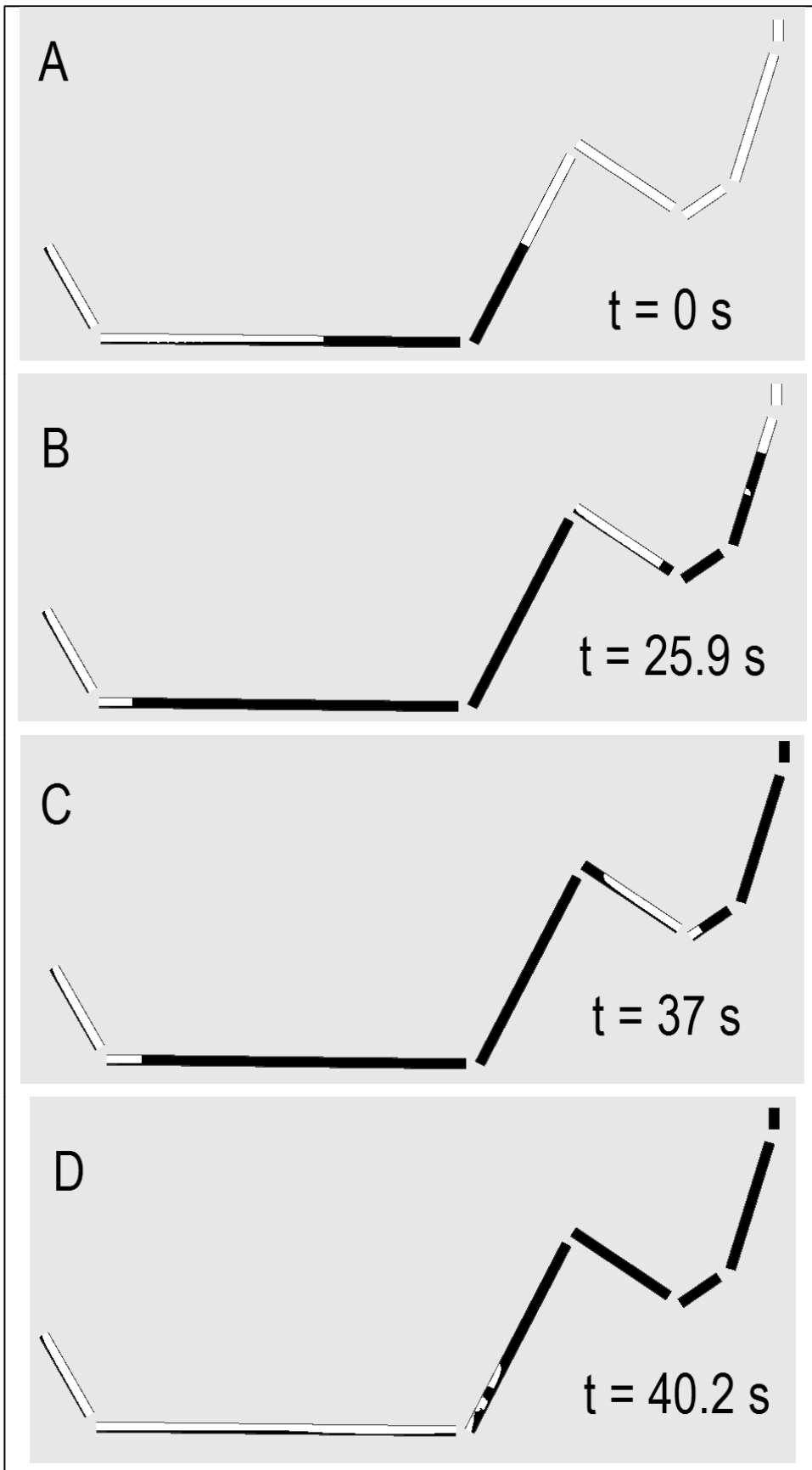


Fig 16: Simulated holdup profile at various instants

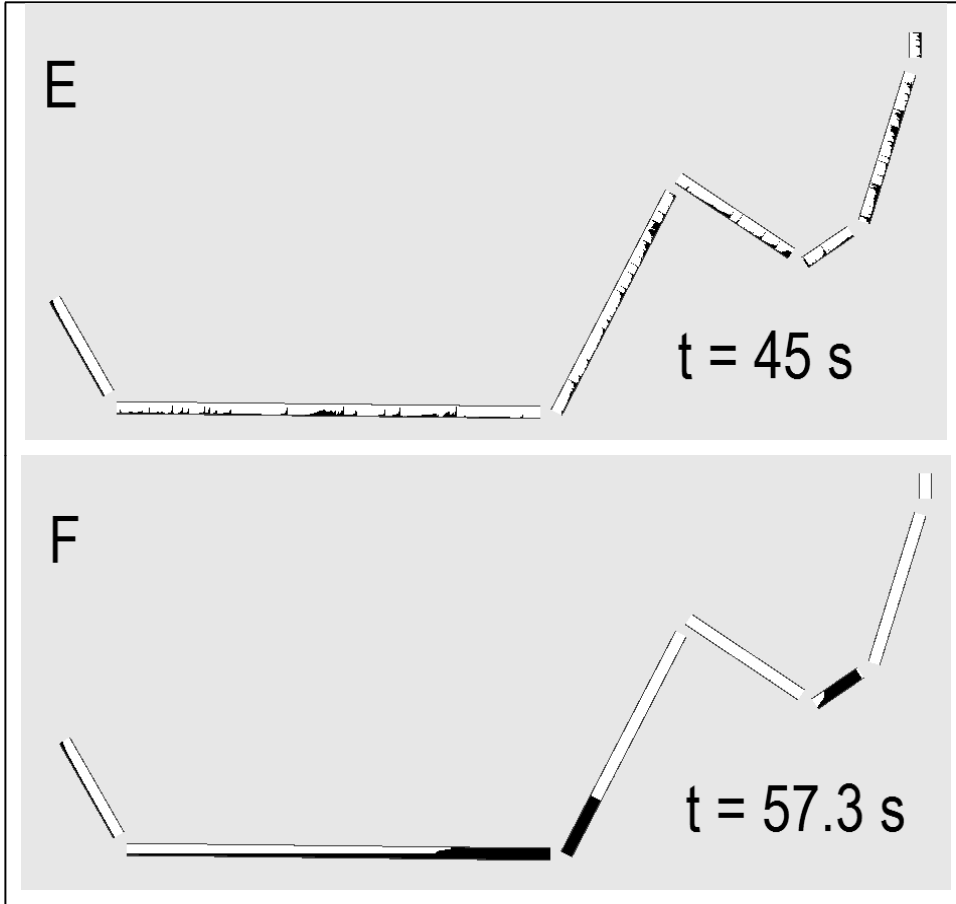


Fig 17: Simulated holdup profile at various instants, continued

On the whole, given its simplicity, its low computational needs (the code is non iterative and its complexity is only proportional to the number of sections within the pipe), and its ability to model accurately the transition from stratified to slug flow, the LASSI scheme can be considered as an interesting simulation tool. It is especially well suited to reproduce most of the lab experiments taking place in small scale loops with complex geometries at low pressure and low velocities. Indeed in those conditions, both of the transition criteria embedded in LASSI (Minimum Holdup and Viscous Kelvin Helmholtz) are to be taken into account for the transition, whereas for high pressure systems the VKH criterion is not of any use.

References

- Barnea, D., Taitel, Y., 1993. Kelving-Helmholtz stability criteria for stratified flow: viscous versus non-viscous (inviscid) approaches. *Int. J. Multiphase Flow* 19 (4), 639-649.
- Bendiksen, K.H., 1984. An experimental investigation of the motion of long bubbles in inclined tubes. *Int. J. Multiphase Flow* 10, 467-483.
- Bendiksen, K.H., Malnes, D., Moe, R., Nuland, S., 1991. The dynamic two-fluid model OLGA: Theory and application. *SPE Production Engineering*, May 1991, 171-180.
- Bendiksen, K.H., Espedal, M., 1992. Onset of slugging in horizontal gas-liquid pipe flow. *Int. J. Multiphase Flow* 18, 234-247.
- Issa, R.I., Kempf, M.H.W., 2003. Simulation of slug flow in horizontal or nearly horizontal pipes with the two-fluid model. *Int. J. Multiphase Flow* 29, 69-95.
- King, M., Hale, C., Lawrence, C., Hewitt, G., 1998. Characteristics of flow rate transients in slug flow. *Int. J. Multiphase Flow* 24, 825-854.
- Kristiansen, O., 2004. Experiments on the transition from stratified to slug flow in multiphase pipe flow. Ph.D. Thesis, NTNU, Trondheim, Norway.
- Lin, P.Y., Hanratty, T.J., 1986. Prediction of the initiation of slugs with linear stability theory. *Int. J. Multiphase Flow* 12, 79-98.
- Minami, K., 1991. Transient flow and pigging dynamics in two-phase pipelines. PhD thesis, University of Tulsa, USA.
- Nydal, O.J., Banerjee, S., 1996. Dynamic slug tracking simulations for gas-liquid flow in pipelines. *Chem. Eng. Commun.* 141-142, 13-39.
- Renault, F., Nydal, O. J., 2007, [1]. A simple slug capturing and slug tracking scheme for gas-liquid pipe flow. Part 1: presentation of the scheme, Preprint.
- Renault, F., Nydal, O. J., 2007, [2]. A simple slug capturing and slug tracking scheme for gas-liquid pipe flow. Part 2: application to slug length determination in a small scale loop, Preprint.
- Ruder, Z., Hanratty, P.J., Hanratty, T.J., 1989. Necessary conditions for the existence of stable slugs. *Int. J. Multiphase Flow* 15, 209-226.
- Taitel, Y., Barnea, D., 1997 Simplified transient simulation of two-phase flow using quasi-equilibrium momentum balances. *Int. J. Multiphase Flow* Vol. 23, No. 3, 493-501.

Taitel, Y., Barnea, D., 2000. Slug-tracking model for hilly terrain pipelines. SPE Journal 5 (1): 102-109.

Taitel, Y., Lee, N., Dukler, A., 1978. Transient gas-liquid flow in horizontal pipes: modelling the flow pattern transitions. AIChE J. 24, 920-934

Woods, B.D., Hanratty, T.J., 1996. Relation of slug stability to shedding rate. Int. J. Multiphase Flow 22, No. 5, 809-828.

Fourth Paper

Influence of dynamic pressure terms on stratified two-phase flow stability.

Fabien Renault and Ole Jørgen Nydal

Presented at the 5th International Conference on Multiphase Flow, Yokohama, Japan, May 30-June 4, 2004

Influence of dynamic pressure terms on stratified two-phase flow stability

Fabien Renault¹, Ole-Jørgen Nydal²

1: Department of Energy and Process Technology, University of NTNU, Trondheim, Norway,
 fabien.renault@kkt.ntnu.no

2: Department of Energy and Process Technology, University of NTNU, Trondheim, Norway,
 ole.j.nydal@maskin.ntnu.no

Abstract This paper presents a modified version of the "Viscous Kelvin Helmholtz" criterion (based on the linear stability analysis of the two-fluid model) predicting transition between stratified and slug flow. In previous works a hydrostatic approximation was used to close the two-fluid model. Here, an approach with a transverse momentum balance to evaluate pressure terms is investigated. The obtained model is compared with the established criteria (Viscous Kelvin Helmholtz, Inviscous Kelvin Helmholtz, Milne-Thompson) and with experimental results. The proposed model compares better to experiments and is able to predict the wavelength of the perturbation responsible for the transition. This analysis might also provide numerical benefits for transient two-phase simulations.

1 Introduction

When gas and liquid flow in a pipe, several flow patterns can be observed, including stratified and slug flow. Starting with Helmholtz, many different theoretical criteria have been proposed to describe the transition from stratified to slug flow. Lin and Hanratty (1986) and Barnea and Taitel (1993) derived a transition criterion based on the linear stability analysis of the two-fluid model, hence taking into account the influence of the shear stresses. Experimental works concluded that this approach gave more accurate results than the previous inviscous theories (Milne-Thompson, 1949).

However several experimentators (Fan et al., 1993; Espedal, 1998; Woods, 1998) noticed that although the critical liquid height was correctly predicted by this "Viscous Kelvin-Helmholtz" theory, slugs were observed to form by a different mechanism than suggested by the VKH theory. Indeed, for low values of the superficial gas velocity, transition appeared to be due to short gravity waves instead of infinitely long waves as predicted by the VKH theory.

The present paper tries to solve this contradiction by taking into account the transverse variations in dynamic pressure. Indeed while the previous authors based their analysis on a standard two-fluid model (i.e. assuming hydrostatic approximation for the pressure), the present paper replaces the hydrostatic approximation by a more complex closure that includes dynamic pressure terms.

2 The 2 fluid model

We use the usual 2 fluid model cross section averaged equations as a starting point

$$\begin{aligned}
 \frac{\partial}{\partial t} (\rho_l A_l) + \frac{\partial}{\partial x} (\rho_l A_l U_l) &= 0 \\
 \frac{\partial}{\partial t} (\rho_g A_g) + \frac{\partial}{\partial x} (\rho_g A_g U_g) &= 0 \\
 \frac{\partial}{\partial t} (\rho_l A_l U_l) + \frac{\partial}{\partial x} (\rho_l A_l U_l^2) &= -\tau_l S_l + \tau_i S_i - \rho_l g A_l \sin \beta + p_{il} \frac{\partial}{\partial x} A_l - \frac{\partial}{\partial x} (A_l P_l) \\
 \frac{\partial}{\partial t} (\rho_g A_g U_g) + \frac{\partial}{\partial x} (\rho_g A_g U_g^2) &= -\tau_g S_g - \tau_i S_i - \rho_g g A_g \sin \beta + p_{ig} \frac{\partial}{\partial x} A_g - \frac{\partial}{\partial x} (A_g P_g)
 \end{aligned}$$

Where p_{il} and p_{ig} stand respectively for the liquid and gas interfacial pressure. It is now required to evaluate the pressure terms in order to end up with only one pressure variable. If the hydrostatic approximation is made then we end up with the following equations:

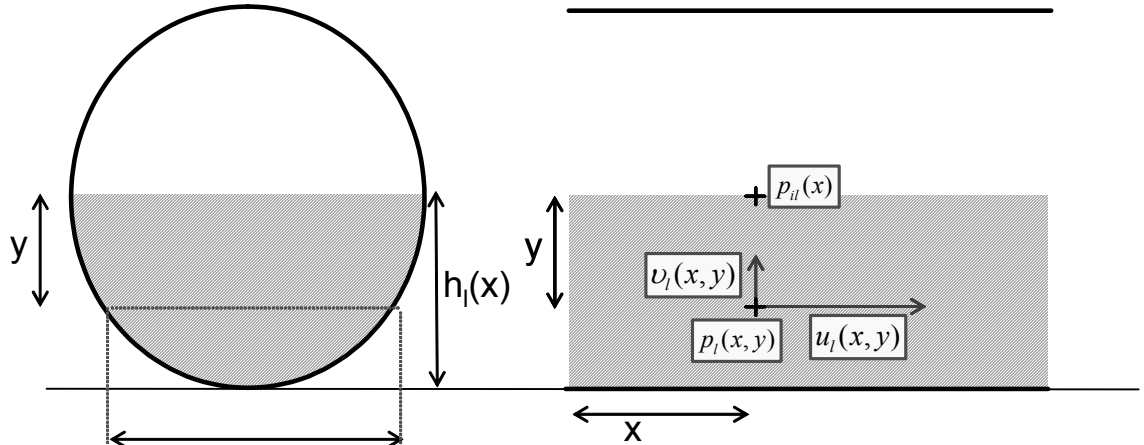
$$p_{ig} - p_{il} = \sigma \frac{\partial^2}{\partial x^2} h_l$$

$$p_{il} \frac{\partial}{\partial x} A_l - \frac{\partial}{\partial x} (A_l P_l) = -A_l \frac{\partial}{\partial x} p_{il} - \rho_l g A_l \cos \beta \frac{\partial}{\partial x} h_l$$

$$p_{ig} \frac{\partial}{\partial x} A_g - \frac{\partial}{\partial x} (A_g P_g) = -A_g \frac{\partial}{\partial x} p_{ig} - \rho_g g A_g \cos \beta \frac{\partial}{\partial x} h_l$$

3 Developing a new pressure closure relation

Main used symbols			
$U_l(x)$	cross-sectional averaged liquid velocity	$U_g(x)$	cross-sectional averaged gas velocity
$A_l(x)$	liquid area	$A_g(x)$	gas area
$P_l(x)$	cross-sectional averaged pressure, liquid	$P_g(x)$	cross-sectional averaged pressure, gas
$p_{il}(x)$	interfacial pressure, liquid phase	$p_{ig}(x)$	interfacial pressure, gas phase
$p_l(x, y)$	local pressure, liquid phase	β	inclination angle of the pipe
ρ_l	liquid density	ρ_g	gas density
$u_l(x, y)$	local liquid velocity, axial component	$v_l(x, y)$	local liquid velocity, transverse component
μ_l^*	liquid turbulent dynamic viscosity	ν_l^*	liquid turbulent kinematic viscosity
$R_l(x)$	liquid volume fraction	$R_g(x)$	gas volume fraction
$A_l'(x)$	$\frac{dA_l}{dh_l}$	$H_l(x)$	$\frac{A_l}{A_l'}$



Sketch of the pipe

3.1 Expressing the pressure term

However, one can give a try in implementing a more complex relation, giving up the hydrostatic approximation and following in the footsteps of [Banerjee S., 1980] or [Ransom V. & Hicks D., 1984]. Nevertheless, both of those systems were shown to be unconditionally unstable in [Prosperetti A., 1987], which is clearly unphysical. In the following, lower case letters will indicate a local value (which depends on x and y) while upper case letters will indicate a cross section averaged value (which depends only on x). We have to evaluate the expression $p_{il} \frac{\partial}{\partial x} A_l - \frac{\partial}{\partial x} (A_l P_l)$. The liquid will always be considered incompressible.

Starting with the definition of the cross-averaged pressure: $A_l P_l = \int_{y=0}^{y=h_L} p_l(y) b(y) dy$ and introducing $p_l'(y)$ as $p_l(y) = p_{il} + p_l'(y)$, we can express the needed pressure term as a function of $p_l'(y)$ using the Leibniz rule of derivation:

$$p_{il} \frac{\partial}{\partial x} A_l - \frac{\partial}{\partial x} (A_l P_l) = -A_l \frac{\partial}{\partial x} p_{il} - \int_{y=0}^{y=h_L} \frac{\partial}{\partial x} p_l'(y) b(y) dy$$

3.2 Y-axis momentum balance

And we now have to make a choice in the modelling of $\frac{\partial}{\partial x} p'_l(y)$ in order to evaluate the integral in the right-hand side. We will use for this a local momentum balance in the y-direction. u_l and v_l are respectively the axial and transverse component of the local liquid velocity.

$$\rho_l \left[\frac{\partial}{\partial t} v_l + u_l \frac{\partial}{\partial x} v_l + v_l \frac{\partial}{\partial y} v_l \right] = -\frac{\partial}{\partial y} p_l - \rho_l g \cos \beta + \frac{\partial}{\partial x} \tau_{xy} + \frac{\partial}{\partial y} \tau_{yy}$$

with the stress tensors taken as $\tau_{xy} = \mu_l^* \left(\frac{\partial}{\partial y} u_l + \frac{\partial}{\partial x} v_l \right)$ and $\tau_{yy} = 2\mu_l^* \frac{\partial}{\partial y} v_l$ with μ_l^* being the equivalent turbulent viscosity. The exact value of μ_l^* is highly uncertain, but is not required to get qualitative results. Hence we can express the pressure within the liquid phase by:

$$p'_l(y) = \rho_l g \cos \beta (h_l - y) + \rho_l \int_{y'=y}^{y'=h_l} \varphi(x, y') dy' \text{ with}$$

$$\varphi(x, y) = \frac{\partial}{\partial t} v_l + u_l \frac{\partial}{\partial x} v_l + v_l \frac{\partial}{\partial y} v_l - \nu_l^* \left(\frac{\partial^2}{\partial x \partial y} u_l + \frac{\partial^2}{\partial x^2} v_l + 2 \frac{\partial^2}{\partial y^2} v_l \right)$$

Differentiating against x , using the Leibniz rule and integrating over y yields:

$$\int_{y=0}^{y=h_l} \frac{\partial}{\partial x} p'_l(y) b(y) dy = \underbrace{\rho_l \int_{y=0}^{y=h_l} g \cos \beta \frac{\partial h_l}{\partial x} b(y) dy}_{I_1} + \underbrace{\rho_l \int_{y=0}^{y=h_l} \varphi(x, h_l) \frac{\partial h_l}{\partial x} b(y) dy}_{I_2}$$

$$+ \underbrace{\rho_l \int_{y=0}^{y=h_l} \left(\int_{y'=y}^{y'=h_l} \frac{\partial}{\partial x} \varphi(x, y') dy' \right) b(y) dy}_{I_3}$$

Which gives, summing up the previous relations,

$$\boxed{p_{il} \frac{\partial}{\partial x} A_l - \frac{\partial}{\partial x} (A_l P_l) = -A_l \frac{\partial}{\partial x} p_{il} - I_1 - I_2 - I_3}$$

$$\boxed{I_1 = \rho_l A_l \frac{\partial h_l}{\partial x} g \cos \beta}$$

$$\boxed{I_2 = \rho_l A_l \frac{\partial h_l}{\partial x} \varphi(x, h_l)}$$

$$\boxed{I_3 = \rho_l \int_{y=0}^{y=h_l} \left(\int_{y'=y}^{y'=h_l} \frac{\partial}{\partial x} \varphi(x, y') dy' \right) b(y) dy}$$

$$\boxed{\varphi(x, y) = \frac{\partial}{\partial t} v_l + u_l \frac{\partial}{\partial x} v_l + v_l \frac{\partial}{\partial y} v_l - \nu_l^* \left(\frac{\partial^2}{\partial x \partial y} u_l + \frac{\partial^2}{\partial x^2} v_l + 2 \frac{\partial^2}{\partial y^2} v_l \right)}$$

The first term I_1 corresponds to the hydrostatic term, while I_2 and I_3 contain the contribution of the transient y-axis acceleration terms. It is now clear that some drastic approximations will be needed in order to reach a simple and useful expression for I_2 and I_3 .

3.3 Making assumptions on the velocity profile

3.3.1 Velocities at the crest

We can use the following exact relation which simply expresses continuity at the interface:

$$v_l(x, h_l) = \frac{\partial h_l}{\partial t} + u_l(x, h_l) \frac{\partial h_l}{\partial x}$$

The term I_2 represents the variation of the transient acceleration terms due to a variation in the water level. Therefore we can neglect the higher order diffusive terms in the expression of $\varphi(x, h_l)$, as well as the $v_l \frac{\partial}{\partial y} v_l$ term, supposed small compared to $\left(\frac{\partial}{\partial t} + u_l \frac{\partial}{\partial x} \right) v_l$.

$$\varphi(x, h_l) \approx \left[\frac{\partial}{\partial t} + u_l \frac{\partial}{\partial x} \right] v_l(x, h_l)$$

Expressing the result as a similar way as in [Banerjee S., 1980]

$$\varphi(x, h_l) \approx \left[\frac{\partial}{\partial t} + u_l(x, h_l) \frac{\partial}{\partial x} \right]^2 (h_l)$$

Now, the remaining choice is to pick a value for $u_l(x, h_l)$. For a turbulent flow within a pipe, any value between $U(x)$ and $1.2 U(x)$ is acceptable for $u_l(x, h_l)$. The simplest expression gives:

$$\varphi(x, h_l) \approx \left[\frac{\partial}{\partial t} + U_l(x) \frac{\partial}{\partial x} \right]^2 (h_l)$$

$$\boxed{I_2 = \rho_l A_l \frac{\partial h_l}{\partial x} \left[\frac{\partial}{\partial t} + U_l(x) \frac{\partial}{\partial x} \right]^2 (h_l)}$$

3.3.2 Bulk velocities

In order to evaluate I_3 we have to find an easily integrable expression for $\varphi(x, y')$.

- As already seen, the y component of the liquid velocity is given at the crest by:

$$v_l(x, h_l) = \frac{\partial h_l}{\partial t} + u_l(x, h_l) \frac{\partial h_l}{\partial x} \approx \frac{\partial h_l}{\partial t} + U_l(x) \frac{\partial h_l}{\partial x}$$

We can now use the global continuity equation for the liquid phase ($\frac{\partial}{\partial t} A_l + \frac{\partial}{\partial x} (A_l U_l) = 0$) in order to get another expression for $v_l(x, h_l)$. Hence this equation can be put in the following non-conservative form: $\frac{\partial h_l}{\partial t} + U_l \frac{\partial h_l}{\partial x} = -\frac{A_l}{A_l'} \frac{\partial}{\partial x} U_l$ with A_l' defined as $A_l' = \frac{dA_l}{dh_l}$. We can then deduce an approximate expression for $v_l(x, h_l)$:

$$v_l(x, h_l) \approx -\frac{A_l}{A_l'} \frac{\partial U_l}{\partial x}$$

Going one step further, $\frac{A_l}{A_l'}$ can be grossly approximated as h_l :

$$v_l(x, h_l) \approx -h_l \frac{\partial U_l}{\partial x}$$

- While at the bottom of the liquid layer, the velocity profile must fit the conditions:

$$\begin{aligned} v_l(x, 0) &= 0 \\ \frac{\partial}{\partial y} v_l(x, 0) &= 0 \end{aligned}$$

- The liquid being assumed incompressible, in the bulk of the liquid layer, the evolution of v_l is governed by:

$$\frac{\partial}{\partial y} v_l(x, y) = -\frac{\partial}{\partial x} u_l(x, y)$$

- We now present an approximation for the local velocity profile within the liquid phase according to the elements mentioned above:

$$\boxed{u_l(x, y) \approx U_l(x)}$$

$$\boxed{v_l(x, y) \approx -y \frac{\partial}{\partial x} U_l(x)}$$

We had to give up the relation $\frac{\partial}{\partial y} v_l(x, 0) = 0$ and to make the approximation $\frac{A_l}{A_l'} \approx h_l$, as well as consider $u_l(x, y) \approx U_l(x)$ valid for most values of y (acceptable for a turbulent flow). However, we now have a coherent and easily integrable velocity profile that will hopefully prove to be accurate enough to get qualitative results.

3.3.3 Evaluation of I_3

We still need to evaluate $I_3 = \rho_l \int_{y=0}^{y=h_l} \left(\int_{y'=y}^{y'=h_l} \frac{\partial}{\partial x} \varphi(x, y') dy' \right) b(y) dy$. Using the proposed bulk velocity profile: $u_l(x, y) \approx U_l(x)$ and $v_l(x, y) \approx -y \frac{\partial}{\partial x} U_l(x)$, we reach:

$$\frac{\partial}{\partial x} \varphi = -y \left[\frac{\partial}{\partial t} + U_l \frac{\partial}{\partial x} - \frac{\partial U_l}{\partial x} - \nu_l^* \frac{\partial^2}{\partial x^2} \right] \left(\frac{\partial^2}{\partial x^2} U_l \right)$$

And the above expression presents the advantage of being proportional to y , hence easily integrable.

$$I_3 = -\rho_l \gamma \left[\frac{\partial}{\partial t} + U_l \frac{\partial}{\partial x} - \frac{\partial U_l}{\partial x} - \nu_l^* \frac{\partial^2}{\partial x^2} \right] \left(\frac{\partial^2}{\partial x^2} U_l \right)$$

with $\gamma = \int_{y=0}^{y=h_l} \left(\int_{y'=y}^{y'=h_l} y' dy' \right) b(y) dy = \frac{1}{2} h_l^2 A_l - \frac{1}{2} \int_{y=0}^{y=h_l} y^2 b(y) dy$

The integral $\int_{y=0}^{y=h_l} y^2 b(y) dy$ can be approximated by the explicit expression $h_l^2 R^2 \sin(\frac{\pi h_l}{4R})$ as shown by figure 1.

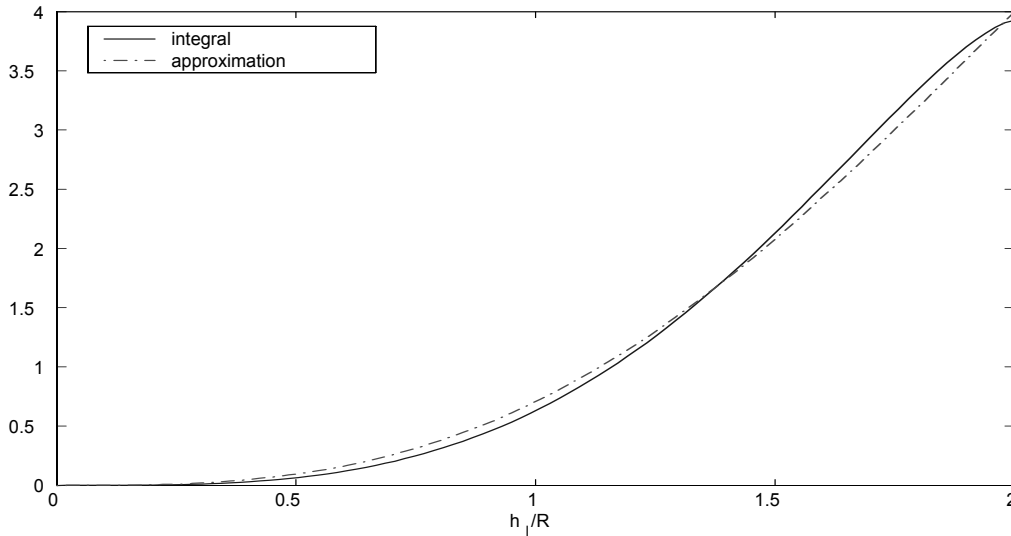


Figure 1: $\int_{y=0}^{y=h_l} y^2 b(y) dy$ and its approximation $h_l^2 R^2 \sin(\frac{\pi h_l}{4R})$, for $R = 1$

We then finally reach an explicit form of I_3 :

$$I_3 = -\rho_l h_l^2 A_l \eta \left[\frac{\partial}{\partial t} + U_l \frac{\partial}{\partial x} - \frac{\partial U_l}{\partial x} - \nu_l^* \frac{\partial^2}{\partial x^2} \right] \left(\frac{\partial^2}{\partial x^2} U_l \right)$$

$$\eta = \frac{1}{2} \left[1 - \frac{1}{\pi} \frac{A}{A_l} \sin\left(\frac{\pi h_l}{4R}\right) \right]$$

3.4 Presented pressure closure: conclusion

The consideration of a transverse momentum balance instead of the usual hydrostatic approximation in the two fluid model gives the following, after several drastic approximations:

$$p_{il} \frac{\partial}{\partial x} A_l - \frac{\partial}{\partial x} (A_l P_l) = -A_l \frac{\partial}{\partial x} p_{il} - I_1 - I_2 - I_3$$

$$I_1 = \rho_l A_l \frac{\partial h_l}{\partial x} g \cos \beta$$

$$I_2 = \rho_l A_l \frac{\partial h_l}{\partial x} \left[\frac{\partial}{\partial t} + U(x) \frac{\partial}{\partial x} \right]^2 (h_l)$$

$$I_3 = -\rho_l h_l^2 A_l \eta \left[\frac{\partial}{\partial t} + U_l \frac{\partial}{\partial x} - \frac{\partial U_l}{\partial x} - \nu_l^* \frac{\partial^2}{\partial x^2} \right] \left(\frac{\partial^2}{\partial x^2} U_l \right)$$

$$\eta = \frac{1}{2} \left[1 - \frac{1}{\pi} \frac{A}{A_l} \sin\left(\frac{\pi h_l}{4R}\right) \right]$$

3.5 Linear stability analysis of the model

3.5.1 Dispersion equation

The Viscous Kelvin Helmholtz (VKH) criterion for determining the transition from stratified to slug flow is derived from the linear stability analysis of the usual 2 fluid model. This criterion gives a much better prediction than the Inviscid Kelvin Helmholtz (IKH) which grossly over-predicts the stratified stability area. We are going to perform a linear stability analysis of the model in order to find out when does the model predict transition from stratified to slug flow. We will use the same method and notations as Barnea and Taitel did for the usual 2 fluid model in [Barnea D. & Taitel Y., 1993]. Starting from the same equations:

$$\begin{aligned}
 1. & \frac{\partial}{\partial t} h_l + H_l \frac{\partial U_l}{\partial x} + U_l \frac{\partial}{\partial x} h_l = 0 \\
 2. & \frac{\partial}{\partial t} h_l - H_g \frac{\partial U_g}{\partial x} + U_g \frac{\partial}{\partial x} h_l = 0 \\
 3. & \rho_l \frac{\partial U_l}{\partial t} - \rho_g \frac{\partial U_g}{\partial t} + \rho_l U_l \frac{\partial U_l}{\partial x} - \rho_g U_g \frac{\partial U_g}{\partial x} + (\rho_l - \rho_g) g \cos \beta \frac{\partial}{\partial x} h_l - \sigma \frac{\partial^3}{\partial x^3} h_l \\
 & + \rho_l \frac{\partial h_l}{\partial x} \left[\frac{\partial}{\partial t} + U_l \frac{\partial}{\partial x} \right]^2 (h_l) - \rho_l h_l^2 \eta \left[\frac{\partial}{\partial t} + U_l \frac{\partial}{\partial x} - \frac{\partial U_l}{\partial x} - \nu_l^* \frac{\partial^2}{\partial x^2} \right] \left(\frac{\partial^2 U_l}{\partial x^2} \right) = F \\
 & \text{with } F = -\frac{\tau_l S_l}{A_l} + \frac{\tau_g S_g}{A_g} + \tau_i S_i \left(\frac{1}{A_l} + \frac{1}{A_g} \right) - (\rho_l - \rho_g) g \sin \beta
 \end{aligned}$$

Starting from equilibrium (all time derivatives and all spatial derivatives but the one of pressure are null), we introduce a linear sinusoidal perturbation in the liquid level $h_l = \bar{h}_l + \tilde{h}_l e^{i(\omega t - kx)}$ where \bar{h}_l is the equilibrium liquid level before perturbation, \tilde{h}_l is the perturbation amplitude and ω and k are the pulsation and wave number of the small wave perturbation. Similarly, all the other variables will vary in the same way ($U_l = \bar{U}_l + \tilde{U}_l e^{i(\omega t - kx)}$ and $U_g = \bar{U}_g + \tilde{U}_g e^{i(\omega t - kx)}$). The liquid and gas mass conservation equations will then give after differentiation:

$$\begin{aligned}
 \tilde{U}_l &= \left[\frac{\omega}{k} - \bar{U}_l \right] \frac{\tilde{h}_l}{H_l} \\
 \tilde{U}_g &= \left[\bar{U}_g - \frac{\omega}{k} \right] \frac{\tilde{h}_l}{H_g}
 \end{aligned}$$

The source term F is a function of 3 variables ($R_l = \frac{A_l}{A}$, U_l^S , U_g^S). Hence

$$\tilde{F} = \left(\frac{\partial F}{\partial R_l} \right)_{U_l^S, U_g^S} \tilde{R}_l + \left(\frac{\partial F}{\partial U_l^S} \right)_{R_l, U_g^S} \tilde{U}_l^S + \left(\frac{\partial F}{\partial U_g^S} \right)_{R_l, U_l^S} \tilde{U}_g^S$$

Reporting the expressions of \tilde{U}_l , \tilde{U}_g and \tilde{F} into the transient holdup equation 3 gives the following dispersion equation:

$$(1 + fk^2) \omega^2 - 2 \left[ak + f \bar{U}_l k^3 - i \left(b - \frac{1}{2} f \nu_l^* k^4 \right) \right] \omega + ck^2 - \left(d - f \bar{U}_l^2 \right) k^4 - \left(ek - f \nu_l^* \bar{U}_l k^5 \right) i = 0$$

using the following Barnea and Taitel's notations:

$$\begin{aligned}
 \rho &= \frac{\rho_l}{R_l} + \frac{\rho_g}{R_g} \\
 a &= \frac{1}{\rho} \left(\frac{\rho_l \bar{U}_l}{R_l} + \frac{\rho_g \bar{U}_g}{R_g} \right) \\
 b &= \frac{1}{2\rho} \left[\left(\frac{\partial F}{\partial U_l^S} \right)_{R_l, U_g^S} - \left(\frac{\partial F}{\partial U_g^S} \right)_{R_l, U_l^S} \right] \\
 c &= \frac{1}{\rho} \left[\frac{\rho_l \bar{U}_l^2}{R_l} + \frac{\rho_g \bar{U}_g^2}{R_g} - (\rho_l - \rho_g) g \cos \beta \frac{H_l}{R_l} \right] \\
 d &= \frac{\sigma}{\rho} \frac{H_l}{R_l} \\
 e &= -\frac{1}{\rho} \left(\frac{\partial F}{\partial R_l} \right)_{U_l^S, U_g^S}
 \end{aligned}$$

and introducing $f = \frac{\rho_l h_l^2 \eta}{\rho R_l}$

Setting $f = 0$ yields Barnea and Taitel's dispersion equation. Naturally the addition of higher order derivatives in the system has brought some higher order terms into the dispersion equation.

3.5.2 Stability

The dispersion equation is a second degree complex equation in ω . The model will predict that stratified flow is stable if both roots of this equation have a negative imaginary part. We can find the neutral stability condition ($\omega_i = 0$) by letting $\omega = \omega_R + i\omega_i = \omega_R$ in the dispersion equation. We then have:

$$2 \left(b - \frac{1}{2} f \nu_l^* k_c^4 \right) \omega_R - (e k_c - f \nu_l^* \bar{U}_l k_c^5) = 0$$

$$\text{and } (1 + f k_c^2) \omega_R^2 - 2 [a k_c + f \bar{U}_l k_c^3] \omega_R + c k_c^2 - (d - f \bar{U}_l^2) k_c^4 = 0$$

The first equation directly yields $\omega_R = \frac{e - f \nu_l^* \bar{U}_l k_c^4}{2b - f \nu_l^* k_c^4} k_c$, hence in this "Full Viscous Kelvin Helmholtz" analysis, the critical wave velocity at the inception of the instability is given by (bearing in mind that both e and b are negative reals):

$$C_F = \frac{e - f \nu_l^* \bar{U}_l k_c^4}{2b - f \nu_l^* k_c^4}$$

Reporting this result in the second equation then gives the stability criterion:

$$\text{stability} \Leftrightarrow (C_F - a)^2 + (c - a^2) + k_c^2 \left[f (C_F - \bar{U}_l)^2 - d \right] < 0$$

4 Compared analysis of the stability criteria

It is natural to compare the obtained stability criterion to the established criteria. It is well-known that the stratified-slug transition is governed by the stratified stability for low gas densities, and by the slug stability for high gas densities. In the present analysis only the liquid vertical momentum balance has been taken into account and not the gas one. Hence we will suppose low gas densities in what follows.

4.1 Milne-Thompson Lamb (MTL) and Inviscid Kelvin Helmholtz (IKH)

Based on inviscid hydrodynamics for a rectangular channel, this analysis was developed by Milne-Thompson ([Milne-Thompson, 1949]) and Lamb ([Lamb H., 1945]). It neglects the influence of the shear stress but it takes into account the vertical momentum of the phases. Here is the obtained dispersion equation yielding the wave velocity C as a solution of a second degree equation (as recalled in [Hurlburt E, Hanratty T., 2002]):

$$k \rho_l (\bar{U}_l - C)^2 \coth(k \bar{h}_l) + k \rho_g (\bar{U}_g - C)^2 \coth(k \bar{h}_g) = g \cos \beta (\rho_l - \rho_g) + \sigma k^2$$

where \bar{h}_l and \bar{h}_g are respectively the liquid and the gas equilibrium height in the channel. Instability occurs when this equation admits a complex solution (then we have two conjugated roots, one of which is unstable). Then comes the following stability criterion:

$$\text{stability} \Leftrightarrow \forall k, (\bar{U}_g - \bar{U}_l)^2 < \left(\frac{\bar{h}_g \tanh(k \bar{h}_g)}{\rho_g k \bar{h}_g} + \frac{\bar{h}_l \tanh(k \bar{h}_l)}{\rho_l k \bar{h}_l} \right) [g \cos \beta (\rho_l - \rho_g) + \sigma k^2]$$

And we can evaluate the wave speed at neutral stability as:

$$C = \frac{\frac{\rho_l}{\bar{h}_l} \frac{k \bar{h}_l}{\tanh(k \bar{h}_l)} \bar{U}_l + \frac{\rho_g}{\bar{h}_g} \frac{k \bar{h}_g}{\tanh(k \bar{h}_g)} \bar{U}_g}{\frac{\rho_l}{\bar{h}_l} \frac{k \bar{h}_l}{\tanh(k \bar{h}_l)} + \frac{\rho_g}{\bar{h}_g} \frac{k \bar{h}_g}{\tanh(k \bar{h}_g)}}$$

From this result we can draw the following conclusions:

- Surface tension is a critical parameter, since if omitted this model will predict unconditional instability for small wavelengths ($k \rightarrow +\infty$).
- Wave speed at neutral stability: whatever the considered wavelength, the wave speed at neutral stability will always be close to the liquid velocity $C \approx \bar{U}_l$
- Many authors consider only the stability at long wavelengths ($k \rightarrow 0$)

– At long wavelengths, the stability criterion then becomes:

$$\boxed{\text{stability} \iff (\bar{U}_g - \bar{U}_l)^2 < \left(\frac{\bar{h}_g}{\rho_g} + \frac{\bar{h}_l}{\rho_l} \right) g \cos \beta (\rho_l - \rho_g)}$$

This criterion is often noted **Inviscid Kelvin Helmholtz** or **IKH**. It corresponds to $(c - a^2) < 0$, in the stability analysis of the two-fluid model, as Barnea noted.

- This criterion was found again in [Taitel Y. & Dukler A., 1976] from the balance between gravity and Bernoulli suction force on a single finite perturbation as $\bar{U}_g < \sqrt{\frac{\rho_l - \rho_g}{\rho_g} g \cos \beta \bar{h}_g}$
- and then an empirical $\left(1 - \frac{\bar{h}_l}{D}\right)$ term on the right-hand side was added by Taitel and Dukler (leading to the Taitel and Dukler criterion) to get a better match with the experimental data.
- As pointed out by Taitel, the IKH criterion can then be seen as the extreme limit for transition: above this point, not only stratified flow will not be stable, but the liquid will nearly instantly bridge the pipe, sucked by the Bernoulli force.
- But as shown in [Hurlburt E, Hanratty T., 2002], the most unstable wavelength is not infinite. A better approach when $\rho_l \gg \rho_g$ is:

– assume $\coth(k\bar{h}_g) \approx \coth(k\bar{h}_l) \approx 1$

– then the criterion becomes: $\text{stability} \iff \forall k, (\bar{U}_g - \bar{U}_l)^2 < \frac{1}{\rho_g} \left[\frac{g}{k} \cos \beta \rho_l + \sigma k \right]$

– $k_{crit} = \sqrt{\frac{g \cos \beta \rho_l}{\sigma}}$ and $(\bar{U}_g - \bar{U}_l)_{crit}^2 = 2 \frac{\rho_l}{\rho_g} \sqrt{\frac{\sigma g \cos \beta}{\rho_l}}$

– for horizontal air-water $k_{crit} \approx 370$ ($\lambda_{crit} \approx 1.7\text{cm}$)

– for a 1 inch pipe with $\frac{\bar{h}_l}{D} = 0.8$ (worst case), we still have $\coth(k\bar{h}_g) \approx 1.05$

– therefore the approximation was founded

The conclusion is that this inviscid analysis finally predicts a **short wavelength instability**, with

$$\boxed{k_{crit} = \sqrt{\frac{g \cos \beta \rho_l}{\sigma}}}$$

and

$$\boxed{\text{stability} \iff (\bar{U}_g - \bar{U}_l)^2 < 2 \frac{\rho_l}{\rho_g} \sqrt{\frac{\sigma g \cos \beta}{\rho_l}}}$$

This criterion is denoted as **MTL** for **Milne-Thompson and Lamb**.

4.2 Viscous Kelvin Helmholtz (VKH)

This criterion is based on the linear stability analysis of the usual 2 fluid model (with the hydrostatic approximation). It takes into account the viscous stresses but not the vertical momentum of the liquid. This was first carried out in [Lin Y., Hanratty T., 1986] and [Barnea D. & Taitel Y., 1993]. We will present this analysis using Barnea and Taitel's notations, which yields a criterion identical to the one found previously, to the difference that f is set to zero in the dispersion equation that becomes:

$$\omega^2 - 2[ak - ib]\omega + ck^2 - dk^4 - eki = 0$$

We can find the neutral stability condition ($\omega_i = 0$) by letting $\omega = \omega_R + i\omega_i = \omega_R$ in the dispersion equation. We then have :

$$2b\omega_R - ek_c = 0$$

$$\omega_R^2 - 2ak_c + \omega_R + ck_c^2 - dk_c^4 = 0$$

We find $\omega_R = \frac{e}{2b}k_c$, hence in this "Viscous Kelvin Helmholtz" analysis, the critical wave velocity at the inception of the instability is given by:

$$C_V = \frac{e}{2b}$$

Reporting this result in the second equation then gives the stability criterion:

$$stability \iff \forall k, (C_V - a)^2 + (c - a^2) - dk^2 < 0$$

This analysis concludes that due to the damping presence of surface tension, the first instability to arise will always be an infinite wave-length ($k = 0$) instability. The wave-speed is determined by the stress tensors only.

4.3 This model (Full Viscous Kelvin Helmholtz) (FVKH)

The critical wave velocity at the inception of the instability is a function of k_c (bearing in mind that both e and b are negative numbers):

$$C_F = \frac{e - f\nu_l^* \overline{U}_l k_c^4}{2b - f\nu_l^* k_c^4}$$

With the following stability criterion:

$$stability \iff \forall k, (C_F - a)^2 + (c - a^2) + k^2 [f(C_F - \overline{U}_l)^2 - d] < 0$$

This model can predict either long or short wavelength instability. Assuming $\rho_l \gg \rho_g$ gives $a \approx \overline{U}_l$ and the stability criterion can be expressed as:

$$stability \iff \forall k, \left(\frac{\frac{e}{2b} - \overline{U}_l}{1 - \frac{f\nu_l^*}{2b} k^4} \right)^2 (1 + fk^2) + (c - a^2) - dk^2 < 0$$

- If $f \left(\frac{e}{2b} - \overline{U}_l \right)^2 < d$ then the left-hand side will reach its maximum for $k_c = 0$, which corresponds to a long wavelength instability and then the model behaves like the VKH model with the same stability criterion $\left(\frac{e}{2b} - a \right)^2 + (c - a^2) < 0$, and the same critical wave velocity $\frac{e}{2b}$.
- If $f \left(\frac{e}{2b} - \overline{U}_l \right)^2 > d$ then the model will predict that the instability arises from a short wavelength perturbation. The left-hand side grows until it reaches a maximum and then decreases to $-\infty$. The critical wave number k_c has to be found numerically. For infinitely short wavelengths, the wave velocity will be equal to \overline{U}_l (as in the MTL model), which is physical. The highly uncertain parameter ν_l^* does not influence the transition between long wavelength and short wavelength instability, and influences only weakly the critical wave number k_c .

4.4 Sum-up of the various criteria

critereon	stability condition		
IKH	$(c - a^2) < 0$		
MTL	$(\overline{U}_g - \overline{U}_l)^2 < 2 \frac{\rho_l}{\rho_g} \sqrt{\frac{\sigma g \cos \beta}{\rho_l}}$		
VKH (BT)	$(\frac{e}{2b} - a)^2 + (c - a^2) < 0$		
FVKH(this model)	$\forall k, (C_F - a)^2 + (c - a^2) + k^2$	$f (C_F - \overline{U}_l)^2 - d$	< 0

Table 1: Stability conditions for the various presented criteria

critereon	Critical wavelength	Critical wave speed
IKH	finite perturbation	
MTL	small(air/wat : 1.7 cm)	$\approx U_l$
VKH (BT)	$+\infty$ (long wave)	$\frac{e}{2b}$
FVKH (this model)	small to long	$\frac{e - f\nu_l^* U_l k_c^4}{2b - f\nu_l^* k_c^4}$ (U_l for small wave-lengths, $\frac{e}{2b}$ for long wavelengths)

Table 2: Critical wave characteristics as predicted by the different criteria

5 Comparisons with experiments : wavelength of the critical perturbation

The wavelength of the "critical wave", the first growing wave appearing during transition to slug flow, before any non-linear phenomenon has had time to occur, is a way to discriminate the models as shown by the table above. However this observation is difficult to make and seldom mentioned by the experimentators.

5.1 Fan et al. horizontal (atmospheric, 9.5 cm, air-water)

In [Fan Z., Lusseyran F., Hanratty T., 1993] experiments were made with air and water in a horizontal 9.5 cm pipe. They write:

"At $U_g^S \leq 3m/s$, slugs appeared at values of \overline{h}_l in agreement with the viscous long-wavelength linear Kelvin-Helmholtz stability analysis. Surprisingly, however, transition was observed to occur by a different mechanism than this analysis suggests. The slugs did not evolve directly from very long-wavelength waves. Rather they evolved indirectly from short-wavelength gravity waves (approximately 8,5 cm). Theses waves double in wavelength as they propagate downstream. This results agrees with a theory by Chen and Saffman (1979,1980) and is the first observation of bifurcation in pipeline flows. The growth in amplitude of $\lambda_1 \cong 8.5$ cm waves, as they propagate downstream, is accompanied by an increase in wave velocity."

Table 3 presents experimental results from Fan et al. and numerical predictions using the proposed model (with $\lambda_i = \lambda_g$ and $\nu_i^* = \nu_l$).

$\frac{U_g^S}{\sqrt{gD}}$	$\frac{\overline{h}_l}{D}$			$\frac{C - \overline{U}_l}{\sqrt{gD}}$		$\frac{\lambda_1}{D}$		$\frac{\lambda_2}{D}$
	Exp	FVKH	VKH	Exp	FVKH	Exp	FVKH	Exp
1.0	0.69	0.62	0.67	0.49	0.35	0.89	1.18	1.78
2.0	0.52	0.53	0.59	0.48	0.32	0.88	1.02	1.76
3.0	0.42	0.47	0.54	0.49	0.30	0.90	0.91	1.81

Table 3: Critical holdup, wavelength and wave velocity, experiments from Fan et al. and predictions

- The FVKH criterion is able to predict that the transition will be due to some short wavelength instability and gives an accurate prediction of the wavelength of the original wave λ_1 . The liquid height prediction is also acceptable. VKH criterion predicts as always long wavelength instability.
- The wave velocity is underestimated, but this is coherent with Fan's observation that *"the growth in amplitude of $\lambda_1 \cong 8.5$ cm waves, as they propagate downstream, is accompanied by an increase in wave velocity"*.
- Furthermore the authors show that for higher values of the gas superficial velocities, instabilities will come from long-wavelength perturbations. This is somehow shown by FVKH to the difference that FVKH predicts this switch from small wavelength to long wavelength instabilities much later, at about 12 m/s.

5.2 Mikal Espedal's PhD thesis (atmospheric, 6cm, air-water, inclined, U_g^S : 3 to 12m/s)

5.2.1 Espedal's observations

In [Espedal M., 1998] the author has made some extensive wave measurements on a 6 cm diameter pipe inclined upwards or downwards. The following table taken from Espedal sums up his observations about wave characteristics:

wave region	$f_{dom} [Hz]$	$\lambda_{dom} [cm]$	comments
small amplitude	10 – 20	3 – 6	most small ampl. experiments
small amplitude	5 – 7	10 – 14	Low U_g^S and U_l^S for -0.5° and -1°
large amplitude	≈ 6	10 – 13	
large amplitude	25 – 35	3 – 6	$U_g^S = 10m/s$ also $f_{dom} = 1Hz$ and $\lambda_{dom} = 1m$

Table 4: Experimental observations from Espedal

5.2.2 The case inclined -0.1°

Large amplitude waves appear only for high flowrates. The power spectrum shown in Figure 2 ($U_g^S = 3$ m/s and $U_l^S = 0.1$ m/s) is typical of the first line of the table above. One can clearly see the presence of one wave of frequency f_1 comprised between 10 to 20 Hz and wavelength ranging between 3 to 6 cm progressively overtaken by another wave of frequency $f_2 = \frac{1}{2}f_1$ when the liquid flowrate increases. This is fully coherent with Fan et al.'s observation of two waves with $\lambda_2 = 2\lambda_1$ and consistent with Hanratty's theory of bifurcation (the wave doubles in wavelength while its speed $C = \lambda f$ remains constant).

As shown by Figure 3 FVKH does not predict a sensibly different liquid height for transition than the Taitel and Dukler's or the VKH criterion. However for $U_g^S < 13$ m/s this criterion predicts that the instability will come from a short wavelength perturbation, and for $U_g^S > 13$ m/s that the instability will come from a long wavelength perturbation. Table 5 shows predictions by the FVKH criterion. Wavelength and frequency of the λ_1 wave are perfectly predicted. Experimentally the transition between small wavelength and long wavelength perturbation happens sooner than predicted by VKH: while at $U_g^S = 8$ m/s a 15 Hz wave is still dominating for low liquid flowrates, long wavelength instabilities seem to be dominating when U_l^S come close to its transitional value. For U_g^S equal to 10 and 12 m/s, long wavelengths perturbations dominate for all liquid flowrates.

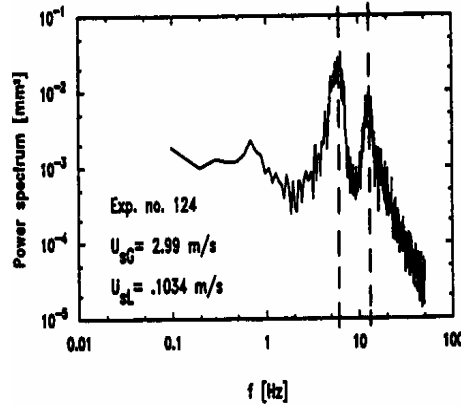


Figure 2: Wave power spectra for $U_g^S = 3 \text{ m/s}$, $U_l^S = 0.1 \text{ m/s}$ and $\beta = -0.1^\circ$. Taken from Espedal.

U _g (m/s)	U _l (m/s)	h _l /D	C (m/s)	lambda (m)	f (Hz)
3	0.16	0.44	0.63	0.06	11.18
4	0.14	0.39	0.63	0.05	12.23
7	0.11	0.29	0.66	0.04	15.46
12	0.07	0.19	0.72	0.04	17.08
13	0.06	0.18	0.73	0.07	10.55
14	0.06	0.16	0.72	Infinite	0.00
18	0.02	0.09	0.68	Infinite	0.00
20	0.01	0.06	0.64	Infinite	0.00

Table 5: Predictions using the proposed model: critical liquid flowrate, liquid height and wave characteristics at transition

5.3 B. Woods' thesis (air-water, atmospheric, 7.63 cm)

In [Woods B., 1998] the author made experiments to study slug initiation. He could identify 3 different mechanisms for slug formation. For zone 1 (low liquid flowrates and $U < 4 \text{ m/s}$) he writes:

"At low gas velocities, slugs evolve from small wavelength (16 to 20 cm), large amplitude waves in horizontal flows. The growth of this wave evolves into a slug when it reaches the top of the pipe. These waves obtain their energy from smaller wavelength waves (8 to 10 cm) through a non-linear growth mechanism. (page iii)

High frequency waves are generated near the inlet. Energy becomes concentrated in waves with $f=10-12 \text{ Hz}$ at $L/D=21.5$. As already shown by Fan et al. (1993), these waves grow and bifurcate, as seen in the spectrum at $L/D=49.1$. The behavior of the 5 Hz waves that result from this bifurcation is very sensitive to the height of the stratified flow." (page 50).

This observation confirms Fan et al.'s and Espedal's works. Woods then indicates that for $U_g^S = 1.8 \text{ m/s}$ and $U_l^S = 0.12 \text{ m/s}$, the wavelength of the dominating wave is 16 – 20 cm with a frequency of 5 Hz (hence a velocity ranging from 0.8 to 1 m/s). This corresponds of course to λ_2 , with $\lambda_2 = 2\lambda_1$ and $f_2 = \frac{1}{2}f_1$. For this case FVKH predicts $\lambda_1 = 8.4 \text{ cm}$, and $C = 0.52 \text{ m/s}$. The wavelength is accurately predicted but the velocity is underestimated. But this is again coherent with Fan's observation that the waves accelerate when they grow.

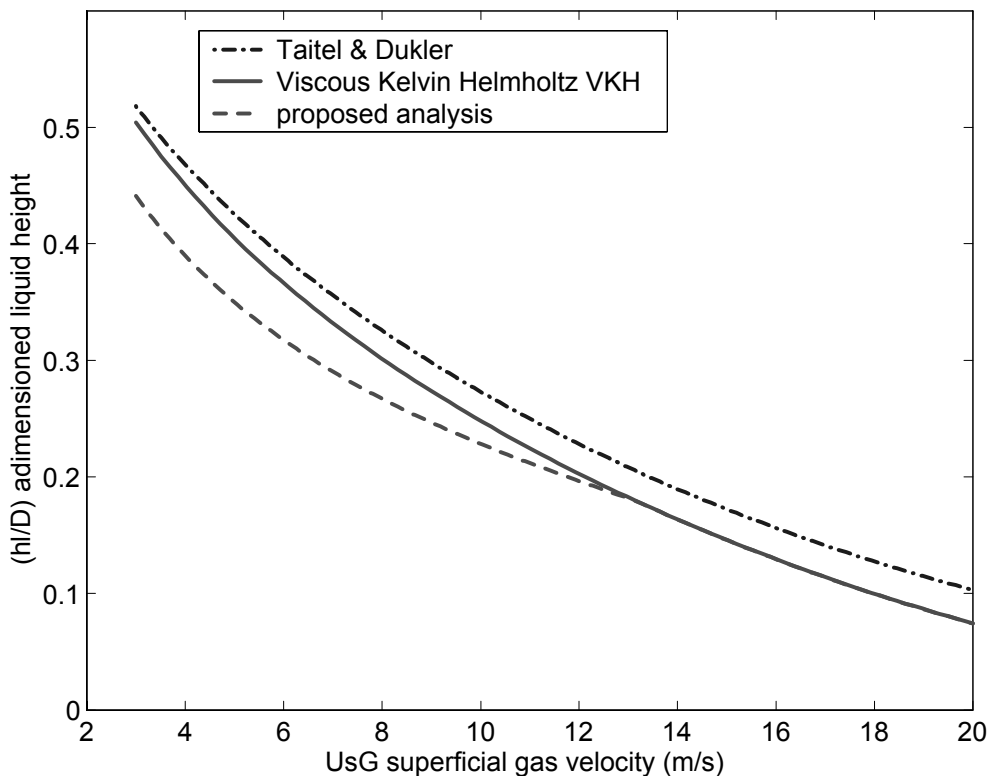


Figure 3: Predicted transition by different criterias, for $U_g^S = 3 \text{ m/s}$, $U_l^S = 0.1 \text{ m/s}$ and $\beta = -0.1^\circ$

6 Numerical benefits

The two-fluid model has recently started to be used to automatically track the initiation of slugs. ([Issa R., Kempf M., 2003]). The code captures automatically the waves which will grow to become slugs. In order to be able to match experiments (moment and location of the slug initiation, wavelength of the critical wave...), some terms which modify small waves growth, like the one proposed, might have to be added. The proposed terms are also a more efficient way to face the ill-posedness that arises when the slugs are initiated numerically than just implementing surface tension. For a normal two-fluid model use (large grid size to track only global mass transport), the proposed additional terms have strictly no influence.

7 Conclusions

The FVKH model seems to predict quite accurately the wavelength of the perturbation responsible for the initiation of slugs. The model predicts also that for high gas superficial velocities, long wavelengths will be responsible for the transition, though this long-short wavelengths transition happens earlier than predicted. In the case of Espedal, who has studied wavy flow (hence at liquid flowrates lower than necessary for transition to slug flow), the velocity of the wave is accurately predicted. The velocity of the wave is under-predicted in the case of Woods and Fan who have studied transition (hence waves growing until transition to slug flow happens), though this is justified by Fan's observation that the waves accelerate when growing. The bifurcation phenomenon (wave doubling in wavelength and halving its frequency, keeping the same speed) is intrinsically a non-linear effect and is not predicted by linear analysis.

References

- [Banerjee S., 1980] Separated Flow Models II Int. Journal Multiphase Flow vol 6. pp 241-248
- [Ransom V. & Hicks D., 1984] Hyperbolic Two-Pressure Models for Two-Phase Flow J. Comp. Physics 33, pp124-131
- [Prosperetti A., 1987] The Linear Stability of General Two-Phase Flow Models II Int. J. Multiphase Flow vol 13, No 2, pp161-171
- [Barnea D. & Taitel Y., 1993] Kelvin-Helmholtz stability criteria for stratified flow: viscous versus non-viscous (inviscid) approaches Int. J. Multiphase Flow vol 19, No 4, pp 639-649
- [Lamb H., 1945] Hydrodynamics, New York Dover Publications
- [Milne-Thompson, 1949] Theoretical Hydrodynamics, MacMillan
- [Taitel Y. & Dukler A., 1976] A model for prediction of flow regime transitions in horizontal and near horizontal gas-liquid flow A.I.C.h.E. J. 22, pp 47-55
- [Hurlburt E, Hanratty T., 2002] Prediction of the transition from stratified to slug and plug flow for long pipes, Int. J. Multiphase Flow 28 pp707-729
- [Fan Z., Lusseyran F., Hanratty T., 1993] Initiation of slugs in horizontal gas-liquid flows. A.I.C.h.E J. 39, pp 1741-1753
- [Espedal M., 1998] An experimental investigation of stratified two-phase pipe flow at small inclinations, PhD thesis, NTNU Trondheim, Norway
- [Woods B., 1998] Slug formation and frequency of slugging in gas-liquid flows, PhD thesis, University of Illinois, USA
- [Lin Y., Hanratty T., 1986] Prediction of the initiation of slugs with linear stability theory, Int. J. Multiphase Flow vol 12, No 1, pp 79-98
- [Issa R., Kempf M., 2003] Simulation of slug flow in horizontal and nearly horizontal pipes with the two-fluid model, Int. J. Multiphase Flow vol